

***MINISTRY OF EDUCATION, RESEARCH,
YOUTH AND SPORT***

UNIVERSITY OF CRAIOVA

ANNALS

MECHANICAL Series

***CRAIOVA
Nr. 1/2010***

ISSN 1223-5296

Scientific committee:

Associate Professor Dan Marghitu PhD, Auburn University USA

Associate Professor Dan Stoianovici PhD, JHU University, Baltimore USA

Prof. univ. dr. ing. Dan Băgnaru, University of Craiova

Prof. univ. dr. ing. Marin Bică, University of Craiova

Prof. univ. dr. ing. Nicolae Dumitru, University of Craiova

Prof. univ. dr. ing. Gheorghe Nanu, University of Craiova

Prof. univ. dr. Adriana Burlea Şchiopoiu, University of Craiova

Conf. univ. dr. ing. Nicolae Crăciunoiu, University of Craiova

Conf. univ. dr. ing. Adrian Sorin Roşca, University of Craiova

Editors:

Conf. dr. ing. Adrian Sorin ROŞCA

Asist.drd.ing. Andrei Gheorghe NANU

CONTENT

1.	JACKSON L. Robert, WILSON W. Everett, MARGHITU B. Dan, CRACIUNOIU Nicolae	Multi-scale thermal contact resistance	3
2.	MARGHITU DAN, SEUNGHUN Lee, CRACIUNOIU Nicolae	Sphere contact with granular media	15
3.	AYKUL Halil, SAYMAN Onur, ÖZYILMAZ Emre, KARA Emre	An analytical elastic–plastic stress analysis in a woven steel reinforced thermoplastic cantilever beam loaded uni- formly	27
4.	ÖZYILMAZ Emre, AYKUL Halil, DALKIZ Mehmet, KARA Emre	On static behavior of dental implants under different load directions	42
5.	HADJOV Kliment, ALEXANDROV Alexander, HALLIL Giunai, MILENOVA Milena, MARIN Mihnea	Creep and damage of rubbers surrounded by aggressive media	48
6.	MARGHITU B. Dan, DIACONESCU Cristian, CRACIUNOIU Nicolae, DUMITRU Nicolae	Dynamics and control of a flexible beam with impacts	62
7.	ILINCIOIU Dan, MIRIȚOIU Cosmin	A shear stress analysis of I-type welded sections (i)	80
8.	DAHAN Marc , RACILA Laurentiu	Some applications for Wohlhart mechanism	88
9.	BOZZINI Fausto, ANOAICA Paul Gabriel	The effects of the modulation power on the energetic sav- ing utilising a condensing boiler	99
10.	KARA Emre, AYKUL Halil, SAYMAN Onur, ÖZYILMAZ Emre	Elastic, plastic and residual stress analysis in symmetric thermoplastic laminated plates under various temperature change through the thickness: analytical solution	107
11.	SEMENESCU Danel, CRACIUNOIU Nicolae, DUMITRU Nicolae, MANEA Ion	Modeling and analysis on adjustable vane	124
12.	Ali UNERI, Marcin BALICKI, James HANDA, Russell TAYLOR, Iulian IORDACHITA	New steady-hand eye robot with microforce sensing and servoing for vitreoretinal surgery	130
13.	PREDA Ion, CIOLAN Gheorghe, ISPAS Nicolae	Optimization study of a car suspension–steering linkage	144

14.	DUMITRU Ilie, POPESCU Simion, VINATORU Matei, POPESCU Traian, CATANEANU Mihnea	Various aspects regarding the design of a gear shift sensor for road vehicles	155
15.	COVACIU Dinu, PREDĂ Ion, FLOREA Daniela, CÂMPIAN Vasile	Development of a driving cycle for brasov city	161
16.	ILINCIOIU Dan, MIRIȚOIU Cosmin	A shear stress analysis of I-type welded sections (ii)	169
17.	KURSUN Ali , ȘENEL Mahomet	Investigations of tension-tension pre-stress effects on glass reinforced composite plates under the low-velocity impact	175
18.	ZAMFIRACHE Marius	Research regarding the roughness of the surfaces titanium unaloyd miling	185
19.	MIRIȚOIU Cosmin, IOVAN Alina	A strength analysis for a metallic bridge truss structure	191
20.	POPESCU Daniel	Study of technologies for recovering silicone rubber from composite insulators	202
21.	CĂLBUREANU Mădălina, MALCIU Raluca, TUTUNEA Dragoș, DIMA Alexandru	Modeling with finite element method the convective heat transfer in civil building eps insulated walls	208

MULTI-SCALE THERMAL CONTACT RESISTANCE

JACKSON L. Robert*, WILSON W. Everett*, MARGHITU B. Dan*,
CRACIUNOIU Nicolae**

* Auburn University, Department of Mechanical Engineering

** University of Craiova, Faculty of Mechanics

Abstract: All surfaces are rough to some extent and therefore only a small portion actually contact when they are brought together. Therefore heat flow from one object to another is obstructed by this incomplete contact, resulting in thermal contact resistance. This work presents a new method for modeling TCR while considering the multi-scale nature of surfaces in the contact mechanics and heat transfer theory. Based on Archard's "protuberance upon protuberance" theory, this method employs sinusoids stacked into layers to represent the rough surface.

Keywords: contact resistance, thermal resistance, roughness, surface contact

1. INTRODUCTION

Economically improving heat conduction from MEMS and micro-electronics is a growing issue in the industry since the size of electronic devices continues to decrease. The decrease in the size of electronic devices reduces the available surface area for heat dissipation, leading to large increases in heat flux. This can yield increases in operating temperatures that exceed design criteria. Thus, the thermal contact resistance (TCR) between these devices and a heat sink is very important, as it limits the rate at which heat can be dissipated. It is well known that the roughness between contacting surfaces can reduce the real area of contact and thus bottleneck the heat flow, which is seen as an increase in the TCR.

There are many different methods to model the contact of rough surfaces including statistical[1-5], fractal [6] and multiscale models[7-9]. Several empirical models of TCR have also been derived [10-13]. The fractal mathematics based methods were derived to account for

different scales of surface features not accounted for by the statistical models. The multiscale models were developed to alleviate the assumption of self-affinity imposed by fractal mathematics and also improve how the mechanics are considered. This work uses a Fourier transform to convert the data into a series of stacked sinusoids see Fig. 1. Also, the surface characteristics necessary to obtain convergence of the iterative multiscale scheme are examined.

The current work will build on an earlier multiscale model of thermal contact resistance[14] that was based on using FEM models of elastic-plastic spherical contact to consider asperity deformation at each scale. Instead, the current work uses recent models of elastic-plastic sinusoidal contact[15, 16] to consider asperity deformation. Later, Wilson et al.[17], showed that surface separation could also be predicted.

2. CONTACT MECHANICS

A. MULTI-SCALE PERFECTLY ELASTIC CONTACT

This work uses the mostly the same underlying assumptions as the multi-scale rough surface contact model by Jackson and Streater [9], except that the asperities are model as wavy or sinusoidal surfaces instead of spheres. The multi-scale model derived by Jackson and Streater [9] uses the same direction of thought as Archard [18], but provides a method that can be easily applied to real surfaces.

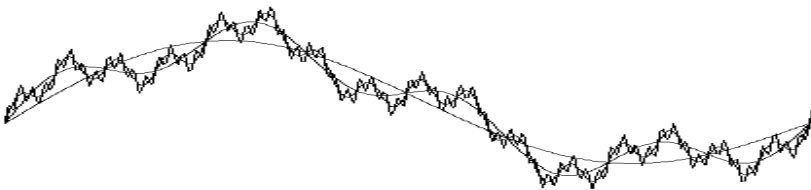


Fig. 1. Schematic depicting the decomposition of a surface into superimposed sine waves. Each line represents a different scale of roughness

First, a fast Fourier transform is performed on the surface profile data. Then the resulting data is a summation of a series of sine and cosine waves. The complex forms of the sine and cosine terms at each frequency are combined using a complex conjugate to provide the amplitude of the waveform at each scale for further calculations. Each

frequency is considered a scale or layer of asperities which are stacked iteratively upon each other (see Fig. 1). In equation form these relationships are given by:

$$A = \left(\prod_{i=1}^{i_{\max}} \overline{A_i \eta_i} \right) A_n, \quad (1)$$

$$P = \overline{P_i \eta_i} A_{i-1}, \quad (2)$$

where A is the real area of contact, η is the areal asperity density, P is the contact load, A_n is the nominal contact area, and the subscript i denotes a frequency level, with i_{\max} denoting the highest frequency level considered.

For wavy or sinusoidal surfaces, the area density of asperities is given as $\eta_i = 2f_i^2 A_{i-1}$

Table 1: Nomenclature

A area of contact	p^* average pressure of complete contact
\overline{A} individual asperity area of contact	R thermal contact resistance
A_n nominal contact area	S_y yield strength
a radius of the area of contact	<i>Greek Symbols</i>
B material dependant exponent	η area density of asperities
C critical yield stress coefficient	δ separation of mean surface height
D contact area factor	λ asperity wavelength
E elastic modulus	Δ asperity amplitude
$E' E/(1-\nu^2)$	Ψ alleviation factor
e_y yield strength to elastic modulus ratio, S_y/E'	ν Poisson's ratio
f spatial frequency (reciprocal of wavelength)	<i>Subscripts</i>
k thermal conductivity	P elastic-plastic regime
L scan length	c critical value at onset of plastic deformation
P contact force	i frequency level
\overline{P} individual asperity contact force	JGH from Johnson, Greenwood, and Higginson [19]
\overline{p} mean pressure	asp asperity
	sur surface

$$(A_{JGH})_1 = \frac{2\pi}{f^2} \left[\frac{3}{8\pi} \frac{\bar{p}}{p^*} \right]^{2/3}, \quad (3)$$

$$(A_{JGH})_2 = \frac{1}{f^2} \left(1 - \frac{3}{2\pi} \left[1 - \frac{\bar{p}}{p^*} \right] \right) \quad (4)$$

For $\frac{\bar{p}}{p^*} < 0.8$

$$A = (A_{JGH})_1 \left(1 - \left[\frac{\bar{p}}{p^*} \right]^{1.51} \right) + (A_{JGH})_2 \left(\frac{\bar{p}}{p^*} \right)^{1.04} \quad (5)$$

For $\frac{\bar{p}}{p^*} \geq 0.8$

$$A = (A_{JGH})_2 \quad (6)$$

Where p^* is the average pressure to cause complete contact between the surfaces and is given by [19] as:

$$p^* = \sqrt{2\pi E' \Delta f} \quad (7)$$

B. MULTI-SCALE ELASTIC-PLASTIC CONTACT

However, many of the asperities at the different frequency levels undergo plastic deformation. Therefore an elastic-plastic sinusoidal contact model is needed to consider this effect. The equations used in the current work to calculate the elastic-plastic contact are derived from FEM results by Krithivasan and Jackson [15, 16]. The methodology is very similar to that of the perfectly elastic case with the exception of using a different set of formulas once a calculated critical pressure and area are reached. The critical load and area are given by [20]:

$$P_c = \frac{1}{6\pi} \left(\frac{1}{\Delta f^2 E'} \right)^2 \left(\frac{C}{2} \cdot S_y \right)^3 \quad (8)$$

$$A_c = \frac{2}{\pi} \left(\frac{CS_y}{8\Delta f^2 E'} \right)^2 \quad (9)$$

Where C is given as

$$C = 1.295 \cdot \exp(0.736\nu) \quad (10)$$

At low loads, $P < P_c$, and consequently small areas of contact, it is acceptable to assume that any deformation of the asperities in contact will behave perfectly elastically. However, as load increases to the critical value, plastic deformation will begin to occur within the asperities. To evaluate the plastic deformation we replace Eq. (3) with:

$$A_p = 2(A_c)^{\frac{1}{1+d}} \left(\frac{3\bar{p}}{4CS_y} \lambda^2 \right)^{\frac{d}{1+d}} \quad (11)$$

$$d = 3.8 \cdot \left(\frac{E'}{S_y} \cdot \frac{\Delta}{\lambda} \right)^{0.11} \quad (12)$$

This replacement results in the following equation for contact area:

$$A = (A_p) \left(1 - \left[\frac{\bar{p}}{p_P^*} \right]^{1.51} \right) + (A_{JGH})_2 \left(\frac{\bar{p}}{p_P^*} \right)^{1.04} \quad (13)$$

$$\frac{p_P^*}{p^*} = \left(\frac{11}{4 \cdot \Delta / \Delta_c + 7} \right)^{\frac{3}{5}} \quad (14a)$$

$$\Delta_c = \frac{\sqrt{2} \cdot S_y \exp\left(\frac{2\nu}{3}\right)}{3\pi E' f} \quad (14b)$$

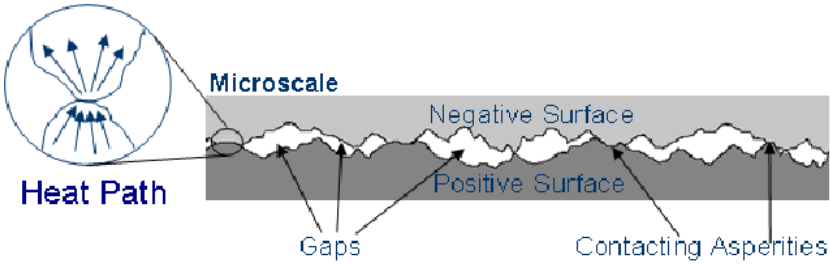


Fig. 2 – Schematic of “bottlenecked” current flow through asperities

3. THERMAL CONTACT RESISTANCE

One of the concerns of this work is calculating the effect of surface roughness on electrical resistance. Assuming that the surfaces in contact are conductors and have some current associated with them, the goal is to determine how the flow of current is affected by the true area of contact for each load level. Since only a few, scattered asperities are actually in contact for any given load level, the current is restricted to very small contact patches when compared to the area of the entire surface. As the current flows through these asperity peaks, it will be effectively “bottlenecked” resulting in some resistance to the conduction as seen in Fig. (2).

Holm [21] gives a simple formula to calculate the electrical resistance due to asperity contact (which is adjusted here for thermal contact resistance).

$$R = \frac{1}{2ak} \quad (15)$$

However, this equation is only good for a single asperity. In the case of multi-scale techniques, additional equations are required to calculate resistance for the entire surface.

A. MULTI-SCALE THERMAL CONTACT RESISTANCE

The multi-scale sinusoidal method presented here is an iterative method that calculated area and resistance for each particular frequency level. The first step is to calculate the average radius of contact per frequency level i :

$$a_i = \sqrt{\frac{A_i}{2 \cdot \pi \cdot A_{i-1} \cdot f^2}} \quad (16)$$

Once the contact radius is established, Eq. (15) is implemented to calculate resistance per asperity per level. Oftentimes, an alleviation factor is used in thermal contact resistance calculations to account for the affect of a large contact radius, a , in relation to the nominal area of contact. For the sinusoidal case, it is assumed that the tip of the asperity is similar to a hemisphere so the spherical radius is used. Though there are various ways to calculate this factor [22], the simplified version offered by Cooper et al. [23] is chosen for this work:

$$\Psi_i = \left(1 - \sqrt{\frac{A_i}{A_{i-1}}} \right)^{1.5} \quad (17)$$

Therefore, the electrical contact resistance per asperity level is:

$$R_i = R \cdot \Psi_i \quad (18)$$

This value is then summed over the all possible iteration levels to find the total resistance for the entire surface in contact.

$$R_{total} = \sum_{i=1}^{i_{max}} R_i / \eta_i A_i \quad (19)$$

It is important to note that this technique calculates the resistance for each frequency level and then sums over all frequency levels to calculate the total resistance (assuming they are in series as shown in Eq. (19)). Also, the methodology does not change depending on the inclusion of plasticity since all resistance calculations are done after obtaining the contacting area.

Table 2: Material Properties of Steel

$E=200\text{GPa}$	$S_V=500\text{ MPa}$
$\nu=0.3$	$K = 43\text{ W/m}^2\text{K}$

4. MODEL PREDICTIONS

Once the data is gathered, a Fast Fourier Transform is performed as mentioned before. The result is then converted to a single amplitude for each frequency level via the complex conjugate. The surface employed in the current work and the resulting spectrum (amplitude as a function of frequency) are shown in Figs. 3 and 4. Note that each frequency of the series represents a scale of asperities on the surface. Then the multi-scale models can be implemented as described above.

This work assumes real material properties for all the results gathered (see Table 2). The material of choice is steel due to its common use in engineering applications. The surface profile is

measured from an arbitrary machined metal sample using a stylus profilometer. To ensure an accurate comparison of the contact models, the material properties are kept constant for all calculations.

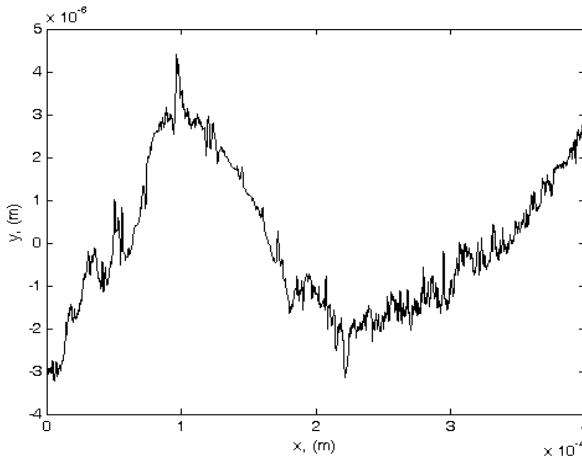


Fig. 3 – Rough surface data recorded from a stylus profilometer and used in the current work

First to illustrate the iterative nature of the model, the real contact area for each scale level or iteration is shown in Fig. (5). At each scale level, also referred to as frequency level, the contact area is reduced because more surface details are included.

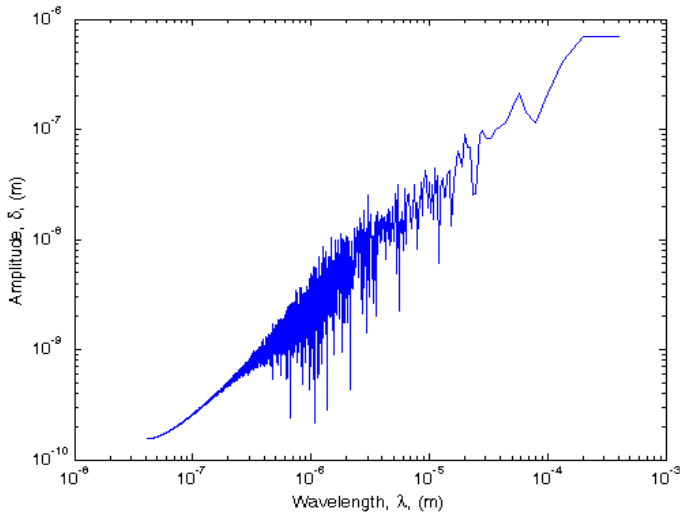


Fig. 4 – Amplitude versus scale spectrum of the surface shown in Fig. 3

In the current methodology and for certain surfaces the real area of contact appears to asymptotically approach a solution as more levels or iterations are included. However, as shown in several works [8, 17, 24], some surfaces possessing a self-affine quality might not converge.

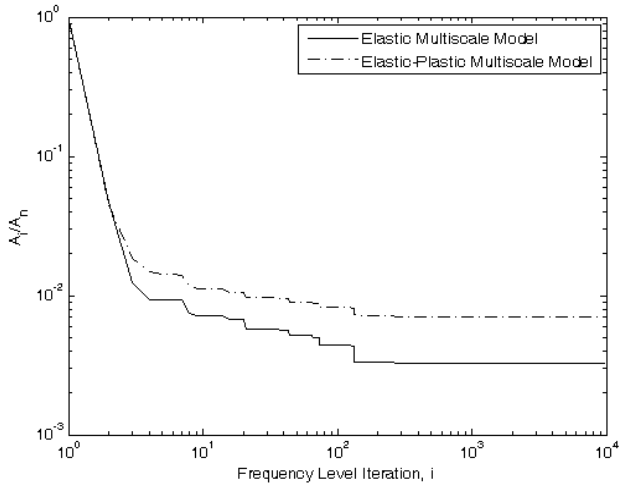


Fig. 5 – Decrease in the real area of contact with iterative inclusion of successive scales or frequencies

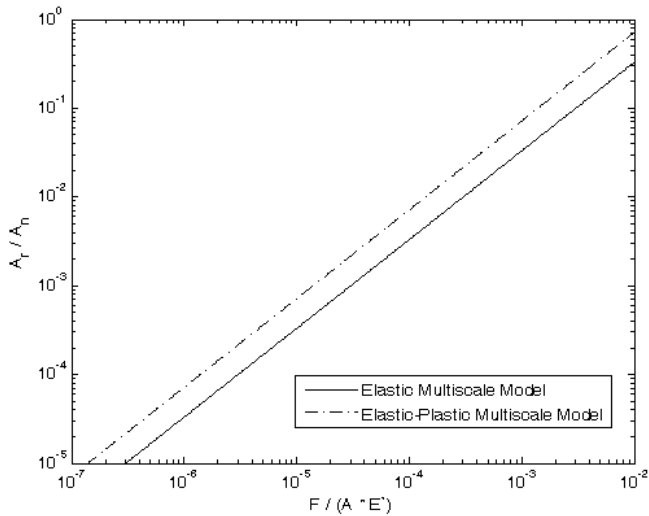


Fig. 6 – Plot of non-dimensional area vs. load

The multiscale methodology is able to also make predictions for the real area of contact as shown in Fig. 6 for the perfectly elastic and elastic-plastic cases. As seen in Fig. 6, higher loads result in a greater area of contact, as would be expected. Greater contact area also results from the inclusion of plastic deformation. This is caused by the behavior of the solid asperities to flow and flatten under plastic deformation. The asperity material tends to “flow” resulting in greater deformation as well as “filling in” the low spots around each asperity. This combines with the higher loads to produce larger amounts of contact.

Fig. 7 shows the calculated results for non-dimensional contact resistance using the multiscale model for the elastic and elastic-plastic cases. To dimensionalize the thermal contact resistance simply multiply by the surface roughness divided by the nominal area and thermal conductivity.

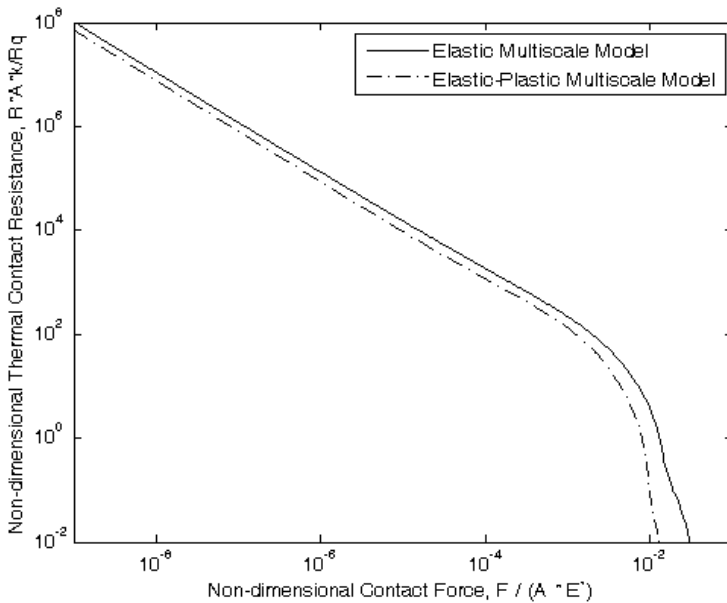


Fig. 7 – Electrical contact resistance as a function of non-dimensional load

However, the shown plot is not a universal curve for different surface profiles and it is suggested that the model be performed individually for each surface of interest. Since the thermal resistance is due to the gaps between the surfaces, it follows naturally that the

thermal resistance curves behave inversely of load. Yet again, the greater contact area and decreased load of the plastic deformation shows in the thermal resistance plot as it results in lower resistance values. Although the contact area appears to be a linear function of load (see Fig. 6) and agrees with the venerable papers of Archard[18] and Greenwood and Williamson[1], the thermal contact resistance shows a more interesting trend at higher loads. The model predicts that as the contact approaches completeness (i.e. no gaps between the surfaces), the thermal contact resistance drops off quickly from its steady decline for lower loads.

5. CONCLUSIONS

This work has presented a new method of calculating elastic-plastic thermal contact resistance based upon a multiscale model of rough surfaces built on stacked sinusoids. The model also shows similar trends whether considering perfectly-elastic or elastic-plastic asperity deformation. As expected, the real contact area increases linearly with load, however the thermal contact resistance decreasing steadily with load, but suddenly drops off as the real contact area approaches the nominal area of contact. The presented model is fairly easy to implement. It should be noted though that there are many effects not considered which may influence the predictions, such as adhesion, scale dependent and temperature dependant properties, and surface resolution.

REFERENCES

1. Greenwood, J.A. and J.B.P. Williamson, Contact of Nominally Flat Surfaces. Proc. R. Soc. Lond. A, 1966. **A295**: p. 300-319.
2. Chang, W.R., I. Etsion, and D.B. Bogy, An Elastic-Plastic Model for the Contact of Rough Surfaces. ASME J. Tribol., 1987. **109**(2): p. 257-263.
3. Greenwood, J.A. and J.H. Tripp, The Contact of Two Nominally Flat Rough Surfaces. Proc. Instn. Mech. Engrs.: Part J, 1971. **185**: p. 625-633.
4. Jackson, R.L., The Effect of Scale Dependant Hardness on Elasto-plastic Asperity Contact between Rough Surfaces. STLE Trib. Trans., 2006. **49**(2): p. 135-150.
5. Jackson, R.L. and I. Green, A Statistical Model of Elasto-plastic Asperity Contact between Rough Surfaces. Trib. Int., 2006. **39**(9): p. 906-914.
6. Majumdar, A. and B. Bushnan, Fractal Model of Elastic-Plastic Contact Between Rough Surfaces. ASME J. Tribol., 1991. **113**(1): p. 1-11.

7. Bora, C.K., E.E. Flater, M.D. Street, J.M. Redmond, M.J. Starr, R.W. Carpick, and M.E. Plesha, Multiscale Roughness and Modeling of MEMS Interfaces. *Tribology Letters*, 2005. **19**(1): p. 37-48.
8. Ciavarella, M., G. Demelio, J.R. Barber, and Y.H. Jang, Linear elastic contact of the Weierstrass Profile. *Proc. R. Soc. Lond. A*, 2000(456): p. 387-405.
9. Jackson, R.L. and J.L. Streater, A Multiscale Model for Contact between Rough Surfaces. *Wear*, 2006. **261**(11-12): p. 1337-1347.
10. Lambert, M.A. and L.S. Fletcher, Review of models for thermal contact conductance of metals. *Journal of Thermophysics and Heat Transfer*, 1997. **11**(2): p. 129-140.
11. Madhusudana, C.V. and L.S. Fletcher, Contact Heat Transfer - The Last Decade. *AIAA Journal*, 1986. **24**(3): p. 510-523.
12. Madhusudana, C.V., L.S. Fletcher, and G.P. Peterson, Thermal conductance of cylindrical joints. A critical review. *Journal of Thermophysics and Heat Transfer*, 1990. **4**(2): p. 204-211.
13. Yovanovich, M.M., Four Decades of Research on Thermal Contact, Gap, and Joint Resistance in Microelectronics. *IEEE Trans. Compon. Packag. Technol.*, 2005. **28**(2): p. 182-206.
14. Jackson, R.L., S.H. Bhavnani, and T.P. Ferguson, A Multi-scale Model of Thermal Contact Resistance between Rough Surfaces. *ASME J. Heat Transfer*, 2008. **130**: p. 081301.
15. Krithivasan, V. and R.L. Jackson, An Analysis of Three-Dimensional Elasto-Plastic Sinusoidal Contact. *Tribology Letters*, 2007. **27**(1): p. 31-43.
16. Jackson, R.L., V. Krithivasan, and W.E. Wilson, The Pressure to Cause Complete Contact between Elastic Plastic Sinusoidal Surfaces. *IMEchE J. of Eng. Trib. - Part J.*, 2008. **222**(7): p. 857-864.
17. Wilson, W.E., S.V. Angadi, and R.L. Jackson, Surface Separation and Contact Resistance Considering Sinusoidal Elastic-Plastic Multi-Scale Rough Surface Contact. Accepted., 2009.
18. Archard, J.F., Elastic Deformation and the Laws of Friction. *Proc. R. Soc. Lond. A*, 1957. **243**: p. 190-205.
19. Johnson, K.L., J.A. Greenwood, and J.G. Higginson, The Contact of Elastic Regular Wavy Surfaces. *Int. J. Mech. Sci.*, 1985. **27**(6): p. 383-396.
20. Jackson, R.L. and I. Green, A Finite Element Study of Elasto-Plastic Hemispherical Contact. *ASME J. Tribol.*, 2005. **127**(2): p. 343-354.
21. Holm, R., *Electric Contacts*. 4th ed. 1967, New York: Springer Verlag. 21.
22. Madhusudana, C.V., *Thermal Contact Conductance*. 1996, New York: Springer-Verlag.
23. Cooper, M.G., B.B. Mikic, and M.M. Yovanovich, Thermal Contact Conductance. *Int. J. Heat Mass Transfer*, 1969(12): p. 279-300.
24. Jackson, R.L., An Analytical Solution to an Archard-type Fractal Rough Surface Contact Model. *Trib. Trans.*, 2009. **In Print**.

SPHERE CONTACT WITH GRANULAR MEDIA

MARGHITU DAN^{*}, SEUNGHUN Lee^{*}, CRACIUNOIU Nicolae^{**}
^{*}*Auburn University, Department of Mechanical Engineering*
^{**}*University of Craiova, Faculty of Mechanics*

Abstract: In this paper a rigid sphere is obliquely impacting a granular media. The influences of initial impact velocity and impact angle are examined. We are using a horizontal and a vertical resistance force of the media upon the rigid body. The penetrating distance is increasing with initial impact velocity as expected. However, the stopping time for most of the cases is decreasing with the initial impact velocity

Keywords: sphere, contact, granular media

1. INTRODUCTION

The impact with a granular media is a very interesting phenomenon because of the characteristics of granular materials similar to a solid and they flow similar to a fluid. The focus of recent works is the observations on a low speed impact and the correlation between initial velocity and stopping time in the granular media [5].

Tsimring and Volfson [9] studied the penetration of large projectiles into dry granular media. They proposed the resistance force model as a velocity dependent drag force and depth dependent friction force. The depth dependant friction force models have been developed for the horizontal motion in [6, 7, 8, 14] and for the vertical motion in [3, 13]. Researchers analyzed the impact results including the impact cratering, the impact depth, and the stopping time based on their model of resistance force. Ambroso *et al.* [10] concluded the stopping time is a function of the geometry and the initial velocities. Hou *et al.* [12] studied the time dependence of the velocity of the projectiles and concluded this velocity is not a linear function of the time. They also found that the granular media have a similar behavior to a fluid during initial impact.

The paper of Katsuragi and Durian [5] has sparked new interest in the field of impact with a granular matter. They applied the resistance force model proposed by [9] and verified the motion of a rigid sphere

with a line-scan digital CCD camera. The force is composed of gravity, static resistance force, and dynamic frictional force. They analyze an interesting phenomenon how rapidly a sphere impacting a granular media slows upon collision. Analysis shows that as the speed at which the spheres impact the media increases, the sooner it will come to rest.

In our study we focus on simulation of the oblique impact with the granular media and we analyze the stopping time, travelling distance, and initial velocities. We considered a sphere with planar motion.

2. FORCE ANALYSIS

In case of impact with penetration, the most important interaction between a rigid body and the media is the resistance force from the moment of impact until the body stops. The resistance forces generated during a rigid body penetration are made up of drag forces proportional to the square of velocity and drag force associated with the plasticity of the media, [1, 4]. The resistance force can be expressed as:

$$F_r = B(x, \dot{x})x^2 + C(x, \dot{x}), \quad (1)$$

where x is the rigid body displacement, \dot{x} is the rigid body velocity, B is the drag coefficient, C is the drag associated with plasticity. For low speed the simplest model is given by Lohse *et al.* [2] where the resistance force is k_x , with k a constant.

The Bingham model $F_r = F_0 + bv$ is applied in the case when the drag is viscous and the Poncelet model $F_r = F_0 + cv^2$ is applied in case when the drag is inertia, where v is the velocity of rigid body relative to media, b and c are the drag coefficients. The Bingham model has recently been advocated for granular impact, while the Poncelet model has long been used for ballistics applications [10]. However, some recent research results [3, 6, 7, 8, 13, 14] indicate that static resistance force defined as constant in the Bingham and the Poncelet model depends on the depth of penetration linearly or non-linearly. Tsimring and Volfson [9] proposed the force law based on the Poncelet model. The total resistance force acting on a moving rigid body in granular media is made up of static resistance force characterized by depth-dependent friction force as well as dynamic frictional force characterized by velocity-dependent drag force:

$$F_r = F_s(z) + F_d(v), \quad (2)$$

where F_s is the static resistance force, F_d is the dynamic frictional force and z is the immersed depth of the rigid body. For some

researchers, the static resistance force F_s is called Coulomb friction force [5], or drag force [3, 6, 8, 13, 14], and the dynamic frictional force F_d is also called inertial drag [5].

2.1 DYNAMIC FRICTIONAL FORCE F_D

The dynamic frictional force, F_d , is a velocity-dependent force, generated by the movement of a rigid body in the granular media from impact moment to stop. Even though the state of granular media is not fluid but solid, once the rigid body moves through granular media, the granular media contacting with the moving rigid body partly act like fluid. From this fluid-like behavior of granular media, the force is assumed to be as a drag force impeding the rigid body motion. The drag force can be modelled as a quadratic drag force $F_d = 0.5\rho AC_d v^2$ or a linear drag force $F_d = bv$, where ρ is the density of the media, v is the speed of the rigid body relative to the fluid, A is the reference area, and C_d as well as b are the drag coefficients. Recent results [5, 9] show that the quadratic drag force model is suitable in case of granular media even at low speed regime. The quadratic drag has been modelled as [9]

$$F_d = \alpha v^2 = \beta A v^2 \quad (3)$$

where β is a drag coefficient determined from experimental results.

2.2 STATIC RESISTANCE FORCE F_s

Static resistance force is an internal resisting force and appears when an external force is applied. The force does not depend on velocity or acceleration of the rigid body and acts such as internal stress. The static resistance force in the granular media is influenced by media properties. Some simple models considered the static resistance force as constant. However, the theoretical model of the force is considerably complex because the force is generated between the rigid body and media in contact as well as between granules of the rigid body circumference or of even bulk scale. The reason of this force acting in wide regional range is that the force acts on following consecutive granular media movement propagation beginning with displacement from path of the rigid body and ending with large scale reorganization of media. This force propagation chain is influenced by properties of media, external form of the rigid body, packaging state of media, even the form of the vessel containing media, and any insignificant changes of these terms [8]. These uncertainties of real impact problem into granular media make the forces not to propagate

uniformly through the granular media but localized along directional force chains. The inhomogeneous force propagation and the irregular grain reorganization cause the fluctuation of the static resistance force in the direction and the magnitude. Due to this complicated process of transmitting the force, there are few general continuum theories completely describing the force [3]. In this paper, we apply a horizontal and vertical static resistance forces developed by theoretical and empirical approaches.

2.2.1 HORIZONTAL STATIC RESISTANCE FORCE F_{SH}

Horizontal static resistance force is defined as the internal impeding force acting on horizontal direction. The researches in this field have been extensively theoretical and experimental and they have considered the force propagation [8]. Albert *et al.* [14] applied the probability approach using the q model developed by Coppersmith *et al.* [15] in order to obtain the mean horizontal static resistance force. In this model, the propagation chains are built up by the force fractions that act on a given particle of media. The force fraction is unequally split into fractional forces and transmitted to the adjacent particles. When a certain force F applied on an rigid body horizontally, $P(j,F)$ is the probability of a certain depth position j exceeding a critical force necessary to make a medium slip relative to another. For a rigid body to move horizontally relative to the medium the probability $P(j,F)$ should simultaneously meet the condition $P(j,F) = 1$ at any depth position. The minimum force F_{sh} for this condition of a vertically immersed cylinder is [14]

$$F_{sh} = \eta_h g \rho_g H^2 d_c \quad (4)$$

where g is the gravitational acceleration, ρ_g is the density of the individual solid grains, H is vertically immersed length of cylinder, d_c is the diameter of the cylinder, and η_h is a constant depending on the media properties such as surface friction, morphology, packing of the grains, etc. Using the same process, the horizontal static resistance force of the cylinder including the state of immersion, at any slope, can be generalized as

$$F_{sh} = \eta_h g \rho_g H d_c z \quad (5)$$

where H is the length of cylinder immersed and z is the depth of immersed cylinder tip. In the case of a sphere, the horizontal static resistance force is

$$F_{sh} = \eta_h g \rho_g d_b^2 z \quad (6)$$

where d_b is the diameter of a sphere. Equations (4), (5), and (6) show that the horizontal static resistances force is a function of granular properties as well as the immersed surface area, and the depth. Regarding the horizontal static resistance force there are two remarks. First, the equations do not reflect the periodical force fluctuation such as stick and slip phenomenon which is confirmed in experimental results. However, experimental data show that the equations can be applied to the static resistance force model not only in the case of little fluctuation phenomenon but also in the case of large fluctuation because the force expressed by equations represents the average static force of fluctuation [6, 8]. Second, the equations reflect that the surface state and the mass of the rigid body scarcely affect the static resistance force and this trend is confirmed in experiments with various rigid bodies of different friction coefficient [8]. In other words, any rigid body only with the same shape can cause almost the same results regardless of the rigid body's properties, such as density and surface friction. In addition, this trend reveals that friction force between media and rigid body surface in contact, as well as the inertia of the rigid body have negligible contribution to the total horizontal static resistance force.

2.2.2 VERTICAL STATIC RESISTANCE FORCE F_{sv}

Vertical static resistance force is defined as the internal impeding resistance acting on vertical axis. The vertical static resistance force is a nonlinear function of the immersion depth. In addition, the effects of the container bottom boundary and of the rigid body moving direction are also primary factors that make this force modelling difficult. There exist very few continuum models for dynamic dense granular system. G. Hill *et al.* [3] suggests empirical equation and coefficients based on their experimental data

$$F_{sv} = \eta_v (z/l)^\lambda g \rho_g V \quad (7)$$

where V is the volume of the rigid body and l is the minimal lateral dimension. The coefficients η_v and λ are depending on the shape of the impact rigid body, the properties of granular media and a rigid body, the shape of media container, and the moving direction such as plunging and withdrawing. However, the orientation of its axis has little effect on the vertical static resistance force for the cylinder type rigid body. Whether the axis is vertical or horizontal, the coefficients η_v and λ are

approximately 1.4 and 10 for plunging motion and 0.5 and 1.7 for withdrawing motion based on the empirical data. Tsimring and Volfson [9] have modelled the vertical static resistance force of a sphere as $F_{sv} = \eta z^2 g \rho_g d_b$.

This force can be rewritten in the form of Eq. (7) with $\eta_v = 6\eta/\pi$ and $\lambda = 2$ where $\eta_v = 15 \pm 3$ and $\lambda = 1.2 \pm 0.1$ in case of a plunging sphere [3]. Katsuragi and Durian [5] use the empirical force $F_{sv} = 1040m_b z$ for their simulation model. This force can be rewritten as $F_{sv} = 14.3(z/l)g\rho V$.

3. MODELLING AND SIMULATION

For this research we focus on the oblique impact with granular media for a sphere in planar motion, a mathematical pendulum, and a compound pendulum. We want to analyze the effect of the impact angle and initial velocity on the stopping time of the rigid body.

3.1 OBLIQUE IMPACT OF RIGID SPHERE

First, the model of an oblique impact of a rigid sphere into the granular media is presented. In the case of the oblique impact of a sphere, the total force acting on the rigid sphere is gravity, static resistance force F_s and dynamic frictional force F_d as shown in Fig. 1(a).

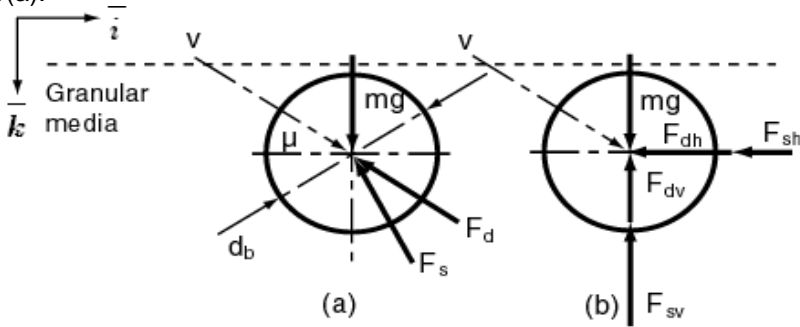


Fig. 1 (a) – Oblique impact of rigid sphere and (b) Free body diagram

Neglecting the rotation of the body, Newton's second law for the sphere gives:

$$m_b \ddot{r} = m_b g + F_s + F_d \quad (8)$$

where $r = x\bar{i} + z\bar{k}$ is the position vector of rigid sphere, $\ddot{r} = a$ is acceleration, and m_b is the mass of a rigid body. The model is based on 3 assumptions. The motion of the rigid body is restricted to 2 dimensional motions within x - z plane. Second, there is no rebound at the impact moment regardless of initial velocity v_i and initial impact angle θ_i . Third, all forces acting on a sphere are assumed to act on the center of the sphere.

On the vertical z direction, the forces acting on the sphere are: the gravity force m_{bg} , the vertical static resistance force F_{sv} , and the vertical component of dynamic frictional force F_{dv} as described in [5, 9]. The forces acting on x -axis are the horizontal static resistance force F_{sh} and the horizontal component of dynamic frictional force F_{dh} . Equations (8), (3)), (6) and (7) give:

$$m_b \ddot{z} = m_b g - F_{sv} - F_{dv} = m_b g - \eta_v (z/d_b)^\lambda g \rho_g V_b - \beta A \dot{z}^2 \quad (9)$$

$$m_b \ddot{x} = -F_{sh} - F_{dh} = -\eta_h g \rho_g d_b^2 z - \beta A \dot{x}^2 \quad (10)$$

The parameters for the simulation are: the mass is $m_b = 0.0692\text{kg}$, the diameter is $d_b = 0.0254\text{m}$, $g = 9.8 \text{ m/s}^2$, the granular density $\rho_g = 1520 \text{ kg/m}^3$, the coefficients are $\eta_v = 14.3$, $\eta_h = 9$, $\beta = 1569.7$, and $\lambda = 1$. These parameters were used in [5].

4. RESULTS

The simulation were performed in MATLAB SIMULINK using the ODE4 (Runge-Kutta) method and also in Mathematica using NDSolve. The impact angles for the simulations are $\theta_i = 5^\circ$, 15° , 45° and 75° .

Figure 2(a) represents the simulation data for the sphere for different impact angles ($\theta_i = 75^\circ$, 45° , and 15°) and different initial velocities ($v_i = 0, 1, 2, 3$, and 4 m/s). Also on the figure the distance of the sphere into the granular media, d_p , is represented ($d_p = \int v dt$) as shown in Fig. 2(b). The stopping distance of the sphere is increasing with the initial velocity for all the cases [Fig. 2(a)]. However for all the simulations when the initial velocity is increased the stopping time into the granular media is decreasing. This interesting characteristic involving how rapidly a particle strikes the granular media slowing down upon contact were reported in [5]. As the speed v_i at which a particle impacts the media increases the sooner it will come to a stop.

Figure 3 shows the impact of the sphere for $\theta_i = 15^\circ$ and two initial velocities ($v_i = 3$ and 4 m/s). Fig. 3(a) shows the vertical velocities v_z

and Fig. 3(b) shows the horizontal velocities v_x . For the initial velocities $v_i = 3$ and 4 m/s the vertical velocities v_z stop at $t_{sv}^{v=3} = 0.0586s$ and at $t_{sv}^{v=4} = 0.0552s$ as shown in Fig. 3(a). The stoppage time for horizontal velocities v_x are $t_{sh}^{v_i=3} = 0.06s$ and $t_{sh}^{v_i=4} = 0.0582s$, as shown in Fig. 3(b).

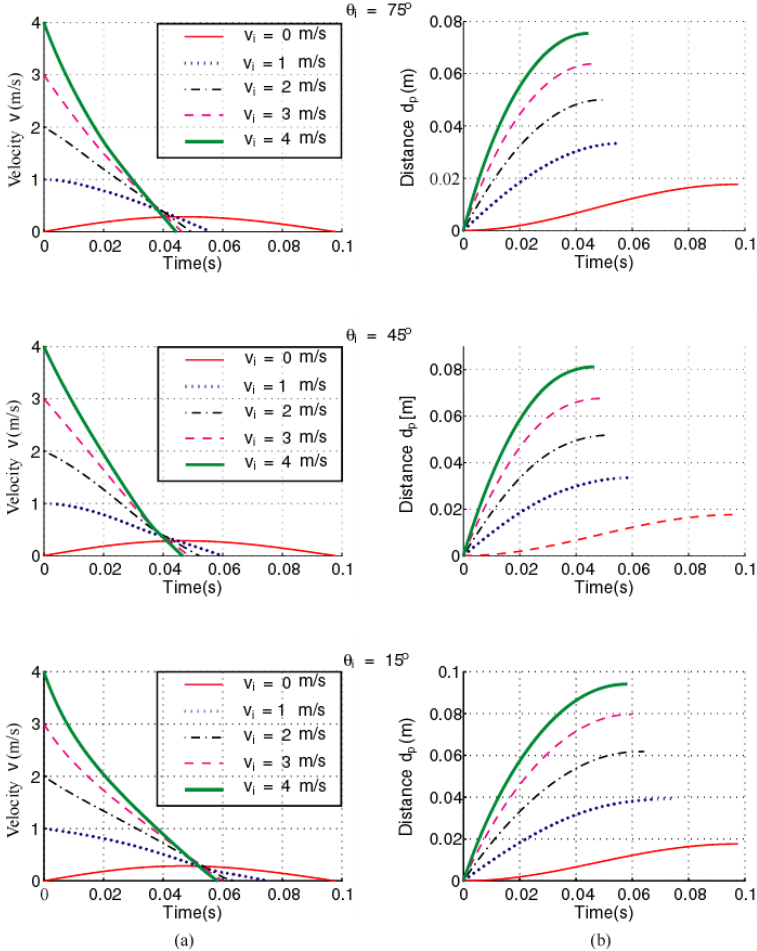


Fig. 2 – (a) Sphere velocity v and (b) penetration distance d_p for different initial impact angles ($\theta_i = 75^\circ$, 45° , and 15°) and different initial impact velocities ($v_i = 0, 1, 2, 3$ and 4 m/s)

We can conclude for this impact with an angle $\theta_i=15^\circ$ that the final stopping time of the sphere is influenced at the end by the horizontal velocity. The velocity v_z becomes zero earlier than the velocity v_x [Fig. 3(a)]. For this case the stopping motion is influenced by v_x and the stopping time is decreasing with the initial velocities [Fig. 3(b)]. For the impact angles $\theta_i=75$ and 45° the horizontal velocity comes to zero first and the final stoppage time is influenced by the vertical component of the velocity.

Figure 4(a) shows the velocity results for the impact angle $\theta_i=5^\circ$. For the initial velocity $v_i=2.5$ m/s the stoppage time is $t_{sv}^{v=2.5}=0.07852s$, for $v_i=3.0$ m/s the stoppage time is $t_{sv}^{v=3}=0.07902s$, and for $v_i=3.5$ m/s the stoppage time is $t_{sv}^{v=3.5}=0.07905s$. For this case the time it takes to stop while travelling on the media is proportional with the initial velocity as $t_s^{v_i=2.5} < t_s^{v_i=3} < t_s^{v_i=3.5}$. This is a very interesting case because for this angle the granular media behave differently from the previous cases.

Figure 4(b) depicts the vertical and horizontal velocity function of the time. Figure 4(b) shows that the stopping time increases proportional to initial velocity. For $v_i=2.5, 3.0$, and 3.5 m/s, the stopping time is influenced at the end by the horizontal velocity v_x .

For $\theta_i=15^\circ$ the final stopping time was also influenced at the end by the horizontal velocity but the stopping time decreases with the initial velocities $t_{sh}^{v_i=3} < t_{sh}^{v_i=4}$ (Fig. 3).

For the impact angle $\theta_i=50$ the stopping time increases with initial velocities so we may conclude that the stopping time is influenced by the small impact angle (Fig. 4). However, the results obtained from Fig. 4 require additional analytical studies and experimental results due to the granular media characteristics.

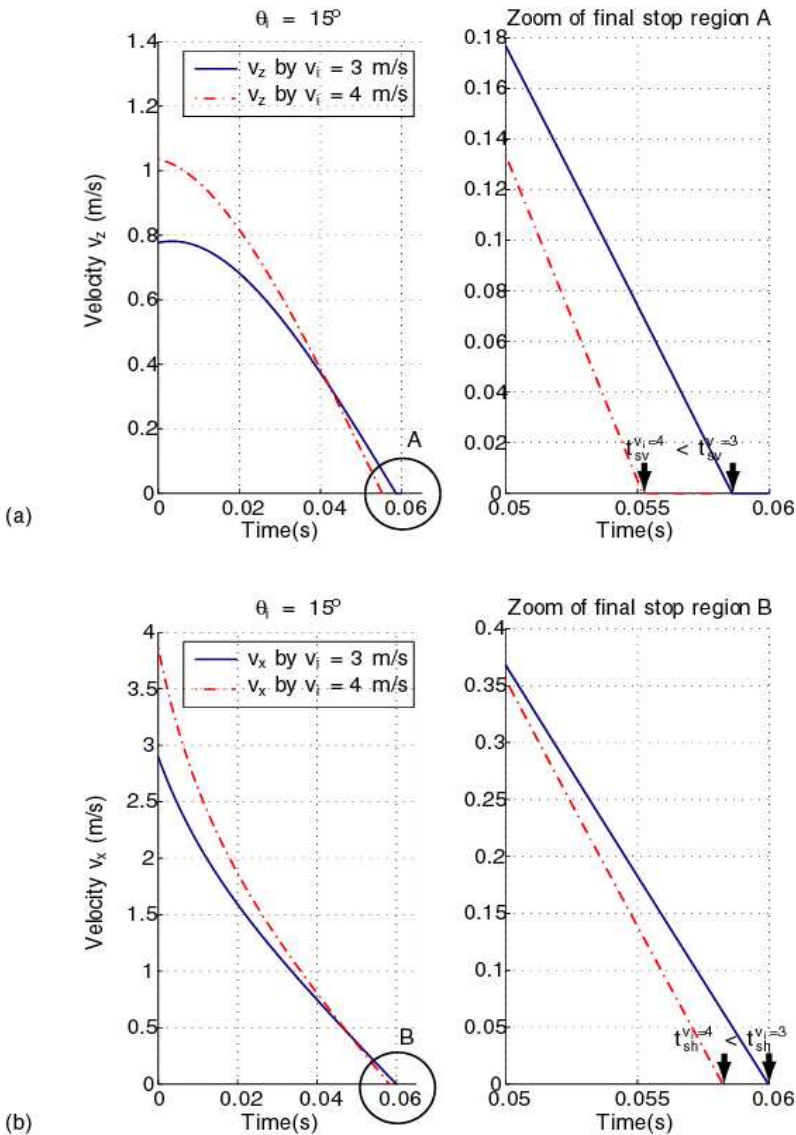


Fig. 3 – (a) Vertical velocity v_z and (b) horizontal velocity v_x of a sphere for the initial impact

$\theta_i = 15^\circ$ and initial impact velocity $v_i = 3$ and 4 m/s

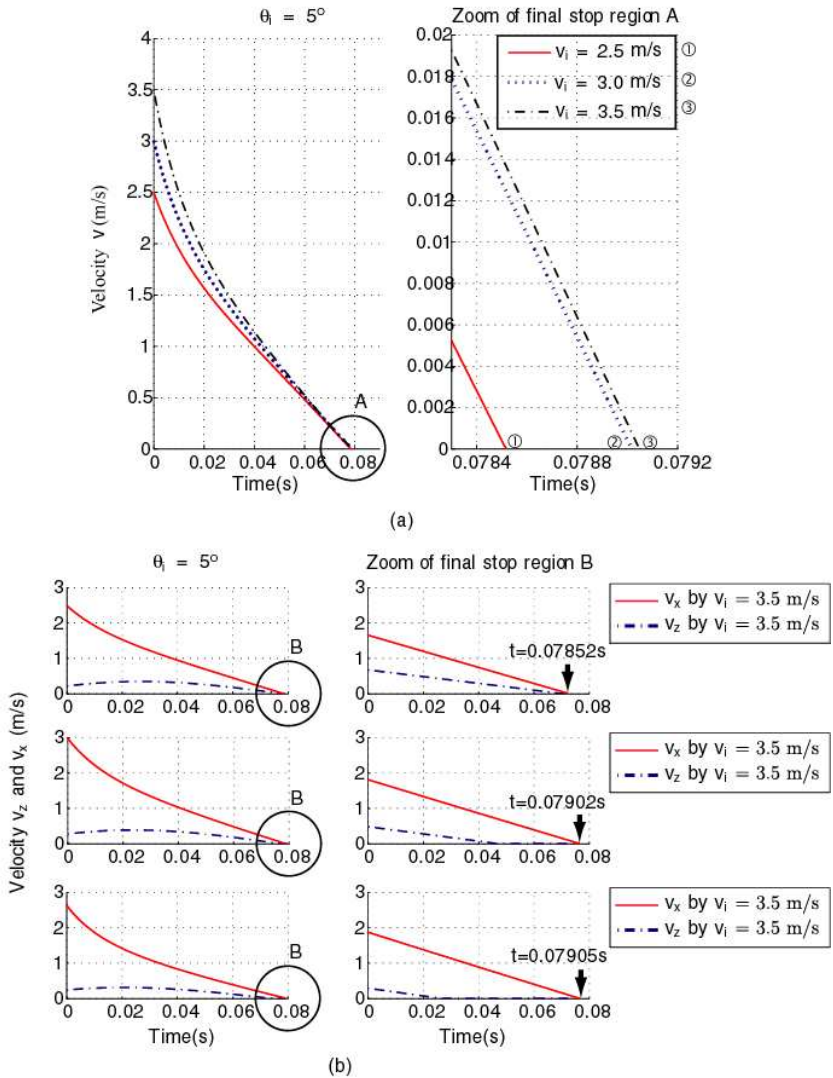


Fig.4 – (a) Sphere velocity v and (b) vertical velocity v_z and horizontal velocity v_x for initial impact angle θ_i and different initial velocities ($v_i = 2.5, 3.0$ and 3.5 m/s)

5. CONCLUSION

For most of the impact cases when the initial velocity is increased the stopping time is decreasing. There are some particular cases, for the impact angle relatively small, when the travelling time is increasing with the initial velocity. This remark requires additional experiments and additional modelling for the reaction force of the granular media on the rigid body.

REFERENCES

1. A.L. Yarin, M.B. Rubin, and I.V. Roisman, *Int. J. Impact Engng.* 16, 801 (1995).
2. D. Lohse, R. Rauhe, R. Bergmann, and D. van der Meer, *Nature* 432, 689 (2004).
3. G. Hill, S. Yeung, and S.A. Koehler, *Europhys. Lett.* 72, 137 (2005).
4. G. Yossifon, A.L. Yarin, and M.B. Rubin, *International Journal of Engineering Science*, 40, 1381 (2002).
5. H. Katsuragi, D.J. Durian, *Nature Physics* 3, 420 (2007).
6. I. Albert, J.G. Sample, A.J. Morss, S. Rajagopalan, A.-L. Barabási, and P. Schiffer, *Phys. Rev. E* 64, 061303 (2001).
7. I. Albert, P. Tegzes, B. Kahng, R. Albert, J.G. Sample, M. Pfeifer, A.-L. Barabasi, T. Vicsek, and P. Schiffer, *Phys. Rev. Lett.* 84, 5122 (2000).
8. I. Albert, P. Tegzes, R. Albert, J.G. Sample, A.-L. Barabási, T. Vicsek, B. Kahng, and P. Schiffer, *Phys. Rev. E* 64, 031307 (2001).
9. L.S. Tsimring, D. Volfson, *Powders and Grains 2005*, edited by R. Garcíá Rojo, H. J. Herrmann, and S. McNamara (Balkema, Rotterdam, 2005).
10. M.A. Ambroso, R.D. Kamien, and D.J. Durian, *Phys. Rev. E* 72, 041305 (2005)
11. M.P. Ciamarra, A.H. Lara, A.T. Lee, D.I. Goldman, I. Vishik, and H.L. Swinney, *Phys. Rev. Lett.* 92, 194301 (2004)
12. M. Hou, Z. Peng, R. Riu, K. Lu, and C.K. Chan, *Phys. Rev. E* 72, 062301 (2005).
13. M.B. Stone, R. Barry, D.P. Bernstein, M.D. Plec, Y.K. Tsui, and P. Schiffer, *Phys. Rev. E* 70, 041301 (2004)
14. R. Albert, M.A. Pfeifer, A.-L. Barabási, and P. Schiffer, *Phys. Rev. Lett.* 82, 205 (1999).
15. S.N. Coppersmith, C.-h. Liu, S. Majumdar, O. Narayan, and T.A. Witten, *Phys. Rev. E* 53, 4673 (1996).

AN ANALYTICAL ELASTIC–PLASTIC STRESS ANALYSIS IN A WOVEN STEEL REINFORCED THERMOPLASTIC CANTILEVER BEAM LOADED UNIFORMLY

AYKUL Halil^{*}, SAYMAN Onur^{**}, ÖZYILMAZ Emre^{*}, KARA Emre^{*}

^{*}*Hitit University –Turkey*

^{**}*Dokuz Eylül University - Turkey*

Abstract: In this investigation, an elastic–plastic stress analysis is carried out in a woven steel fiber reinforced thermoplastic (LDPE, F.2.12) composite cantilever beam loaded uniformly at the upper surface. Closed form solution is found satisfying both the governing differential equation and boundary conditions. The beam is loaded by a small uniform force at the upper surface, therefore during the solution of the problem for the elastic–plastic case; the normal stress σ_y is neglected in comparison with other stress components. The orientation angles of the fibers are chosen as 0° , 15° , 30° and 45° . The intensity of the residual stress component of σ_x is maximum at the upper and/or lower surfaces of the beam. The intensity of the residual stress component of the shear stress τ_{xy} is maximum on or around the x axis.

Keywords: Elastic–plastic stress analysis; Residual/internal stress, thermoplastic composite, cantilever beam.

1. INTRODUCTION

Among fiber-reinforced composites, thermoplastic matrix composites are gaining popularity due to many advantages. They offer improved interlaminar fracture toughness, increased impact resistance and higher solvent resistance than thermoset composite systems. In addition to their competitive mechanical properties, thermoplastic composites do not require complex chemical reactions to be processed

and can be formed without lengthy curing process. These features offer engineers a potential for cost-effective forming processes and the capability of the integrating material processing and structure design into a single step.

Jeronimidis and Parkyn [1] obtained residual stresses in carbon fibre-thermoplastic matrix (ICI plc.) laminates. Akay and Özden [2] measured the thermal residual stresses in injection moulded thermoplastics by removing thin layers from specimens and measuring the resultant curvature or the bending moment in the remainder of the specimens. Akay and Özden [3] investigated the influence of residual stresses on the mechanical and thermal properties of injection moulded ABS copolymer and polycarbonate.

Experimental investigations on the forming of thermoplastic composites can be found in Refs. [4–8]. Domb and Hansen [9] developed a numerical model for prediction of the process-induced thermal residual stresses in thermoplastic composite laminates.

The finite element technique allows an excellent simulation in elasto-plastic stress analysis in composites structures [10-12]. Sayman and Çallıoğlu [13] investigated an elastic-plastic analysis of thermoplastic composite beams loaded by bending moments. In these solutions Bernoulli-Navier hypothesis are used. The close agreement between the numerical finite element model is certainly sufficiently accurate for the characterization of creep behavior of composites [14]. This method appears to be an attractive way for applying finite element models in the prediction of viscoelastic properties for composites.

In the present study, an elastic-plastic stress analysis is carried out in a low density polyethylene thermoplastic composite cantilever beam reinforced by woven steel fibers. In this study, the solution is carried out for small plastic deformations. Residual stresses are determined by subtracting elastic stresses from elastic-plastic stresses.

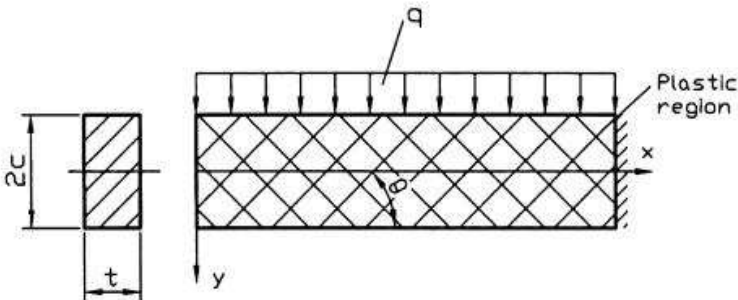


Fig. 1 - Thermoplastic composite beam

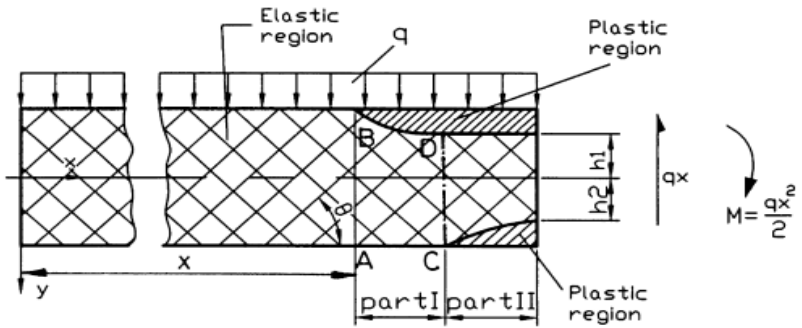


Fig. 2 - Elastic and elastic-plastic regions in the composite beam

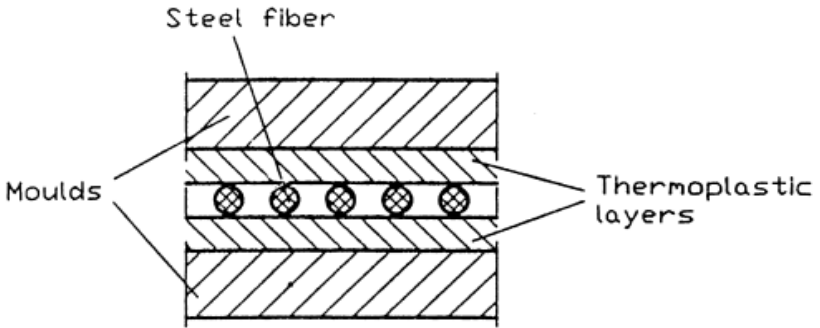


Fig. 3 - Production of the composite beam material

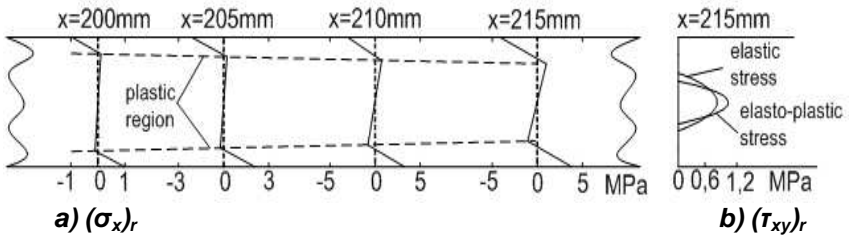


Fig. 4- Distribution of $(\sigma_x)_r$, $(\tau_{xy})_r$ and the expansion of the plastic region for 0° orientation angle

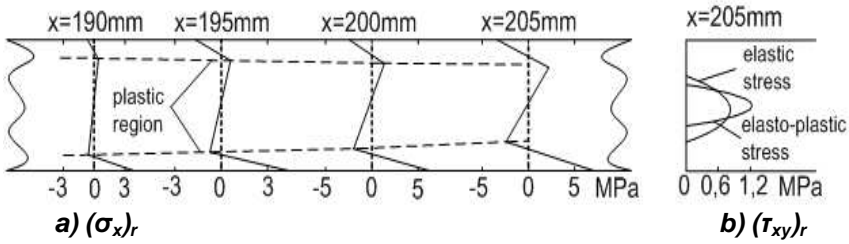


Fig.5-Distribution of $(\sigma_x)_r$, $(\tau_{xy})_r$ and the expansion of the plastic region for 15° orientation angle

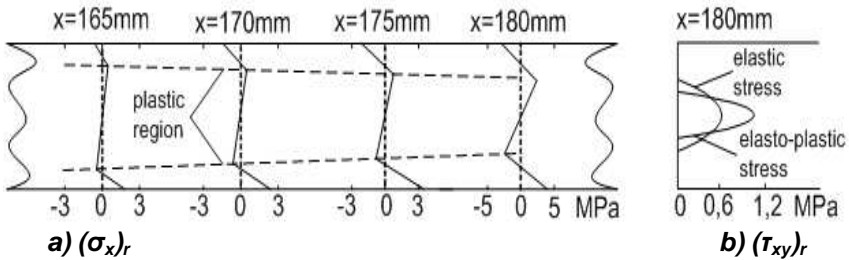


Fig.6-Distribution of $(\sigma_x)_r$, $(\tau_{xy})_r$ and the expansion of the plastic region for 30° orientation angle

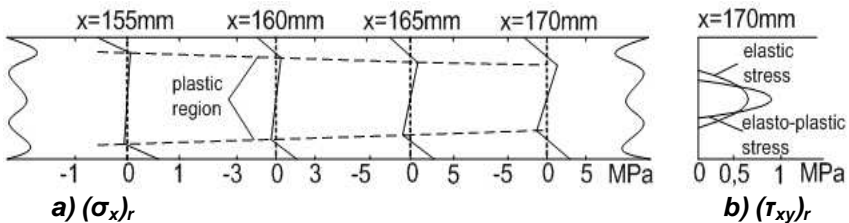


Fig.7-Distribution of $(\sigma_x)_r$, $(\tau_{xy})_r$ and the expansion of the plastic region for 45° orientation angle

2. SOLUTIONS AND PRODUCTION

2.1 ELASTIC SOLUTION

The elastic solution of an orthotropic cantilever beam loaded uniformly is given by Lekhnitskii [15], as shown in Fig. 1. The governing differential equation of a plane stress case is given as,

$$a_{22} \frac{\partial^4 F}{\partial x^4} - 2a_{26} \frac{\partial^4 F}{\partial x^3 \partial y} + (2a_{26} + a_{66}) \frac{\partial^4 F}{\partial x^2 \partial y^2} - 2a_{16} \frac{\partial^4 F}{\partial x \partial y^3} + a_{11} \frac{\partial^4 F}{\partial y^4} = 0 \quad (1)$$

where F is a stress function and a_{ij} are the components of the compliance matrix [16],

$$\begin{aligned} a_{11} &= S_{11}m^4 + (2S_{12} + S_{66})m^2n^2 + S_{22}n^4 \\ a_{12} &= S_{12}(m^4 + n^4) + (S_{11} + S_{22} + S_{66})m^2n^2 \\ a_{22} &= S_{11}n^4 + (2S_{12} + S_{66})m^2n^2 + S_{22}m^4 \\ a_{16} &= (2S_{11} - 2S_{12} - S_{66})nm^3 - (2S_{22} - 2S_{12} - S_{66})n^3m \\ a_{26} &= (2S_{11} - 2S_{12} - S_{66})n^3m - (2S_{22} - 2S_{12} - S_{66})nm^3 \\ a_{66} &= 2(2S_{11} + 2S_{22} - 4S_{12} - S_{66})m^2n^2 + S_{66}(m^4 + n^4) \end{aligned} \quad (2)$$

where $m=\cos\theta$, $n=\sin\theta$, $S_{11}=1/E_1$, $S_{22}=1/E_2$, $S_{12}=-\nu_{12}/E_1$, $S_{66}=1/G_{12}$.

A trial polynomial solution for the differential equation is chosen as [14],

$$F = \frac{d}{6}x^2y^3 + \frac{e}{12}xy^4 + \frac{f}{20}y^5 + \frac{k}{2}xy^2 + \frac{g}{6}y^3 + \frac{b}{2}x^2y + \frac{a}{2}x^2 \quad (3)$$

Substituting in Eq. (1), gives

$$x(-4a_{16}d + 2ea_{11}) + y(4a_{12}d + 2a_{66}d - 4a_{16}e + 6fa_{11}) = 0$$

In order to satisfy the equation, each term of x and y must be equal to zero as,

$$e = sd \quad (4)$$

where $s = 2a_{16}/a_{11}$ and

$$f = rd$$

where,

$$r = \frac{2a_{16}s - 2a_{12} - a_{66}}{3a_{11}} \quad (5)$$

The stress components become,

$$\begin{aligned} \sigma_x &= \frac{\partial^2 F}{\partial y^2} = dx^2y + sdy^2 + rdy^3 + kx + gy \\ \sigma_y &= \frac{\partial^2 F}{\partial x^2} = \frac{d}{3}y^3 \\ \tau_{xy} &= -\frac{\partial^2 F}{\partial x \partial y} = -dxy^2 - \frac{sd}{3}y^3 - ky - bx \quad (6) \end{aligned}$$

The boundary conditions are:

$$\sigma_y = \frac{-q}{t} \text{ at } y = -c \quad \sigma_y = 0 \text{ at } y = +c \quad \tau_{xy} = 0 \text{ at } y = \pm c$$

σ_x is not zero at the free end. But according to the Saint-Venant's principle the change of distribution of the load at the free end is equivalent to the superposition of a system of forces statically equivalent to zero force and zero couple (see, Timoshenko and Goodier [17, p. 39]).

$$\int_{-c}^c \sigma_x t dy = 0 \text{ at the free end}$$

$$\int_{-c}^c \sigma_x t y dy = 0 \text{ at the free end} \quad (7)$$

where $2c$ and t are the height and the thickness of the beam, respectively. By solving the above equations, the unknown constants are determined and stress components become [15],

$$\begin{aligned} \sigma_x &= -\frac{q}{2I} \left(x^2y + xy^3 + sxy^2 - \frac{1}{3}c^2sx - \frac{3}{5}rc^2y \right) \\ \sigma_y &= -\frac{q}{2I} \left(\frac{1}{3}y^3 - c^2y \right) - \frac{q}{2t} \quad (8) \\ \tau_{xy} &= -\frac{q}{2I} \left(-xy^2 - \frac{1}{3}sy^3 + c^2x + \frac{1}{3}sc^2y \right) \end{aligned}$$

where I is the inertia moment of the cross section of the beam.

2.2 ELASTIC–PLASTIC SOLUTION

In the plastic region stress components have to satisfy the equations of equilibrium for a plane-stress case as:

$$\begin{aligned}\frac{\partial \sigma_x}{\partial x} + \frac{\partial \tau_{xy}}{\partial y} &= 0 \\ \frac{\partial \tau_{xy}}{\partial x} + \frac{\partial \sigma_y}{\partial y} &= 0\end{aligned}\quad (9)$$

The uniform force q is chosen at a small value; therefore σ_y can be neglected in comparison with the other stress components. Substituting $\sigma_y=0$ in the second equation gives the shear stress component τ_{xy} as a function of y or a constant. The Tsai–Hill theory is used as a yield criterion in this solution. X and Y are the yield points in the 1st and 2nd principal axes, respectively. For the simplicity of the solution, the yield point (Z) in the third principal direction is assumed to be equal to Y , though the alignments of the fibers in those directions are different. S is the yield point in the 1–2 plane for the simple pure shear. Also the yield points in 1–3 and 2–3 planes for the simple pure shear are assumed to be equal to S . For this condition it can be written as,

$$\left[\frac{\sigma_1^2}{X^2} - \frac{\sigma_1 \sigma_2}{X^2} + \left(\frac{\sigma_2}{Y} \right)^2 + \left(\frac{\tau_{12}}{S} \right)^2 \right]^{1/2} = 1 \quad (10)$$

$$\sigma_e = \left[\sigma_1^2 - \sigma_1 \sigma_2 + \left(\frac{\sigma_2 X}{Y} \right)^2 + \left(\frac{\tau_{12} X}{S} \right)^2 \right]^{1/2} = X$$

where σ_e is the equivalent stress, and σ_1 , σ_2 and τ_{12} are the stress components in principal material directions as,

$$\begin{aligned}\sigma_1 &= \sigma_x \cos^2 \theta + 2\tau_{xy} \sin \theta \cos \theta \\ \sigma_2 &= \sigma_x \sin^2 \theta - 2\tau_{xy} \sin \theta \cos \theta \\ \tau_{12} &= -\sigma_x \sin \theta \cos \theta + \tau_{xy} (\cos^2 \theta - \sin^2 \theta)\end{aligned}\quad (11)$$

Substituting the stress components in Eq. (10) and differentiating it with respect to x , gives $\delta \sigma_x / \delta x = 0$. Putting in the first equation of equilibrium, it is obtained as $\delta \tau_{xy} = \delta y = 0$ and τ_{xy} as a constant. Yielding begins at the upper or lower surfaces of the beam, $\sigma_x = X_1$ and $\tau_{xy} = 0$ on these surfaces. From the yield criterion, the stress component σ_x which causes the material to yield is determined as,

$$X_1 = \frac{X}{\sqrt{\cos^4 \theta - \sin^2 \theta \cos^2 \theta + \frac{X^2 \sin^4 \theta}{Y^2} + \frac{X^2 \sin^2 \theta \cos^2 \theta}{S^2}}} \quad (12)$$

where θ is the orientation angle of the fibers. As a result of this, in the plastic region the stress components σ_x and τ_{xy} are equal to X_1 and zero, respectively.

Part I: In this part the plastic region expands only at the upper surface up to $h_1 = h_1(x)$; the lower side of the beam is completely elastic, (as shown in Fig. 2), the boundary conditions can be written as,

$$\tau_{xy} = 0 \text{ at } y = -h_1 \quad \tau_{xy} = 0 \text{ at } y = c \quad \int_{-h_1}^c \tau_{xy} t dy = -qx$$

where the positive τ_{xy} is in the opposite direction of qx , therefore qx takes a negative sign.

$$\sigma_x = X_1 \text{ at } y = -h_1$$

The resultant of σ_x at any section is equal to zero:

$$X_1 (c - h_1) t + \int_{-h_1}^c \sigma_x t dy = 0 \quad (13)$$

The moment of σ_x in this section is equal to,

$$X_1 (c - h_1) \frac{c + h_1}{2} t - \int_{-h_1}^c \sigma_x t y dy = \frac{qx^2}{2}$$

where positive σ_x produces an opposite moment of $qx^2/2$. Therefore the integration takes a negative sign.

For satisfying both the governing differential equation and the boundary conditions (13), the stress function is chosen as:

$$F = \frac{d}{6} x^2 y^3 + \frac{e}{12} xy^4 + \frac{f}{20} y^5 + \frac{p}{2} xy^2 + \frac{g}{6} y^3 + \frac{b}{2} x^2 y + \frac{k}{2} y^2 \quad (14)$$

The stress components from this polynomial are found as,

$$\sigma_x = \frac{\partial^2 F}{\partial y^2} = dx^2 y + sdy^2 x + rdy^3 + px + gy + k \quad (15)$$

$$\tau_{xy} = -\frac{\partial^2 F}{\partial x \partial y} = -dxy^2 - \frac{sd}{3} y^3 - py - bx$$

where

$$e = sd, \quad s = 2 \frac{a_{16}}{a_{11}}, \quad f = rd, \quad r = \frac{2a_{16}s - 2a_{12} - a_{66}}{3a_{11}}$$

and q is chosen at a small value, therefore σ_y can be neglected in comparison with the other stress components.

The six constants are found by using the boundary conditions:

$$p = -dx(c - h_1) - \frac{sd}{3}(h_1^2 - h_1c + c^2)$$

$$b = -dh_1c + \frac{sdh_1c}{3x}(h_1 - c)$$

$$g = -\frac{4X_1c}{(h_1 + c)^2} - dx^2 + \frac{2sdx}{3}(2h_1 - c) + \frac{rd}{2}(-3h_1^2 + 2h_1c + c^2)$$

$$k = X_1 + dx^2h_1 - sdxh_1^2 + rdh_1^3 + gh_1 + dx^2(c - h_1) + \frac{sdx}{3}(h_1^2 - h_1c + c^2)$$

$$d = \frac{\frac{-12qx}{t}}{(h_1 + c)^3 [2x + s(c - h_1)]} d \left[\frac{r}{60}(3h_1^5 - 2c^5 + 10h_1^4c + 10h_1^3c^2 - 5h_1c^4) - \frac{sx(c + h_1)^4}{36} \right] - \frac{qx^2}{2t} - \frac{2X_1c(h_1 - 2c)}{3} = 0 \quad (16)$$

Solving the last equation by using the Newton–Raphson method gives h_1 and the other constants can be determined.

Part II: In this part, the plastic region expands from the upper and lower surfaces of the beam up to $h_1 = h_1(x)$ and $h_2 = h_2(x)$, respectively. The boundary conditions for any section in this part are written as,

$$\tau_{xy} = 0 \text{ at } y = -h_1 \quad \tau_{xy} = 0 \text{ at } y = -h_2$$

$$\int_{-h_1}^{h_2} \tau_{xy} t dy = -qx \quad \sigma_x = X_1 \text{ at } y = -h_1 \quad \sigma_x = -X_1 \text{ at } y = h_2 \quad (17)$$

$$X_1(c - h_1)t - X_1(c - h_2)t + \int_{h_1}^{h_2} \sigma_x t dy = 0$$

$$X_1(c - h_1) \frac{c + h_2}{2} t + X_1(c - h_2) \frac{c + h_2}{2} t - \int_{h_1}^{h_2} \sigma_x t y dy = \frac{qx^2}{2}$$

For satisfying both the governing differential Eq. (1) and the boundary conditions (17) in the elastic part of the elastic–plastic zone, the stress function is chosen as:

$$F = \frac{d}{6}x^2y^3 + \frac{e}{12}xy^4 + \frac{f}{20}y^5 + \frac{p}{2}xy^2 + \frac{g}{6}y^3 + \frac{b}{2}x^2y + \frac{k}{2}y^2 \quad (18)$$

The stress components from this polynomial are found as,

$$\sigma_x = \frac{\partial^2 F}{\partial y^2} = dx^2 y + sdy^2 x + rdy^3 + px + gy + k \quad (19)$$

$$\tau_{xy} = -\frac{\partial^2 F}{\partial x \partial y} = -dxy^2 - \frac{sd}{3} y^3 - py - bx$$

where

$$e = sd, \quad s = 2a_{16}/a_{11}, \quad f = rd, \quad r = \frac{2a_{16}s - 2a_{12} - a_{66}}{3a_{11}}$$

and q is chosen at a small value, therefore σ_y can be neglected in comparison with the other stress components.

The stress function satisfies both the governing differential equation and the boundary conditions (17) the seven unknown constants are found as,

$$p = -dx(h_2 - h_1) - \frac{sd}{3}(h_1^2 - h_1 h_2 + h_2^2)$$

$$b = -dh_1 h_2 + \frac{sdh_1 h_2}{3x}(h_1 - h_2)$$

$$g = -\frac{2X_1}{h_1 + h_2} - dx^2 - rd(h_1^2 - h_1 h_2 + h_2^2) + sdx(h_1 - h_2)$$

$$k = rdh_1 h_2 (h_1 - h_2) - dx^2 (h_1 - h_2) + \frac{sdx}{3}(h_1^2 - 4h_1 h_2 + h_2^2) - \frac{X_1(h_1 - h_2)}{h_1 + h_2}$$

$$d = \frac{-\frac{qx}{t}}{\frac{x}{6}(h_1 + h_2)^3 + \frac{s}{12}(h_1 + h_2)^3(h_2 - h_1)}$$

$$u = \frac{3qxr + 2X_1xt - \sqrt{(3qxr + 2X_1xt)^2 - 8qX_1ts^2x^2}}{2X_1st}$$

$$\frac{d}{60} \left\{ r(2h_2 + u) \left[8(h_2 + u)^4 + 8h_2^4 + 2h_2(h_2 + u)^3 + 2h_2^3(h_2 + u) - 12h_2^2(h_2 + u)^2 \right] \right. \\ \left. - 5sxu(2h_2 + u)^3 \right\} - \frac{X_1}{3} \left[(h_2 + u)^2 + h_2^2 - h_2(h_2 + u) \right] - \frac{qx^2}{2t} + X_1c^2 = 0$$

u is found by using the given constants. Subsequently, solving the last equation by using the Newton–Raphson method gives h_2 and then the other parameters are determined. For the 0 or 90 and 45° the orientation angles s is zero and subsequently by taking the limit, u is found as zero. As a result of this h_1 is obtained to be equal to h_2 for these orientation angles. Eqs. (1) and (3) are used for the solutions in the linear elastic region of the beam and Eqs. (14) and (18) are used in the elastic region of the plastically deformed parts of the beam, as long as plastic flow is no more than 5%.

2.3 PRODUCTION OF THE COMPOSITE BEAM

The composite beam material consists of low density polyethylene as a thermoplastic (LDPE, F.2.12) and woven steel fibers. Granules of the polyethylene are put into the moulds and they are heated up to 160°C by using electrical resistance. Subsequently, the material is held for 5min under 2.5 MPa at this temperature. The temperature is decreased to 30°C under 15 MPa pressure in 3 min. Thus a polyethylene layer is obtained. The woven steel fibers beam are placed between two plastic layers and processed in the same way defined above, as shown in Fig. 3. Thus the composite beam material is obtained. Mechanical properties and yield points of the beam material are determined by using the Shimadzu Autograph test machine and strain gauges, as given in Tab. 1.

3. RESULTS, DISCUSSIONS AND CONCLUSIONS

3.1 RESULTS AND DISCUSSIONS

The thermoplastic composite beam is loaded uniformly. The intensity of the uniform force is chosen at a small value 0,2 N/mm. So in the elastic–plastic solution, the normal stress component of σ_y is neglected. Yielding begins at the upper and/or lower surfaces of the beam. Yield points for 0, 15, 30 and 45° orientation angles are given in the Tab. 2. As seen from this table, yielding occurs earlier at the upper surface for 15 and 30° orientation angles. However it starts at the same distances from the free end for 0° and 45° orientation angles due to the symmetry of the material properties with respect to the x axis or the plane passing through that axis.

Tab.1 Mechanical properties and yield strengths of the composite beam

E_1 (MPa)	E_2 (MPa)	G_{12} (MPa)	ν_{12}	Axial strength (X) (MPa)	Transverse strength (Y) (MPa)	Shear strength (S) (MPa)
9550	9550	670	0.4	18.5	18.5	5.8

Tab.2 Yield points at the upper and lower surfaces

Orientation angle($^\circ$)	0	15	30	45
Yield point at the upper surface (mm)	195	169,9	153,10	150,60
Yield point at the lower surface (mm)	195	185,30	161,50	150,60
X_1 (MPa)	18.5	15,37	12,08	11,06

The plastically collapsed points at a constant q (0.2 N/mm) are given for 0, 15, 30 and 45 $^\circ$ orientation angles in the Table 3. As seen from this table the distance between the free end and yield points is maximum for 0 $^\circ$ orientation angle ($x = 238.3$ mm).

Tab.3 Plastically collapsed points

Orientation angle($^\circ$)	0	15	30	45
Plastically collapsed points (mm)	238,3	217,3	192,6	184,3

The elastic, plastic and residual stress component of σ_x are given in Tab. 4, for 0, 15, 30 and 45 $^\circ$ orientation angles. The intensity of the residual stress component of σ_x at the upper surface is greater than that at the lower surface for 15 and 30 $^\circ$ orientation angles. It is the same for 0 $^\circ$ and 45 $^\circ$ orientation angles.

Tab.4 Residual stress components of σ_x (MPa)

	x	h_1 mm	h_2 mm	$(\sigma_x)_p$ y=c	$(\sigma_x)_e$ y=c	$(\sigma_x)_r$ y=c	$(\sigma_x)_p$ y=-c	$(\sigma_x)_e$ y=-c	$(\sigma_x)_r$ y=-c
0	200	7.5638	7.5638	-18.500	-19.4752	0.9752	18.500	19.4752	-0.9752
	205	7.0943	7.0943	-18.500	-20.4640	1.9640	18.500	20.4640	-1.9640
	210	6.5784	6.5784	-18.500	-21.4771	2.9771	18.500	21.4771	-2.9771
	215	6.0044	6.0044	-18.500	-22.5147	4.0147	18.500	22.5147	-4.0147
15	190	6.7194	7.6814	-15.3700	-16.2094	0.8394	15.3700	19.0697	-3.6997
	195	6.1103	7.0976	-15.3700	-17.1117	1.7417	15.3700	20.0473	-4.6773
	200	5.4147	6.4274	-15.3700	-18.0384	2.6684	15.3700	21.0493	-5.6793
	205	4.5934	5.6314	-15.3700	-18.9895	3.6195	15.3700	22.0757	-6.7057
30	165	7.1462	7.2117	-12.0800	-12.6260	0.546	12.0800	13.9801	-1.9001
	170	6.5128	6.5803	-12.0800	-13.4233	1.3433	12.0800	14.8185	-2.7385
	175	5.7858	5.8579	-12.0800	-14.2451	2.1651	12.0800	15.6813	-3.6013
	180	4.9334	5.0048	-12.0800	-15.0913	3.0113	12.0800	16.5685	-4.4885
45	155	7.5034	7.5034	-11.0600	-11.7350	0.6750	11.0600	11.7350	-0.675
	160	6.8858	6.8858	-11.0600	-12.5040	1.4440	11.0600	12.5040	-1.4440
	165	6.1843	6.1843	-11.0600	-13.2975	2.2375	11.0600	13.2975	-2.2375
	170	5.3661	5.3661	-11.0600	-14.1153	3.0553	11.0600	14.1153	-3.0553

The expansion of the plastic region and the residual stress distribution of σ_x along the sections of the beam are given in Fig. 4, for 0° orientation angle. As seen from this figure, the stress components of σ_x and τ_{xy} , and the plastic region are symmetric with respect to the x axis. The plastic region expands slowly along the beam. The intensity of the residual stress component of σ_x is maximum at the upper and lower surfaces of the beam. The distribution of the shear stress is given only for $x = 215$ mm. As seen from this figure, the intensity of the residual stress component of τ_{xy} is maximum on the x-axis.

The expansion of the plastic region and the residual stress distribution of σ_x along the sections of the beam are given in Fig.5, for 15° orientation angle. As seen from this figure, the plastic region spreads rapidly at the upper side. The intensity of the residual stress component of σ_x at the upper surface is greater than that at the lower surface. The residual stress component of the shear stress is maximum around the x axis, at $x=205$ mm.

The expansion of the plastic region and the residual stress distribution of σ_x along the sections of the beam are given in Figs. 6 and 7, for 30 and 45° orientation angles.

As seen from these figures, the intensity of the residual stress component of σ_x is maximum at the upper surface for 30° orientation angle, however it is symmetric for 45° orientation angle. The residual stress component of τ_{xy} for 30 and 45° orientation angles is given for $x=180$ and $x=170$ mm; respectively. The residual stress component of τ_{xy} is maximum for 30 and 45° orientation angles, on or around the x axis, respectively. σ_x is the largest stress component in the beam.

3.2 CONCLUSIONS

In this investigation, an exact elastic–plastic stress analysis is carried out in a thermoplastic cantilever beam loaded uniformly.

1. Yielding begins first at the upper or lower surfaces of the beam. It starts earlier of the upper surface for 15° and 30° orientation angles. It has the same distances for 0° and 45° due to the symmetry of the material properties with respect to the x axis.

2. The intensity of the residual stress component of σ_x is maximum at the upper surface for 15° and 30° orientation angles. It is the same for 0° and 45° orientation angles.

3. The plastic region spreads rapidly at the upper side of the beam for 15° and 30° orientation angles.

4. The intensity of the residual stress component of σ_x is greater than that of the shear stress component of τ_{xy} .

5. The maximum residual shear stress component of τ_{xy} is on or around the x axis.

REFERENCES

1. Jeronimidis G, Parkyn AT, - Residual stress in carbon fibre-thermoplastic matrix laminates, *Journal of Composite Materials*, 22(5):401–15, 1998
2. Akay M, Özden S, - Measurement of residual stresses in injection moulded thermoplastics, *Polymer Testing*, 13:323–54, 1994
3. Akay M, Özden S, - The Influence of residual stresses on the mechanical and thermal properties injection moulded ABS copolymer, *Journal of Materials Science*, 30:3358, 1995
4. Jegley D, - Impact-Damaged Graphite-Thermoplastic Trapezoidal-Corrugation Sandwich and Semi-Sandwich Panels, *Journal of Composite Materials*, 27(5): 526-38, 1993

5. Cantwell W. J, - The Influence of Stamping Temperature on the Properties of a Glass Mat Thermoplastic Composite, *Journal of Composite Materials*, 30(11): 1266-81, 1996
6. Shi F., - The Mechanical Properties and Deformation of Shear-Induced Polymer Liquid Crystalline Fibers in an Engineering Thermoplastic, *Journal of Composite Materials*, 30(14): 1613-26, 1996
7. Tavman I. H., - Thermal and Mechanical Properties of Aluminum Powder Filled High Density Polyethylene Composites, *Journal of Applied Polymer Science*, 62: 2161-67, 1996
8. Chen C. H. and Cheng C. H., - Secant Moduli of a Glass Bead-Reinforced Silicone Rubber Specimen, *Journal of Composite Materials*, 30(1), 69-83, 1996
9. Domb MM, Hansen JS, - The Effect of Cooling Rate on Free-Edge Stress Development in Semi-Crystalline Thermoplastic Laminates, *Journal of Composite Materials*, 32(4): 361-85, 1998
10. Owen DRJ, Figueiras JA., - Anisotropic Elasto-Plastic Finite Element Analysis of Thick and Thin Plates and Shells, *International Journal For Numerical Methods in Engineering*, 19: 541-66, 1983
11. Özcan R., - Elasto-Plastic Stress Analysis in Thermoplastic Composite Laminated Plates under in-plane loading, *Composite Structures*, 49: 201-8, 2000
12. Aykul H, Ataş C, Akbulut H., - Elastic-Plastic Stress Analysis and Plastic Zone Propagation in Fiber Reinforced Thermoplastic Laminates Using Finite Element Method, *Journal of Reinforced Plastics and Composites*, 20(15): 1301-25, 2001
13. Sayman O, Çallıoğlu H., - An Elastic–Plastic Analysis of Thermoplastic Composite Beams Loaded by Bending Moments, *Composite Structures*, 50: 199-205, 2000
14. Wen YF., Gibson RF., - Prediction of Momentary Transverse Creep Behavior of Thermoplastic Polymer Matrix Composites Using Micromechanical Models, *Journal of Composite Materials*, 31(21): 2124-45, 1997
15. Lekhnitskii SG., - *Anisotropic Plates*, Gordon and Breach, New York, 1968
16. Jones RM, - *Mechanics of Composite Materials*, McGraw-Hill, Tokyo, 1975
17. Timoshenko SP, Goodier JN., - *Theory of Elasticity*, 3rd ed. McGraw-Hill, New York, 1970

ON STATIC BEHAVIOR OF DENTAL IMPLANTS UNDER DIFFERENT LOAD DIRECTIONS

ÖZYILMAZ Emre^{*}, AYKUL Halil^{*}, DALKIZ Mehmet^{**}, KARA Emre^{*}
^{}Hitit University – Turkey*
*^{**}Mustafa Kemal University - Turkey*

Abstract: One of the most important factors that determine implant success is the achievement and maintenance of implant stability. This numerical study was carried out using three – dimensional finite element method (FEM) and aimed to investigate static behaviors of dental implant under different load directions. Solid models of implants were built up in Solid Works and then transferred to a mesh model in FEM (ANSYS) to perform a stress analysis. The distribution of the equivalent stresses and total deformations in the dental implant components (abutment, implant and bone) is presented.

Keywords: dental implant, static behavior, finite element method

1. INTRODUCTION

Successful long-term results of dental implants have caused to an increase in their usage in many clinical situations [1]. Since dental implants were introduced for rehabilitation of the completely edentulous patients in the late 1960s, a recognition and subsequent demand for this type of therapy have increased in this field. The use of implants have revolutionized dental treatment modalities and provided excellent durable results. In evaluation of the long-term achievement of a dental implant, the reliability and the stability of the implant-abutment and implant-bone interfaces plays an essential role. In general, the success of the treatment depends on many factors which effects on the bone-implant, implant-abutment and abutment prosthesis interfaces [2].

Dental implants have been comprehensively used in oral rehabilitation and orthopedics as replacements of lost or partially damaged natural teeth to restore human mastication functions.

However, implant treatments still fail often. One of the most important reasons for this failure is that an artificial implant may never function as perfectly as the living tissues it replaces. Ideal biomaterials for use in dental implants need to simultaneously satisfy many requirements such as biocompatibility, strength, fatigue durability, non-toxicity, corrosion resistance and sometimes aesthetics [3]. An important characteristic of the human face is the look of the upper front teeth. A discontinuity or an interface in color generally gives a negative impression of the person [4].

The mechanical distribution of stress occurs firstly where bone is in contact with the implant. The density of bone is directly related to the amount of implant-to bone contact [5]. The biomechanical factors have been stressed by different authors. Micro movement of the implant components and excessive stress at the implant-bone interface has been suggested as potential cause for peri-implant bone loss and failure. [1] A detailed view of a dental implant and teeth is shown in Figure 1.

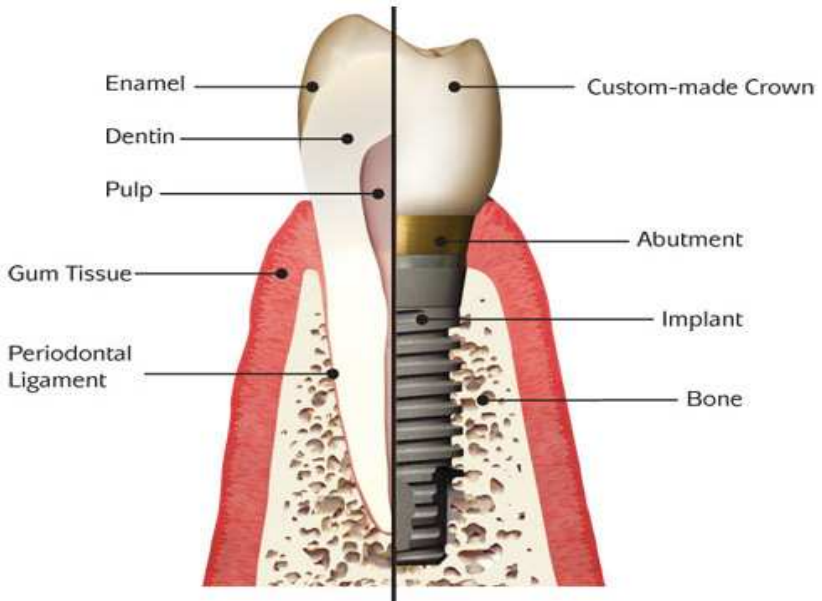


Fig. 1 – System assembly

The purpose of the present study is to investigate the static behavior of dental implants numerically. A detailed model of the mandible, implant and other components are designed to obtain reliable

results. And then this 3D model is transferred to ANSYS for evaluating stress distributions on dental implant.

2. GEOMETRICAL MODEL

The three dimensional model of the mandible were scanned with use of Nextengine laser scanner to obtain more realistic design and results. On the other hand, 3D model of dental implants were designed with Solid Works 2009 for each kind of teeth. The dimensions of modeled dental implant for molars, premolars and incisors are given in Table 1. Afterwards, the created CAD model was transferred to a mesh model in ANSYS Workbench to perform a stress analysis. The numbers of nodes and elements are given in Table 2. The implants were designed as standards and its material properties are listed in Table 3. Finite Element Model of implant and mandible is shown at Figure 2. On the other hand, after meshing process the force was applied from upper surface of the mandible abutment on x, y and z directions. The equivalent (Von-Misses) Stress and total deformation are presented in Figure 2 and 3.

Tab.1 The dimensions of implants

	Lower diameter(mm)	Great diameter(mm)	Pitch (mm)	Total length(mm)
Type 1(molars)	3.2	5	0.5	15
Type 2(premolars)	2.6	4	1	15
Type 3(incisors)	2	3	1	17

Tab.2 The numbers of nodes and elements for implants and mandible

	Elements	Nodes
Implant and Mandible	151248	278098

Tab.3 Elastic Properties of Materials Modeled

	Modulus of Elasticity (E)	Poisson's Ratio (ν)
Titanium	96,000	0.36
Cortical Bone	14,700	0.30
Spongy Bone	1,370	0.30

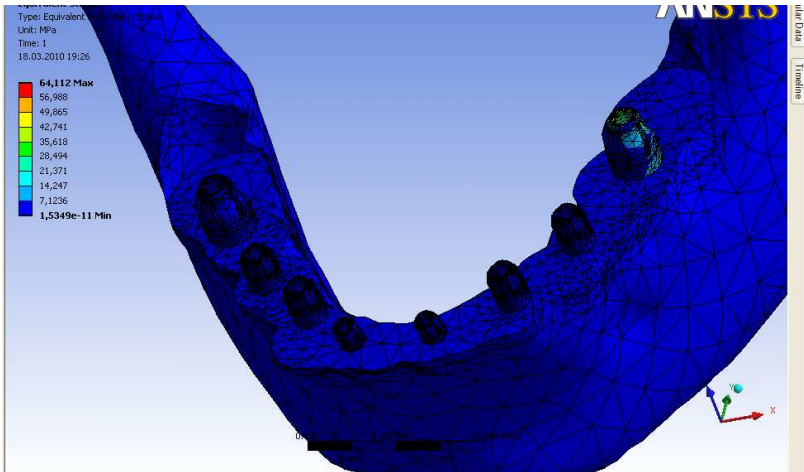


Fig. 2 – Equivalent (von-Misses) Stress on implant-mandible system

3. ANALYSIS RESULTS

The distribution of equivalent stresses and total deformation in the mandible and implant components are presented in this study. These distributions and deformations were analyzed under the effect of three mechanical loadings on x, y and z directions.

According to these loadings the maximum equivalent stresses and total deformations for all bodies and just molar implant were observed. The maximum total deformations are strongly concentrated on frontal part of mandible and the equivalent stresses are on the molar implant as shown in Figure 2 and Figure 3. The most important factor for the success of a dental implant is the stability of implant-abutment interface. The stress distributions on the abutment surface are presented in Figure 4. Meanwhile, the maximum value of total deformations and Von Mises stresses on each part are listed in Table 4.

Tab.4 The Maximum Stress distributions and total deformations

	Stress distributions (MPa)	Total deformations (mm)
Implant	64.112	0.014643
Abutment	24.817	0.014580
Mandible	21.985	0.022934

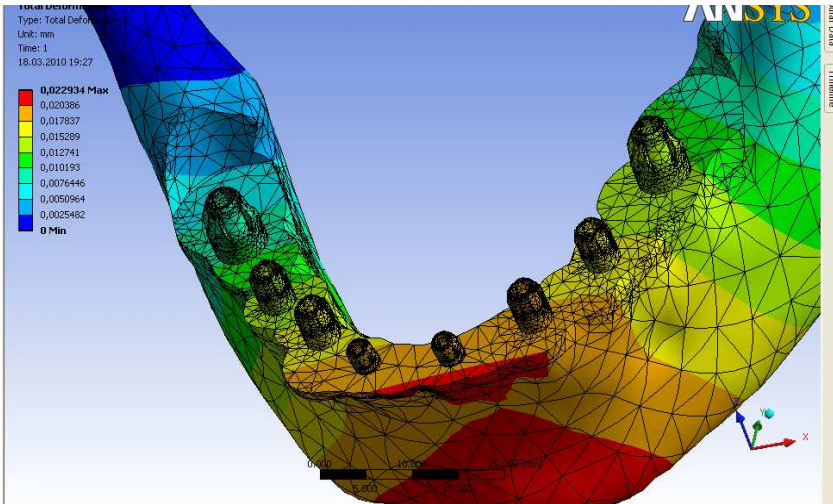


Fig. 3 – Total deformation on implant-mandible system

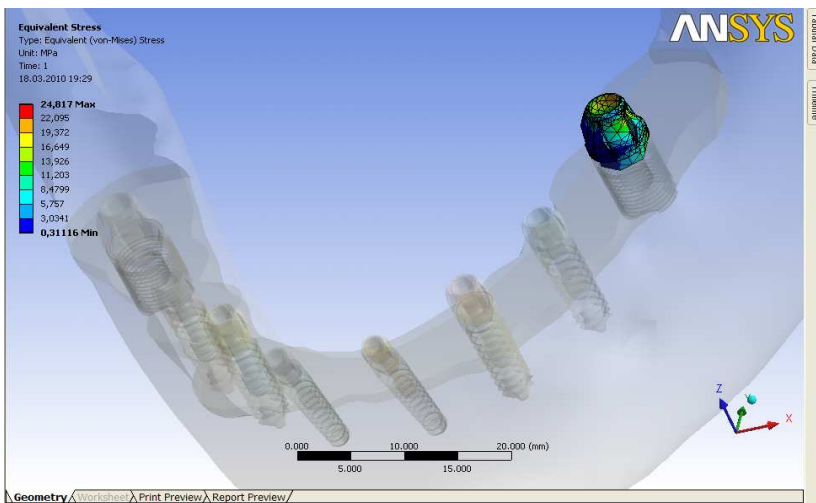


Fig. 4 – Equivalent (von-Mises) stress on abutment

To make observations understandable the mechanical behavior of the contact regions between bone - implant and implant - abutment were analyzed under loading conditions. The intensities of the stresses in the other parts of the implant under same cases are slightly weak. It is realized that maximum von - Mises stress in the dental implant is

located in the upper surface of the implant and implant – abutment connection region.

4. CONCLUSIONS

This study was carried out in order to analyze static behaviors of dental implants under different loading directions with use of three dimensional finite element method. According to these analysis reports some important points can be concluded. The maximum stress distributions and total deformations are concentrated on implant-abutment interface and frontal part of the mandible. These results can be taken into account for newly designed dental implants to have more stability on them. However, implant treatment failures can be decreased efficiently with these considerations.

REFERENCES

1. Şimşek B., Erkmen E., Yılmaz D., Eser A. - Effects of different inter-implant distances on the stress distribution around endosseous implants in posterior mandible: A 3D finite element analysis, *Medical Engineering & Physics* 28 (2006) 199-213.
2. Kayabaşı O., Yüzbaşıoğlu E., Erzincanlı F. - Static, dynamic and fatigue behaviors of dental implant using finite element method, *Advances in Engineering Software* 37 (2006) 649-658.
3. Yang J., Xiang H.J. - A three dimensional finite element study on the biomechanical behavior of an FGBM dental implant surrounding bone, *Journal of Biomechanics* 40 (2007) 2377-2385.
4. Aykul H., Toparlı M., Dalkız M. – A calculation of stress distribution in metal- porcelain crowns by using three dimensional finite element method, *Journal of Oral Rehabilitation* 29 (2002) 381-386.
5. Sevimay M., Turhan F., Kılıçarslan M.A., Eskitaşçıoğlu G. - Three-dimensional finite element analysis of the effect of different bone quality on stress distribution in an implant-supported crown, *J Prosthet Dent* 93 (2005) 227-234.

CREEP AND DAMAGE OF RUBBERS SURROUNDED BY AGGRESSIVE MEDIA

HADJOV Kliment*, ALEXANDROV Alexander*, HALLIL Giunai*,
MILENOVA Milena*, MARIN Mihnea**

**University of Chemical Technology & Metallurgy–Bulgaria*

***University of Craiova –Romania*

Abstract: The aim of this work is to develop theoretical and experimental procedures for modeling the behavior of rubbers. The models will be aimed at predicting their durability based on monitoring the processes of diffusion, creep and damage. Attention is focused on specific industrial problems related to the use of band samples located in aggressive environments. The validation of models for damage evolution under the combined impact of environment, temperature and mechanical stress is a problem requiring a solution of the Flick's equation by variable diffusion coefficient and using a damage model taking into account the different areas of penetration. To solve these problems a generalization of the models of Ashby and Kachanov is required, which will lead to more complex systems of differential equations.

Keywords: rubbers, damage, creep, diffusion, coupled problem

1. INTRODUCTION

Rubbers are increasingly used in modern industry [1-3]. In modern car there is around 300 - 400 polymer pieces in airplane about 10 000, in large ships they reach 30 000 units. Resinous materials and rubbers are elasto-viscous solids. They are very deformable and possess non-linear behaviors. Their creep is also non-linear according to the applied stresses. We assume diffusion governed by the Fick's law. New model concerning the damage accumulation was adopted. Two zones are introduced. The first one is intact and the second one contains penetrated fluid. To describe the damage rate a power law was used. The coupled problem was resolved by solving a system of differential

equations. Theoretical creep curves well agree with the experimental results.

2. ENVIRONMENTALLY INDUCED DAMAGE

The proposed in [4] two zone model of damage dealing with two different structural zones of the material will be used in this work to more precise account the damage process. After adopting of a damage rate law one obtains the following Woehler's curve:

$$t_f = \frac{\int_0^{D^*} \phi^{-m} dD}{H (\sigma_f)^m} \quad (1)$$

where $\phi(D) = \frac{f}{1-D} + \frac{1-f}{D}$ is a function of stresses concentration,

D – the damage parameter. The relative volume fraction without imperfections f in the general case is a structural (morphological) parameter. This part can be seen, however, as part of an environmental fluid penetration with concentration far from the limit one, unlike the other one, which is submitted to accelerated damage accumulation, due to the reach of the concentration limit.

If a polymer composite is subjected to the influence of penetrating media, the latter penetrates through the so-called matrix diffusion[5]. Effects of diffusion on the creep and durability of polymer composites are temperature dependent. The purpose of this modeling is to present some data on the kinetics of fluid penetration provoked by creep at normal and higher temperatures and to obtain a mathematical description of the effect of this damage on the creep resistance. The precise micro mechanism causing damage as a result of fluid diffusion is not of great importance for this phenomenological model.

One investigates band samples with large dimensions in y and z directions, while the band thickness h in the x direction is much smaller. In this case, the solution of the Fick's equation using series development looks like [6,7]:

$$c(x,t) = \sum_{i=1}^N (-1)^{i+1} \left(\operatorname{erfc}\left(\frac{(2i-1)h-2x}{8\sqrt{D_{ox}t}}\right) + \operatorname{erfc}\left(\frac{(2i-1)h+2x}{8\sqrt{D_{ox}t}}\right) \right) \quad (2)$$

Here $\operatorname{erfc}(z) = 1 - \operatorname{erf}(z)$. Moreover, the coordinate system is placed in the middle and x varies from $-h/2$ to $+h/2$. Therefore, the relative area of penetration is $1 - 2x'_d/h$, where x'_d is already the

decreasing coordinate at the penetration front measured at the sample center in the following limits $-h/2 \leq x'_d \leq h/2$ - (figure 1).

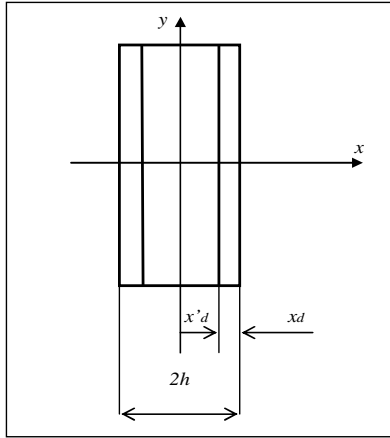


Fig. 1 – Depth and areas of penetration and damage zones

The proposed by us in [8] solution in this case looks like

$$c(x, t) = 1 - \frac{2}{\pi} \arccos \frac{1}{\exp\left(\frac{\pi k}{8D_{ox}} \frac{(h - 2x)^2}{4t}\right)} \quad (3)$$

The difference between eq.(2) and (3) is negligible [8] but, equation (3) can be resolved beside the depth of penetration measured at the end x_d (border of the plate with the environment)

$$x_d = \sqrt{Kt} \quad (4)$$

where

$$K = \frac{8D}{\pi k} \ln\left(\sec \frac{\pi}{2} \left(1 - \frac{c_f}{c_s}\right)\right) \quad (5)$$

From figure 1 it is evident that to the relative area of penetration we have

$$w = \frac{2x_d}{h} \quad (6)$$

From (5) and (6) after differentiation we have

$$\dot{w} = K / hx_d \quad (7)$$

From these equations to the relative penetration area we obtain

$$w(t) = \frac{2\sqrt{Kt}}{h} \quad (8)$$

From (6) and (7) we express the rate of the relative penetration area by itself

$$\dot{w} = \frac{2K}{h^2 w} \quad (9)$$

To the relative zone with accelerated damage 1-f we make the following. For $t \rightarrow t_c$ the relative surface of the damaged area $w(t_c) \rightarrow 1$ and simultaneously $x_d \rightarrow h/2$ - it can be seen from (6). Then from (8) follows

$$w(t_c) = \frac{2\sqrt{Kt_c}}{h} = 1 \quad (10)$$

By similar reasoning to the relative failure zone $w_f(t_c)$ we have

$$w_f(t_c) = \frac{2\sqrt{K_f t_c}}{h} \quad (11)$$

Taking into account that $w(t_c) \rightarrow 1$, resolving equation (11) beside the time $t_c = \frac{(wh)^2}{4K}$ and substituting in (11), we have

$$w_f = \sqrt{\frac{K_f}{K}} \quad (12)$$

Finally from the above equation (12) and equation (10) we have

$$f = 1 - \sqrt{\frac{K_f}{K}}, \text{ where } \frac{K_f}{K} = \frac{\ln(\sin \frac{\pi c_f}{2 c_s})}{\ln(\sin \frac{\pi c_c}{2 c_s})} \quad (13)$$

In the case of uncoupled problem (pre-exposition in the media with subsequent loading) it is necessary to resolve in advance equations (9) beside the respective relative damage areas

$$w(t) = \frac{2\sqrt{Kt}}{h} \cdot w_f(t) = \frac{2\sqrt{K_f t}}{h} \quad (14)$$

Note. In the coupled problem to the second zone we need to transform equation (9) replacing K with K_f .

Thus, the sample is divided into two damage zones. In the first one (inside with an average concentration $c = c_c$) the damage is more slowly, in the second one (outside with an average concentration $c = c_f$) the damage is accelerated. To found these two characteristic concentrations we need to use thin samples. The concentration does not depend on the coordinates, it should be time dependent. We deal with the. average relative. First we find a relative where a noticeable durability (Wöhler's curve change) is observed (sample durability shortening by 15%). We assume that until this concentration the damage is not accelerated and after them it is accelerated. From the Fick's equation (for thin band or thin square (cylindrical) sample) we calculate the relative concentration between the start at $t = 0$ and $t = t_g$ where t_g is the time to reach c_g . Thus, to the first and the second critical concentration we obtain

$$c_c = \frac{1}{t_g} \int_0^{t_g} c_m(t) dt, \quad (15a)$$

$$c_f = \frac{1}{t_1 - t_g} \int_{t_g}^{t_s} c_m(t) dt, \quad (15b)$$

where t_s is the saturation time.

It is clear that we could introduce more specific areas of penetration, but (according to our experience) in this case we do not obtain significantly improved predictions from our model.

3. ENVIRONMENTALLY INDUCED CREEP

The mechanical response to this diffusion attack, can be modeled under the assumption that:

- a). The intact area deforms by potency law [9]

$$\dot{\varepsilon}_u = \dot{\varepsilon}_o \left(\frac{\sigma_u}{\sigma_o} \right)^n. \quad (16)$$

Here $\dot{\varepsilon}_u$ is the strain rate of the intact (undamaged) area, σ_u the axial stress in this area, σ_o – the linearity limit of the axial stress and $\dot{\varepsilon}_o$ - the respective limit strain rate (in the region of material linear behavior), which can be expressed through the kernel of Koltunov [10]

$$\dot{\varepsilon}_o = \varepsilon(\sigma) \frac{\exp(-\beta t)}{t} \sum_{n=1}^{\infty} \frac{(A\Gamma^n(\alpha)t^{\alpha n})}{\Gamma(\alpha n)}. \quad (17)$$

where $\varepsilon(\sigma)$ represent the Neo-Hookean-for the BN, or Mooney-Rivlin-for the PI strain-stress constitutive law. The respective expressions are complicated and can be found in [10]; A , β and α are viscous parameters [11] identifiable from the creep or relaxation curves in the region of linear behavior. All these parameters depend on temperature, but not so strong as the elastic modulus E . Therefore, assuming that the coefficient of diffusion depends on the temperature, we need to perform a time transformation [12] and take into account the time dependence of the elastic modulus via the temperature. This can be done directly, without introducing a transformed time because beside the elasticity module E we do not perform differential or integral operators.

b) The penetration area - w , without the failure part w_f is governed by the creep law [9]

$$\dot{\varepsilon}_w = \dot{\varepsilon}_o \left(\frac{\sigma_w}{\sigma_o} \frac{1}{1-D(t)} \right)^n. \quad (18a)$$

Here $D(t)$ is the damage parameter of Kachanov [13,14], σ_w is the traction stress in the area of slow damage (penetration with lower concentration).

c) The failure area w_f is governed by the creep law [9]

$$\dot{\varepsilon}_f = \dot{\varepsilon}_o \left(\frac{\sigma_f}{\sigma_o} \frac{1}{1-D(t)} \right)^n. \quad (18b)$$

Here σ_f is the traction stress in the accelerated damage area (penetration with a concentration close to the limit one).

Equilibrium and compatibility require respectively

$$\sigma = \sigma_f w_f + (w - w_f) \sigma_w + (1 - w) \sigma_u \quad (19)$$

$$\dot{\epsilon}_f + \dot{\epsilon}_w = \dot{\epsilon}_u = \dot{\epsilon} \quad (20)$$

In (19, 20) σ is the global traction stress and $\dot{\epsilon}$ - the global (effective) creep rate.

Combining equations (16, 17, 18, 19, 20) after transformation, to the stress in the slowly damaged area (area of penetration with concentration $c = c_c$) and to the global strain rate we obtain

$$\sigma_w = \frac{\sigma(1 - D(t))}{1 - D(t)w(t)} \quad (21)$$

$$\dot{\epsilon} = \dot{\epsilon}_o \left(\frac{\sigma}{\sigma_o} \right)^n \left(\frac{1}{1 - D(t)w(t)} \right)^n \quad (22)$$

If we assume, that damage exists only in the penetration zone, the damage law can be written as

$$\frac{dD}{dt} = H \left(\frac{\sigma_w}{\sigma_o} \right)^m \phi_d(D, t)^m \quad (23)$$

where H and T are determined by the Wöhler's curves for a material with initial penetration concentration $c = c_c$, while the concentration function has the form:

$$\phi_d(D, t) = \frac{\sigma}{1 - D} f(t) + \frac{\sigma}{D} (1 - f(t)) \quad (24)$$

Here in equation (24) the parameter f indicating the relative material zone with relatively low penetration and damage and subjected to the law of Kachanov, can be expressed as

$$f(t) = 1 - \frac{w_f(t)}{w(t)} \quad (25)$$

Finally from (21,23) to the damage accumulation we have:

$$\frac{dD}{dt} = H \left(\frac{\sigma}{\sigma_o} \right)^m \left(\frac{1 - \frac{w_f(t)}{w(t)} \left(2 - \frac{1}{D(t)} \right)}{1 - D(t) w(t)} \right)^m \quad (26)$$

The four equations (9-with K and Kf, 22 and 26) represent a system of four differential equations governing the creep, damage and penetration evolution of samples subjected to traction and ambient diffusion attack. It contains the information necessary to describe the creep behavior of materials under different loads and temperatures and can predict the durability in the case of coupled problems, if a failure criterion is adopted. As such a criterion could be considered the critical damage concentration, identified from samples with critical concentration $c = c_c$. For the special case of preexposition (samples are held in the surrounding media without load and then are loaded registering their creep), equations (5.12) or the first two of (5.24) must be integrated first (uncoupled problem) to reach the typical depths of penetration (damaged areas) after some preexposition time. These depths are then replaced in equations (5.19, 5.23), or the last two equations (5.24) to obtain creep and damage evolution. The function of

the stress concentration $\phi_d(D, t) = \frac{\sigma}{1-D} f(t) + \frac{\sigma}{D} (1-f(t))$, where

$f(t) = 1 - \frac{w_f(t)}{w(t)}$ depends on time through the depth of penetration and

this should be considered when solving the system (9-with K and Kf., 22, 26).

4. RESULTS AND COMPARISONS

The effect of prior exposure into oxygen, water, engine oil and sulfuric acid, and the effect of the coupled problem (similar loading and penetration) on the creep was studied on samples of butadiennitril (BN) and polyisoprene (PI) rubbers. The surrounding media penetrate into the rubber and form zones of lower (first critical concentration c_c) and stronger (second critical concentration c_f) damage that reduce the creep resistance. Creep experiments in the presence of surrounding medias at constant traction stress and normal pressure were carried out at 20 °C. The necessary data for both rubbers are systematized in

Tables 1, 2 and 3. The following figures 2 to 9 illustrates the theoretical and experimental results for damage and creep evolution concerning the coupled problem and two times of pre-exposure (concerning the uncoupled problem) of BN and PI band rubbers (thickness $h = 3$ [mm], width $b = 15$ [mm] and length $l = 150$ [mm] - see figure 1) respectively, in water and engine oil.

Table 1 Elasto-viscous characteristics of the investigated rubbers

characteristics	elasto-viscous					
	instantaneous			hereditary		
parameters	E	σ_o	n	A	α	β
dimension	MPa	MPa	-	-	-	-
PI rubber	1.420	0.75	1.71	0.0032	0.97	0.0140
BN rubber	3.025	0.50	1.55	0.0029	0.77	0.0089

Table 2 Strength and diffusion characteristics of the investigated rubbers in media

characteristics	strength				diffusion	
	damage	durability		instant.	1 critical	2 critical
parameters	D^*	$H \times 10^{-6}$	m	σ_f	c_c / c_s	c_f / c_s
dimension	-	-	-	MPa	-	-
PI § water	0.74	0.2218	5.172	10.45	0.596	0.953
PI § engine oil	0.43	0.3551	4.911	10.00	0.579	0.863
BN § water	0.69	3.6840	3.548	27.45	0.374	0.814
BN § engine oil	0.58	2.2580	3.809	29.95	0.420	0.950

Table 3 Diffusion coefficients of the investigated rubbers in media

parameter	D
dimension	$m^2/h \times 10^{-9}$
PI § water	2.425
PI § engine oil	4.829
BN § water	2.271
BN § engine oil	1.504

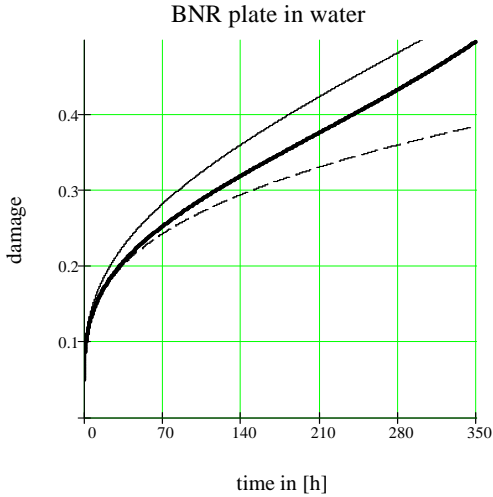


Fig.2 - Damage accumulation for BN in water. Thick line-coupled problem. Thin & dashed lines-uncoupled problem. Pre-exposition times 280 and 7 hours respectively.

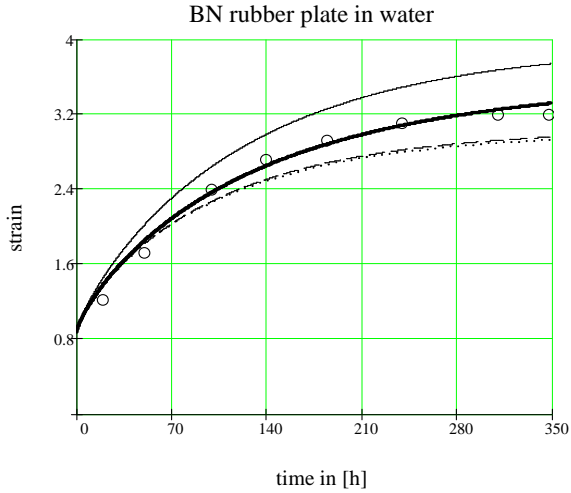


Fig.3- Creep for BN in water. Coupled problem - bold. Uncoupled one- thin and dashed lines: pre-exposition times 280 and 7 hours respectively. Circles-experimental data.

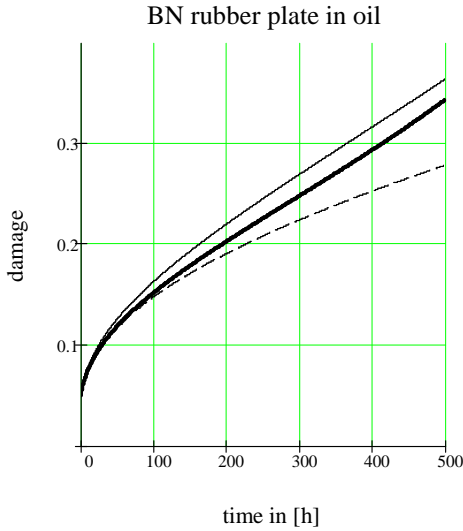


Fig 4- Damage accumulation for BN in engine oil. Thick line-coupled problem. Thin & dashed lines-uncoupled problem. Pre-exposition times 400 and 10 hours respectively.

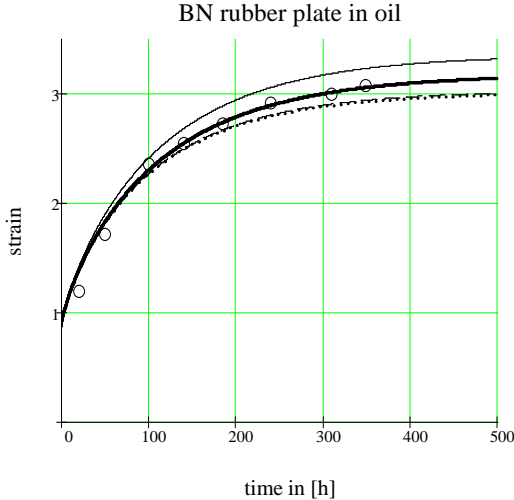


Fig. 5- Creep for BN in engine oil.. Coupled problem - bold. Uncoupled one-thin and dashed lines: pre-exposition times 400 and 10 hours respectively. Circles-experimental data.

Below are given the similar curves for PI (in the same media and under the same loads).

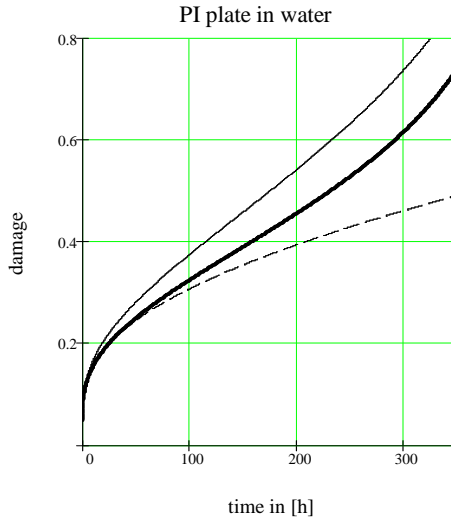


Fig.6 - Damage accumulation for PI in water. Thick line-coupled problem. Thin & dashed lines-uncoupled problem. Pre-exposition times 280 and 7 hours respectively.

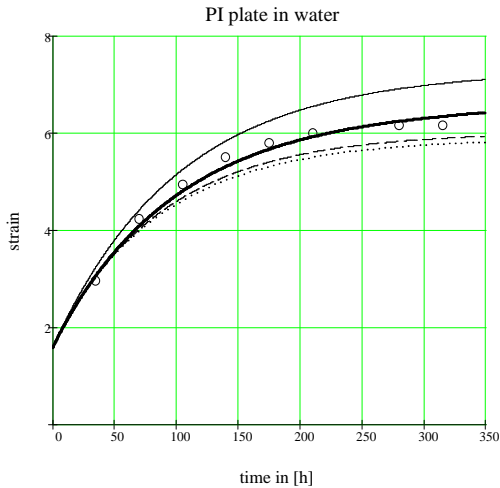


Fig.7 - Creep for PI in water. Coupled problem - bold. Uncoupled one-thin and dashed lines: pre-exposition times 280 and 7 hours respectively. Circles-experimental data.

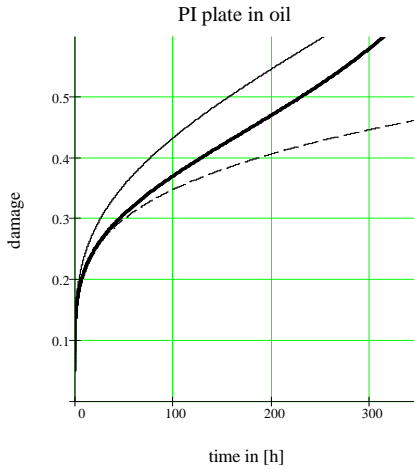


Fig.8- Damage accumulation for PI in engine oil. Thick line-coupled problem. Thin & dashed lines-uncoupled problem. Pre-exposition times 750 and 7 hours respectively.

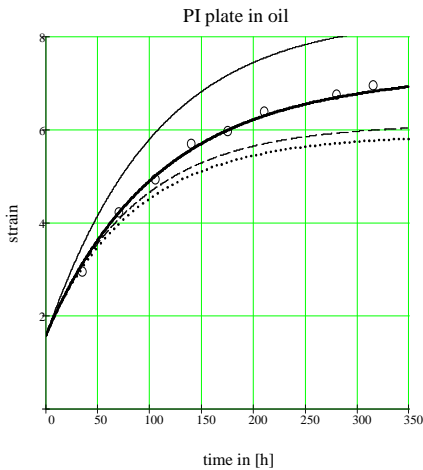


Fig. 9- Creep for PI in engine oil. Coupled problem - bold. Uncoupled one-thin and dashed lines: pre-exposition times 275 and 7 hours respectively. Circles-experimental data.

5. CONCLUSIONS

The proposed model is able to describe the coupled processes of diffusion, damage and creep in rubbers. Large deformations are taken into account using the Neo-Hookean and Mooney-Rivlin laws. Nonlinear viscous effects are described with the help of the hereditary theory of Volterra. In the case of aggressive environment the damage enhancement curve is S shaped. Such behavior is observed even in the case of pre-exposure, but less pronounced. The coupled damage-time curves are between the respective curves at small and large pre-exposition. Similar is the situation concerning the creep curves.

REFERENCES

1. Alexandrov A., Tzolov Tz., Creep Strength Under Viscoelastic Conditions, International Journal of Differential Equations and Applications, 3, 2001.
2. Tzolov Tz., A.Alexandrov, G Geshev , Elastomeric Compounds Containing Phenol – Formaldehyde Oligomers and Hexamethylenetetramine – Possibilities to Improve Their Homogeneity, International Journal of Pure and Applied Mathematics 2003.
3. Naskar K.: Thermoplastic elastomer based on PP/EPDM blends by Dynamic vulcanization – A review, Rubber Chemistry and Technology, 80, 504–510, 2007.
4. K.Hadjov & D.Dontchev, A model predicting damage and durability under cyclic loading, 9th International Conference on Mechanics &Technology of Composite Materials, BAS, Sofia, 2000.
5. Crank, J., Park G., Diffusion in Polymers, Acad. Press, London, 1968.
6. Crank J. Mathematics of diffusion. Oxford Univ. Press, 1956.
7. Likov A., Theory of Thermal Conductivity, Vishaia Shkola, Moskow, 1977 (in russian).
8. Hallil G Hadjov K., Alexandrov A., Sur une Approximation de la Solution de l'Equation de Fick Concernant des Elastomères, Revue Génie Industriel, 2010 (accepted).
9. Ashby M.F., Dyson B.F. Advances in fracture research, ed. S.R.Valluri et al., vol 1, Pergamon Press, Oxford, 1984.
10. Hadjov K., Alexandrov A., Hallil G. Nonlinear elasto-viscosity of rubbers at large deformations, Revue Génie Industriel, 2010.
11. Koltunov M.A., Creep and Relaxion, Nauka, Moskow, 1976.
12. Weitsman Y. Diffusion with Time-Varying Diffusivity, with Application to Moisture-Sorption in Composites, J. Comp. Mater., vol.10, 1976.
13. Katchanov L.M., Durability under Creep Conditions, Izvestia Akademii Nauk SSSR, Otdelenie Tehnicheskih Nauk, Mechanika I Mashinostroenie, 8, 1958.
14. Lemaitre J., Chaboche J.-L. Mécanique des matériaux solides, Dunod, Paris, 1985.

DYNAMICS AND CONTROL OF A FLEXIBLE BEAM WITH IMPACTS

MARGHITU B. Dan^{*}, DIACONESCU Cristian^{*},
CRACIUNOIU Nicolae^{**}, DUMITRU Nicolae^{**}

^{*}*Auburn University, Al, 3684, USA*

^{**}*University of Craiova –Romania,*

Abstract: The linear control of a parametrically excited impacting flexible link in rotational motion is considered. The equation of motion for such a system contains time periodic coefficients. To suppress the vibrations resulting after the impact with an external rigid body, a linear controller is designed via Lyapunov-Floquet transformation. In this approach the time periodic equations of motion are transformed into a time invariant form, which are suitable for the application of standard time invariant controller design techniques. The momentum balance method and an empirical coefficient of restitution is used to model the collision between the two bodies.

Keywords: Flexible beam, impacts, Lyapuno-Floque transformation

1. INTRODUCTION

Impact dynamics of colliding bodies is one of the classical problems of mechanics. The design of impacting systems, such as walking machines, variable geometry wheeled and tracked vehicles, active cord mechanisms, robot manipulators, gear trains, etc., has received attention from many engineers. A special attention has been given to the analysis of elastic links that impact rigid surfaces. Yigit *et al.* (1990) verified the validity of using the algebraic generalized impulse momentum equations of a radially rotating beam, transversely impacting an external surface. Their conclusion was that the momentum balance method and an empirical coefficient of restitution can be used with confidence in the impact of radially rotating beam.

However, active control of vibrations of an impacting beam has not been studied by many authors. Tanaka and Kikushima (1992) studied the impact vibration control using a semi-active damper, driven by

releasing a damper mass from an initial displacement. Optimal design conditions for the semi-active damper were derived.

Boghiu and Marghitu (1998) studied the periodic impacts that occurred between an elastic beam attached to a rotating base and a rigid beam. The lag motion of the elastic beam was studied and fuzzy logic control strategy was employed to suppress the oscillations of the beam tip.

Parametrically excited beams have also received a special attention from several authors. Crespo da Silva and Glynn (1977, 1978) studied the planar and nonplanar oscillations of a cantilever beam subjected to a planar periodic excitation. The stability of out-of-plane motion was performed taking into account damping and geometric nonlinearities in the differential equations of motion. Crespo da Silva (1978) also studied the nonlinearly coupled flexural-flexural motion of the Beck's column subjected to a planar distributed harmonic excitation. In this work, the column could also twist about its neutral axis. The analytical results were compared with those obtained by numerical integration of a set of non-linear differential equations obtained by the application of Galerkin's method to the original equations.

Rotating elastic beams have also been studied extensively. Vyas and Rao (1992) derived the equations of motion of a blade mounted on a disk rotating with variable angular velocity. Crespo da Silva and Hodges (1986a, 1986b) derived the differential equations of motion and their boundary conditions for a helicopter rotor blade. The influence of higher order nonlinearities on the motion were investigated for a range of values of collective pitch.

Cannon and Schmitz (1984) considered an elastic arm, modeled as a pinned-free beam, attached to a hub. The objective of their work was to carry out experiments designed to determine the necessary control torque applied at the base of the link using only the tip position measurement. A more complex system was analyzed by Berbyuk (1984). His work was related to the problem of controlling the plane rotational motions of two rigid bodies connected by an elastic rod. Asymptotic methods were used to obtain a solution of the control problem for some limiting cases.

The control of the flap motion of a parametrically excited rotating beam was considered by Boghiu *et al.* (1996). The linear control design was based on Lyapunov-Floquet transformation technique (Sinha and Joseph, 1994, Sinha *et al.*, 1996). Both full state feedback and observer based controllers were employed to suppress the vibrations of the elastic beam.

In this paper, a parametrically excited rotating elastic beam subjected to periodic impacts has been considered. The elastic beam is

attached to a massless base that has an oscillatory motion of constant amplitude and frequency. The entire assembly can rotate in a horizontal plane with a constant angular velocity. Periodic impact occurs between the elastic link and a rigid beam. A controller has been designed using Lyapunov-Floquet (L-F) transformation to damp out the vibrations of the elastic beam. Simulated results are provided to demonstrate the applicability of the L-F transformation technique in the study of this class of problems.

2. THE SYSTEM MODEL

Figure1 shows the system under consideration. The slender flexible beam AB is cantilevered onto a rigid massless base, with negligible dimensions. The base is attached to a rigid link OO_1 of variable length $L_0+L_1\sin\omega t$ which rotates with a constant angular velocity Ω in the horizontal plane. The flexible beam has length L , a constant flexural rigidity EI and a uniformly distributed mass per unit length $\rho = m/L$, where m is the total mass of the elastic beam.

The base can perform small rotational deflections $\phi(t)$ about the z axis passing through the point O_1 . A spring (of constant k) and a damper (of constant c) are connected to the base and the rigid link in order to avoid large rotation of ϕ . The system is controlled through a control torque u applied to the massless base.

The impacted rigid body, of length l_b and mass m_b can rotate around the fixed point S . The rigid link is connected to the ground through a spring (of constant k_b) and a damper (of constant c_b), avoiding large values of the angle ξ . The spring and the damper are designed such that, after each impact between the two links, the angle ξ goes rapidly to zero, before a new impact. Two reference frames are considered: a "fixed" reference frame (N), of unit vectors \mathbf{i} , \mathbf{j} and \mathbf{k} , whose origin is at O , and a rotating reference frame (R), of unit vectors \mathbf{m}_1 , \mathbf{m}_2 and \mathbf{m}_3 , with the origin at O and attached to the rigid link OO_1 . The unit vectors are related by the transformation

$$\begin{bmatrix} m_1 \\ m_2 \\ m_3 \end{bmatrix} = \begin{bmatrix} \cos \Omega t & -\sin \Omega t & 0 \\ \sin \Omega t & \cos \Omega t & 0 \\ 0 & 0 & 1 \end{bmatrix} \begin{bmatrix} i \\ j \\ k \end{bmatrix}, \quad (1)$$

Let x be the position of any point P on the elastic beam with respect to the end A of the base, and y be the elastic deflection. The elastic deflection is denoted by y_L and y_t is the total beam deflection (Figure 1). The position vector of the point P is

$$r_p = (L_o + L_1 \sin \omega t + x \cos \phi - y \sin \phi)m_1 + (y \cos \phi + x \sin \phi)m_2 \quad (2)$$

The elastic deflection of the beam is computed as

$$y(x,t) = \sum_{i=1}^n \Psi_i(x)q_i(t), \quad (3)$$

where $q_i(t)$ are the generalized elastic coordinates, and $n \in N$ is the total number of vibrational modes (N is the set of natural numbers).

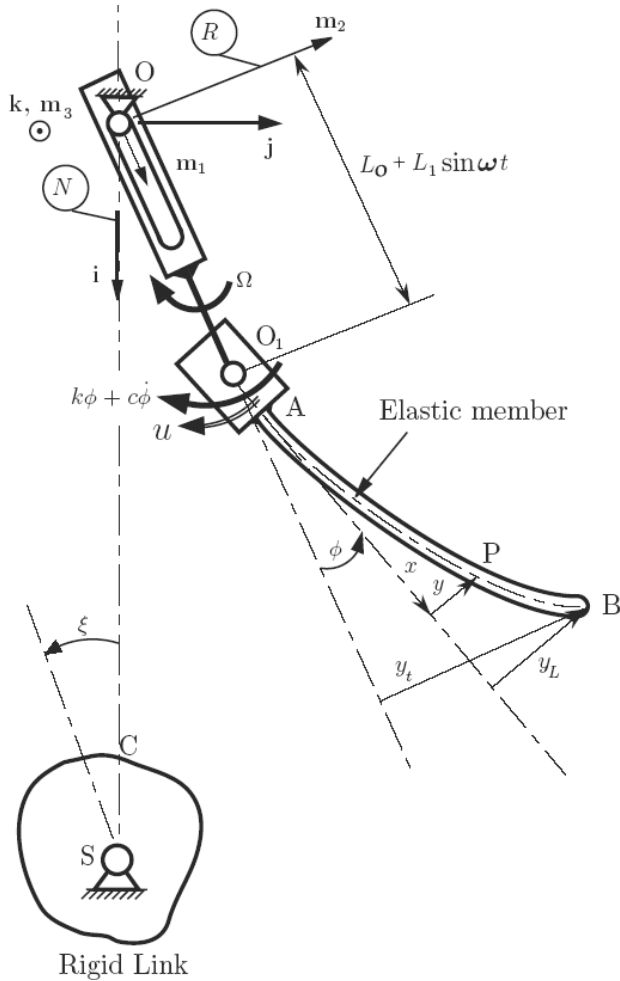


Fig. 1 – Parametrically excited impacting system

The functions $\Psi_i(x)$ are chosen as the mode shapes of a cantilever beam and are defined by the expression

$$\Psi_i(z) = \cosh(z) - \cos(z) - \frac{\cosh(\lambda_i) + \cos(\lambda_i)}{\sinh(\lambda_i) + \sin(\lambda_i)} (\sinh(z) - \sin(z)) \quad (4)$$

where

$$z = \frac{x\lambda_i}{L}, \quad (5)$$

and λ_i ($i = 1, \dots, n$) are the first n^{th} consecutive roots of the transcendental equation

$$\cos(\lambda) \cosh(\lambda) = -1 \quad (6)$$

The velocity of the point P , in the fixed reference frame (M), is computed with the expression

$$v_P = \frac{{}^R d\mathbf{r}_P}{dt} + \boldsymbol{\Omega} \times \mathbf{r}_P \quad (7)$$

where the first term of the right hand side represents the derivative with respect to time in the moving reference frame (R), and $\boldsymbol{\Omega} = -\boldsymbol{\Omega}_k$

The total kinetic energy of the system is

$$K = \frac{\rho}{2} \int_0^L \mathbf{v}_P \cdot \mathbf{v}_P dx + K_b \quad (8)$$

where K_b is the kinetic energy of the impacted rigid body.

The total potential energy of the system is computed as

$$U = \frac{EI}{2} \int_0^L \frac{\partial^2 y}{\partial x^2} dx + \frac{1}{2} k \phi^2 + \frac{1}{2} k_b \xi^2 \quad (9)$$

A three mode approximation ($n=3$) is considered, and the linearized equations of motion around the null equilibrium position are of the form

$$\mathbf{M}\ddot{\mathbf{x}}(t) + \mathbf{C}\dot{\mathbf{x}}(t) + [\mathbf{K}_0 + \mathbf{K}_1(t)]\mathbf{x}(t) = \mathbf{d}u(t) \quad (10)$$

where $\mathbf{x}(t) = [\phi, q_1, q_2, q_3, \xi]^T$ is the vector of generalized coordinates. The mass matrix is \mathbf{M} , the damping matrix is \mathbf{C} , the constant part of the stiffness matrix is \mathbf{K}_0 , the time varying part of the stiffness matrix is $\mathbf{K}_1(t)$, and the input vector is \mathbf{d} . In state space form, equation (10) can be written as

$$\dot{\boldsymbol{\varepsilon}}(t) = \mathbf{A}(t)\boldsymbol{\varepsilon}(t) + \mathbf{b}u(t) \quad (11)$$

where $\boldsymbol{\varepsilon}(t) = [\mathbf{x}(t), \dot{\mathbf{x}}(t)]^T$ is the state space vector. The matrix $\mathbf{A}(t)$ and \mathbf{b} are defined as

$$\mathbf{A}(t) = \begin{bmatrix} \mathbf{0}_{4 \times 4} & \mathbf{I}_{4 \times 4} \\ -\mathbf{M}^{-1}(\mathbf{K}_o + \mathbf{K}_1(t)) & -\mathbf{M}^{-1}\mathbf{C} \end{bmatrix}, \mathbf{b} = \begin{bmatrix} \mathbf{0}_4 \\ \mathbf{M}^{-1}\mathbf{d} \end{bmatrix}, \quad (12)$$

where $\mathbf{0}_{4 \times 4}$ and $\mathbf{I}_{4 \times 4}$ are the null and identity matrices of order 4, respectively, and $\mathbf{0}_4$ is a 4×1 null vector. The matrix $\mathbf{A}(t)$ is periodic with period $T = 2\pi/\omega$.

3. IMPACT EQUATIONS

The equations of impulsive motion were determined following the procedure described by Marghitu and Hurmuzlu (1995). Following their work it was assumed that the configuration of the bodies is held constant in the analysis of the collision process, with no significant change in mass and moments of inertia i.e., $\mathbf{x}(t) \approx \text{constant}$. Let \mathbf{F}_c be the impact force, which in this case has only a vertical component, i.e.,

$$\mathbf{F}_c = [0, F_c, 0]. \quad (13)$$

The friction during impact was neglected. Let \mathbf{v} be the vector of generalized speeds for the flexible link, defined as:

$$\mathbf{v} = [\dot{\phi}, \dot{q}_1, \dot{q}_2, \dot{q}_3, \dot{\xi}]^T = [v_j]_{j=1,2,3,4,5} \quad (14)$$

An integrated form of the differential equations were

$$\frac{d}{dt} \frac{\partial K}{\partial v_j} = Q_j, \quad (15)$$

where Q_j are the generalized impulsive forces during impact and K is the kinetic energy of the system. Equation (15) establishes a relationship between the time derivative of the generalized vector \mathbf{v} and the contact force F_c , which leads to the matrix form:

$$\mathbf{M}\mathbf{v} = \mathbf{D}(\mathbf{x}) F_c, \quad (16)$$

where $\mathbf{D}(\mathbf{x})$ is a vector that depends on pre-impact positions.

Taking into account that at the impact moment ξ can be expressed in terms of ϕ , q_1 , q_2 and q_3 , only the first four components of the generalized vector \mathbf{v} are independent.

Let \mathbf{v}_B^- and \mathbf{v}_B^+ be the velocities of the elastic beam tip before and after impact, respectively. Let \mathbf{v}_C^- and \mathbf{v}_C^+ be the velocities of the impacted rigid end link before and after impact, respectively. With these notations, one can write

$$\mathbf{v}_C^+ - \mathbf{v}_B^+ = e(\mathbf{v}_B^- - \mathbf{v}_C^-), \quad (17)$$

where e is the coefficient of restitution. Solving the system of equations (16) and (17) the unknown velocities after impact $(\dot{\phi}^+, \dot{q}_1^+, \dot{q}_2^+, \dot{q}_3^+, \dot{\xi}^+)$ are determined.

4. STATE FEEDBACK CONTROLLER DESIGN

Returning back to equation (11) the objective is to determine a linear time varying control law of the type

$$u = \mathbf{F}\varepsilon \quad (18)$$

where \mathbf{F} is the feedback matrix. It is assumed that all states are available for control, by measurement. The controller design is based on Lyapunov-Floquet transformation, and the procedure developed by Sinha and Joseph (1994) is applied.

To determine the Lyapunov-Floquet Transformation, one must first compute the fundamental matrix (or state transition matrix) $\Phi(t)$. This can be done either analytically using the Chebyshev polynomials expansion approach (Joseph *et al.*, 1993), or by numerical integration of the matrix differential equation

$$\dot{\Phi}(t) = \mathbf{A}(t)\Phi(t), 0 < t \leq T, \quad (19)$$

with the initial condition

$$\Phi(0) = \mathbf{I}_4 \quad (20)$$

For a time $t_1 > T$, the state transition matrix can be computed using the expression

$$\Phi(t_1) = \Phi(t + rT) = \Phi(t) \Phi^r(T), \quad (21)$$

where r is a suitable integer and $\Phi(T)$ is the state transition matrix evaluated at the end of the principal period. This matrix is also called *Floquet Transition Matrix (FTM)*. The matrix $\Phi(t)$ can be factored as

$$\Phi(t) = \mathbf{Q}(t) e^{\mathbf{R}t}, \quad (22)$$

where $\mathbf{Q}(t)$ is a $2T$ real periodic matrix, and \mathbf{R} is a real constant matrix. Due to the periodicity of the matrix $\mathbf{Q}(t)$, matrix \mathbf{R} is computed using the expression

$$\mathbf{R} = \frac{1}{2T} \ln \Phi(2T) = \frac{1}{2T} \ln \Phi^2(T), \quad (23)$$

Applying the Lyapunov-Floquet transformation

$$\varepsilon(t) = \mathbf{Q}(t) \mathbf{z}(t), \quad (24)$$

to equation (11) the following system is obtained}

$$\dot{\mathbf{z}}(t) = \mathbf{R}\mathbf{z}(t) + \mathbf{Q}^{-1}(t)\mathbf{b}u(t). \quad (25)$$

At this point an auxiliary time invariant system of the type

$$\dot{\bar{z}}(t) = R\bar{z}(t) + B_o v(t), \quad (26)$$

is constructed. In equation (26)), B_o is a full rank constant matrix, such that the pair (R, B_o) is controllable. The control vector $v(t)$ of the system given by equation (26) is determined by designing a full state feedback controller using either the pole placement technique or the optimal control theory. Thus one can write

$$v(t) = F_o \bar{z}(t), \quad (27)$$

where F_o is a constant feedback gain. Defining $e(t) \equiv z(t) - \bar{z}(t)$, the dynamic error between the state vectors $z(t)$ and $\bar{z}(t)$, equations (25) and (26) yield

$$\dot{e}(t) = (R + B_o F_o)e(t) + Q^{-1}(t)bu(t) - B_o F_o z(t), \quad (28)$$

Since $(R + B_o F_o)$ is the stability matrix, the systems defined by the equations (25) and (26) can be made equivalent if

$$Q^{-1}(t)bu(t) = B_o F_o z(t). \quad (29)$$

Because condition (29) can not be exactly satisfied, these systems are made equivalent in the least square sense. For this purpose, first the error vector is defined as

$$\eta = bu(t) - Q(t) B_o F_o z(t), \quad (30)$$

and $u(t)$ is computed such that the performance index $\eta^T \eta$ is minimized. This procedure yields (Sinha and Joseph, 1994)

$$u(t) = b^* Q(t) B_o F_o z(t), \quad (31)$$

where b^* is the generalized inverse of matrix b , defined as

$$b^* = (b^T b)^{-1} b^T. \quad (32)$$

Applying the inverse Lyapunov-Floquet transformation to equation (31), we obtain

$$u(t) = b^* Q(t) B_o F_o Q^{-1}(t) \bar{z}(t). \quad (33)$$

Comparing equation (33) with equation (18), the desired feedback gain matrix $F(t)$ is

$$F(t) = b^* Q(t) B_o F_o Q^{-1}(t) \quad (34)$$

It should be observed that the feedback matrix from equation (34) can be computed off line and stored into the computer memory since $Q(t)$ and $Q^{-1}(t)$ are $2T$ periodic and information for $t > 2T$ is not needed. This is important for a real time implementation of the control algorithm.

4.1 STATE OBSERVER DESIGN

In this section we assume that only one state θ (out of eight) can explicitly be measured. In this situation an observer must be designed in order to estimate the other states of vector ϵ .

The observer state equations are given by (Kwakernaak and Sivan, 1955)

$$\dot{\boldsymbol{\varepsilon}}_e(t) = \mathbf{A}(t) \boldsymbol{\varepsilon}_e(t) + \mathbf{b}u(t) + \mathbf{G}(t)(\mathbf{J}\boldsymbol{\varepsilon}_e(t) - \boldsymbol{\sigma}(t)), \quad (35)$$

$$\boldsymbol{\sigma}_e(t) = \boldsymbol{\varepsilon}_e(t), \quad (36)$$

where $\boldsymbol{\varepsilon}_e(t)$ is the estimated states vector of the system given by equation (11) and $\boldsymbol{\sigma}_e(t)$ is the output of the observer. Here $\mathbf{G}(t)$ is the estimation law and the objective is to determine $\mathbf{G}(t)$ via the Lyapunov-Floquet transformation technique. This observer, called the Luenberger observer, and the original system have the same dimension and estimates all the states, including the measurable ones. Therefore, in case of a large scale system, a real time implementation of the observer can be a problem due to the large number of calculations required. In such cases, a reduced order observer should be implemented.

To design the observer, first, the dual system of equation (11) is considered

$$\dot{\bar{\boldsymbol{\varepsilon}}}(t) = \mathbf{A}^T(t) \bar{\boldsymbol{\varepsilon}}(t) + \mathbf{J}^T \bar{u}(t),$$

$$\bar{\boldsymbol{\sigma}}(t) = \mathbf{b}^T \bar{\boldsymbol{\varepsilon}}(t). \quad (37)$$

Due to the duality, the observer design procedure is similar to the controller design procedure developed in the previous section. Thus, the Floquet transition matrix $\Phi_e(T)$ has a factorization

$$\Phi_e(t) = \mathbf{Q}_e(t) e^{\mathbf{R}_e t}, \quad (38)$$

where $\mathbf{Q}_e(t)$ is a $2T$ real periodic matrix, and \mathbf{R}_e is a real constant matrix. Using the transformation

$$\bar{\boldsymbol{\varepsilon}}(t) = \mathbf{Q}_e(t) \mathbf{z}(t). \quad (39)$$

one obtains

$$\dot{\mathbf{z}}(t) = \mathbf{R}_e \mathbf{z}(t) + \mathbf{Q}_e^{-1}(t) \mathbf{J}^T \bar{u}(t). \quad (40)$$

An auxiliary time invariant system

$$\dot{\mathbf{z}}(t) = \mathbf{R}_e \mathbf{z}(t) + \mathbf{J}_o \mathbf{p}(t), \quad (41)$$

is constructed, such that \mathbf{J}_o is a full rank constant matrix, and the pair $(\mathbf{R}_e, \mathbf{J}_o)$ is controllable.

A state feedback controller is designed for the system given by the equation (41) (using either the pole placement technique or optimal control theory) such that

$$\mathbf{p}(t) = \mathbf{G}_o \mathbf{z}(t), \quad (42)$$

where \mathbf{G}_o is a constant gain matrix. Similar to the case of controller design, the minimization of the dynamic error between the Eqs.(40) and (41) yields}

$$\mathbf{F}_e(t) = \mathbf{J}^{T*} \mathbf{Q}_e(t) \mathbf{J}_o \mathbf{G}_o \mathbf{Q}_e^{-1}(t), \quad (43)$$

where \mathbf{J}^{T*} is the generalized inverse of the matrix \mathbf{J}^T . The desired estimation law $\mathbf{G}(t)$ is the transposed of the matrix $\mathbf{F}_e(t)$, i.e.

$$\mathbf{G}(t) = \mathbf{F}_e^T(t). \quad (44)$$

Once again, the observer law can be computed off line and stored into the computer memory. The observer-based closed-loop system, obtained by joining the equations (11) and (35) is

$$\begin{bmatrix} \dot{\boldsymbol{\varepsilon}}(t) \\ \dot{\boldsymbol{\varepsilon}}_e(t) \end{bmatrix} = \begin{bmatrix} \mathbf{A} & \mathbf{bF}(t) \\ -\mathbf{G}(t)\mathbf{J} & \mathbf{A} + \mathbf{bF}(t) + \mathbf{G}(t)\mathbf{J} \end{bmatrix} \begin{bmatrix} \boldsymbol{\varepsilon}(t) \\ \boldsymbol{\varepsilon}_e(t) \end{bmatrix}. \quad (45)$$

5. SIMULATION

5.1 NUMERICAL DATA FOR SIMULATIONS

The following numerical values were used for simulations:

- for the elastic beam (steel) and its massless base: distance between the massless base to the rotation center $L_o = 0.02$ m, excitation amplitude $L_1 = 0.005$ m, excitation frequency $\omega = 10$ rad/s, length of elastic beam $L = 1.5$ m, radius of beam 0.005 m, mass/unit length $\rho = 0.6126$ kg/m, angular velocity of rotation $\Omega = 1$ rad/s, spring constant $k = 2$ Nm/rad and damping constant $c = 0.05$ Nms/rad.
- for the impacted rigid link and its support: beam mass $m_b = 0.3$ kg, spring constant $k_b = 16$ Nm/rad and damping constant $c_b = 5.6$ Nms/rad. The values of the various coefficients involved in the nonlinear equations of motion were shown in Table 1.

5.2 RESULTS

A computer program was developed to simulate the impact of the elastic beam with the rigid link. The integration of the nonlinear equations of motion was performed using the Gear method of FORTRAN IMSL library (Visual Numerics, 1994). The initial conditions of the system states were $\phi = 0.05$ rad, $q_1 = 0$ m, $q_2 = 0$ m, $q_3 = 0$ m, $\xi = 0$ rad and zero velocities at $t = 0$ s. The initial value of the total beam tip deflection was $y_i = 0.075$ m. A kinematic coefficient of restitution $e = 0.5$ for the elasto plastic impact of the two bodies was considered.

Simulations were performed for both undamped and damped systems. In both cases the evolution of the controlled and uncontrolled systems were studied. During the simulations, it was noticed that the second and third elastic coordinates (q_2 and q_3 respectively) have very small values and only the first elastic coordinate q_1 is represented. In all cases, the first impact moment is at $t = 6.28$ s. For the controlled case the system with observer based controller was studied.

Table 1. – The value of the coefficients involved in the equation of motion (10)

	$L = 1$ m	$L = 1.5$ m
F_1 [Kg m]	0.3484	0.7840
F_2 [Kg m]	0.0556	0.1251
F_3 [Kg m]	0.0198	0.0446
G_1 [Kg]	0.6126	0.9189
G_2 [Kg]	0.6126	0.9189
G_3 [Kg]	0.6126	0.9189
H_1 [m ⁻¹]	12.3623	3.6629
H_2 [m ⁻¹]	485.5188	143.8574
H_3 [m ⁻¹]	3806.5462	1127.8655
V_1 [Kg]	0.4796	0.7195
V_2 [Kg]	0.2658	0.3987
V_3 [Kg]	0.1558	0.2337

Figure 2 shows the behavior of the undamped uncontrolled system. The total beam deflection y_t is represented in Figure 2.a. Oscillations with magnitude of 0.28 m are noticed. The amplitude remains constant until a new impact reoccurs. Figure 2.b shows the evolution of the angle ϕ . The magnitude of oscillations increase to 0.2 rad after impact, when vibrations of high frequencies are noticed. The elastic coordinate q_1 is represented in Figure 2.c. Oscillations with a much larger amplitude superimposed on angle ϕ , appears after impact.

The results for the undamped controlled system are shown in Figure 3.

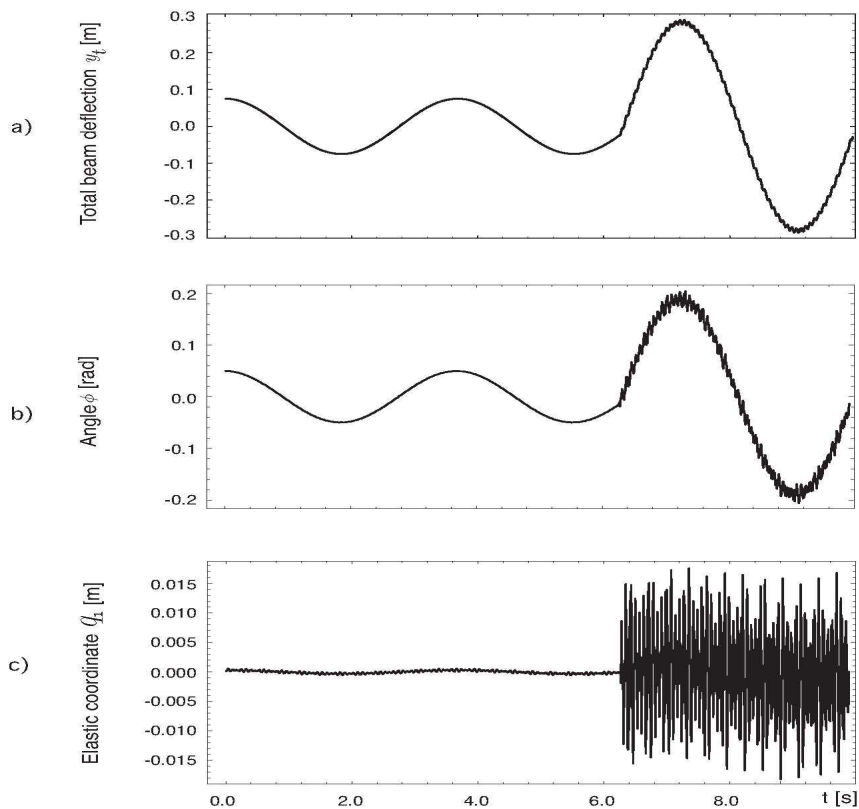


Fig. 2 – Uncontrolled case for undamped system

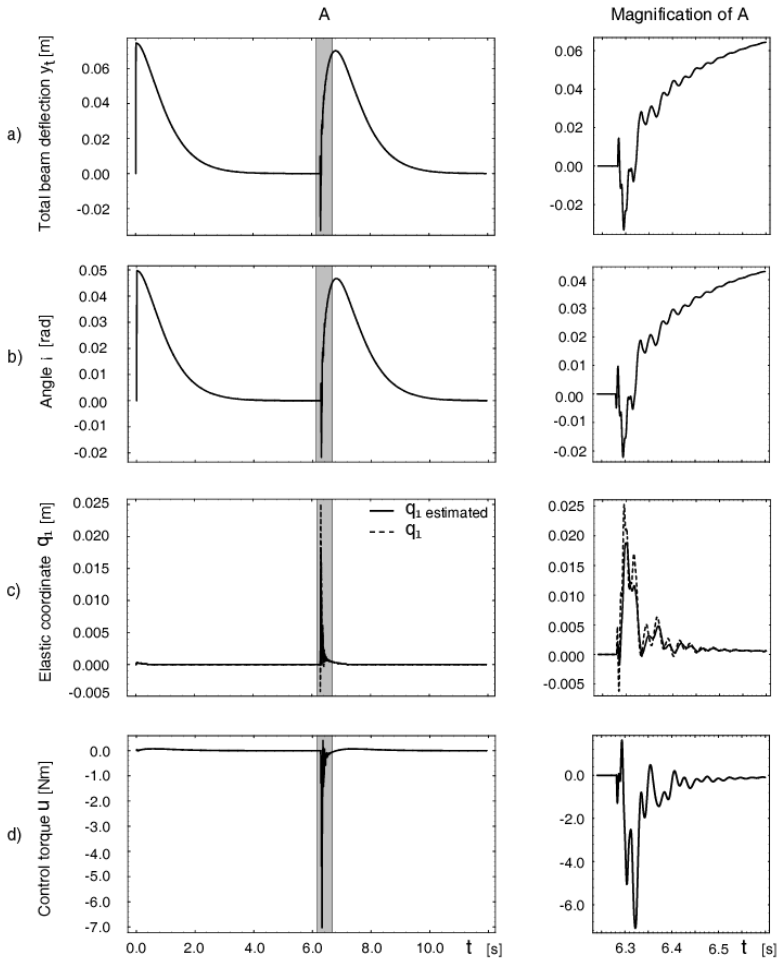


Fig. 3 – Controlled case for undamped system

The top picture represents the total deflection of the beam tip y_t . After impact, a maximum deflection of $y_t = 0.07$ m is noticed. The vibrations of the elastic beam vanishes in less than 5 s, before a new impact. The angle ϕ is shown in the Figure 3.b. The magnitude of $\phi = 0.045$ rad is observed. Due to the control torque applied, the angle ϕ vanishes in a short period of time and no superimposed vibrations are noticed. Figure 3.c shows the elastic coordinate q_1 . The dash line represents the evolution of the system with a full-state controller, and

the continuous line represents the evolution of the same system using an observer based controller.

Immediately after the impact moment, a peak of 0.025 m is noticed, but q_1 goes to zero in a very short period of time, long before a new impact to occur. The estimated value of q_{1e} follows the real value of q_1 . The control torque u applied to the massless base is represented in Figure 3.d. A maximum value of $u = 7$ Nm is noticed. In less than 0.1 s the control torque vanishes and the system has a free evolution to the steady state regime.

The behavior of the damped uncontrolled system is shown in Figure 4.

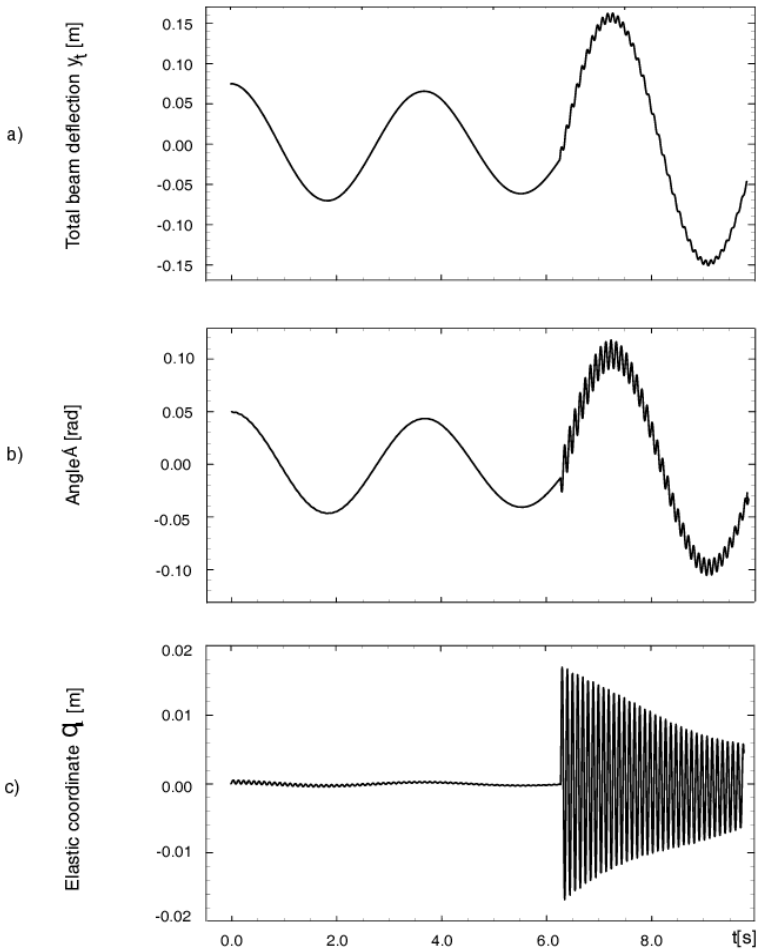


Fig. 4 – Uncontrolled case for damped system

The total beam deflection is represented in Figure 4.a. A maximum deflection of 0.16 m, less than the undamped uncontrolled case is noticed. Then the magnitude of oscillations decrease in time because of the damping ($c = 0.05$ Nms/rad). Figure 4.b shows the angle ϕ . After impact the maximum value of ϕ is 0.12 rad. Compared to Figure 2.b, the amplitude of the superimposed high frequency vibrations are damped out. The elastic coordinate behavior is shown in Figure 4.c. Due to the damping, the magnitude of oscillations decreases in time.

The damped controlled case is presented in Figure 5.

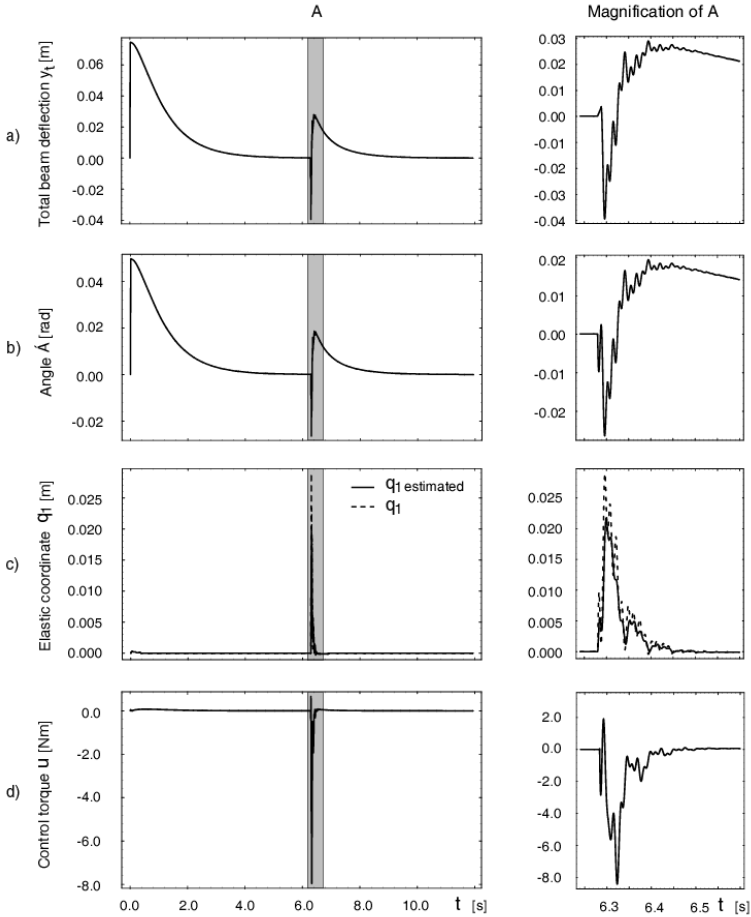


Fig. 5 – Controlled case for damped system

As expected, the maximum value of the total beam deflection y_t (Figure 5.a) is 0.025 m, smaller than in the case of the undamped controlled system. The deflection y_t vanishes before a new impact occurs. Figure 5.b shows the behavior of the angle ϕ . After impact a maximum value of 0.018 rad is noticed, but ϕ goes to zero in a short time. The elastic coordinate q_1 and the estimated value q_{1e} are shown in Figure 5.c, while Figure 5.d represents the applied control torque. Similar conclusions with the undamped controlled case can be drawn. Both q_1 and u have large peak values immediately after impact, and then they go to zero in a very short time interval.

6. CONCLUSIONS

The control problem associated with a parametrically excited rotating flexible link impacting periodically with a rigid beam was studied. A three mode approximation of the flexible link was considered and it was noticed that the second and third elastic coordinates can be neglected. The linearized equations of motion have periodic coefficients that depends on the excitation frequency ω . A full-state feedback as well as an observer based controller was designed using the Lyapunov-Floquet transformation technique. Simulations were performed to show the behavior of both uncontrolled and controlled systems. Both damped and undamped cases were analyzed. In all cases, the first impact moment was 6.28 s. For the uncontrolled system, the total beam tip deflection y_t and the angle ϕ did not vanish before a new impact. The elastic coordinate q_1 was very oscillatory and had a constant amplitude between two consecutive impacts, in the undamped case. For a controlled system, all states vanished before a new impact occurred. The elastic coordinate q_1 had the fastest variation, going to zero in a very short period. The system controller applied a large control torque immediately after the impact moment. The results obtained showed that Lyapunov-Floquet transformation is a powerful tool for linear controllers design. The technique is simple and suitable for a real time implementation.

ACKNOWLEDGEMENTS

This project has been funded in part by the National Research Council under the Collaboration in Basic Science and Engineering Program. The contents of this publication do not necessarily reflect the views or policies of NRC, nor does mention of trade names, commercial products or organizations imply the endorsement by the NRC.

REFERENCES

1. Berbyuk, V.E., 1984, "On the controlled rotation of a system of two rigid bodies with elastic elements," *PMM U.S.S.R.*, Vol. 48, No. 2, pp. 164-170.
2. Boghiu, D., and Marghitu, D.B., 1998, "The control of an impacting flexible link using fuzzy logic strategy," accepted for publication in the *Journal of Vibration and Control*.
3. Boghiu, D., Marghitu, D., and Sinha, S.C., 1996, "Stability and control of a parametrically excited rotating beam," *The 6th Conference on Nonlinear Vibrations, Stability and Dynamics of Structures*, Blacksburg, Virginia.
4. Cannon, R., and Schmitz, E., 1984, "Initial experiments on the end-point control of a flexible one-link robot," *The International Journal of Robotics Research*, Vol. 3, No. 3, pp. 62-75.
5. Crespo da Silva, M. R. M., 1978, "Flexural-flexural oscillations of Beck's column subjected to a planar harmonic excitation," *Journal of Sound and Vibrations*, Vol. 60(1), pp. 133-144.
6. Crespo da Silva, M. R. M., and Glynn, C.C., 1978, "Nonlinear-flexural-torsional dynamics of inextensional beams. II: Forced motions", *J. Struct. Mech.*, Vol. 6, pp. 449-461.
7. Crespo da Silva, M. R. M., and Hodges, D. H., 1986a, "Nonlinear flexure and torsion of rotating beams, with application to helicopter rotor blades-I. Formulation", *Vertica*, Vol. 10, No. 2, pp. 151-169.
8. Crespo da Silva, M. R. M., and Hodges, D. H., 1986b, "Nonlinear flexure and torsion of rotating beams, with application to helicopter rotor blades-II: Response and stability results", *Vertica*, Vol. 10, No. 2, pp. 171-186.
9. Glynn, C. C., and Crespo da Silva, M. R. M., 1977, "Nonplanar forced vibrations of a nonlinear beam under several support conditions", *University of Cincinnati, Engineering Science Department, Report No. E.S.77-116*.
10. Joseph, P., Pandiyan, R., and Sinha, S. C., 1993, "Optimal control of mechanical systems subjected to periodic loading via Chebyshev polynomials," *Optimal Control Applications and Methods*, Vol. 14, pp. 75-90.
11. Marghitu, D.B., and Hurmuzlu, Y., 1996, "Nonlinear Dynamics of an Elastic Rod with Frictional Impact," *International Journal of Nonlinear Dynamics*, Vol. 10, pp. 187-201.
12. Sinha, S. C., Pandiyan, R., and Bibb, J. S., 1996, "Lyapunov-Floquet transformation: computation and applications to periodic systems," *Journal of Vibration and Acoustics*, Vol. 118, pp. 209-219.
13. Sinha, S. C. and Joseph, P., 1994, "Control of general dynamic systems with periodically varying parameters via Lyapunov-Floquet transformation," *ASME Journal of Dynamic Systems, Measurement, and Control*, Vol. 116, pp. 650-658.

14. Tanaka, N., and Kikushima, Y., 1992, "Impact vibration control using a semi-active damper", *Journal of Sound and Vibration*, Vol. 158, No. 2, 277-292.
15. Visual Numerics Inc., IMSL Math/Library. Fortron subroutines for mathematical applications.
16. Vyas, N. S., and Rao, J. S., 1992, "Equations of motion of a blade rotating with variable angular velocity", *Journal of Sound and Vibrations*, Vol. 156(2), pp. 327-336.
17. Yigit, A., Ulsay, A. G. and Scott, R. A., 1990, "Dynamics of a radially rotating beam with impact. Part I: Theoretical and computational model", *Journal of Vibration and Accoustics*, Vol. 112, pp. 65-70.

A SHEAR STRESS ANALYSIS OF I-TYPE WELDED SECTIONS (I)

Dan ILINCIOIU¹, Cosmin MIRIȚOIU²

^{1,2}*University of Craiova, Faculty of Mechanics*

Abstract: In this paper there is made a mathematical model of shear stress calculus for an I-type welded section. Starting from the standard values of core thickness and from the geometrical characteristics values depending on this thickness, it is realised an analytical model where more loading schemes of I-type beam are represented and analysed in terms of strength. The shear stresses that occur in welding for every calculus chosed hypothesis will be computed. The loadings, the calculated shear forces and the obtained shear stresses depend on the beam's length and on the bead's thickness.

Keywords: mechanical strength, mathematical model, I-type profile, welding, calculus hypothesis, shear stresses.

1. INTRODUCTION

For rational design of welded flatbars metallic structures of various types of sections, in addition to the analytical definition of the geometrical characteristics of their section, the strength calculus is essential to highlight if the metallic structure withstands the stresses to which is subjected. Also, in the strength calculus, the shear stresses that occur in the welded joints must be studied to.

Usually, when welded flatbars metallic constructions are made, the following sections are used: I, U, T, L and their combinations. In most cases, welded flatbars I-type profiles are found to be most used. Therefore, in this paper, we will deal with the study of these types of sections.

Based on the core thickness standard values and on the geometrical characteristics values depending on this thickness (according to [1]), it is achived an analytical mathematical model where more loading schemes for a beam made of such profile are represented and analyzed in terms of strength. The shear stresses that occur in welding for every chosed calculus hypothesis will be computed.

2. THEORETICAL BACKGROUND

2.1 GENERALITIES

According to [1], a welded construction I-profile flat bar has the optimum shape from fig. 1.a, where δ is the thickness bead. In fig. 1.b. the section dimensions of an unwelded I-profile are sketched, and in fig.1.c the sheat stresses distribution in the material is presented.

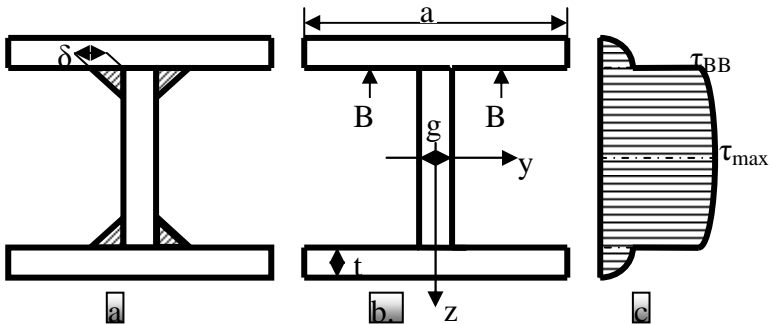


Fig.1.a. optimum shape of an I-welded section; b. section dimensions for an unwelded profile; c. shear stress distribution

It is known that the shear stresses in every material are computed using relation (1) known as the Juravski Formula. Fig. 2 shows how this formula is applied for a circular section.

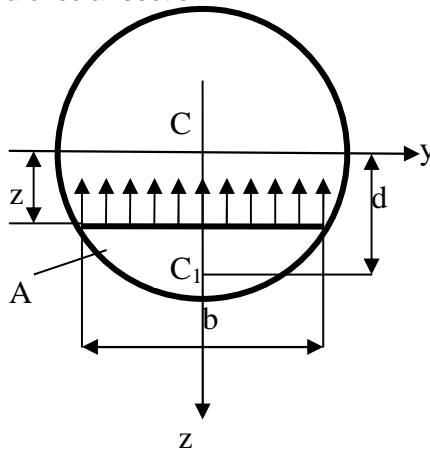


Fig.2. Juravski Formula schematization

$$\tau = \frac{T \cdot S_y}{b \cdot I_y} \quad (1)$$

where T is the shear force from section; S_y is the static inertia moment of the surface under the line which the stress is computed on; I_y is the section inertia moment from y axis; C is the section centroid; C_1 is the section centroid under the line which the stress is computed on (this part tends to slide along the bar under the shear forces action). Formula (1) allows the shear stress calculation on a line parallel to the O_y axis of the chosen reference system.

2.2 LOADING SCHEMES

The loading schemes that mostly occur in the engineering practice for welded flatbar I profiles are shown in fig3.a.,b.,...,f where several variants are met:

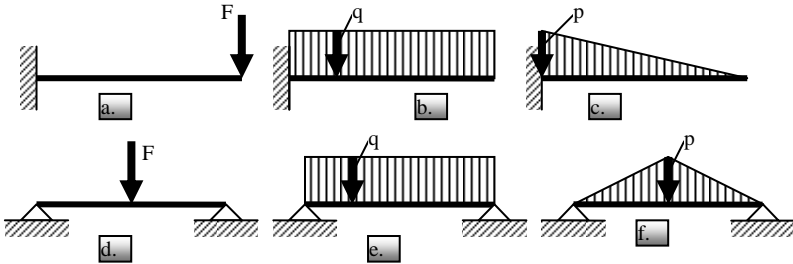


Fig.3. beams loading schemes

- variant 1 – the bar is immovable at one end with a concentrated force at the other end:

$$F = \frac{M_{\max}}{l} \quad (2)$$

- variant 2 – the bar is immovable at one end with uniformly distributed pressure of value:

$$q = \frac{F}{l}; F = \frac{2 \cdot M_{\max}}{l} \quad (3)$$

- variant 3 – the one end immovable bar with triangullary distributed pressure of value:

$$p = \frac{2 \cdot F}{l}; F = \frac{3 \cdot M_{\max}}{l} \quad (4)$$

- variant 4 – bar double supported at the ends with concentrated force at the middle:

$$F = \frac{4 \cdot M_{\max}}{l} \quad (5)$$

- variant 5 – double supported bar with uniformly distributed pressure of value:

$$q = \frac{F}{l}; F = \frac{8 \cdot M_{\max}}{l} \quad (6)$$

- variant 6 – double supported bar with double triangular distributed pressure of value:

$$p = \frac{2 \cdot F}{l}; F = \frac{4 \cdot M_{\max}}{l} \quad (7)$$

Note: the beams from fig.3. have the same "l" length and the value of the maximum moment M_{\max} is determined from the strength condition at bending:

$$M_{\max} = \sigma_a \cdot W_y \quad (8)$$

where σ_a is the material admissible stress from which the beam is made of; W_y is the axial strength modulus.

3. SHEAR STRESSES DETERMINING

3.1 BENDING MOMENT AND SHEAR FORCE DIAGRAMS

In order to determine the shear stresses, we must draw the bending moment and shear force diagrams for every considered variant. In table 1, there are presented the shear force and bending moment calculus relations depending on the x distance ($x=0..l$).

Table 1. calculus relations of shear force and bending moment

Variant	Shear Force	Bending Moment
1	$T(x) = F$	$M(x) = F \cdot x$
2	$T(x) = \frac{F \cdot x}{l}$	$M(x) = \frac{F \cdot x^2}{2 \cdot l}$
3	$T(x) = F \cdot \frac{x^2}{l^2}$	$M(x) = \frac{F \cdot x^3}{3 \cdot l^2}$
4	$T(x) = 0,5 \cdot F$	$M(x) = 0,5 \cdot F \cdot x$
5	$T(x) = 0,5 \cdot F - \frac{F \cdot x}{l}$	$M(x) = 0,5 \cdot F \cdot x - \frac{F \cdot x^2}{2 \cdot l}$
6	$T(x) = 0,5 \cdot F - \frac{2 \cdot F \cdot x^2}{l^2}$	$M(x) = 0,5 \cdot F \cdot x - \frac{2 \cdot F \cdot x^3}{3 \cdot l^2}$

Based on the relations presented in table 1, the shear force and bending moment diagrams are drawn in fig 4.

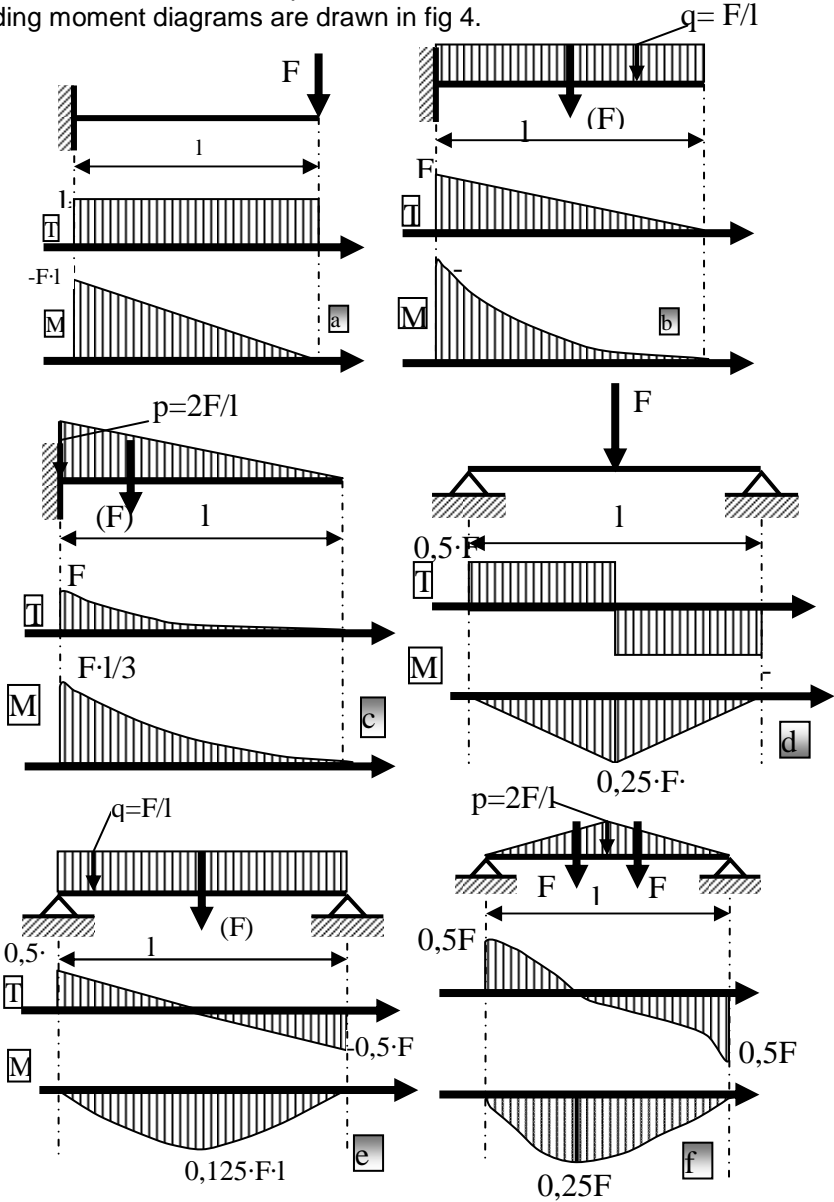


Fig.4. shear force and bending moment diagrams

3.2 SHEAR STRESS CALCULUS

In fig.5 it is considered the general case of an I-profile welded construction beam loaded by a system of certain forces F_1, \dots, F_n , by any system of uniformly distributed pressures q_1, \dots, q_n and by a M concentrated moment. There are also presented the beam's parts : 1-base, 2-core and 3- the welding. There are schematically drawn the section force and bending moment diagrams.

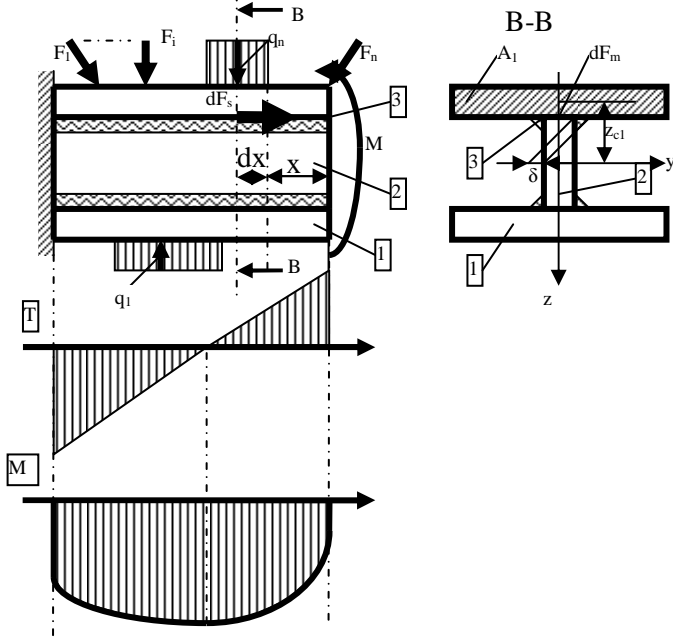


Fig.5. the loading scheme of a welded construction I-profile beam with shear force and bending moment diagrams drawn; beam parts presentation where 1 is the base, 2 is the core and 3 is the welding

For such beams the following types of shear stresses appear:

- the material shear stress computed with relation (1)
- the welding shear stress

Isolating a dx – length elementary part at the x distance from the right end, the two stresses produce two elementary forces in both welding and material. The forces are calculated with relations (9) and (10).

$$dF_s = \tau_s \cdot \delta \cdot dx \quad (9)$$

$$dF_m = \tau_m \cdot g \cdot dx \quad (10)$$

where dF_s is the elementary force produced by the welding shear stress, dF_m is the elementary force produced by the material shear stress; δ is the bead's thickness; g is the thickness of the profile's core.

Equaling the relations (9) and (10) we can obtain a connection between the two shear stresses, expressed with relation (11).

$$\tau_s = \frac{g}{\delta} \cdot \tau_m \quad (11)$$

For the case from fig.4., the parameters that are in the material shear stress from relation (1) will be computed using the relations (12). The I-section notations from fig.1.b will be used in calculus. The I_y inertia moment is computed according to the notations from [1], chapter 2, calculus variant 1, and T is the shear force from the current section.

$$b=g; A_1=a \cdot t; z_{c1}= 0,5(h-t); S_y= A_1 \cdot z_{c1} \quad (12)$$

4. CONCLUSIONS

In this paper, it is made a shear stress analysis of I-type metallic profiles made of flatbar. Starting from the Juravski Formula of shear stress calculus, it is made an analytical model where the most met in practical engineering loading schemes for an I-type beam are presented and analyzed in terms of strength.

The force and the pressure from the loading schemes are presented depending on the maximum bending moment which can be obtained from the strength condition (8) and on the beam's length.

In chapter 3, in order to determine the shear stress there have been presented the calculus relations (in table 1) and there have been drawn the diagrams (in fig.4) of shear force and bending moment for all the considered variants.

Table 2. calculus relations of welding shear stress

Variant	Shear Stress Formula
1	$\tau_s = 0,5 \cdot F \cdot a \cdot t \cdot \frac{h-t}{\left[\frac{g \cdot (h-2t)^3}{12} + \frac{a \cdot t^3}{6} + 0,5 \cdot a \cdot t \cdot (h-t)^2 \right] \cdot \delta}$
2	$\tau_s = 0,5 \cdot F \cdot a \cdot t \cdot \frac{x \cdot (h-t)}{\left[\frac{g \cdot (h-2t)^3}{12} + \frac{a \cdot t^3}{6} + 0,5 \cdot a \cdot t \cdot (h-t)^2 \right] \cdot \delta \cdot l}$
3	$\tau_s = 0,5 \cdot F \cdot a \cdot t \cdot \frac{x^2 \cdot (h-t)}{\left[\frac{g \cdot (h-2t)^3}{12} + \frac{a \cdot t^3}{6} + 0,5 \cdot a \cdot t \cdot (h-t)^2 \right] \cdot \delta \cdot l^2}$

Variant	Shear Stress Formula
4	$\tau_s = 0,25 \cdot F \cdot a \cdot t \cdot \frac{h-t}{\left[\frac{g \cdot (h-2t)^3}{12} + \frac{a \cdot t^3}{6} + 0,5 \cdot a \cdot t \cdot (h-t)^2 \right]} \cdot \delta$
5	$\tau_s = 0,5 \cdot F \cdot a \cdot t \cdot \frac{(0,5 \cdot F \cdot l - F \cdot x) \cdot (h-t)}{\left[\frac{g \cdot (h-2t)^3}{12} + \frac{a \cdot t^3}{6} + 0,5 \cdot a \cdot t \cdot (h-t)^2 \right]} \cdot \delta \cdot l$
6	$\tau_s = 0,5 \cdot F \cdot a \cdot t \cdot \frac{(0,5 \cdot F \cdot l^2 - F \cdot x^2) \cdot (h-t)}{\left[\frac{g \cdot (h-2t)^3}{12} + \frac{a \cdot t^3}{6} + 0,5 \cdot a \cdot t \cdot (h-t)^2 \right]} \cdot \delta \cdot l^2$

Then, in order to determine the shear stress from the welding, the relations (9) and (10) have been used by equalling them. The following calculus hypothesis has been made: the shear stress from the material must be equal with the shear stress from the welding. There have been obtained the relation (11) that expresses a connection between the two shear stresses.

In table 2 there are presented the values of shear stress for each considered variant taking into account the relation (1), (11), (12) and the values of shear forces from table 1.

The mathematical model can be easily computed with a specialised software like MatLab, MathCad or Maple.

ACKNOWLEDGMENT

This work was partially supported by the strategic grant POSDRU/88/1.5/S/50783 (2009) co-financed by the European Social Fund- Investing in People, within the Sectoral Operational Programme Human Resources Development 2007-2013.

REFERENCES

1. Ilincioiu, D., Mirițoiu, C., A Geometrical Analysis of INP Rolled Profiles Used at Welded Constructions, The 8th International Conference, Structural Integrity of Welded Structures, pp.58-65, Timișoara 2010
2. Ilincioiu, D., Mirițoiu, C., A Strength Analysis of Welded INP Metallic Profiles, The 8th International Conference, Structural Integrity of Welded Structures, pp.52-58, Timișoara 2010
3. Ilincioiu, D., Mirițoiu, C., Pădeanu, A., Strength of Materials, Universitaria Publishing House, Craiova, 2010
4. Johrend, H., Ilincioiu, D., The Strength of Centrifugal Impellers, Sitech Publishing House, Craiova, 2010

SOME APPLICATIONS FOR WOHLHART MECHANISM

DAHAN Marc *, RACILA Laurentiu **

*FEMTO-ST, University of Franche-Comté- France

**University of Craiova- Romania

Abstract: The paper presents some possible applications for a special class of over constrained mechanisms. In the large family of over constrained mechanisms we consider only the close-loop mechanisms with revolute joints and more precisely with six revolute joints. In a very special spatial disposition the movements of this particular class of over constrained mechanisms changes. We impose three of the six revolute joints to remain in a fixed horizontal plane. The others three joints will define another plane. This plane will be always parallel with the fixed one. For this spatial disposition some possible applications are presented.

Keywords: over constrained mechanisms, industrial applications

1. INTRODUCTION

Over constrained mechanisms is a particular class of mechanisms, normally having a mobility zero or negative according to usual mobility criterions. But despite this, these mechanisms are mobile thanks to a special geometry of linkages.

In 1853 Sarrus [16] presents his mechanism, a closed-loop mechanism with six revolute joints (6R mechanism) capable to transform a rotational movement in a translational one. This mechanism is considered today the first spatial over constrained mechanism.

Many years later, Raoul Bricard (1897) described in his paper [4] three types of over constrained mechanisms: the line-symmetric, the plane-symmetric and the double collapsible octahedral linkages. Thirty later years [5] he presents another three over constrained mechanisms with six revolute joints: the line-symmetric, the plane-symmetric and the trihedral (rectangular) mechanism.

After Sarrus and Bricard others researchers have published papers describing overconstrained mechanisms, like Bennett [3], Myard

[12] or Goldberg [10], Schatz [17], Waldron [19], Mavroidis and Roth [11], Wohlhart [20] or Dietmaier [7]. Between these authors, Karl Wohlhart presents in 1987 a new 6R-overconstrained mechanism with three partial symmetry planes [20]. This mechanism can be considered as a generalization of Bricard rectangular mechanism, and, so, we will call it the Wohlhart mechanism.

A particular case of this mechanism is represented by its symmetric. In this particular case all six links are equals and the twists angles are complementary.

A particular aspect for these mechanisms is practical applications. Over constrained mechanisms were always being in attention of many researchers, but in the most cases only from theoretical point of view. One of the first authors who makes a deep analyze of the 6R closed-loop over constrained mechanisms was J.E. Baker [1, 2].

The industrial applications for 6R over constrained mechanisms are practically nonexistent. Excepting "Turbula" mechanism presented by Paul Schatz [17], derived from Bricard rectangular mechanism and some deployable structure of Chen [6] and Gan [9], the closed-loop over constrained mechanisms with six revolute joints have not found application in industry.

Another possible application for these mechanisms is the 6R-Translator, presented by Racila and Dahan [14] and developed in Laboratory of Applied Mechanics in Besancon-France. This translator is based on Wohlhart symmetric mechanism (all links are equals) but it is used in a new spatial disposition.

In this new spatial disposition three non successive joints remain in a fixed plane, called the reference (or fixed) plane. The joint remains in this reference plane will have an imposed movement. Due of the mechanism symmetry these joints will form an equilateral triangle. These three actuated joints are imposed to make displacements along the heights of equilateral triangle, to the centre of the triangles circumscribed circle. In fact to obtain a movement only one joint from the three ones are needed to be actuated, for the others two only a prismatic guide being necessary.

Few important properties derive from this new spatial disposition. The first one is that the non-actuated joints will define a new plane. This plane will be parallel to the fixed one all the time. A second important property is the orthogonally between the line determined by the intersection point of odd and even joints axes (call vertical line) and the two parallels planes described below. Another important property is the disposition of the driven (non-actuated) joints, in the corners of an equilateral triangle.

All these properties can be used to realize some applications for this new device.

2. CLOSURE EQUATIONS

We consider the Denavit-Hartenberg parameterization for a mechanism with revolute joints [8]. The twist angle between two successive joints (i) and (i+1) is noted α_i , the bar lengths is noted a_i and the offset distance between two elements (i-1) and (i) is noted d_i . The fourth parameter is the angle between two successive elements (i-1) and (i), noted θ_i .

Figure 1 shows the schematic representation of the revolute joints with the Denavit and Hartenberg notations, with a_i , α_i and d_i the geometric parameters and θ_i the kinematical variable.

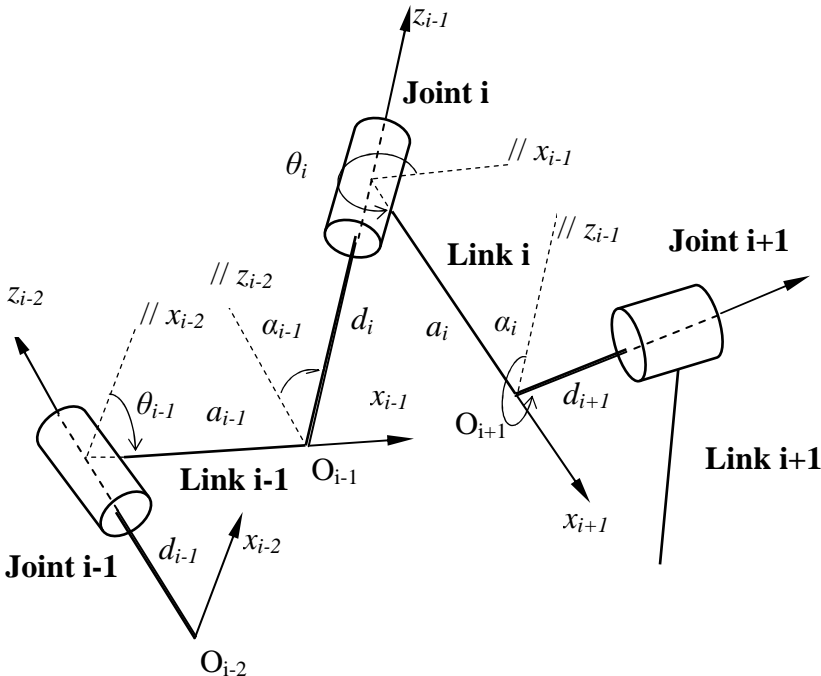


Fig. 1 – Denavit – Hartenberg parameters

To pass from a reference frame (i-1) to the next one (i), four transfer matrixes are necessary. The first is a translation along to the z_{i-1} axes with the distance d_i . The second is a rotation around z_{i-1} axes with θ_i angle and the third is a translation along to the x_i axes with the distance a_i . The last one is a rotation to x_i axes with α_i angle.

The homogeneous form for the transfer matrix is obtained multiplying the four transfer matrixes. So, the final form for the transfer matrix is:

$${}^{i-1}Q_i = \begin{bmatrix} \cos \theta_i & -\cos \alpha_i \cdot \sin \theta_i & \sin \alpha_i \cdot \sin \theta_i & a_i \cdot \cos \theta_i \\ \sin \theta_i & \cos \alpha_i \cdot \cos \theta_i & -\sin \alpha_i \cdot \cos \theta_i & a_i \cdot \sin \theta_i \\ 0 & \sin \alpha_i & \cos \alpha_i & d_i \\ 0 & 0 & 0 & 1 \end{bmatrix} \quad (1)$$

The closure condition for a 6R single loop mechanism expresses that the six transfer matrix product is equal with the unity matrix, but can be also written:

$${}^3Q_4 \cdot {}^4Q_5 \cdot {}^5Q_6 = {}^3Q_2 \cdot {}^2Q_1 \cdot {}^1Q_6 \quad (2)$$

The left and right sides of previous equation are both 4x4 matrices in the form:

$$Q = \begin{bmatrix} r_{11} & r_{12} & r_{13} & t_{11} \\ r_{21} & r_{22} & r_{23} & t_{21} \\ r_{31} & r_{32} & r_{33} & t_{31} \\ 0 & 0 & 0 & 1 \end{bmatrix} \quad (3)$$

The 3x3 r_{ij} sub-matrix on the left side is the rotation transfer matrix and the 3x1 sub-matrix on the right side is the translation vector. Developing this equation we obtain a twelve equations system and four identities. This system is identical with the system obtained by Waldron and cited by Baker [2].

In the case of Wohlhart symmetric mechanism (fig. 2) these twelve equations will be simplified according to the geometrical conditions for this mechanism:

$$\begin{cases} d_1 = d_2 = d_3 = d_4 = d_5 = d_6 = 0 \\ \alpha_1 = \alpha_3 = \alpha_5 = \alpha \\ \alpha_2 = \alpha_4 = \alpha_6 = 2\pi - \alpha \\ a_1 = a_2 = a_3 = a_4 = a_5 = a_6 = a \end{cases} \quad (4)$$

The first four closure equations of this mechanism can be obtained by geometrical reasoning or solving the 12 closure equation system [15]:

$$\begin{cases} \theta_1 = \theta_3 = \theta_5 = \theta \\ \theta_2 = \theta_4 = \theta_6 = \varphi \end{cases} \quad (5)$$

The 12 closure equations system can be reduced to a single one, between the input angle θ and the output angle φ :

$$\begin{aligned} & \cos \theta \cdot \cos \varphi \cdot (1 + \cos^2 \alpha) + (\cos \theta + \cos \varphi) \cdot \sin^2 \alpha - \\ & - 2 \cdot \sin \theta \cdot \sin \varphi \cdot \cos \alpha + \cos^2 \alpha = 0 \end{aligned} \quad (6)$$

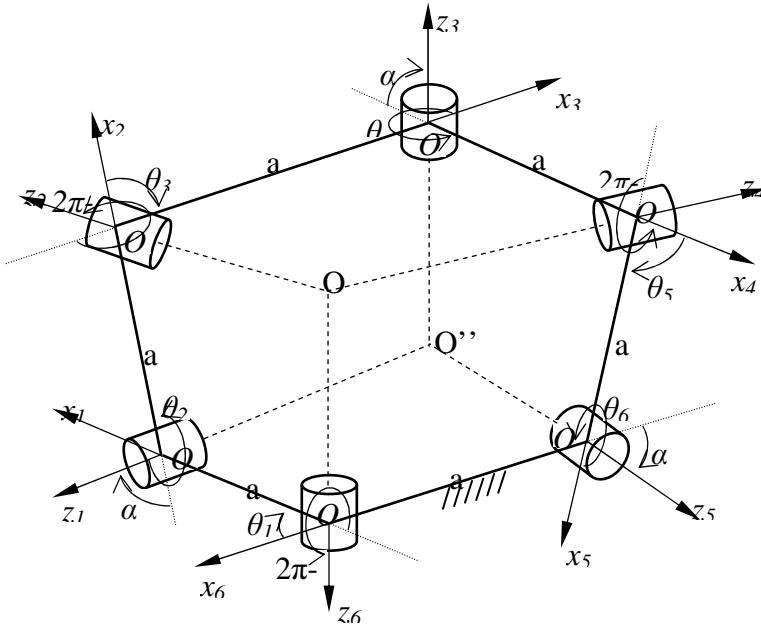


Fig. 2 Wohlhart symmetric mechanism

It is interesting to note that the input-output equation is symmetrical in θ and φ , so the output angle can also serve as input angle.

For a twist angle $\alpha = \pi/2$, we obtain the input-output equation of Bricard symmetric rectangular mechanism:

$$\cos \theta \cdot \cos \varphi + \cos \theta + \cos \varphi = 0 \quad (7)$$

3. NEW SPATIAL DISPOSITION

We consider now Wohlhart symmetric mechanism and we constrain three revolute joints O_1 , O_3 and O_5 to remain and make a displacement on three line segments, to the centre of their circumscribed circle. The others three joints O_2 , O_4 and O_6 will remain always in a parallel plane with the first one.

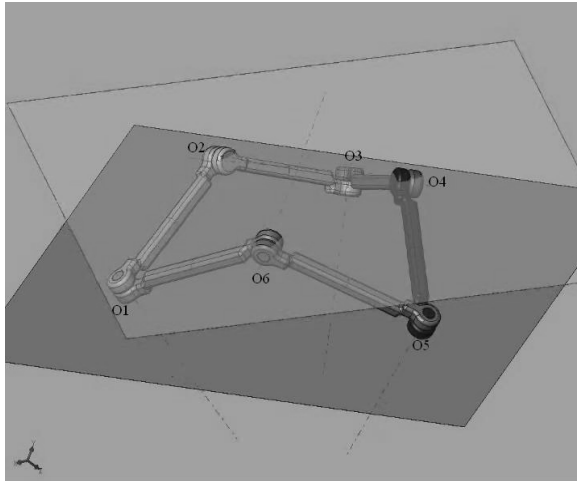


Fig. 3 The new spatial disposition

Figure 3 and 4 shows the new spatial disposition. We note with subscript the joints number and with superscript the position of the joints in its displacements.

Due to the mechanism symmetry, when the joints O_1 , O_3 and O_5 make a displacement to the long of the heights of the initial horizontal triangle $O_1^1 O_3^1 O_5^1$, the joints O_2 , O_4 and O_6 make movements in perpendicular planes on the horizontal plane.

We note with b the distances $O_1^1 O_1^2$, the joints displacements in the horizontal plane of movement (fig. 4).

When $b = 0$ all the six joints are in the initial position in the horizontal plane and the input angle θ is zero. When b increases the joints O_2 , O_4 and O_6 make movements in perpendicular planes to the horizontal one and the input angle θ increase.

The joints O_2 , O_4 and O_6 will arrive to a maximal height from the horizontal plane. Increasing b , the joints will continue their displacements but this time going down to the horizontal plane.

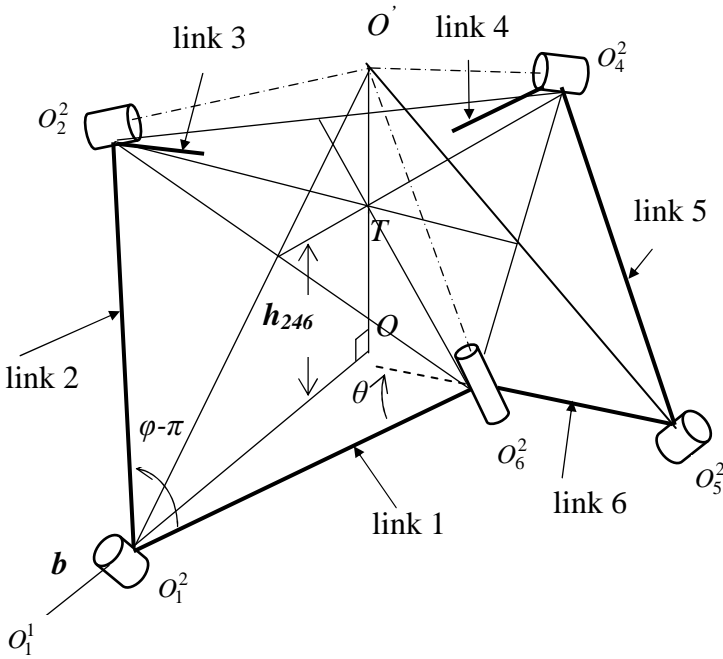


Fig. 4 Intermediary position of the mechanism

3. NUMERICAL RESULTS

A first possible application for this device is as parallel translator. We note with h_{246} the distance between the two planes. This distance between the horizontal plane (135) and the mobile plane (246) is [13]:

$$h_{246} = a \cdot \sqrt{\frac{4}{3} \cdot \left(1 - \frac{(2a - b\sqrt{3})^2}{4a^2}\right) \cdot \left(1 - \frac{a^2}{(2a - b\sqrt{3})^2}\right)} \quad (8)$$

The dependence of the output h_{246} according to the input distance b are given in the figure 5 for three values of links length a ($a = 40$, $a = 80$, $a = 120$) and for a twist angle $\alpha = 120^\circ$.

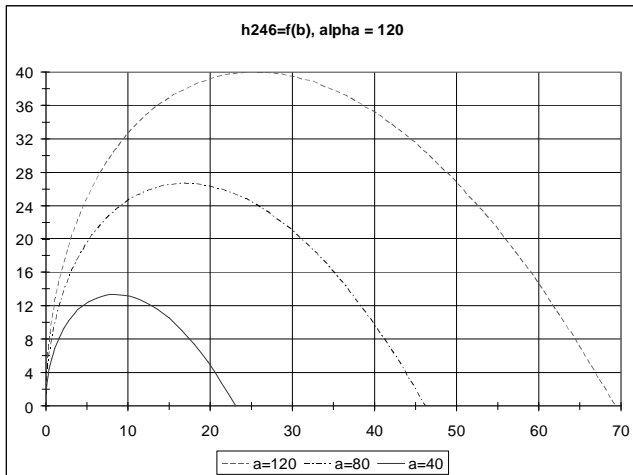


Fig. 5 The variation $h_{246} = f(b)$ for $\alpha = 120^\circ$

Another possible utilization for this type of device is in the machine tools as concentric chuck. The even joints form an equilateral triangle and their displacements follow the radius of their circumscribed circle. The dependence of the radius according to the input b is [13]:

$$R_{246} = \frac{2a^2}{2a\sqrt{3} - 3b} \quad (9)$$

The curves of variation for h_{246} according to the distance b are given fig. 6 for three values of links length ($a=40$, $a=80$, $a=120$).

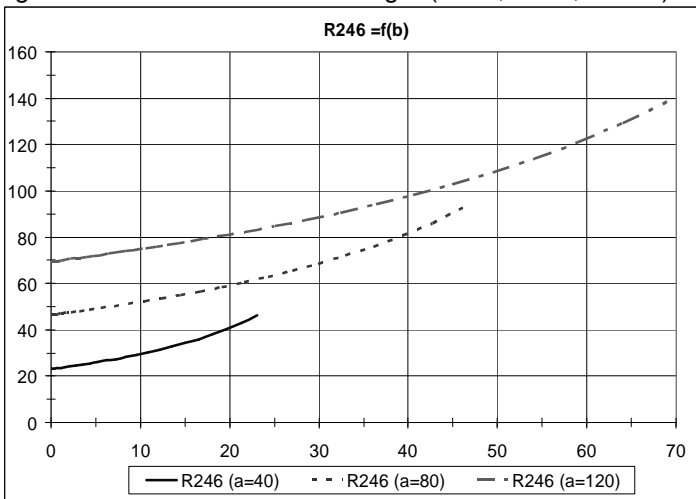


Fig. 6 Variation of the radius R_{246} according to b

Of course others possible applications can be found and many input or output parameters can be used for this device, according to the domain where will be used.

4. PROTOTYPES

Two prototypes was realized at the Applied Mechanical Laboratory in Besançon (France), both for a twist angle $\alpha = \pi/2$.

The second prototype is more accurate and confirms experimentally the numerical results presented in chapter 3.



Fig. 7 Two prototypes of the device

The displacements of the actuated joints in the reference plane are obtained by a screw-ball transmission. To make more accurate this type of device it must increase the twist angle to 120° or 150° .

5. CONCLUSIONS

In this paper we present some interesting properties of Wohlhart symmetric mechanism. The first one is that three non successive joints will define a parallel plane with the reference plane formed by the others three joints. The second property is the orthogonality between the line determined by the intersection point of odd and even joints axes (call vertical line) and the two parallels planes described bellow. The third important property is the disposition of the driven (non-actuated) joints, in the corners of an equilateral triangle.

These properties permit to put this mechanism in a new spatial disposition. If in its classical position the mechanism have one fixed element, in this new spatial disposition the mechanism have no fixed elements, but three non successive joints are imposed to remain in a fixed plane. We obtain finally a new device which can be used in many industrial applications, like in optical devices as focusing plane, as

universal chuck in machine tools industry, or as translational device in many industrial areas.

The biggest advantage of this translator is to present an important surface in translation, a plane surface defined with a good precision by three points.

Two prototypes was built until now, the second having a better accuracy. A third prototype of the translator, with a twist angle $\alpha=150^\circ$ or $\alpha=150^\circ$, will assure a better precision.

REFERENCES

1. Baker JE, An Analysis of the Bricard Linkages, Mechanism and Machine Theory, vol. 15, pp. 267–286, 1980;
2. Baker JE, Displacement-closure equations of the unspecialized double-Hooke's-joint linkage, Mechanism and Machine Theory, vol. 37, p. 1127-1144, 2002;
3. Bennett GT, A new Mechanism, Engineering 76, p. 777–778, 1903;
4. Bricard R, Mémoire sur la théorie de l'octaèdre articulé, Journal de Mathématiques pures et appliquées, Liouville 3, 113–148, 1897 ;
5. Bricard R, Leçons de Cinématique, Tome II - Cinématique Appliquée, Gauthier–Villars, Paris, 1927 ;
6. Chen Y, You Z, Tarnai T, Threefold-symmetric Bricard Linkages for Deployable Structures, International Journal of Solids and Structures, vol. 42, p. 2287-2301, 2005;
7. Dietmaier P, A new 6R space mechanism, Proc. 9th World Congress on the Theory of Machines and Mechanisms, vol. 1, pp. 52–56, Milano, Italy, 1995;
8. Denavit J, Hartenberg RS, A Kinematic Notation for Lower–Pair Mechanism Based on Matrices, Journal of Applied Mechanics, vol. 22, pp. 215–221, 1995;
9. Gan WW, Pellegrino S, Closed-loop deployable structures, AIAA 2003-1450, Proc. of 44th AIAA /ASME/ ASCE/ AHS/ ASC Structures, Structural Dynamics, and Materials Conference, Norfolk, 7-10 April 2003;
10. Goldberg M, New five–bar and six–bar linkages in three dimensions, Transaction of the A.S.M.E., vol. 65, p. 649–663, 1943;
11. Mavroidis C, Roth B, Analysis and Synthesis of Overconstrained Mechanisms, Proc. of the 1994 ASME Design Technical Conferences, vol. DE- 70, pp. 115-133, Minneapolis, September 1994;
12. Myard FE, Chaîne fermée à cinq couples rotoïdes, déformable au premier degré de liberté, Comptes Rendus Hebdomadaires des Séances de l'Académie des Sciences, vol. 192, p. 1352-1354, 1931 ;
13. Racila L, Contributions sur les mécanismes surcontraints à six liaisons rotoïdes, Ph.D. dissertation, University of Franche-Comté, Besançon, 2006 ;
14. Racila L, Dahan M, Bricard mechanism used as translator, Proc. Of 12th World Congress IFToMM, vol. 3, pp. 337–341, Besançon, 2007;

15. Racila L, Dahan M., Spatial properties of Wohlhart symmetric mechanism, *Meccanica*, Springer, ISSN 0025-6455, iuly 2009;
16. Sarrus PF, Note sur la transformation des mouvements rectilignes alternatifs, en mouvements circulaires ; et réciproquement, *Comptes Rendus des Séances de l'Académie des Sciences*, Vol. 36, p. 1036-1038, 1853 ;
17. Schatz P, *Rhythmusforschung und Technik*, Verlag freies Geistesleben, Stuttgart, 1975;
18. Waldron KJ, Symmetric Overconstrained Linkages, *Transactions of the ASME, Journal of Engineering for Industry*, V91, p. 158-162, 1969;
19. Waldron KJ, Overconstrained Linkages, *Environment and Planning B*, Vol. 6, pp. 393-402, 1979;
20. Wohlhart K, A New 6R Space Mechanism, *Proc. 7 th World Congress IFToMM*, vol. 1, pp. 193–198, Sevilla, 1987.

THE EFFECTS OF THE MODULATION POWER ON THE ENERGETIC SAVING UTILISING A CONDENSING BOILER

BOZZINI Fausto^{*}, ANOICA Paul Gabriel^{}**

^{}Thermo-Technical Engineering Application- Italy*

*^{**}University of Medicine and Pharmacy Craiova-Romania*

Abstract: In this paper, we present a theoretical study based on the energetic saving analysis obtained by working in partial loads across the modulation effect of the condensing boiler comparative to traditional boiler. The climate dates utilized for this study are obtained from the geophysical station of the country.

Keywords: modulation burn, reduction of energy, thermal optimization, boiler, condensation

1. INTRODUCTION

The study is based on a real case of a house with isolated perimeter wall. The heating system is constituted by floor radiant panels heated by condensing boiler with 24 kW thermal power. The boiler is equipped with an incorporated electronic regulator witch controls a volumetric energy counter for heating and sanitary warm water.

In the house it is installed a electronic unit with external probe, that receives and displays all signals transmitted from the condensing boiler through a bus cable. The unit can be program mated day by day.

The norms impose that a heating installation with nighttime attenuation of the temperature of maximum to 2°C in comparison to the standard value of 20°C (e.g. indoor temperature of 18°C), conducts to a greater energetic saving that in the case of turning off.

In our case, the indoor temperature reduces very slowly during the night because of the high level of the walls isolation (after 10 hours it reduces by appreciatively 0.5°C).

In these conditions the floor gets cool because the boiler doesn't work if the indoor temperature doesn't go down under the 18°C leading to a certain level of discomfort in the first hours of the morning. It has been decided therefore to avoid the nocturnal attenuation, keeping 20°C indoor temperature also during the night.

So, the boiler works: 14 h by day and 10 h by night, following the external temperature. The scheme of this kind of installation is shown in figure 1.

2. THEORETICAL ANALYSIS OF A CONCRETE CASE ⁽¹⁾

The study was conducted in northern Italy, Piemonte region, in the city of Novara.

The heating period was considered between 15th October and 15th April. The power of the heat generators was sized to a standard outside temperature of 268 K (-5°C).

The boiler works when the external temperature goes down under the 10°C. It has been signed the numbers of the days every months, which corresponds to such temperatures.

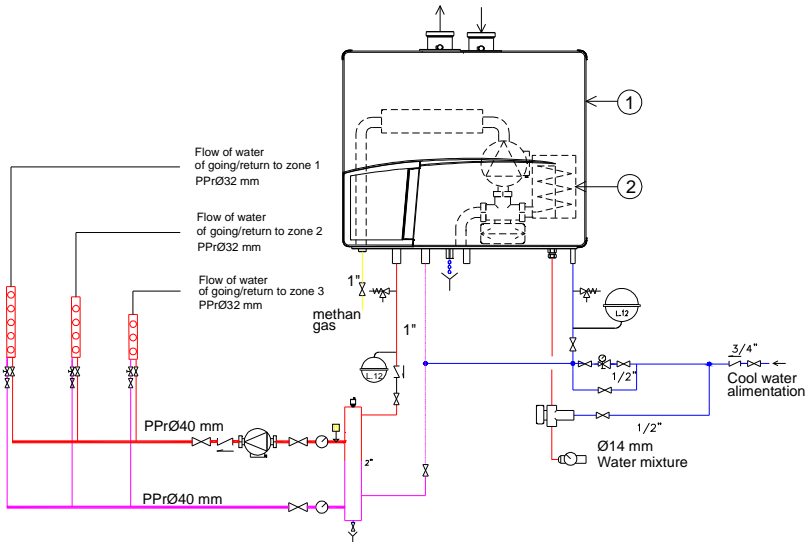


Fig.1 – Scheme of the installation: 1) The condensing boiler with boiler of capacity 14 l, 2) Incorporated boiler

The chart I shows the number of operating hours in the heating period, the thermal power as a function of average outdoor temperature

¹Analysis of combustion of the heating installation with condensing boiler in a house situated in Via Amendola 19, - Casalino (NO) - Novara - Italy

and the load factor, using actual values of the temperatures detected by the geophysical station of the locality [1]. We observe that the power of 24 kW is never reached. The heat generator reaches a maximum thermal power of 16 kW, which corresponds to a 67% load factor during the whole heating period. In the diagram in figure 2 it is showed the variation of the percent operation load of the condensing boiler and its operation hours in function of the heating period.

We observe that the generator has been working in this period at partial loads with a power range from 10 kW to 16 kW. The thermal energy is obtained by multiplying the monthly power of the heat generator P by the working hours number in the respective month (see Chart II).

To this thermal energy for heating we added the energy due to the consumption of sanitary warm water whose power usage is always 24 kW.

Chart I. Thermal load, Load factor, Operation hours, Percent operation hours in function of the external temperature in every months

Progressive number	Months	T _{me, winter}	Operation hours	Percent operation hours	Load factor FL	Thermal power load P
		°C	h	%		kW
1	October	9,55	24	0,85	0,42	10,03
2	November	5,41	360	12,82	0,58	14,01
3	December	3,24	744	26,50	0,67	16,09
4	January	4,65	720	25,64	0,61	14,74
5	February	6,18	624	22,22	0,55	13,27
6	March	7,98	288	10,26	0,48	11,54
7	April	8,73	48	1,71	0,45	10,82
			2808			

Based on the incorporated energy counter, the number of the hours for the use a sanitary warm water during a whole years is 271 h: 206 h in winter and 65 h in summer period.

The consumption for the use of sanitary warm water is approximately considered constant for each month.

The fuel consumption is obtained by the following formula (see chart II):

$$V_c = \frac{Q_{tot_winter}}{\eta \cdot Hi} \quad [m^3/year] \quad (1)$$

where:

$$Q_{tot} = Q_{tot_winter} + Q_{tot_summer},$$

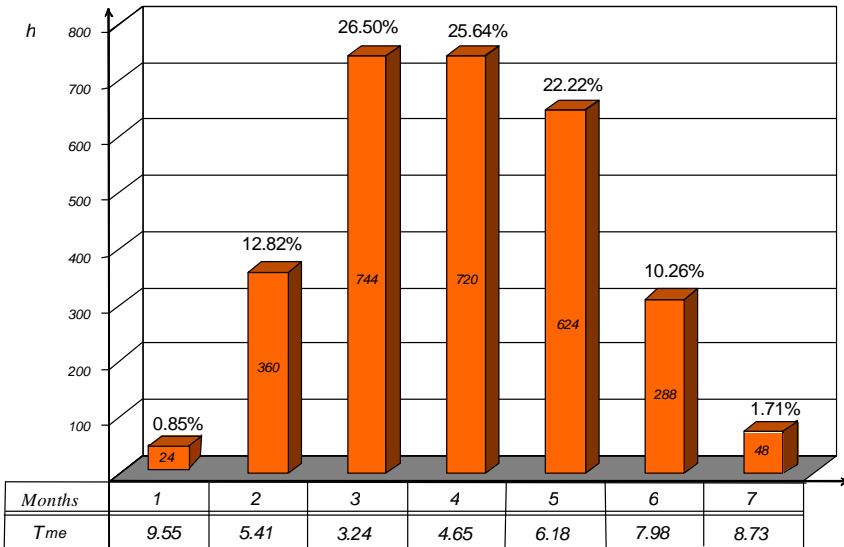


Fig.2 - Monthly variation of the thermal load in function of external temperature

η_s represents the seasonal average performance, and not only the one burning generator. In fact it can be written using the following expression:

$$\eta_s = \eta_c \eta_e \eta_r \eta_d \quad (2)$$

The four performances are respectively the combustion, emission, regulation and distribution performances [2][3].

The emission performance depends on the type of the heating indoor installation (Radiant Floor). The regulation performance depends on the type of electronic controller installation and on its management (electronic regulator with outside probe and delivery probe). The distribution performance is a function of isolation pipes degree of the installation.

According to the latest European standards (UNI/TS 11300-1 and 2) the values of the performances in this studied case are:

$$\eta_c = 1,06; \eta_e = 0,98; \eta_r = 0,97; \eta_d = 0,97; \quad (3)$$

Figure 3 shows the variation of the combustion performance as a function of the load factor for different types of boilers.

Chart II. Thermal energy and consumption of methane in winter and summer periods

Progressiv number	Months	hours	T_{me_winter}	Q_{heat_winter}	Q_{hw_winter}	Q_{tot_winter}	η_{ib_s}	η_{cb_s}	V_{tb}	V_{cb}
		HW_winter	°C	kWh	kWh	kWh			m ³	m ³
		h								
1	october		9,55	241	4944,0	5184,8	0,775	0,977	694,5	550,3
2	november		5,41	5043	4944,0	9987,5	0,775	0,977	1337,8	1060,1
3	december		3,24	11968	4944,0	16912,3	0,761	0,968	2306,5	1812,2
4	gennarie		4,65	10613	4944,0	15557,4	0,761	0,968	2121,7	1667,1
5	februarie		6,18	8279	4944,0	13223,4	0,775	0,977	1771,2	1403,6
6	march		7,98	3324	4944,0	8267,5	0,775	0,977	1107,4	877,6
7	april		8,73	520	4944,0	5463,6	0,775	0,977	731,8	579,9
		206		39988	34608	74596,4	0,771	0,97	10070,8	7950,8
Progressiv number	Months	hours			Q_{hw_summer}	Q_{tot_summer}	η_{ib_s}	η_{cb_s}	V_{tb}	V_{cb}
		HW_summer			kWh	kWh			m ³	m ³
		h								
1	six months	65			1560,0	1560,0	0,771	0,97	210,0	166,0
		271							10280,9	8116,9

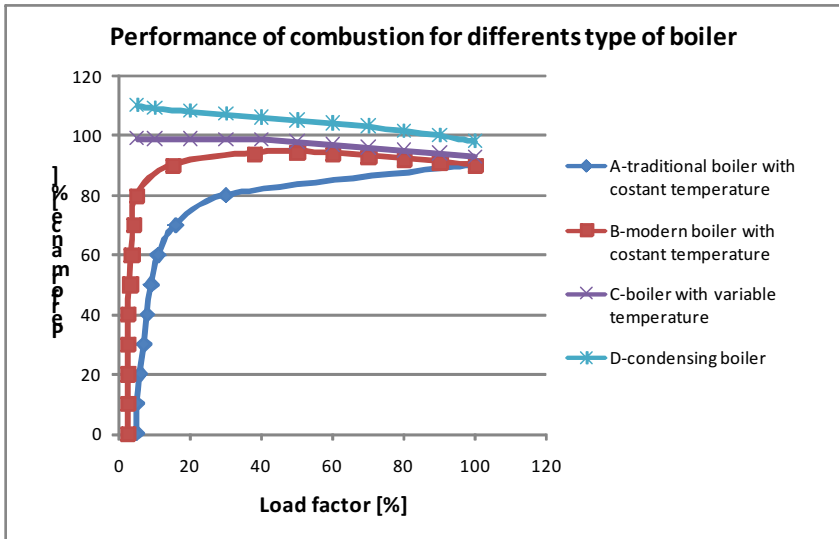


Fig.3 - Performance percentage in function of the load factor percentage

The diagram of Figure 4 shows the variation of the load factor of thermal power and the outside temperature in function of the heating period. The boiler operates at a maximum power corresponding to the outside lowest temperature. The maximum load factor is 0.67. This means that during the heating period the maximum power reached by the condensing boiler for heating was only 67% of the nominal power which is 24 kW.

This result highlights the fact that a good modulation of the burner leads to a good exploitation of the heat without useless waste of fuel. The results of the monthly consumption obtained, are presented in the diagram of Figure 5. The difference between the two years consumption is obtained in the following way:

$$\Delta V = V_{tb} - V_{cb} = 2164 \text{ m}^3 \cdot \text{year}^{-1} \quad (4)$$

The fuel is distributed to the technical conditions of temperature and pressure (288 K (15°C) and 1013 mbar). This value is transformed using the following formula [5]:

$$\Delta V' = \Delta V \cdot \left(\frac{(273 + 15) \cdot 1013}{273 \cdot (1013 + 15)} \right) = 2278 \text{ m}^3 \cdot \text{year}^{-1} \quad (5)$$

the percentage of fuel saving is:

$$\Delta V' = \frac{\Delta V'}{V_{tb(\text{year})}} \cdot 100 = 21,15\% \quad (6)$$

Multiplying this result by the current price of natural gas, we obtain the following fuel economy:

$$\Delta C = \Delta V' \cdot c = 2278 * 0,72 = 1640,00 \text{ €} \quad (7)$$

where:

c – represents the specific actual cost of methane (0,72 €kWh⁻¹).

The variation of fuel saved in the heating period was compared with those obtained using a traditional boiler whose seasonal performance is shown in the *chart II*.

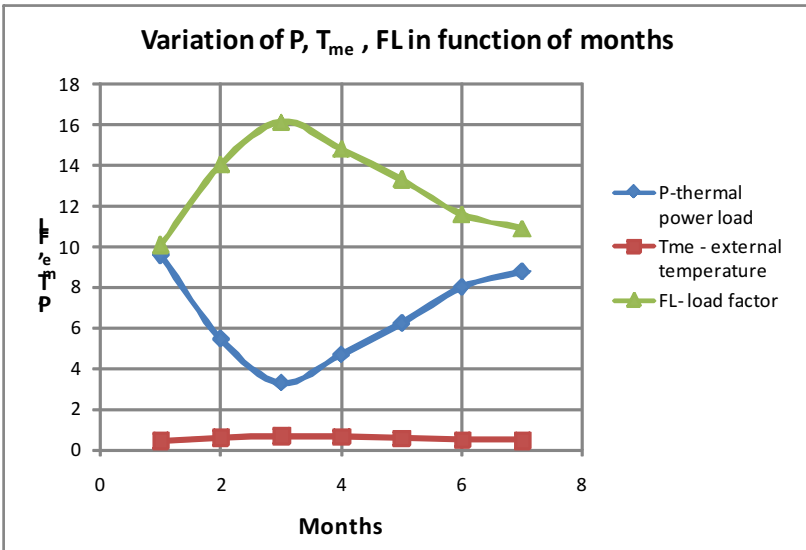


Fig.4 - Variation of thermal load, external temperature and load factor in function of the winter period

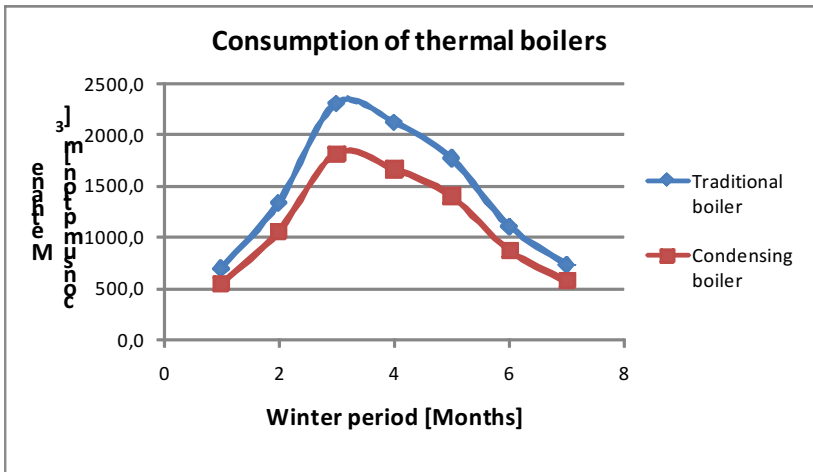


Fig.5 - Variation of consumptions in function of winter period

3. CONCLUSIONS

We observe that at partial loads the condensing boiler follows faithfully the thermal load by turning on and off less than a conventional heat generator. Thus, we obtained high performances, due also to the reducing of the heat losses of the boiler stack and envelopment.

In our case we compared two type of installation, with condensing boiler and traditional one and we obtained a 21.15% fuel energy saving in the case with condensing boiler installation.

Generally the installations are obsolete, with low heat performance traditional boiler unable to reach the maximum regime and therefore the maximum performance.

We can affirm that the substitution of the traditional boiler with a condensing one, can lead to more than 40% energy saving with consequently economical gain return [4]:

The condensing boilers can be used in any application, but if there are used in industrial settings could lead to energy savings even more important.

4. NOMENCLATURES

- T_{me_winter} – external air temperature [°C]
- FL – load factor
- P_n – thermal nominal power of condensing boiler [kW]
- P – thermal power load monthly [kW]
- H_i - net heat value of fuel [MJ·m⁻³]
- Q_{heat_winter} – heat energy monthly [kWh]

Q_{hw_winter}	– warm water energy monthly	[kWh]
Q_{tot_winter}	– total energy monthly	[kWh]
η_s	- season efficiency of the boilers	
η_{tb_s}	- season efficiency of the traditional boiler	
η_{cb_s}	- season efficiency of the condensing boiler	
λ	- indice di eccesso d'aria per la combustione	
V_{tb}	– consumption of methan with traditional boiler cucina ..	[m ³]
V_{cb}	– consumption of methan with condensing boiler	[m ³]
ΔV	– consumption difference fuel	[m ³ year]
$\Delta V'$	– consumption difference distribution fuel	[m ³ year]
ΔC	– cost difference	[€]
c	– specific cost of fuel	[€kWh ⁻¹]

REFERENCES

1. "Meteorological Bulletin" for years 2008 and 2009 – Geophysical Observatory of Novara.
2. UNI/TS 11300–1: Energy performance of buildings - Part 1: Evaluation of energy need for space heating and cooling, 2008
3. UNI/TS 11300–2: Energy performance of buildings - Part 2: Evaluation of primary energy need and of system efficiencies for space heating and domestic hot water production, 2008.
4. F. Bozzini., M. Marinescu "Energetic redevelopment of the buildings: Thermal and economic comparative analysis bifore and after the substitution through condensing boiler", International Conference of thermotecnics CNT'17 with international participation, Edition XVIIa, 21-22 may 2009, section: Masini si Instalatii Termice, Brasov, Romania, Vol.2(51) Series I ISSN 2065-2119 Special IssueNo.1, Vol.2, 2009 ISBN 978-973-598-524-0.
5. F. Palmizi, "Vademecum del Termotecnico", Editoriale PEG, 1990.

ELASTIC, PLASTIC AND RESIDUAL STRESS ANALYSIS IN SYMMETRIC THERMOPLASTIC LAMINATED PLATES UNDER VARIOUS TEMPERATURE CHANGE THROUGH THE THICKNESS: ANALYTICAL SOLUTION

KARA Emre^{*}, AYKUL Halil^{*}, SAYMAN Onur^{**}, ÖZYILMAZ Emre^{*}
^{*}Hitit University - Turkey
^{**}Dokuz Eylül University - Turkey

Abstract: In this study, thermal elastic, plastic and residual stress analysis are carried out on simply supported symmetric cross-ply $[0^\circ/90^\circ]_2$ and angle-ply $[15^\circ-15^\circ]_2$, $[30^\circ-30^\circ]_2$, $[45^\circ-45^\circ]_2$, $[60^\circ-60^\circ]_2$ thermoplastic laminated plates under various temperature change through the thickness of plates. In the solution, mechanical properties and yield strengths of the composite layer have been inserted in the program which has been designed within FORTRAN software. Elastic, plastic and residual stresses which are determined in the symmetric cross-ply and angle-ply laminated plates for small deformations are prepared as a table. Residual stresses on the X and Y axes have been plotted for each of the orientation angles which are mentioned above. The composite materials are assumed to be strain hardening. The Tsai-Hill Theory is used as a yield criterion. The intensity of stress components in the symmetric cross-ply laminated plate is higher than in angle-ply laminated plate due to the differences among the stiffness of layers. Plastic yielding occurs in all the laminated plate at the same temperature.

Keywords: composite materials, thermoplastic composite, laminated plates, residual stress analysis, the Tsai-Hill theory, elastic-plastic analysis

1. INTRODUCTION

The field of fiber-reinforced thermoplastic composite materials is now rapidly growing both in terms of industrial applications and fundamental research.

Jeromidis and Parkyn [1] investigated the residual stress in carbon fiber-thermoplastic matrix laminates. Jiang et al. [2] developed an analytical model to study influence of thermal residual stresses on the elastic and yield behaviors of aligned short fiber-reinforced metal-matrix composites. Ifju et al. [3] developed a novel method or a nondestructive method called the Cure Referencing Method (CRM) to measure the residual stresses in laminated composites. Ersoy and Vardar [4] applied two experimental techniques as layer removal and compliance method for the measurement of through-the-thickness residual stresses in layered composite plates. Trende et al. [5] investigated residual stresses and dimensional changes in the compression molded glass-mat-reinforced thermoplastic (GMT) parts. Fenn et al. [6] measured triaxial residual strains in a thermosetting resin of the type used in high performance fiber composite materials. Atas and Sayman [7] used a finite element method for elastic-plastic stress analysis and expansion of plastic zone in clamped and simply supported aluminum metal-matrix laminated plates, using first-order shear deformation theory for small deformations. Sayman et al. [8] carried out an elastic-plastic stress analysis for a thermoplastic composite cantilever beam loaded by a bending moment at the free end. Karakuzu et al. [9-11] carried out elastic-plastic stress analysis in aluminum metal-matrix laminates under external forces. Oosthuizen and Stone [12] investigated residual stresses in CSM/vinyl ester resin laminates due to postcure shrinkage. Barnes [13] investigated the thermal expansion behaviors of a variety of thermoplastic composites based on the ICI Victrex polymers, Polyarylether etherketone (PEEK), Intermediate Temperature Semicrystalline Polymer "Victrex", ITX (an aromatic copolymer), Victrex Intermediate Temperature Amorphous Polymer ITA (a polyether sulfone) and Victrex High Temperature Amorphous Polymer HTA (a bisphenyl-modified polyester sulfone).

In this study, the plane stress assumption has been made for modeling the problem.

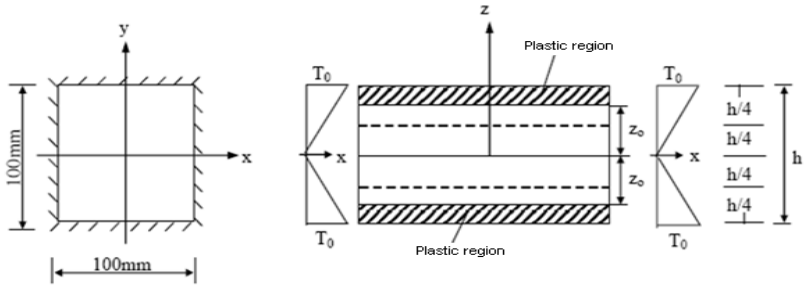


Fig. 1 – Symmetric thermoplastic laminated plate under nonlinear thermal load T

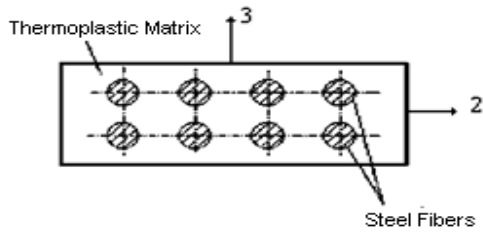


Fig. 2 – Structure of a composite layer

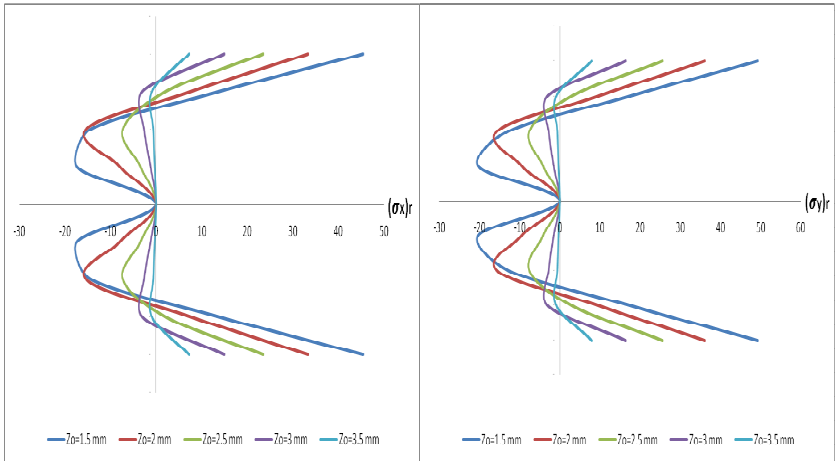


Fig. 3 – The distribution of the residual stress component σ_x, σ_y at the $[0/90]_2$ orientation angle

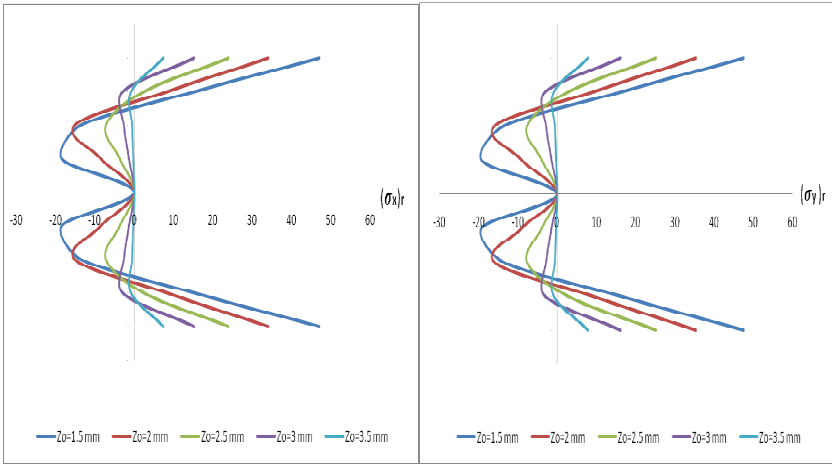


Fig. 4 – The distribution of the residual stress component σ_x , σ_y at the $[15^\circ-15^\circ]$ orientation angle

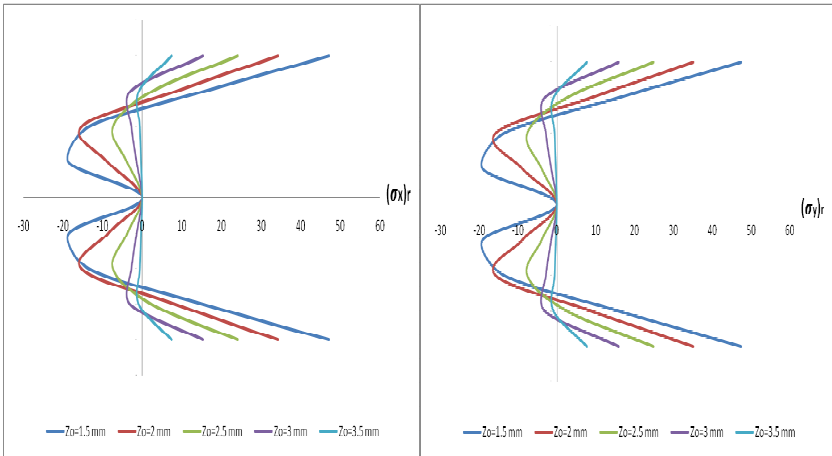


Fig. 5 – The distribution of the residual stress component σ_x , σ_y at the $[30^\circ-30^\circ]$ orientation angle

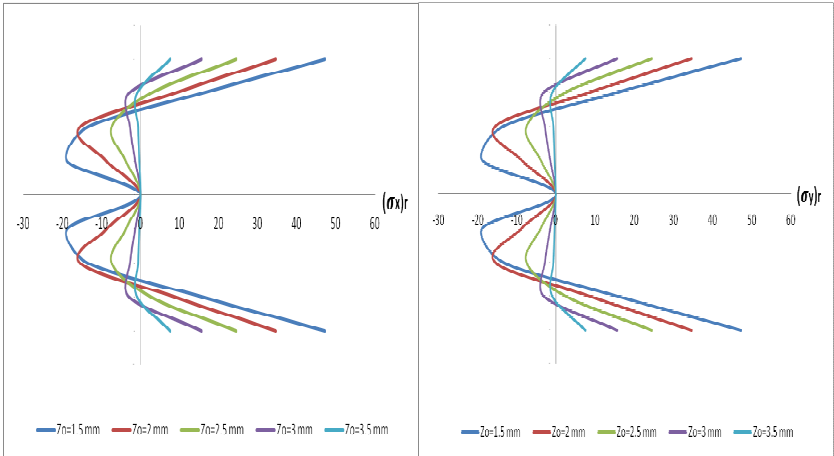


Fig. 6 – The distribution of the residual stress component σ_x , σ_y at the $[45^\circ-45^\circ]_2$ orientation angle

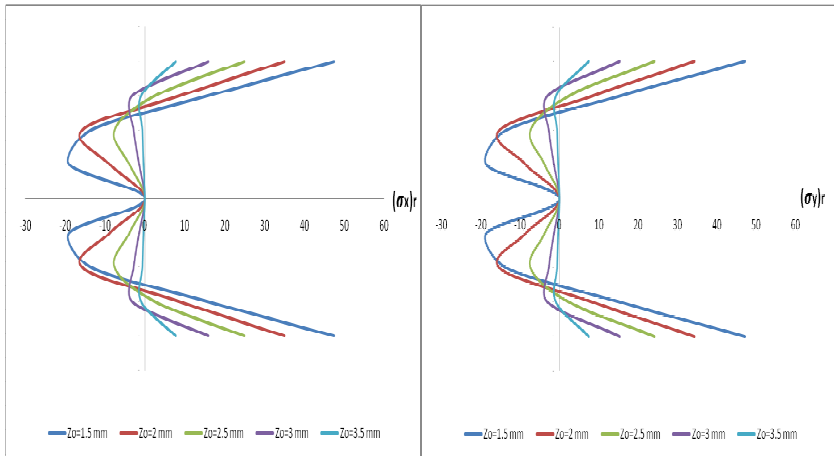


Fig. 7 – The distribution of the residual stress component σ_x , σ_y at the $[60^\circ-60^\circ]_2$ orientation angle

2. PRODUCTION, ANALYSIS AND SOLUTIONS

2.1 PRODUCTION OF THERMOPLASTIC LAMINATED PLATES

The thermoplastic laminated plates consist of high-density polyethylene as a thermoplastic matrix and steel fibers, as shown in Fig. 2. Polyethylene is placed into the molds and they are heated up to 190°C by using an electrical heater. Subsequently, the material is held for 5min under 2.5 MPa at this temperature. The temperature is decreased to 30° C under 15 MPa pressure in 3 min, and a polyethylene layer is manufactured. The steel fibers are placed at equal distance between three thermoplastic layers and processed in the same way described above. The mechanical properties and the yield strengths of the plate are measured by using strain gauges and a Shimadzu Autograph tensile machine, as given in Tab. 1.

2.2 THERMAL STRESS ANALYSIS

A symmetric thermoplastic laminated plate under various thermal distributions is shown in Figs. 1 and 2. Its dimensions are chosen as 100 mm x 100 mm in order to prevent buckling of the plate.

The temperature, at any point can be written as;

$$T = \left| \frac{2T_0 z}{h} \right| \quad (1)$$

According to the Classical Lamination Theory, the thermal forces and moments can be written as [14],

$$\begin{bmatrix} N_x^T \\ N_y^T \\ N_{xy}^T \end{bmatrix} = [A] \cdot \begin{Bmatrix} \epsilon_x^0 \\ \epsilon_y^0 \\ \gamma_{xy}^0 \end{Bmatrix} + [B] \cdot \begin{Bmatrix} k_x \\ k_y \\ k_{xy} \end{Bmatrix} - [T^*] \cdot T ;$$

$$\begin{bmatrix} M_x^T \\ M_y^T \\ M_{xy}^T \end{bmatrix} = [B] \cdot \begin{Bmatrix} \epsilon_x^0 \\ \epsilon_y^0 \\ \gamma_{xy}^0 \end{Bmatrix} + [D] \cdot \begin{Bmatrix} k_x \\ k_y \\ k_{xy} \end{Bmatrix} - [T^{**}] \cdot T \quad (2)$$

where [A], [B], and [D] are extensional stiffnesses, coupling stiffnesses, and bending or flexural stiffnesses of the laminate respectively, and

$$[T^*] = \int \begin{bmatrix} \varphi_{11} & \varphi_{12} & \varphi_{16} \\ \varphi_{12} & \varphi_{22} & \varphi_{26} \\ \varphi_{16} & \varphi_{26} & \varphi_{66} \end{bmatrix}_k \begin{Bmatrix} \alpha_x \\ \alpha_y \\ \alpha_{xy} \end{Bmatrix}_k z \cdot dz ; \quad (3)$$

$$[T^{**}] = \frac{1}{2} \int \begin{bmatrix} \varphi_{11} & \varphi_{12} & \varphi_{16} \\ \varphi_{12} & \varphi_{22} & \varphi_{26} \\ \varphi_{16} & \varphi_{26} & \varphi_{66} \end{bmatrix}_k \begin{Bmatrix} \alpha_x \\ \alpha_y \\ \alpha_{xy} \end{Bmatrix}_k z^2 \cdot dz$$

$$\begin{aligned} \alpha_x &= \alpha_1 c^2 + \alpha_2 s^2 \\ \alpha_y &= \alpha_1 s^2 + \alpha_2 c^2 \\ \alpha_{xy} &= 2cs(\alpha_1 - \alpha_2) \end{aligned} \quad (4)$$

where $c = \cos \theta$ and $s = \sin \theta$, α_1 and α_2 are the thermal expansion coefficients in the principal material directions.

For a balanced symmetric laminate, elements in $[T^{**}]$ matrix and also k_x , k_y and k_{xy} are zero. Equation (2) can be written in this form as,

$$\begin{bmatrix} A_{11} & A_{12} & A_{16} \\ A_{12} & A_{22} & A_{26} \\ A_{16} & A_{26} & A_{66} \end{bmatrix} \begin{Bmatrix} \varepsilon_x^0 \\ \varepsilon_y^0 \\ \varepsilon_{xy}^0 \end{Bmatrix} - \begin{Bmatrix} T_1^* \\ T_2^* \\ T_3^* \end{Bmatrix} T = \begin{Bmatrix} 0 \\ 0 \\ 0 \end{Bmatrix} \quad (5)$$

The stress components in each layer are obtained by using the stress-strain relation as follows,

$$\begin{Bmatrix} \sigma_x \\ \sigma_y \\ \sigma_{xy} \end{Bmatrix} = \begin{bmatrix} \varphi_{11} & \varphi_{12} & \varphi_{16} \\ \varphi_{12} & \varphi_{22} & \varphi_{26} \\ \varphi_{16} & \varphi_{26} & \varphi_{66} \end{bmatrix}_k \left\{ \begin{Bmatrix} \varepsilon_x^0 \\ \varepsilon_y^0 \\ \varepsilon_{xy}^0 \end{Bmatrix} - \begin{Bmatrix} \alpha_x \\ \alpha_y \\ \alpha_{xy} \end{Bmatrix} \cdot T \right\} \quad (6)$$

and the stress component in the principal material direction are written as,

$$\begin{Bmatrix} \sigma_1 \\ \sigma_2 \\ \tau_{12} \end{Bmatrix} = \begin{bmatrix} c^2 & s^2 & 2sc \\ s^2 & c^2 & -2sc \\ -sc & sc & c^2 - s^2 \end{bmatrix} \cdot \begin{Bmatrix} \sigma_x \\ \sigma_y \\ \tau_{xy} \end{Bmatrix} \quad (7)$$

For the yield temperature of a lamina;

$$\begin{Bmatrix} \varepsilon_x \\ \varepsilon_y \\ \gamma_{xy} \end{Bmatrix} = \begin{bmatrix} \bar{a}_{11} & \bar{a}_{12} & \bar{a}_{16} \\ \bar{a}_{12} & \bar{a}_{22} & \bar{a}_{26} \\ \bar{a}_{16} & \bar{a}_{26} & \bar{a}_{66} \end{bmatrix} \begin{Bmatrix} \sigma_x \\ \sigma_y \\ \tau_{xy} \end{Bmatrix} + \begin{Bmatrix} \alpha_x T \\ \alpha_y T \\ \alpha_{xy} T \end{Bmatrix} \quad (8)$$

where;

$$\bar{a}_{11} = S_{11} \cos^4 \theta + (2S_{12} + S_{66}) \sin^2 \theta \cos^2 \theta + S_{22} \sin^4 \theta$$

$$\bar{a}_{12} = S_{12} (\sin^4 \theta + \cos^4 \theta) + (S_{11} + S_{22} - S_{66}) \sin^2 \theta \cos^2 \theta$$

$$\bar{a}_{22} = S_{11} \sin^4 \theta + (2S_{12} + S_{66}) \sin^2 \theta \cos^2 \theta + S_{22} \cos^4 \theta$$

$$\bar{a}_{16} = (2S_{11} - 2S_{12} - S_{66}) \sin \theta \cos^3 \theta - (2S_{22} - 2S_{12} - S_{66}) \sin^3 \theta \cos \theta$$

$$\bar{a}_{26} = (2S_{11} - 2S_{12} - S_{66}) \sin^3 \theta \cos \theta - (2S_{22} - 2S_{12} - S_{66}) \sin \theta \cos^3 \theta$$

$$\bar{a}_{66} = 2(2S_{11} + 2S_{22} - 4S_{12} - S_{66}) \sin^2 \theta \cos^2 \theta + S_{66} (\sin^4 \theta + \cos^4 \theta)$$

where;

$$S_{11} = \frac{1}{E_1}, \quad S_{22} = \frac{1}{E_2}, \quad S_{12} = -\frac{\nu_{12}}{E_1}, \quad S_{66} = \frac{1}{G_{12}}$$

At the boundary conditions, $\varepsilon_x=0$, $\varepsilon_y=0$, $\gamma_{xy}=0$

$$\begin{Bmatrix} \varepsilon_x \\ \varepsilon_y \\ \gamma_{xy} \end{Bmatrix} = \begin{bmatrix} \bar{a}_{11} & \bar{a}_{12} & \bar{a}_{16} \\ \bar{a}_{12} & \bar{a}_{22} & \bar{a}_{26} \\ \bar{a}_{16} & \bar{a}_{26} & \bar{a}_{66} \end{bmatrix} \begin{Bmatrix} \sigma_x \\ \sigma_y \\ \tau_{xy} \end{Bmatrix} + \begin{Bmatrix} \alpha_x T \\ \alpha_y T \\ \alpha_{xy} T \end{Bmatrix} = \begin{Bmatrix} 0 \\ 0 \\ 0 \end{Bmatrix} \quad (9)$$

$$\begin{bmatrix} \bar{a}_{11} & \bar{a}_{12} & \bar{a}_{16} \\ \bar{a}_{12} & \bar{a}_{22} & \bar{a}_{26} \\ \bar{a}_{16} & \bar{a}_{26} & \bar{a}_{66} \end{bmatrix} \begin{Bmatrix} \sigma_x \\ \sigma_y \\ \tau_{xy} \end{Bmatrix} = - \begin{Bmatrix} \alpha_x T \\ \alpha_y T \\ \alpha_{xy} T \end{Bmatrix} \quad (10)$$

$$\tau_{xy} = - \frac{\alpha_{xy} T + \bar{a}_{16} \sigma_x + \bar{a}_{26} \sigma_y}{\bar{a}_{66}}$$

$$\sigma_x \underbrace{(\bar{a}_{11} \bar{a}_{16} - \bar{a}_{16}^2)}_{R_1} + \sigma_y \underbrace{(\bar{a}_{12} \bar{a}_{66} - \bar{a}_{26} \bar{a}_{16})}_{R_2} = \quad (11)$$

$$\underbrace{(\alpha_{xy} \bar{a}_{16} - \alpha_x \bar{a}_{66})}_{U_1} \cdot T \Rightarrow \sigma_y = \frac{U_1 T - \sigma_x R_1}{R_2}$$

$$\sigma_x \underbrace{(\bar{a}_{12} \bar{a}_{66} - \bar{a}_{16} \bar{a}_{26})}_{R_2} + \sigma_y \underbrace{(\bar{a}_{22} \bar{a}_{66} - \bar{a}_{26}^2)}_{R_3} = \quad (12)$$

$$\underbrace{(\alpha_{xy} \bar{a}_{26} - \alpha_x \bar{a}_{66})}_{U_2} \cdot T \Rightarrow \sigma_x R_2 + \sigma_y R_3 = U_2 \cdot T$$

$$\sigma_x = \frac{(R_2 U_2 - R_3 U_1)}{R_2^2 - R_1 R_3} T, \quad \sigma_x = f_1 \cdot T \quad (13)$$

$$\sigma_y = \frac{(R_2 U_1 - R_1 U_2)}{R_2^2 - R_1 R_3} T, \quad \sigma_y = f_2 \cdot T \quad (14)$$

$$\tau_{xy} = - \frac{\alpha_{xy} + \bar{a}_{16} f_1 + \bar{a}_{26} f_2}{\bar{a}_{66}} T, \quad \tau_{xy} = f_3 \cdot T \quad (15)$$

These stress components are transformed to the principal material directions as follows,

$$\begin{Bmatrix} \sigma_1 \\ \sigma_2 \\ \tau_{12} \end{Bmatrix} = \begin{bmatrix} c^2 & s^2 & 2sc \\ s^2 & c^2 & -2sc \\ -sc & sc & c^2 - s^2 \end{bmatrix} \cdot \begin{Bmatrix} \sigma_x \\ \sigma_y \\ \tau_{xy} \end{Bmatrix} \quad (16)$$

$$\sigma_1 = \underbrace{(c^2 f_1 + s^2 f_2 + 2scf_3)}_{F_1} T \Rightarrow \sigma_1 = F_1 T \quad (17)$$

$$\sigma_2 = \underbrace{(s^2 f_1 + c^2 f_2 - 2scf_3)}_{F_2} T \Rightarrow \sigma_2 = F_2 T \quad (18)$$

$$\tau_{12} = \underbrace{(-csf_1 + csf_2 + (c^2 - s^2)f_3)}_{F_3} T \Rightarrow \tau_{12} = F_3 T \quad (19)$$

from the Tsai–Hill yielding criteria;

$$\sigma^{-2} = \sigma_1^2 - \sigma_1 \sigma_2 + \sigma_2^2 \frac{X^2}{Y^2} + \tau_{12}^2 \frac{X^2}{S^2} \quad (20)$$

at the yielding point;

$$\begin{aligned} \bar{\sigma} = X &\Rightarrow X^2 = \sigma_1^2 - \sigma_1 \sigma_2 + \sigma_2^2 \frac{X^2}{Y^2} + \tau_{12}^2 \frac{X^2}{S^2} \\ X^2 &= F_1^2 T^2 - F_1 F_2 T^2 + F_2^2 \frac{X^2}{Y^2} T^2 + F_3^2 \frac{X^2}{S^2} T^2 \end{aligned} \quad (21)$$

$$X^2 = \left(F_1^2 - F_1 F_2 + F_2^2 \frac{X^2}{Y^2} + F_3^2 \frac{X^2}{S^2} \right) \cdot T^2$$

yield temperature can be written as,

$$T = \frac{X}{\sqrt{F_1^2 - F_1 F_2 + F_2^2 \left(\frac{X^2}{Y^2} \right) + F_3^2 \left(\frac{X^2}{S^2} \right)}} \quad (22)$$

2.3 PLASTIC SOLUTION

The solution is carried out for small plastic deformations. The yield condition for Tsai–Hill criterion can be written as;

$$\frac{\sigma_1^2}{X^2} - \frac{\sigma_1 \sigma_2}{X^2} + \frac{\sigma_2^2}{Y^2} + \frac{\tau_{12}^2}{S^2} = 1 \quad (23)$$

Multiplying it by X, gives the equivalent stress in the first principal material direction,

$$\bar{\sigma} = \sqrt{\sigma_1^2 - \sigma_1\sigma_2 + \sigma_2^2 \frac{X^2}{Y^2} + \tau_{12}^2 \frac{X^2}{S^2}} \quad (24)$$

where equivalent stress $\bar{\sigma}$ is given by the Ludwik equation as,

$$\bar{\sigma} = \sigma_y = \sigma_0 + K\varepsilon_p^n \quad (25)$$

The plastic strain increments are obtained by using the potential function,

$$f = \bar{\sigma} - \sigma(\varepsilon_p)$$

The total strain increments in the principal material directions are written as,

$$\begin{Bmatrix} d\varepsilon_1^e \\ d\varepsilon_2^e \\ d\varepsilon_{12}^e \end{Bmatrix} = \begin{bmatrix} a_{11} & a_{12} & 0 \\ a_{12} & a_{12} & 0 \\ 0 & 0 & \frac{a_{66}}{2} \end{bmatrix} \begin{Bmatrix} d\sigma_1 \\ d\sigma_2 \\ d\tau_{12} \end{Bmatrix} + \begin{Bmatrix} \alpha_1 dT \\ \alpha_2 dT \\ \alpha_{12} dT \end{Bmatrix} \quad (26)$$

$$\begin{Bmatrix} d\varepsilon_1^p \\ d\varepsilon_2^p \\ d\varepsilon_{12}^p \end{Bmatrix} = \begin{Bmatrix} \frac{\partial f}{\partial \sigma_1} d\lambda \\ \frac{\partial f}{\partial \sigma_2} d\lambda \\ \frac{\partial f}{\partial \tau_{12}} d\lambda \end{Bmatrix} \quad (27)$$

$$d\varepsilon_1 = d\varepsilon_1^e + d\varepsilon_1^p$$

$$d\varepsilon_2 = d\varepsilon_2^e + d\varepsilon_2^p \quad (28)$$

$$d\varepsilon_{12} = d\varepsilon_{12}^e + d\varepsilon_{12}^p$$

Thus;

$$d\varepsilon_1 = a_{11}d\sigma_1 + a_{12}d\sigma_2 + \frac{2\sigma_1 - \sigma_2}{2\sigma_y} d\varepsilon_p + \alpha_1 dT$$

$$d\epsilon_2 = a_{12}d\sigma_1 + a_{22}d\sigma_2 + \frac{-\sigma_1 + \left(2\sigma_2 \frac{X^2}{Y^2}\right)}{2\sigma_y} d\epsilon_p + \alpha_2 dT \quad (29)$$

$$d\epsilon_{12} = \frac{a_{66}}{2} d\tau_{12} + \frac{2\tau_{12} \left(\frac{X^2}{S^2}\right)}{2\sigma_y} d\epsilon_p$$

They can be transformed to x-y axes by using transformation formula as,

$$\begin{Bmatrix} d\epsilon_x \\ d\epsilon_y \\ d\epsilon_{xy} \end{Bmatrix} = \begin{bmatrix} c^2 & s^2 & -2sc \\ s^2 & c^2 & 2sc \\ sc & -sc & c^2 - s^2 \end{bmatrix} \cdot \begin{Bmatrix} d\epsilon_1 \\ d\epsilon_2 \\ d\epsilon_{12} \end{Bmatrix} \quad (30)$$

They can be written in a short and differential form as,

$$\begin{aligned} \Delta\epsilon_x &= a_1\Delta\sigma_1 + b_1\Delta\sigma_2 + c_1\Delta\tau_{12} + d_1\Delta\epsilon_p + e_1T = 0 \\ \Delta\epsilon_y &= a_2\Delta\sigma_1 + b_2\Delta\sigma_2 + c_2\Delta\tau_{12} + d_2\Delta\epsilon_p + e_2T = 0 \\ \Delta\epsilon_{xy} &= a_3\Delta\sigma_1 + b_3\Delta\sigma_2 + c_3\Delta\tau_{12} + d_3\Delta\epsilon_p + e_3T = 0 \end{aligned} \quad (31)$$

The yield criterion can be evaluated in the differential form,

$$\begin{aligned} (2\sigma_1 - \sigma_2)d\sigma_1 + \left(-\sigma_1 + 2\sigma_2 \left(\frac{X^2}{Y^2}\right)\right) d\sigma_2 \\ + \left(2\tau_{12} \left(\frac{X^2}{S^2}\right)\right) d\tau_{12} - 2K\bar{\sigma} d\epsilon_p = 0 \end{aligned} \quad (32)$$

Using its written symbols,

$$a_4\Delta\sigma_1 + b_4\Delta\sigma_2 + c_4\Delta\tau_{12} + d_4\Delta\epsilon_p = 0 \quad (33)$$

Above equations (31) and (33) can be written in the matrix form,

$$\begin{bmatrix} a_1 & b_1 & c_1 & d_1 \\ a_2 & b_2 & c_2 & d_2 \\ a_3 & b_3 & c_3 & d_3 \\ a_4 & b_4 & c_4 & d_4 \end{bmatrix} \begin{Bmatrix} \Delta\sigma_1 \\ \Delta\sigma_2 \\ \Delta\tau_{12} \\ \Delta\epsilon_p \end{Bmatrix} = \begin{Bmatrix} -e_1 \\ -e_2 \\ -e_3 \\ 0 \end{Bmatrix} \cdot T \quad (34)$$

The stress components σ_1 , σ_2 , τ_{12} and equivalent plastic strain ϵ_p can be found per step as,

$$\begin{aligned}
(\sigma_1)_i &= (\sigma_1)_{i-1} + (\Delta\sigma_1)_i \\
(\sigma_2)_i &= (\sigma_2)_{i-1} + (\Delta\sigma_2)_i \\
(\tau_{12})_i &= (\tau_{12})_{i-1} + (\Delta\tau_{12})_i \\
(\varepsilon_p)_i &= (\varepsilon_p)_{i-1} + (\Delta\varepsilon_p)_i
\end{aligned} \tag{35}$$

where Δ represents the tiny step.

2.4 RESIDUAL STRESSES

The resultant elastic stress components are obtained as,

$$\begin{aligned}
N_x &= \sum_{k=1}^n (-\sigma_x)_k (h_k - h_{k-1}); \quad N_y = \sum_{k=1}^n (-\sigma_y)_k (h_k - h_{k-1}); \\
N_{xy} &= \sum_{k=1}^n (-\tau_{xy})_k (h_k - h_{k-1})
\end{aligned} \tag{36}$$

where N_x, N_y, N_{xy} are the loads in the global coordinate system. The stress components during the release of external forces is determined as,

$$\sigma_x^e = \frac{\sigma_x N_x^p}{N_x^e}; \quad \sigma_y^e = \frac{\sigma_y N_y^p}{N_y^e}; \quad \tau_{xy}^e = \frac{\tau_{xy} N_{xy}^p}{N_{xy}^e} \tag{37}$$

The superposition of the elastic and plastic stresses gives the residual stress components as,

$$\sigma_x^r = \sigma_x^p - \sigma_x^e; \quad \sigma_y^r = \sigma_y^p - \sigma_y^e; \quad \tau_{xy}^r = \tau_{xy}^p - \tau_{xy}^e \tag{38}$$

3. RESULTS AND DISCUSSION

In this study, steel fiber-reinforced thermoplastic matrix laminated plates were used and all the results were obtained by using the analytical solution. The mechanical properties and yield strengths of a layer are given in Tab. 1.

Tab. 1 Mechanical properties and yield strengths of the composite layer

E_1 (MPa)	E_2 (MPa)	G_{12} (MPa)	ν_{12}	X (MPa)	Y (MPa)	S (MPa)	K (MPa)	α_1 (1/°C)	α_2 (1/°C)
110000	87000	41000	0.4	130	104	49	1250	18E-6	22E-6

Results for the stress components at the beginning of plastic yielding in the first layer are shown in Tab. 2.

Tab. 2 Stress components at the beginning of the plastic yielding in the first layer

Orientation Angles	T (°C)	$(\sigma_x)_e$ (MPa)	$(\sigma_y)_e$ (MPa)	$(\tau_{xy})_e$ (MPa)
(0/90)	34.79	-109.39	-101.21	0.00
(30/-30)	34.79	-107.34	-103.25	-3.54
(45/-45)	34.79	-105.30	-105.30	-4.09
(60/-60)	34.79	-103.25	-107.34	-3.54
(15/-15)	34.79	-108.84	-101.76	-2.04

For nonlinear temperatures, the elastic-plastic and residual stresses at the upper surface for all the plates are given in Tab. 3.

Tab. 3 Plastic stresses, residual stresses, and elastic stresses at the upper surface for the nonlinear temperatures

Orientation Angles	T (°C)	Z ₀ (mm)	$(\sigma_x)_p$ (MPa)	$(\sigma_y)_p$ (MPa)	$(\tau_{xy})_p$ (MPa)	$(\sigma_x)_r$ (MPa)	$(\sigma_y)_r$ (MPa)	$(\tau_{xy})_r$ (MPa)	$(\sigma_x)_e$ (MPa)	$(\sigma_y)_e$ (MPa)	$(\tau_{xy})_e$ (MPa)
[0/90] ₂	39.77	3.5	-116.63	-106.54	0.00	7.23	7.92	0.00	-123.86	-114.46	0.00
	46.40	3	-125.64	-113.12	0.00	14.97	16.36	0.00	-140.61	-129.48	0.00
	55.68	2.5	-137.18	-121.51	0.00	23.49	25.58	0.00	-160.67	-147.09	0.00
	69.60	2	-152.63	-132.69	0.00	33.35	36.13	0.00	-185.98	-168.82	0.00
	92.80	1.5	-174.67	-148.64	0.00	45.42	49.34	0.00	-220.09	-197.98	0.00
[15/-15] ₂	39.77	3.5	-115.96	-107.21	-2.52	7.30	7.86	-0.14	-123.26	-115.07	-2.38
	46.40	3	-124.80	-113.96	-3.13	15.14	16.17	-0.18	-139.94	-130.13	-2.95
	55.68	2.5	-136.13	-122.56	-3.92	23.86	25.18	-0.10	-159.99	-147.74	-3.82
	69.60	2	-151.29	-134.02	-4.99	34.07	35.34	0.18	-185.36	-169.36	-5.17

Orientation Angles	T (°C)	Z ₀ (mm)	(σ _x) _p (MPa)	(σ _y) _p (MPa)	(τ _{xy}) _p (MPa)	(σ _x) _r (MPa)	(σ _y) _r (MPa)	(τ _{xy}) _r (MPa)	(σ _x) _e (MPa)	(σ _y) _e (MPa)	(τ _{xy}) _e (MPa)
	92.80	1.5	-172.92	-150.38	-6.51	47.04	47.59	0.53	-219.96	-197.97	-7.04
[30/-30] ₂	39.77	3.5	-114.11	-109.06	-4.37	7.41	7.74	-0.23	-121.52	-116.80	-4.14
	46.40	3	-122.51	-116.25	-5.42	15.36	15.95	-0.32	-137.87	-132.20	-5.10
	55.68	2.5	-133.26	-125.43	-6.79	24.14	24.90	-0.18	-157.40	-150.33	-6.61
	69.60	2	-147.64	-137.67	-8.64	34.34	35.07	0.31	-181.98	-172.74	-8.95
	92.80	1.5	-168.16	-155.15	-11.27	47.16	47.48	0.92	-215.32	-202.63	-12.19
[45/-45] ₂	39.77	3.5	-111.58	-111.58	-5.05	7.58	7.58	-0.27	-119.16	-119.16	-4.78
	46.40	3	-119.38	-119.38	-6.26	15.65	15.65	-0.37	-135.03	-135.03	-5.89
	55.68	2.5	-129.34	-129.34	-7.84	24.52	24.52	-0.20	-153.86	-153.86	-7.64
	69.60	2	-142.66	-142.66	-9.97	34.70	34.70	0.35	-177.36	-177.36	-10.32
	92.80	1.5	-161.65	-161.65	-13.01	47.32	47.32	1.06	-208.97	-208.97	-14.07
[60/-60] ₂	39.77	3.5	-109.06	-114.11	-4.37	7.74	7.41	-0.23	-116.8	-121.52	-4.14
	46.40	3	-116.25	-122.51	-5.42	15.95	15.36	-0.32	-132.20	-137.87	-5.10
	55.68	2.5	-125.43	-133.26	-6.79	24.90	24.14	-0.18	-150.33	-157.40	-6.61
	69.60	2	-137.67	-147.64	-8.64	35.07	34.34	0.31	-172.74	-181.98	-8.95
	92.80	1.5	-155.15	-168.16	-11.27	47.48	47.16	0.92	-202.63	-215.32	-12.19

In Fig. 3, for a symmetric cross-ply [0°/90°]₂ laminated plate, residual stress distributions are shown through the thickness depending on the temperature variations.

Figs. 4, 5, 6 and 7 show residual stress distributions with the temperature varying nonlinearly through the thickness for symmetric angle-ply laminates.

The residual stresses grow through the inside of the plates and the stress distributions are symmetric with respect to the horizontal axis.

$(\sigma_x)_r$ and $(\sigma_y)_r$ stresses increase and are dependent on the temperature increment.

4. CONCLUSIONS

1. When the temperature is up to 34.79°C, symmetric cross-ply laminated plates yield without regard to the stacking sequences.

2. Although the elastic-plastic stress components of $(\sigma_x)_p$ and $(\sigma_y)_p$ have some magnitude, the shear stress component $(\tau_{xy})_p$ is zero, and similarly, the residual stress components of $(\sigma_x)_r$ and $(\sigma_y)_r$ have some magnitude whereas the stress components of $(\tau_{xy})_r$ are zero for the symmetric crossply laminates.

3. All the elastic, plastic and residual stress components increase with the temperature increment.

4. Linear and nonlinear variations of thermal loads produce different elastic-plastic and residual stresses through the thickness.

REFERENCES

1. Jeronimidis G. and Parkyn A.T.- Residual Stress In Carbon Fiber-Thermoplastic Matrix Laminates, *Journal of Composite Materials*, 22: 401–415, 1998
2. Jiang Z. , Lian J. , Yang D. and Dong S.- An Analytical Study of The Influence of Thermal Residual Stresses on the Elastic and Yield Behaviors of Short Fiber-Reinforced Metal-Matrix Composites, *Material Science and Engineering*, A248: 256–275, 1998
3. Ifju P.G., Kilday B.C. , Niu X. and Liu S. - A Novel Method to Measure Residual Stresses in Laminated Composites, *J. Composite Materials*, 33(16), 1999
4. Ersoy N. and Vardar O. - Measurement of Residual Stresses in Layered Composites by Compliance Method, *J. Composite Materials*, 34(07), 2000
5. Trende A., Astrom B.T. and Nilson G. - Modeling of Residual Stresses in Compression Molded Glass-Mat Reinforced Thermoplastics Composites, Part A: *Applied Science and Manufacturing*, 31: 1241–1254, 2000
6. Fenn R.H., Jones A.M. and Wells G.M. - X-Ray Diffraction Investigation of Triaxial Residual Stresses in Composite Materials, *J. Composite Materials*, 27(14), 1993
7. Atas C. and Sayman O. - Elasto-Plastic Stress Analysis and Expansion Of Plastic Zone in Clamped and Simply Supported

- Aluminum Metal-Matrix Laminated Plates, *Composite Structures*, 49: 9–19, 2000
8. Sayman O., Aksoy S. and Aykul H. - An Elastic/Plastic Solution for A Thermoplastic Composite Cantilever Beam Loading by Bending Moment, *Composite Science and Technology*, 60: 2739–2745, 2000
 9. Karakuzu R. and Sayman O.-Elasto-Plastic Finite Element Analysis of Orthotropic Rotating Discs with Holes, *Computers and Structures*, 51: 695–703, 1993
 10. Karakuzu R., Ozel A. and Sayman O. - Elastic-Plastic Finite Element Analysis of Metal Matrix Plates with Edge Notches, *Computers and Structures*, 63: 551–558, 1997
 11. Karakuzu R. and Ozcan,R. - Exact Solution of Elasto-Plastic Stresses in a Metal-Matrix Composite Beam of Arbitrary Orientation Subjected to Transverse Loads, *Composite Science and Technology*, 56: 1383–1389, 1996
 12. Oosthuizen J.F. and Stone M.A.- Residual Stresses in CSM/Vinyl Ester Resin Laminates Due to Post-Cure-Shrinkage, *Composite Structures*, 39: 303–307, 1997
 13. Barnes J.A. - Thermal Expansion Behavior of Thermoplastic Composites, *J. Material Science*, 28: 4974–4982, 1993
 14. Reddy J.N. - *Mechanics of Laminated Composite Plates, Theory and Analysis*, CRC Press, Inc, Texas, Chapter 5, 1997
 15. Jones R.M. - *Mechanics of Composite Materials*, Taylor & Francis, Philadelphia, 2nd edn, Chapter 4, 1999

MODELING AND ANALYSIS ON ADJUSTABLE VANE

SEMENESCU Danel^{*}, CRACIUNOIU Nicolae^{**}, DUMITRU Nicolae^{**},
MANEA Ion^{**}

^{*}SC HIDROSERV Iron Gates SA

^{**}University of Craiova, Faculty of Mechanics

Abstract: This paper presents the tools used to develop a 3D CAD model for the adjustable vane, subassembly of the wicket gate. Due to the work heavy conditions of the wicket gate is important to model and analyse the adjustable vane from a hydro electric generator. First, a solid model is developed and then a finite element analysis for the adjustable vane is performed.

Keywords: adjustable vane, 3D CAD model, acceleration

1. INTRODUCTION

The main function of the directory apparatus is to assure the access of water from the spiral camera to rotor, the water flux respectively and optimum conditions to transform the kinetic energy in mechanical energy, but with the minimum hydraulics loss.

One of the most important functions of the directory apparatus is to assure the debit variation, and, as a consequence, the adjustment of the turbine torque.

The main parts of the directory apparatus of the hydraulic turbine are:

- Wicket gate with adjustable vane set, witch can control revolution around the axis. The adjustable vane can revolute in the vertical plan. For the closed position, the water admission is stopped;
- Two servomotors with 300 mm pistons stroke.

The paper presents the modelling of the adjustable vane, subassembly of the directory apparatus and the main parts of this, and, also the result of some experimental tests carried out in frame of a hydro electric generator in view to determine the dynamic characteristics of the directory apparatus.

2. MODELING OF THE ADJUSTABLE VANE

2.1. MAIN PARTS OF THE WICKET GATE

The wicket gate, part of the turbine assembly (fig. 1) assures the water access to the turbine blades, and, as a consequence, the motion of the turbine generator shaft.

The open position of the adjustable vane make possible the water access and the close position stop the water access to the turbine blades.

The main parts of the wicket gate (fig. 2) are:

- the palettes, the main bushings, the threaded clutches;
- journal bearings, and the arms with journal bearings.

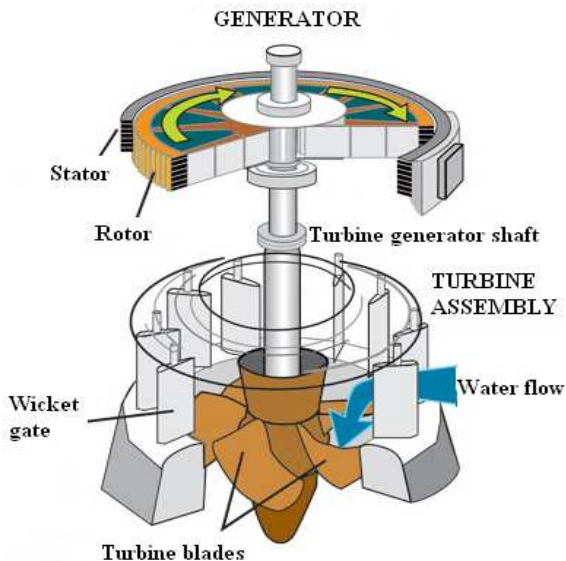


Fig.1 - The main parts of a hydraulic turbine [3]

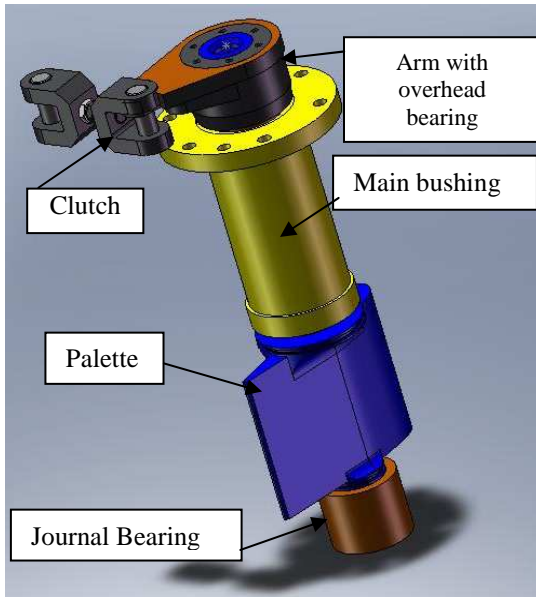


Fig. 2 - The main parts of the wicket gate

2.2. THE GEOMETRIC MODEL OF THE PALETTE

The main part of this subassembly is the pallet, whose assure the access or non-access of the water jet to the turbine blades. From this point of view is very important the profile, because the geometry and precision hereof affect the water jet direct to the turbine blade.

Taking into account the profile and the geometry of the palette (fig. 3), a solid model (fig. 4) was developed.

3. EXPERIMENTAL DETERMINATION OF FUNCTIONAL CHARACTERISTICS OF THE PALETTE

3.1. MEASURING APPARATUS AND TRANSDUCERS

In order to measure the accelerations in horizontal and vertical direction of the overhead palette journal bearing the next equipment was used (fig. 5):

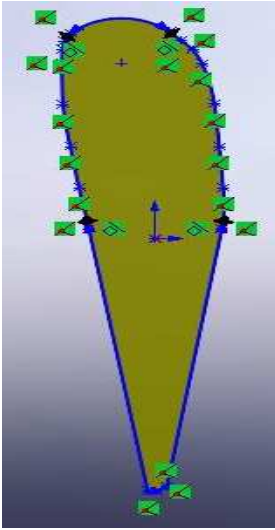


Fig. 3- The pallet profile



Fig. 4 - Solid model of the pallet

- acquisition system Spider 8;
- accelerometers Bruel & Kjaer;
- inductive transducers for linear stroke;
- rotation potentiometer transducer;
- force transducer.

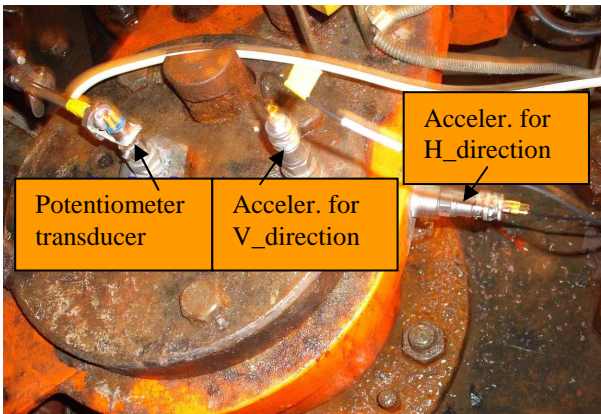


Fig. 5 - Transducers assembly for the acceleration measurement

3.2. EXPERIMENTAL DETERMINATIONS

The test was done without affect the normal regime of hydro electric generator. The transducers and the measure equipments were attached when the turbine is stopped. Due to the importance for the study of the recorder parameters, the work was done with the simultaneous recording for the all parameters, using a sampler frequency, witch cover the vibration frequency domain and relevant term of the process.

The recording conditions were: sampler frequency – 1200 samples/sec, and the recording time –30 min max. (at the turbine start). For every testing condition, the experimental data was collected, for the next processing, like a “.dat” files.

The rotational stroke of the palette was determinate using a potentiometer transducer, having a 5 kΩ film resistance. The transducer was attached in order to respect the rotational axis of the palette (fig. 5). The accelerations on the vertical and horizontal directions for the overhead palette bearing were determinate using acceleration transducers attached on the bearing level.

3.3. THE DATA PROCESSING

The turbine start was done with the progressive increase of the hydro generator power and power constant level maintain, with a reasonable time.

In fig. 6, the original registration taking on the hydro generator start is presented. The registered graph was divided in 14 representative zones, turbine start. For each zone the medium value was determinates: the actuating force of the palette, the rotational stroke of the palette, and the acceleration RMS.

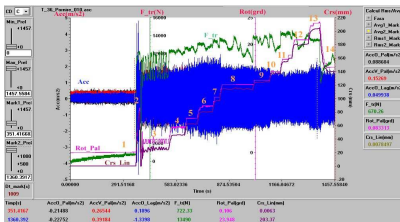


Fig. 6. - Original recording at the start

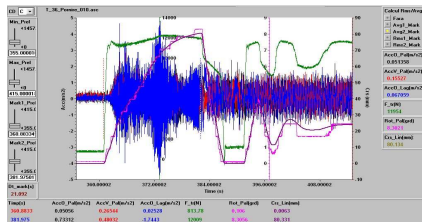


Fig. 7 – Original recording for zone two

Fig. 7 shows the original recording, for zone 2, and the variation of acceleration as function of the power is presented in fig. 8. As it is represented, the main vibration source is due to the turbine.

NEW STEADY-HAND EYE ROBOT WITH MICROFORCE SENSING AND SERVOING FOR VITREORETINAL SURGERY

Ali UNERI, Marcin BALICKI, James HANDA, Russell TAYLOR,
Julian IORDACHITA

*Center for Computer-Integrated Surgical Systems and Technology
(CISST ERC) at The Johns Hopkins University*

Abstract: Vitreoretinal surgeons use tubular instruments to manipulate delicate tissue inside the eye, by applying imperceptible forces while avoiding damage to the retina. We present here a system designed to enhance surgical performance by measuring these forces directly at the tool tip, in order to robotically regulate the forces applied by the surgeon. The system is based on a new generation of a cooperatively controlled microsurgery robot with a remote center-of-motion (RCM) mechanism. It integrates a custom microforce sensing surgical hook to provide conventional surgical function as well as force limiting, force scaling, force setting, and auditory feedback to the user. System experiments on phantom models identify some of the dynamic characteristics of vitreoretinal membrane peeling operations and quantify the range of forces associated with it.

Keywords: vitreoretinal membrane, microforce sensor, microsurgery, teleoperation, epiretinal membrane

1. INTRODUCTION

Microsurgical tasks involve forces that are well below human tactile sensation [1], where the range of possible tasks is limited by the surgeon's manual dexterity and the quality of available instruments. Imprecise movements during these operations can be due physiological hand tremor, fatigue, lack of kinesthetic feedback, as well as patient movement. Retinal microsurgery is one such example, where the common risks and limitations are further complicated by surgical inaccessibility, poor visibility, tissue fragility and the flexibility of the

delicate (20 Ga to 25 Ga) surgical instruments. A typical case for this would be epiretinal membrane (ERM) peeling, where a thin membrane is carefully delaminated off the surface of the retina by grasping the membrane's edge with microforceps and pulling it free from the retinal surface. Due to unstable manipulation and excessive forces applied to the tissue, the maneuver is associated with the risks of retinal hemorrhage and tearing, with potentially irreversible damage.

There are a number of research robots designed to minimize physiological hand tremor and provide the required control in vitreoretinal surgery. Micron from Carnegie Mellon University is a hand held device that uses piezoactuators to counteract undesirable hand tremor and scale input motions [2]. Another recent approach is a teleoperation system developed at the University of Tokyo [3]. The steady-hand Eye Robot—based on earlier work in our laboratory [4]—relies on its stiff structure and non-backdrivable actuators to provide stability. However, none of these systems can provide feedback of tool-tissue interaction forces to the surgeon.

Furthermore, they use relatively flexible instruments that can cause kinematic control inconsistencies, which along with involuntary patient motion have potential for damaging collisions with the retina. End-point sensing by employing intraocular instruments with integrated sensors can monitor force application contributed by robot and/or external factors, enabling us to develop smarter systems. Previous microforce sensing research work attempted to measure tool to tissue interaction forces with instruments that had sensing elements built into the handle, as with the 6-DOF sensor by Berkelman et al. [5]. This sensor is not practical for vitreoretinal surgery because the shaft of the instrument is inserted through the sclera. The friction between the tool and the trocar, and lateral forces from the transacting sclera with the tool can significantly attenuate or distort the propagation of the forces to the tissues inside of the eye. We address this limitation with a set of surgical tools that incorporate force sensing elements in the shaft of the instrument along a section that is typically located inside the eye [6].

The integrated system allows us to explore control methods, such as: force limiting, where the surgeon's force input is limited in order to minimize inadvertent force generation application that causes retinal tearing during membrane peeling; force setting, where the desired tip force is commanded; and force scaling, where the surgeon's input forces are scaled down and applied by the robot on the tissue itself. This is based on our earlier work [5], and allows the surgeon to apply significantly perceptible forces on the user interface which is generally not practiced for most conventional vitreoretinal tasks.

This paper is an overview of the integrated system, specifically the design of the new Eye Robot, summary of force sensing approach and

the use of force sensing in cooperative control. It will further present preliminary data for experiments carried out on phantom eye models.

2. EYE ROBOT: VERSION 2

Eye Robot is a collaborative steady-hand 5-DOF robotic system (Fig. 1) developed by the CISST 1 ERC2 at Johns Hopkins University (JHU), and is capable of manipulating the retinal tissue with micro-scale precision.

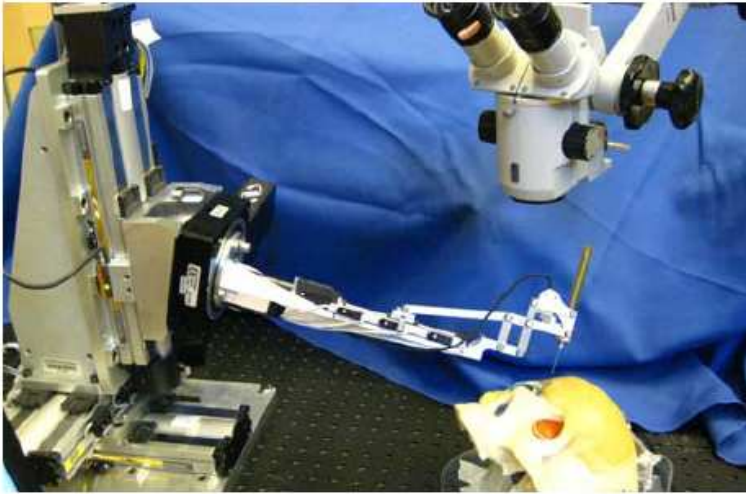


Fig. 1- Eye Robot (version 2).

A. Eye Robot 1

Retinal microsurgery, as with many other invasive procedures, requires the tool to be constrained by an insertion point, i.e. in this case the sclerotomy opening. Conventionally the surgeon can achieve this manually, but a software or hardware solution is also possible, which would not only provide an additional safety measure, but also relieve the surgeon from the extra duty of maneuvering around a pivot point.

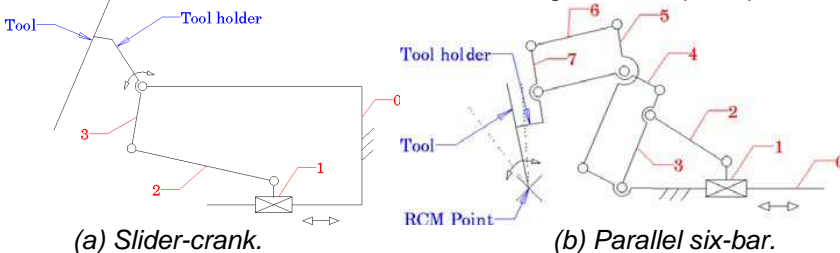


Fig. 2- Tilting mechanisms of the two Eye Robots.

The first version of Eye Robot (Eye Robot 1) was based on our earlier versions of JHU Steady-Hand robot, with the main design goal of achieving high precision without impinging too much on the surgical workspace [4]. It uses a slider-crank mechanism at the handle (Fig. 2a) that when compared with similar options and the new design described in the next section, provides a compact design with minimal connections and joints. However, Eye Robot 1 does not provide a mechanical RCM, and has to rely on software constraints to replicate the same functionality. A virtual RCM is thus implemented using constraint control optimization [7], such that the tool axis is programmatically constrained to always intersect the sclerotomy opening on the eye.

The precision of this system relies on the high gearings of the actuators, which results in an admittance-type system that also helps filter tremors, shakes and low-frequency drift [8] of the surgeons' hand movements during surgery. It utilizes a 6-DOF force/torque sensor mounted at the handle that senses user input and reacts accordingly, thereby allowing the surgeon to guide the robot in the desired direction. This collaboration between the surgeon and the robot—called cooperative control—provides fine control over the position of the tool, while filtering out any undesired motion.

However, recent experiments showed that this version cannot achieve the intended accuracy of 2 μ m to 5 μ m, and its susceptibility to wear diminished its repeatability over time, further motivating the design of a newer version.

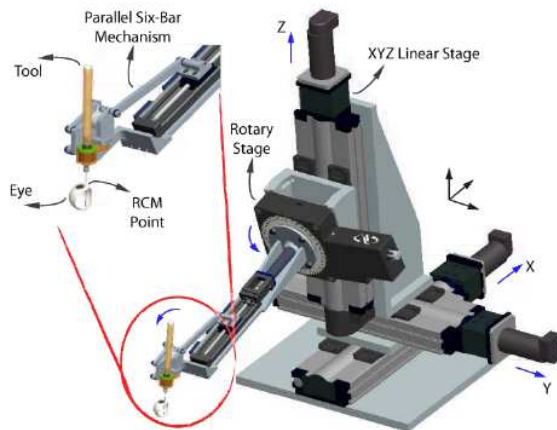


Fig. 3 - CAD model of Eye Robot 2 with close up view of the end-effector

B. Eye Robot 2

Eye Robot 2 (Fig. 3) is a major revision over the last one, and includes many new features to address the design flaws of the earlier version. The main motivation behind this upgrade was to 1) increase the accuracy and repeatability, 2) provide and evaluate the mechanical RCM approach, 3) increase the range of motion, and 4) improve usability and control. Analyzing the new design implementation, the manipulator itself consists of four modular subassemblies: 1) XYZ linear stages for translation, 2) a rotary stage for rolling, 3) a tilting mechanism with a mechanical RCM, and 4) a tool adaptor with a force sensor.

Parker Daedal 404XR linear stages (Parker Hannifin Corp., Rohnert Park, CA) are used to provide 100mm travel along each axis with a bidirectional repeatability of 3 μ m and positioning resolution of 1 μ m. A Newport URS 100B rotary stage (Newport Corp., Irvine, CA) is used for rolling, with a resolution of 0:0005 μ and repeatability of 0:0001 $^\circ$.

A THK KR15 linear stage (THK America Inc., Schaumburg, IL) with travel of 100mm and repeatability of 3 μ m is used to provide tilting motion. Finally a custom designed RCM mechanism is attached to the end-effector which also house a 6-DOF ATI Nano17 force/torque sensor (ATI Industrial Automation, Apex, NC) for sensing the user input forces. These components are assembled in a structurally similar fashion to that of Eye Robot 1 [4], resulting in the following specifications (Tab. I).

Tab. 1. Eye robot 2 performance specifications for motions in Approach (a), insetion (i), and retinal surgery (r) phases.

Specification	Value
XYZ motion	± 50 mm
Roll/tilt motion	$\pm 60^\circ$
XYZ precision	2 μ m
Roll/tilt precision	$\sim 0.000\ 05$ rad
Net precision at the retina	~ 5 μ m
Cartesian tip speed	10 mm s $^{-1}$ (A) 5 mm s $^{-1}$ (I) <1 mm s $^{-1}$ (R)
Deviation of tool shaft from the center of sclerotomy point	<1 mm (A) <0.2 mm (I) <0.2 mm (R)

C. Benefits

a) Precision: The precision has been improved in two stages. One main drawback with Eye Robot 1 is the flexibility of the extending arm, therefore a more rigid arm design was implemented to minimize the error introduced.

The other improvement is the use of better linear stages at the Cartesian joints. The leadscrews of Eye Robot 1 were chosen to eliminate backlash. However it was observed that they had to be regularly tightened and calibrated. A different design approach was chosen for Eye Robot 2, where ball screws were used, which although introduce minimal backlash, produce a more repeatable response in the long use.

b) Mechanical RCM: Although the virtual RCM was successful at constraining the motion, it caused large concurrent joint velocities at the tip, which created vibrations in the system due to high gearing. To address this issue and to evaluate the use of a mechanical design, a parallel six-bar mechanism has been implemented (Fig. 2b) which inherits an RCM by default.

c) Range of motion: The tilting rotation on Eye Robot 1 is limited to _25_, which has been increased to _60_ in order to allow for a wider workspace.

d) Software: The robot software underwent a major revision to be compatible with the CISST Surgical Assistant Workstation3 (SAW), enabling the robot control software to use the resources that are provided with it. This is a crucial step in better handling the existing interfaces, introducing new devices and smart tools to the systems, as was done in the following section.

Even with the recent updates it should be stressed that Eye Robot 2 is an intermediate design towards a stable and fully capable microsurgery assistance robot. The endproduct of the current design process is to have a system to evaluate microsurgical procedures in order to have a better understanding on the exact requirements, a device to carry out our research on, and a test bench for a multitude of smart tools like the one described in the next section.

3. TIP FORCE SENSING AND APPLICATIONS

Although Eye Robot can achieve the micron resolution required for vitreoretinal microsurgery, its performance is greatly limited by its end effector, i.e. the flexible surgical tool. The unknown interaction forces at the tool tip result in deformations on both the tool and the tissue, which negates the advantage of robot's high accuracy positioning.

Quantifying these forces would not only help compensate for this deformation, but also allow more informative control schemes coupled

with safety measures to minimize the risks associated with microsurgical tasks.

A. Force Sensing

Vitreoretinal microsurgical applications introduce certain limitations on the exact choice of force sensor by demanding specific characteristics. Some of the main requirements are:

1) Sub-mN accuracy to be able to accurately sense the tool-to-tissue forces associated with delicate movements like ERM peeling or retinal vessel dissection. Some preliminary ex-vivo results [1], [9] indicate that these forces routinely can be less than 7:5mN. However, to our knowledge, there are no published in-vivo results of measurements taken to quantify these forces when sclera interaction forces are present.

2) Miniature size, such that it would be possible to insert it through a 25 Ga sclerotomy opening and obtain measurements below the sclera.

3) Ability to sense forces at the instrument's tip. This is due to the flexible nature of the conventional tool. Being away from the tip would require the forces to propagate up the tool to the sensor, which in turn require the tool to be rigid.

In a related research, fiber Bragg grating (FBG) sensors were chosen as a candidate to achieve such tasks [10].

These are optical sensors capable of detecting changes in force, pressure and acceleration, without interference from electrostatic, electromagnetic or radio frequency sources.

They are passive and make no use of electronic components, working by reflecting a narrow bandwidth of light which responds robustly to changes in temperature and strain.

A tool with integrated 2-DOF FBG sensors was manufactured for this purpose, following the design of Lordachita et al. [6]. Three optical fibers are placed along the tool shaft (Fig. 4) and by measuring the bending of the tool, they allow for calculation of the force in the transverse plane, i.e. parallel to the retina, with a sensitivity of 0:25mN.

The sensor is integrated on Eye Robot 2, utilizing the new RCM design. An interface was developed within SAW framework, such that the robot can communicate with the FBG interrogator over TCP/IP and integrate the sensed force into its governing control law.

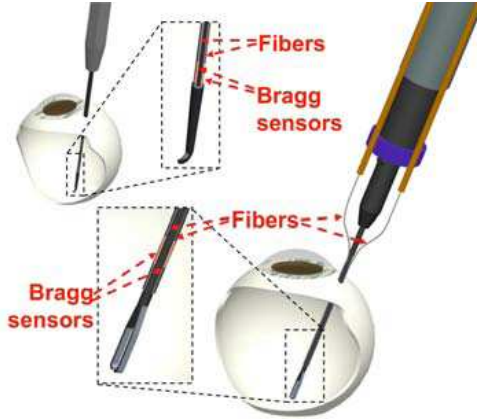


Fig. 4 - Tool with FBG force sensors attached, inserted through a sclerotomy opening.

B. Force Servoing

The ability to sense forces at the tool tip with a micron precision robot allows for increased control of tool-tissue interaction forces during microsurgical tasks.

e) Force Limiting: This control algorithm is mainly a safety feature. The aim here is to define an upper bound on the allowed force for any given axis. When a force that is over the limit is introduced, the robot backs up with a velocity that is proportional to the difference between the limit and the current tip force.

f) Force Scaling: A common type of force servoing is scaling, where the output is a scaled version of the input. In our design the handle sensor provides the input force from the user, while the control law regulates the robot as to apply a linearly scaled version.

$$\epsilon = \nu f_h - f_t$$

where f_h and f_t are the handle and tip forces respectively, ν is the scaling factor and ϵ is the error. We then generate a desired force input f_e using an exponential map

$$f_e = \text{sgn}(\epsilon) (\exp(k_p |\epsilon|) - 1)$$

where k_p is the proportional gain. From this we can find the desired joint velocities $\dot{\theta}$ using the Jacobian of the tip J_t .

$$\dot{\theta} = J_t^{-1} f_e$$

The apparent result of this algorithm allows the surgeon to carry out the same procedure in a force-magnified environment. It also provides a safety measure, since not only unintentional user input, but

also patient motion can be compensated, i.e. the robot reacts to external forces and retracts back to a safety even without user input.

This control mode could also theoretically provide haptic feedback to the user. However the admittance-type nature of the robot as a result of its high gearing prevents high frequency feedback. Rather than feeling the reaction force, the surgeon can only sense the force he/she has to apply, which is amplified above perception thresholds.

g) Force Setting: Another feature is setting the force to a certain value. The implementation of this is an update to the previous algorithm, where instead of $v f_h$ a desired force f_d is supplied as the input. This simple change allows one to apply a controlled input, which was used in the last set of experiments.

C. Auditory Sensory Substitution

We have explored several sensory substitution methods to improve the force information available to the surgeon beyond what is provided by haptic feedback. Methods explored include: 1) Visual feedback using image overlays to provide graphical cues, 2) Haptic feedback using vibrotactile stimulation, or 3) Audio feedback. Although vibration display techniques such as [11] have been used to increase fidelity of haptic force feedback, these techniques require the surgeon to evaluate these forces haptically and have the potential drawback of introducing significant vibration into the system, which could adversely affect the robot's precision and system's usability, i.e. the surgeon might prefer a stable-feeling environment during a delicate membrane peeling operation.

Visual cues are generally the easiest to perceive. However, since the surgeon's spatial resolution is limited and the surgeon needs to concentrate on the tool and tissue, the extra visual cues might create an information overload.

Although auditory signals are common in the operating room, mainly associated with physiological monitoring devices, they are not generally used as an active, integral form of feedback to the surgeon. This situation allows for a diverse range of options. Our current implementation, which has been updated in light of the feedback from the surgical staff, gives the user the option to choose a unique discrete or continuous sound, where the frequency increases proportionally with force. The parameters (Fig. 5) are adjustable in runtime, from the robot application's graphical user interface (GUI).

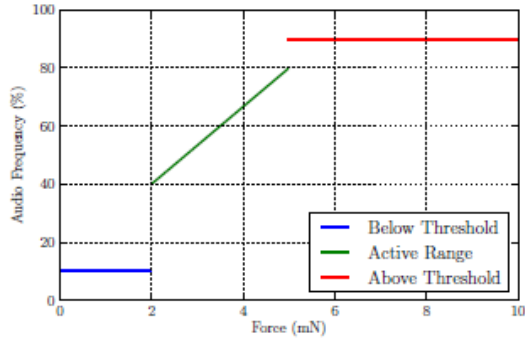


Fig. 5- Figure showing the current audio response, where the active range has been set to 2mN to 5mN.

4. MEMBRANE PEELING EXPERIMENTS

We have conducted a series of preliminary experiments of the force sensing and control capabilities of our new robot. The phantom task chosen for these preliminary experiments was peeling the membrane from the interior shell of a raw chicken egg. Although the characteristics of this membrane are not the same as actual retinal tissue, the general properties are similar enough for this model to be useful, and it is routinely used in our laboratory.

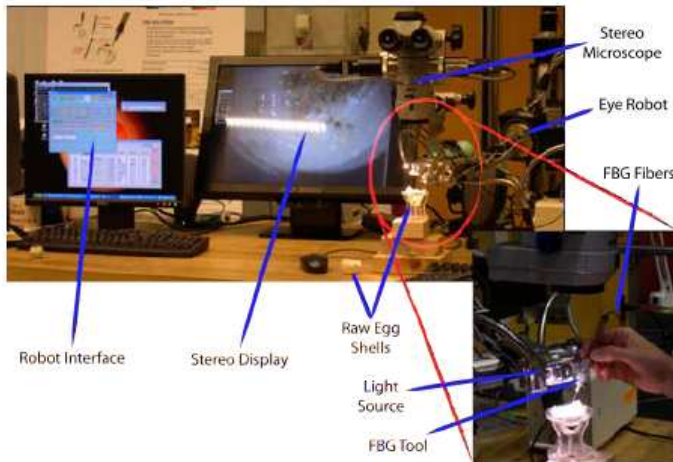


Fig. 6 - Workstation for membrane peeling experiments.

The setup workstation (Fig. 6) consists of the newly developed equipment along with a stereo microscope to aid in visualizing small manipulations. Simultaneous video capturing was performed to relate the measurements to video frames.

For all experiments, the robot was moved to the target zone and the hook was attached to the membrane prior to initializing data collection. Forces exerted at the tool tip, on the handle and the tool velocity were recorded.

A. Force Scaling

Measurements obtained from the force scaling trials capture the distinct behaviour of our algorithm. When interacted with tissue, the tip force regulates the robot motion in order to track a scaled version of the handle force. For the case presented in Fig. 7a, the tool tip force buildup of the peeling operation (from 40 s to 50 s) is met by a decreasing tool velocity. At 50 s, the membrane begins to tear, which results in a sudden velocity increase powered by the user input.

Force scaling was also tested on a wood surface, in order to neglect the dynamics due to tissue compliance. Fig. 8 depicts the tracking of the signals, where the tracking error is of a few mN.

B. Force Setting

In force setting experiments (Fig. 7b), the robot was manually set to apply a gradual force to the membrane along the y-axis, during membrane peeling. Each increment was enforced by the speed of the tool, i.e. each time the robot came to a full stop due to the force exerted by the membrane.

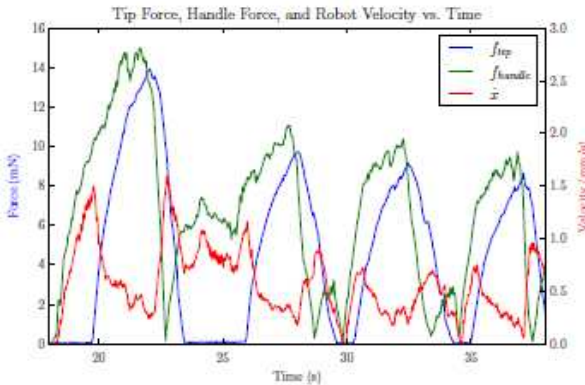


Fig. 8 - Force scaling on a rigid surface.

The results show that $\approx 7\text{mN}$ force was enough to peel an egg membrane. It can also be observed that during peeling when the tissue

is teared, the tip force drops, which results in an increased speed on the robot.

While force scaling is better suited for collaborative control, force setting allows more control on the robot motion, which makes it a good candidate for our future experiments.

C. Force Limiting

It was observed in the previous experiments that 4mN was rarely enough to peel the membrane. Setting this as the upper tip force limit, we tried to do membrane peeling.

As expected, anytime the limit force was reached, the robot reacted with a sudden stop, and backed up until the tool was back in the safe zone (Fig. 7c).

Force limiting can be used in conjunction with the aforementioned servoing algorithms to provide the system with an upper safety limit. One other possible application would be to increase the limit on need basis, meaning the surgeon can increase the limit as he/she sees fit.

5. CONCLUSION AND FUTURE WORK

A. Conclusion

We have developed a new steady-hand microsurgical robot with the particular goal of assisting vitreoretinal surgeries. At its current state, it is still an intermediate step towards this main goal, and provided us with insights into future requirements.

We believe that through the work presented here, we could extend the control of the robot from its end effector, down to the tissue level. The micron resolution control, coupled with tool tip force sensing, the governing control laws and a natural sensory substitution enabled the user to carry out conventional tasks with more ease. As with all research, the most exciting part is always the next.

B. Future Work

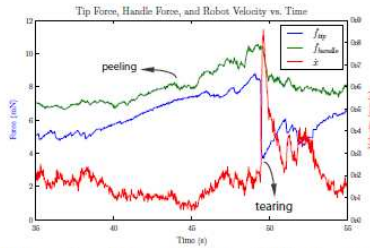
Eye Robot 2 is primarily a research platform for providing experimental data to guide development of practical “smart” instruments and clinically useful robots. Its precision will enable us to determine the resolution required for typical retinal surgery tasks. The new mechanical RCM may influence both user ergonomics and the ultimate surgical workstation design (i.e. how it affects the other equipment, specifically the stereo microscope).

The introduction of a tip sensor also affects the design needs of Eye Robot. In the current implementation the tool is fixed on to the robot. However, future designs might require the ability for rotating the tool about its axis in order to allow the surgeon to properly orient the

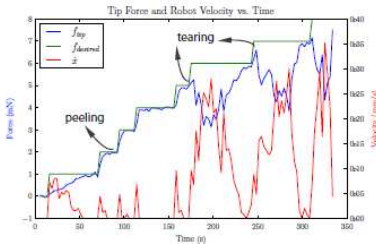
hook with respect to tissue plane. To ensure that the tool frame maps to the robot frame, this rotation will need to be encoded.

For the force servoing, current application reacts only to translational motion, which was observed to be limiting during the membrane peeling experiments. As the next step, it will be extended to support all 5-DOF of the robot.

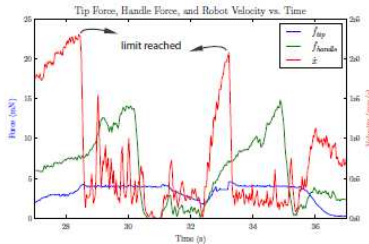
The next series of experiments will focus on membrane peeling experiments on animal eyes, since quantifying range of forces would enable us to 1) define the range of forces we are dealing with, and develop warning signals for the surgeon if the forces are exceeded, 2) compare human free-hand and robotic assisted performance for the intended application. 3) design virtual models to be used as the basis of a surgical training set.



(a) Force scaling with a scaling factor of 800, where handle forces have been scaled down accordingly to match the tip forces.



(b) Gradual force setting.



(c) Force limiting where the limit is 4 mN. Handle forces have been scaled down by 300.

Fig. 7 - Force servoing algorithms.

REFERENCES

1. P. K. Gupta, P. S. Jensen, and E. d. Juan, "Surgical forces and tactile perception during retinal microsurgery," in MICCAI '99: Proceedings of the Second International Conference on Medical Image Computing and Computer-Assisted Intervention. London, UK: Springer-Verlag, 1999, pp. 1218–1225.

2. C. Riviere, W. T. Ang, and P. Khosla, "Toward active tremor canceling in handheld microsurgical instruments," *Robotics and Automation, IEEE Transactions on*, vol. 19, no. 5, pp. 793–800, Oct. 2003.
3. T. Nakano, N. Sugita, T. Ueta, Y. Tamaki, and M. Mitsuishi, "A parallel robot to assist vitreoretinal surgery," *International Journal of Computer Assisted Radiology and Surgery*, 2009.
4. B. Mitchell, J. Koo, M. Iordachita, P. Kazanzides, A. Kapoor, J. Handa, G. Hager, and R. Taylor, "Development and application of a new steady-hand manipulator for retinal surgery," in *Robotics and Automation, 2007 IEEE International Conference on*, April 2007, pp. 623–629.
5. P. Berkelman, L. Whitcomb, R. Taylor, and P. Jensen, "A miniature microsurgical instrument tip force sensor for enhanced force feedback during robot-assisted manipulation," *Robotics and Automation, IEEE Transactions on*, vol. 19, no. 5, pp. 917–921, Oct. 2003.
6. I. Iordachita, Z. Sun, M. Balicki, J. Kang, S. Phee, J. Handa, P. Gehlbach, and R. Taylor, "A sub-millimetric, 0.25 mm resolution fully integrated fiber-optic force-sensing tool for retinal microsurgery," *International Journal of Computer Assisted Radiology and Surgery*, vol. 4, no. 4, pp. 383–390, 06 2009.
7. A. Kapoor, M. Li, and R. Taylor, "Constrained control for surgical assistant robots," in *Robotics and Automation, 2006. ICRA 2006. Proceedings 2006 IEEE International Conference on*, 15-19, 2006, pp. 231–236.
8. C. Riviere, R. Rader, and P. Khosla, "Characteristics of hand motion of eye surgeons," in *Engineering in Medicine and Biology Society, 1997. Proceedings of the 19th Annual International Conference of the IEEE*, vol. 4, Oct-2 Nov 1997, pp. 1690–1693 vol.4.
9. A. Jagtap and C. Riviere, "Applied force during vitreoretinal microsurgery with handheld instruments," in *Engineering in Medicine and Biology Society, 2004. IEMBS '04. 26th Annual International Conference of the IEEE*, vol. 1, Sept. 2004, pp. 2771–2773.
10. Z. Sun, M. Balicki, J. Kang, J. Handa, R. Taylor, , and I. Iordachita, "Development and preliminary data of novel integrated optical development and preliminary data of novel integrated optical micro-force sensing tools for retinal microsurgery," in *Robotics and Automation, 2009 IEEE International Conference on*, April 2009, pp. 1897–1900.
11. D. A. Kontarinis and R. D. Howe, "Tactile display of vibratory information in teleoperation and virtual environments," *Presence*, vol. 4, pp. 387–402, 1996.

OPTIMIZATION STUDY OF A CAR SUSPENSION–STEERING LINKAGE

PREDA Ion*, CIOLAN Gheorghe*, ISPAS Nicolae*
**Transilvania University of Brasov – Romania*

Abstract: The study presents the main steps and some results of a design, analysis and optimization process of a complex articulated mechanism required for a car suspension and steering. The authors used a top-down approach, starting from the requirements of the assembly and the close connections between the vehicle suspension and steering. Then the computer model was successively refined and new components were added as the design solutions became clearer. More steps were done, starting with a simplified analysis aiming geometrical optimization, continuing with a multibody study of the mechanism, part and assembly manufacturability-oriented CAD-modeling, a finite element analysis of some important parts and finishing with corrections and tunings of the CAD models.

Keywords: MacPherson suspension linkage, rack-and-pinion steering, multibody analysis, finite element analysis, optimization

1. INTRODUCTION

Designing a suspension-steering mechanism for an automotive vehicle is a complex task. Starting from the very beginning, a lot of requirement must be fulfilled. The process needs considering the vehicle kinematics and dynamics, continues with aspects regarding the general layout, packaging and compatibility with the other systems of the vehicle and finalizes with fine tuning, manufacturability and durability. The existence of many specialized software programs can be today very helpful for the automotive engineer. Such computer programs, used for part and assembly design, engineering computations and virtual testing, represent valuable tools in the engineering activities, assisting the teams to finalize projects in shorter time, with fewer mistakes and with smaller costs. This paper presents

one computer aided approach to model and virtually test a suspension and steering mechanism for cars.

2. PRELIMINARY ANALYSIS OF LINKAGES GEOMETRY

The MacPherson articulated axle (schematized in figure 1 as a Catia-V5 2D-model) consist on a swing arm, connected to the vehicle body by a revolute joint placed in the lower side of the mechanism, and on a strut, connected to the body by elements behaving as an spherical joint.

The strut is made of two parts, having two degrees of freedom one vs. other: a translation along the strut axis, permitting the wheel bump-rebound movement, and a rotation around the same axis, permitting the wheel steering. The function of this cylindrical joint is taken by the suspension damper (shock absorber), reducing thus the number of parts needed to ensure the main suspension functions: cushioning, damping and wheel guiding.

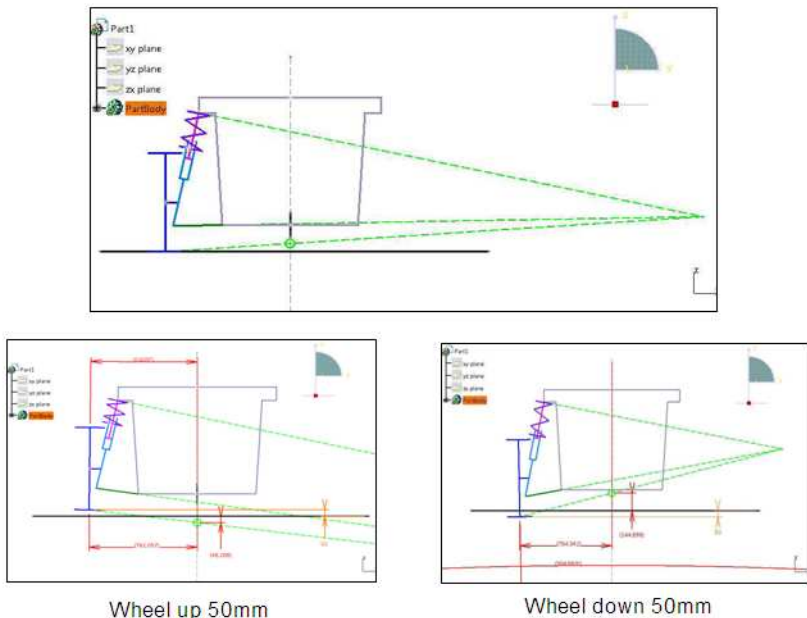


Fig. 1 – Schematic representation and behavior of the MacPherson suspension linkage

The MacPherson linkage is now commonly used on cars and vans because needs less lateral space on the vehicle, leaving enough free space for a transversal engine-transaxle mounting.

A vehicle steering mechanism consists of two subsystems:

- a steering linkage, (or better, a correlation mechanism), used to relate the swivel angles of all the steerable wheels (figure 2), so that to minimize positioning error of these wheels during cornering;
- an actuation mechanism, needed to transfer the rotation of the driver's steering wheel as a positioning command of the steering linkage.

For cars and vans, the most spread steering mechanism uses a rack and pinion steering box. In this type of steering mechanism, the rack is part of both steering linkage and actuation mechanisms, making this the simplest steering mechanism for wheeled vehicles.

Figure 2 schematizes the main components of such a rack and pinion steering linkage in the case of two-axle vehicle with independent front suspension. The actuation mechanism transmits the rotation (imposed by the driver) of the steering wheel through the steering shaft to the pinion. The pinion rotation will determine the lateral translation of the rack and the change of the linkage position will force the road wheels to steer.

The project started with a multi-parametric optimization in a vertical-transversal plane of the suspension-linkage 2D-model. The parameters modified during optimization, between the limits permitted by packaging requirements, were: the arm's length and laying angle, the wheel scrub radius, the kingpin angle and the height of the strut-body joining point.

During wheel bouncing displacement, the optimization goals were:

- ensuring sufficient wheel bump-rebound travel;
- ensuring an acceptable ground clearance;
- maintaining minimal change of the wheel camber, so that to permit maximal tire grip;
- maintaining minimal change of the vehicle track width, avoiding thus the "fight" of the axle wheels, that generates useless "consume" of grip, poor handling and supplementary stress for linkage;
- maintaining the axle's roll-center as high as possible, in order to have small body roll, so diminishing its influence when cornering and consequently reducing the change of the wheel camber and track width.

Figure 1 shows graphical representations of the 2D simplified mechanism behavior during vertical wheel bouncing, obtained at the end of the 2D optimization process.

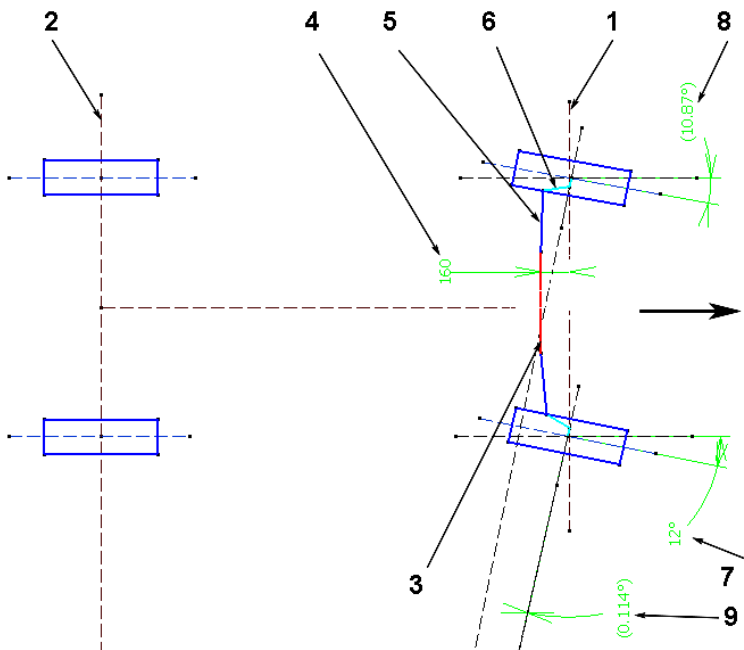


Fig. 2 – Simple steering model used to primarily adopt the design dimensional parameters

A similar geometrical optimization was made for the planar model of the rack and pinion linkage. As shown in figure 2, this mechanism contains two steering arms 6, two steering rods 5, the rack 3 and the vehicle body as mechanism base.

In the lack of lateral forces on tires, a correct positioning of the steerable wheels (in this case, the ones of the front axle) can be realized only if the projections on the ground surface of the front-wheels centerlines intersect both, in the same point, the similar centerline projection of the rear wheels (position 2 on the figure 2). That is also called the Ackermann condition or the geometrical correct steering condition [2].

Later, on the 3D model, the optimization process was resumed, considering supplementary the lateral slip angles affecting tires under medium to hard cornering maneuvers.

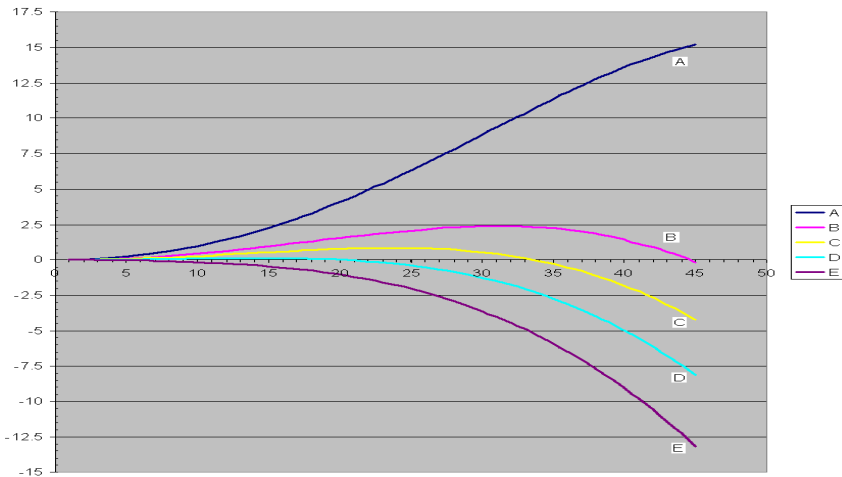


Fig. 3 – Exemplification of the error-angle variations as function of the inner-wheel's steering-angle for different rack positions

The fulfillment of that condition was the starting point for the multi-parametric optimization of the steering linkage. Considering as independent variable the inner-wheel's steering-angle γ , the aim of optimization ([1], [2]) was to reduce the error angle ϵ , i.e. the difference between the Ackermann-angle and the actual steering-angle of the outer-wheel (the first is the wanted angle, while the second is the actual linkage angle – position 8 in figure 2). The parameters changed during optimization (figure 2) were: the length of the rack 3; the position 4 of the rack with respect to the front-axle 1; the length of the steering arm 6; the position angle of the steering arm with respect to the corresponding-wheel's centerline.

The way the error-angle is changing versus the linkage dimensions and inner-wheel's steering-angle it is presented in figure 3. To appreciate the quality of a certain linkage layout (defined by a set of parameters considered at a time), the error angle was weighted in function of inner-wheel's steering-angle: biggest weighting values for small to mean values of the steering angles, which correspond to vehicle high speeds.

The layout noted with C in figure 3 was found to be the best. The procedure was repeated three times with different geometrical parameters and had as result the optimal layout for a planar model of the linkage. The process was also used to calculate the maximal steering angles that can be realized without the locking danger for the correlation mechanism.

3. MULTIBODY MODELING

Using the main dimensions obtained by the 2D geometrical optimization, the next step was to realize a draft Catia-V5 3D-model. The main parts of the suspension and steering systems were modeled, adding also the disk brake and the components of the wheel (hub, rim and tire), figure 4. The parts were then virtually assembled so that to respect packaging requirements and to avoid geometrical interferences.

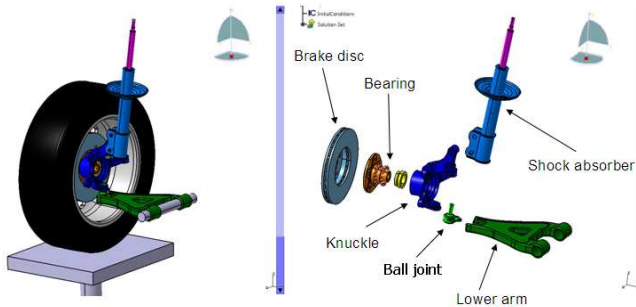


Fig. 4 – CAD (right) and MBS (left) models of the suspension

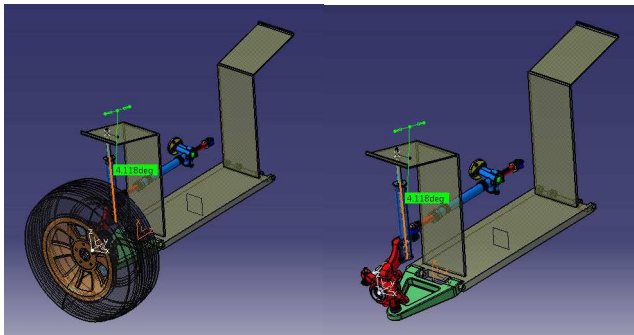


Fig. 5 –CAD model of the suspension-steering, considering the caster angle

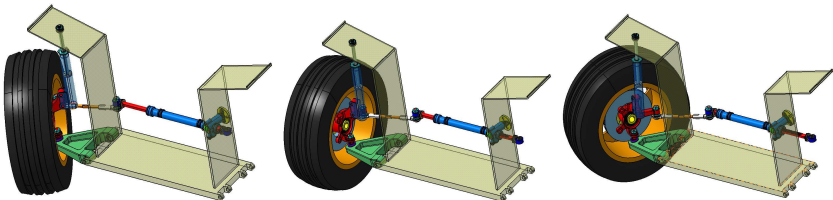


Fig. 6 – The multibody model subjected to the analysis
left – extreme left-steering, middle – straight-line travel, right – extreme right-steering

Together with the wheel camber and the kingpin positioning angles, the other laying angle of the kingpin-axis, the caster-angle, was supplementary introduced into the CAD model (fig. 5) and considered as design parameters for a new optimization stage [1], [4], [6], [7].

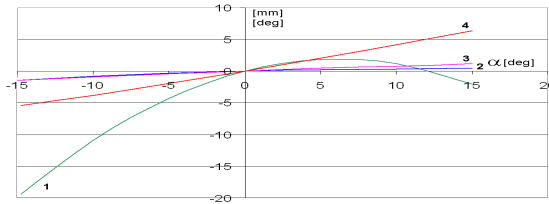


Fig. 7 – Multibody analysis results of axle kinematic-behavior on jounce-rebound (straight-line motion): independent parameter – the lower-arm swing-angle; 1 – track-width change; 2 – camber-angle change; 3 – steering angle change (bump-induced steering); 4 – wheel lift, divided by 10

Starting from the three-dimensional Catia model and using LMS Virtual Lab Motion software, a new model was realized. This multibody model (presented in figure 6, in the case of steering with no vertical-motion for the wheel) permitted to study the kinematics and dynamics of the steering-suspension mechanism. Final simulation results are presented in figure 7.

4. CAD MODELING

After the narrow examination of the mechanism behavior by multibody simulation, the parts design was revised, having in mind functional and manufacturing requirements. Consequently, the CAD models included the shapes of the preformed part and some intermediate manufacturing stages [3], fig. 8. All the parts were virtually assembled to form firstly subassemblies (fig. 9) and then the complex mechanism of steering and suspension. The packaging of all the parts and the mounting-dismounting possibilities were also being verified.

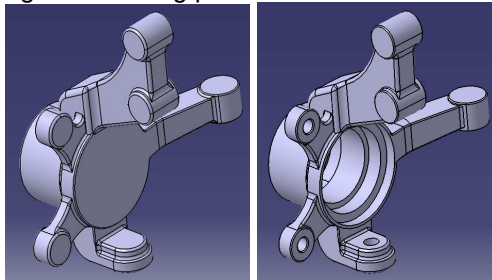


Fig. 8 – Manufacturing-oriented CAD modeling (knuckle)

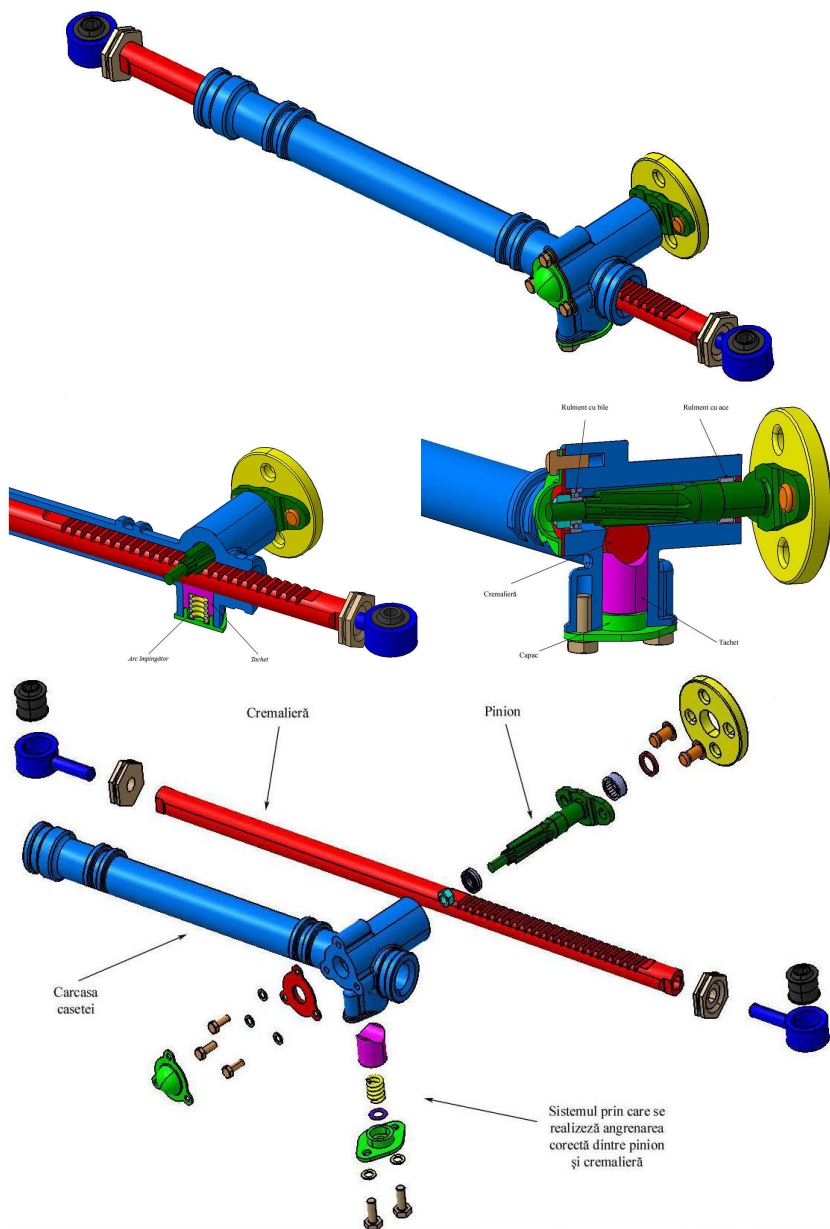


Fig. 9 – Subassembly CAD model included into the designed mechanism – rack and pinion steering box

5. FINITE ELEMENT ANALYSIS

To verify if the parts were well designed and dimensioned, a study of the stresses and deformations was necessary. The finite element analysis (FEA) represent today the method used most often to verify if a part resists under the loads or if is stiff enough to fulfill its function. The steps involved by this method [3] and applied for the main parts are presented further for the most complex stressed part of the designed mechanism – the steering knuckle, figures 10-12.

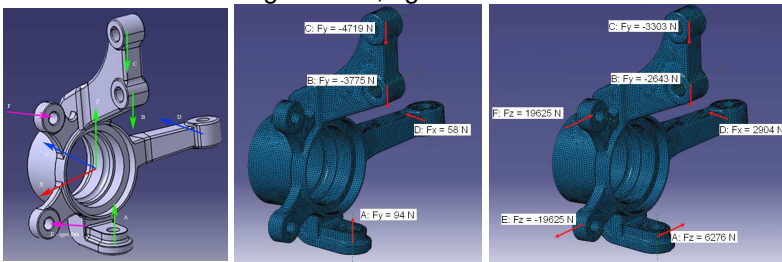


Fig. 10 – Knuckle's coordinate system and forces orientation

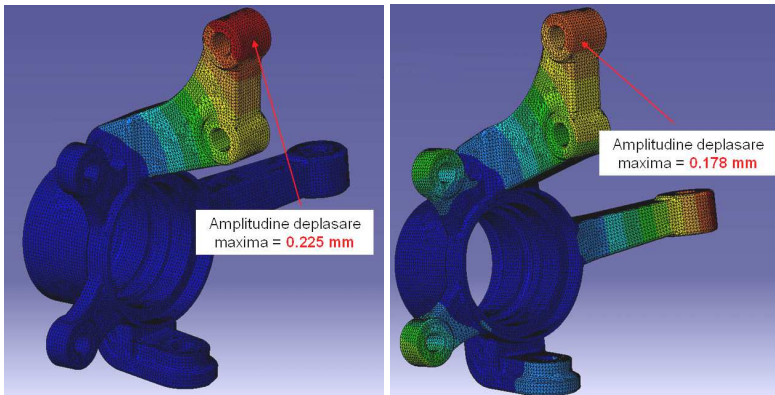


Fig. 11 – Knuckle deformation: left – bump passing, right – braking

The material adopted for the knuckle was a forged allied steel. Firstly, a coordinate system was chosen, accordingly with the ISO standard. For the study, the knuckle was considered supported by the wheel bearings and the interactions with the other parts were replaced by forces, figure 10, left. Two very important load cases were analyzed [1], [5], [8]: passage over road unevenness (singular bump) and hard braking on a quality road. The orientations of the forces for these cases are presented in figure 10, middle and right, respectively. The magnitudes of the forces were obtained through the multibody simulation. Comparing with the bump passing, the braking case

presents smaller vertical forces, but new big forces act due to the braking torque.

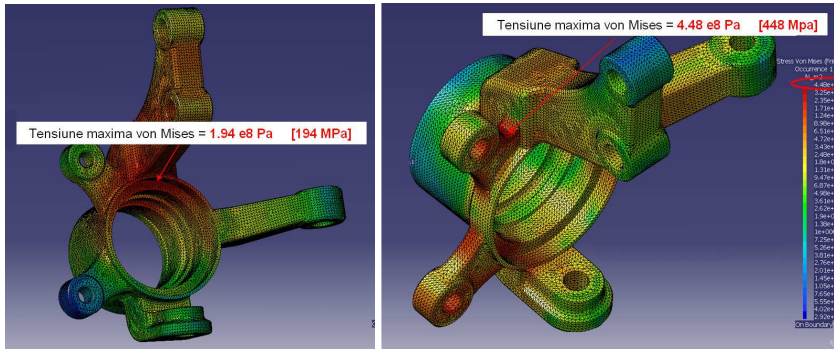


Fig. 12 – Knuckle stress: left – bump passing, right - braking

The CAD model of the knuckle was imported into LMS Virtual Lab software where it was divided in finite elements, figures 10-12. This mesh, containing approximately 314000 elements and 63000 de nodes, was refined so that it was obtained a good discretization quality of 98%.

The deformations and stresses resulted, after the FE model solving, are shown in figures 11 and 12 respectively. The figures' left-side corresponds to the bump passing and the right-side, to the braking.

The maximal deformations and stresses, also indicated in the figures, show high but normal levels, meaning that this complex part was well designed. The maximal von Mises stresses for the two case studies were 194 MPa (bump) at the damper-support end and 448 MPa (braking) at the caliper's upper fixing element. Comparing these stress values to 950 MPa, the tensile strength of the chosen material (41MoC11 alloy steel), result the safety coefficient values: 8 for bump passing and 2.5 for hard braking. Also, the places where these maximal efforts appear represent indication for the areas that may be subjected to a further shape optimization.

6. CONCLUSIONS

The paper showed a possible way to design, study and optimize a complex mechanism as a car suspension-steering linkage (MacPherson strut and rack and pinion). The authors used a top-down approach, starting from the requirements of the assembly and successively refining and adding components as the design solutions became clearer. The main mechanism dimensions were obtained using very simple 2D models, which permit to judge and interpret easier the

mechanism behavior. After this geometrical and kinematic optimization, more other steps were done, as the multibody study of the mechanism, part and assembly CAD modeling aiming manufacturability, finite element analysis of some important parts and, finally, corrections and tunings of the CAD models.

7. ACKNOWLEDGMENTS

This work, made partly as a graduate projects, beneficiates of the LMS subsidiary in Brasov's support, consisting in study themes, knowledge, suggestions and hardware and software resources for computation. It was intended to be a new step in the co-operation between Transilvania University of Brasov and LMS Romania.

REFERENCES

1. Untaru, M. e.a. - Calculul și construcția automobilelor. (Calculus and Design of Motor Vehicles). E.D.P., Bucuresti, 1982.
2. Gillespie, T. - Fundamentals of Vehicle Dynamics. SAE, Warrendale, USA, 1992.
3. Preda, I. - Inginerie asistată pentru autovehicule (Assisted Engineering for Automotive Vehicles). "Transilvania" University of Brasov Publishing, 1998.
4. Reimpell, J., Stoll, H., Betzler, J. - The Automotive Chassis. Butterworth-Heinemann, 2001.
5. Mitscke, M., Wallentowitz, H. - Dynamik der Kraftfahrzeuge. (Motor Vehicle Dynamics). Springer-Verlag, Berlin, 2004.
6. Enache, V., Preda, I., Vulpe, V., Dogariu, M., Dima, D.S. - Theoretical and experimental research for vehicles' handling improvement. The X-nth International Conference CONAT, paper 1063, Brasov, 2004.
7. Preda, I., Vulpe, V., Enache, V. - Simulation of driver behaviour in cornering manoeuvre. The X-nth International Conference CONAT, paper 1070, Braşov, 2004.
8. Ciolan, Gh., Preda, I. - Dinamica autovehiculelor – Partea I (Motor Vehicle Dynamics – Part I). „Transilvania” University of Brasov, 2008.

VARIOUS ASPECTS REGARDING THE DESIGN OF A GEAR SHIFT SENSOR FOR ROAD VEHICLES

DUMITRU Ilie^{*}, POPESCU Simion^{**}, VINATORU Matei^{*},
POPESCU Traian^{*}, CATANEANU Mihnea^{*}
^{*}*University of Craiova –Romania*
^{**}*University Transilvania Of Brasov*

Abstract: During time there has been a major concern regarding the reduction of fuel consumption, concern which has led the authors of this paper to the idea of designing of an electronic sensor dedicated to the determination of the appropriate gear. This sensor is regarded as part of a complex informational system which would allow the engine to run all the time on the optimum running curves. The sensor is designed based on electronic components and is calibrated for a certain type of gearbox.

Keywords: fuel consumption, gearshift sensor, electronic components

1. INTRODUCTION

Based on the analysis of various engine-running modes and on the already existing data from specific scientific literature, the authors have outlined the fact that the optimum working areas are the ones between maximum torque engine speed and maximum power engine speed. A part from this, the existence of external factors due to the movement of the vehicle imposes the use of the appropriate gear so that the fuel consumption would be at its best possible value. The gear selection is also based on the real vehicle speed (which is influenced by the existence of the sliding phenomenon) and on the right engine speed. Based on all this and also on the constructive characteristics of the engine, the engine range for each gear can be defined between a minimum engine speed (n_{\min}) and a maximum engine speed (n_{\max}), values for which a gear shift is requested, down in case of (n_{\min}) value and up in case of (n_{\max}) one. The picture from below presents how the entire range of speed is covered in case of a theoretical gearbox.

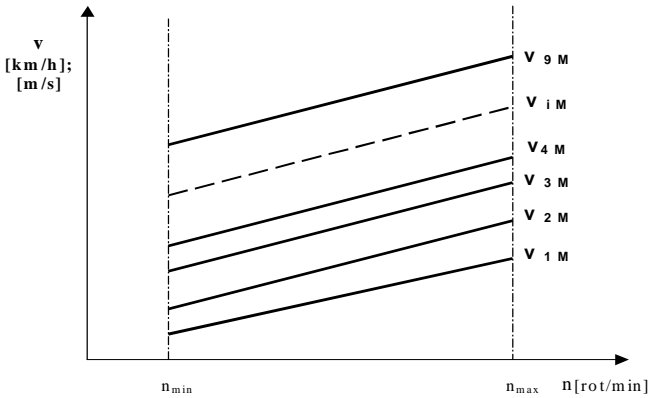


Fig. 1

2. ALGORITHM AND SPECIFIC PROCEDURES

The algorithm consists of:

Input data

- the following are required:

Determination of:

v - vehicle real speed;

M_e - effective engine torque;

T - gearbox gear.

Defining n_{rel} [%] and M_{rel} [%].

Determination of the optimum gear:

The vehicle speed is compared with the limits of the speed range for the selected gear (according with the technical data) and the appropriate shift is indicated on the dashboard.

Checking the optimum engine torque and speed.

The engine speed n_e is compared with the engine maximum power speed n_n and in case then the driver is notified to change it (by means of increasing or decreasing it).

In order to design the informational system that corresponds with the imposed requests and with the results of the mathematical model, the following procedures are necessary:

1. "optimum gear selection" step (ATO)

The logical diagram for selecting the optimum gear is based on comparing the vehicle speed with the defined range values for each gear.

2. optimum engine speed step

If the vehicle speed is within the range value for the gear in case then the procedure for determining the optimum engine speed is initiated.

3. determination of optimum engine speed

It is based on three comparing circuits which compare engine speed with maximum power engine speed and then, if necessary, the signal indicating “accelerate” or “decelerate” is switched on. This step is based on the researches results indicating that the optimum working area for an engine concerning fuel consumption is near to the maximum power engine speed area.

3. ELECTRONIC COMPONENTS FOR THE SYSTEM

The system is based on 0÷10V CMOS circuit analogue.

Comparing circuit (fig. 2) (hysteresis type)

If:

$U_1 < (U_{REF} + \Delta U_H / 2)$, then $U_0 = 0 \text{ V}$ (logic value 0)

$U_1 > (U_{REF} + \Delta U_H / 2)$, then $U_0 = 10 \text{ V}$ (logic value 1),

Hysteresis value is obtained by the right choose for R_1 și R_2 resistors:

$$\Delta U_H = \frac{R_1}{R_2} \cdot U_+$$

For instance $R_1 = 330 \text{ k}\Omega$, $R_2 = 3,3 \text{ M}\Omega$, $\Delta U_H = 0,1 \text{ V}$

Signal adaptor

The signal from vehicle speed sensor (which usually is 0÷12V) is adapted using a 0÷10 V operational amplifier.

R_1 și R_2 resistors are determined based on the vehicle speed sensor voltage. $R_2 = 10 \text{ k}\Omega$ $R_2 = 2U_{TV} - 10 \text{ k}\Omega$

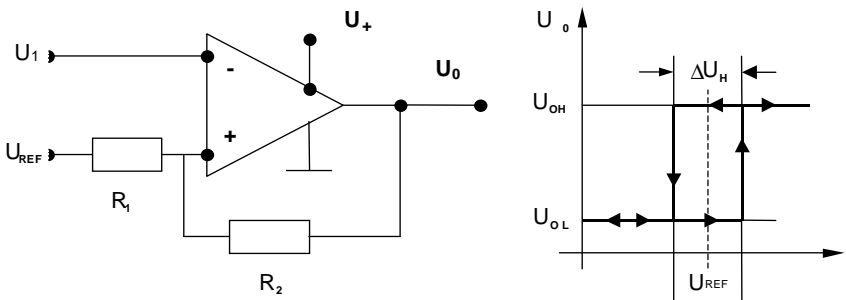


Fig. 2. Electronic diagram for hysteresis circuit

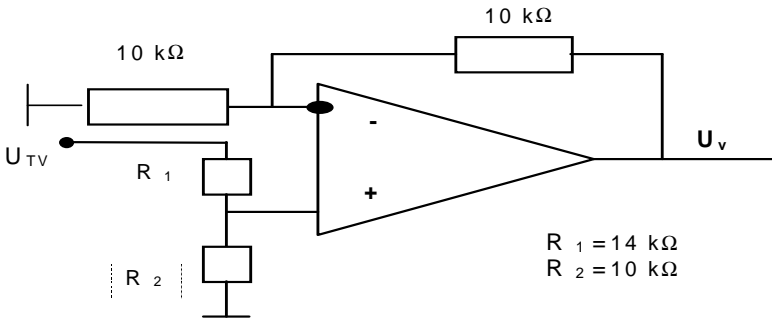


Fig. 3. Electronic diagram for signal adaptor

4. DESIGN OF THE SENSOR FOR GEAR SHIFT

The vehicle speed range limits for different gears $V_{1M}, V_{2M} \dots V_{9M}$ correspond to 0÷10 V voltage range as in fig 4. These voltages U_V are applied to a set of 4 or 5 comparing circuits as fig. 2 for which v_{ref} is determined based on v_{imax} requested by each comparing circuit.

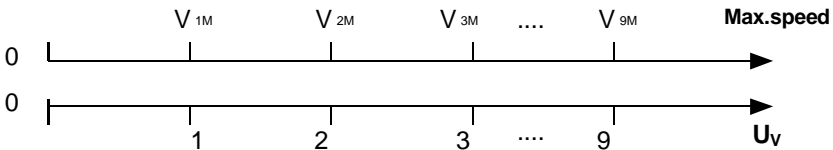


Fig. 4. Relation voltage – maximum speed value for each gear

The gearbox lever can be connected to a set of nine switches $c_1 \dots c_9$ that operate a switch c_i (ground) when the corresponding i gear is selected. The proposed solution for the switches uses two CMOS-4009BT that is manufactured by various companies and has six reversing switches inside. 1 MΩ resistors are connected between the 12 V source and the reversing switch input, therefore when the switch is open, there is a constant 12 V voltage on the input of the reversing switch. If this solution is not used and the input would not be connected like this then there is the risk that an undefined voltage due to induction or other causes is picked up and the value is uncertain (0 or 1).

These resistors are tuned up between 10 kΩ and 1 MΩ based on the type of circuit so that the result is a precise logic signal 0 (0 V) on the output of the reversing switch in case of opened switch.

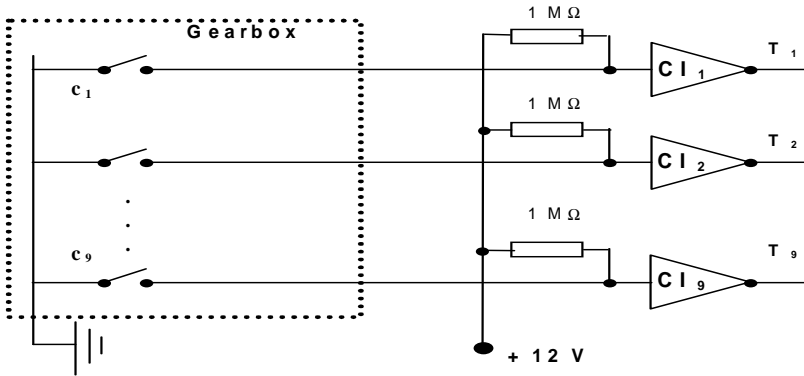


Fig. 5. Electric diagram for „gearbox” module

The result is: $T_i = 0$ ($i = 1 \div 9$) if C_i is open and $T_i = 1$ (corresponds to 10 V) if C_i is closed

Tab. 1

Speed	Output signals											U_p	
	U_{v0}	U_{v1}	U_{v2}	U_{v3}	U_{v4}	U_{v5}	U_{v6}	U_{v7}	U_{v8}	U_{v9}	U_{v10}		
0	0	0	0	0	0	0	0	0	0	0	0	0	
$0 < v < V_{1M}$	1	0	0	0	0	0	0	0	0	0	0	0	0,1 V
$V_{1M} < v < V_{2M}$	1	1	0	0	0	0	0	0	0	0	0	0	1 V
$V_{2M} < v < V_{3M}$	1	1	1	0	0	0	0	0	0	0	0	0	2 V
$V_{3M} < v < V_{4M}$	1	1	1	1	0	0	0	0	0	0	0	0	3 V
$V_{4M} < v < V_{5M}$	1	1	1	1	1	0	0	0	0	0	0	0	4 V
$V_{5M} < v < V_{6M}$	1	1	1	1	1	1	0	0	0	0	0	0	5 V
$V_{6M} < v < V_{7M}$	1	1	1	1	1	1	1	0	0	0	0	0	6 V
$V_{7M} < v < V_{8M}$	1	1	1	1	1	1	1	1	0	0	0	0	7 V
$V_{8M} < v < V_{9M}$	1	1	1	1	1	1	1	1	1	0	0	0	8 V
$V_{9M} < v < V_{10M}$	1	1	1	1	1	1	1	1	1	1	0	0	9 V
$V_{10M} < v$	1	1	1	1	1	1	1	1	1	1	1	1	10 V

5. CONCLUSIONS

The design of a sensor that monitors the selection of the right gear to use has to be made based on an algorithm on specific procedures. The aim is to improve the speed of the vehicle in order to obtain a fuel consumption decrease. The electronic circuit is made using hysteresis comparing circuit in case of comparing modules and 0 –10 0 –10 V logic circuit. For a certain type of gearbox with a definite number of gears the comparing circuits were designed as well as the signal adaptors and of course the main sensor for the gearbox. In this case, the minimum and maximum speed for different gears correspond to 0÷10 V voltage range. These voltages are applied to a set of comparing circuits for which v_{ref} is determined according to the necessary v_{imax} . 1 M Ω resistors have been connected between the 12V source and the input of each reversing switch so that the signal is certain on this input when the gearbox switch is open, otherwise there is a chance of electronic interferences that would make the output result uncertain (0 or 1). These resistors are tuned between 10 k Ω și 1 M Ω according to the type of circuit so that in case of open switch, the output result is 0 logic (0 V).

REFERENCES

1. Dumitru, I., Motoare pentru automobile și tractoare. Metode moderne de optimizare a parametrilor energetici ai motoarelor Diesel cu injecție directă, Editura Universitaria, ISBN: 973-8043-85-9, Craiova, 192 pg, 2005;
2. Guzzela. L., Onder, C., Introduction to modeling and control of internal combustion engine systems, Springer, ISBN 3-540-22274, Zurich, 2005;
3. M. Dekker, Inc., New York, Basel, 2002. F. Zhao, D.Harrington,, Automotive Gasoline

DEVELOPMENT OF A DRIVING CYCLE FOR BRASOV CITY

COVACIU Dinu*, PREDA Ion*, FLOREA Daniela*, CÂMPIAN Vasile*
Transilvania University of Brasov –Romania

Abstract: A driving cycle is a standardised driving pattern, described by means of a velocity-time table. The typical driving profile comprises accelerations, decelerations and stops and it is simulated on a laboratory chassis dynamometer. The European Driving Cycle is the common reference in Europe, but this cycle could not describe satisfactorily the driving characteristics in Brasov. The objective of this paper is to propose a realistic driving cycle for Brasov, based on real data collected using the instrumented vehicle method. The onboard data acquisition equipment was GPS devices and the collected data covers typical roads of the city. It was developed a dedicated software tool for analysing data and for identification of the driving pattern. The process has three steps: first, each track is represented as a collection of point and line entities, with custom metadata attached; second, a speed/time diagram is generated for each recorded track; finally, a representative diagram is created after an automated analysis of all the existing diagrams.

Keywords: driving cycles, NEDC, vehicle dynamics, road traffic, vehicle speed

1. INTRODUCTION

The vehicle's driving cycle is a set of data concerning the speed versus time variation. Usually, the driving cycles are established by organisations from various countries or regions, as standard conditions for testing the vehicles performances, like fuel consumption and emissions level.

Some cycles are established theoretically, like the official European Driving Cycle, other are determined experimentally, based on measurements of driving characteristics and identification of driving patterns. There are two kinds of driving cycles:

- transitory cycles, with many changes in speed;
- modal cycles, with longer periods of driving at constant speed.

As examples, the north-american cycle FTP-72 (also FTP-75) and the european HYZEM cycle are transitory cycles, since the New European Driving Cycle NEDC and the japanese 10-15 cycle are modal cycles.

The standard cycles used in European Union are ECE 15 (also known as UDC – Urban Driving Cycle) for cities and EUDC (Extra Urban Driving Cycle) for extra-urban roads. By putting together four ECE segments and one EUDC segment it results the New European Driving Cycle, NEDC (figure 1).

The main parameters of a driving cycle are: average speed, maximum speed, duration and length. For the composing segments of EUDC, these parameters are listed in table 1.

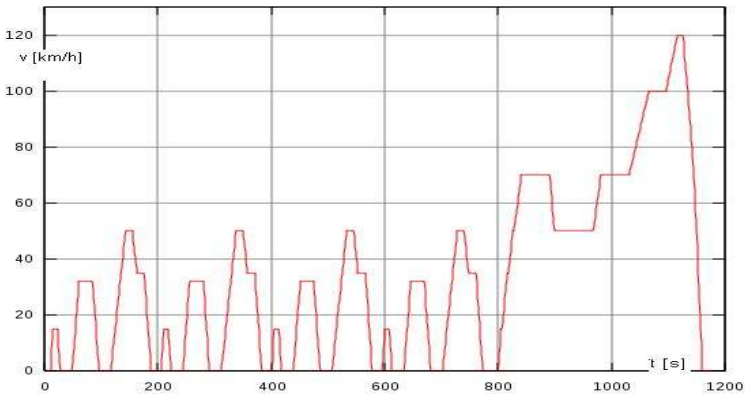


Fig. 1 – New European Driving Cycle – NEDC

Tab. 1

Characteristics	unit	ECE 15	EUDC
Distance	km	4x1.013	6.955
Duration	s	4x195	400
Average speed	km/h	18.7	62.6
Maximum speed	km/h	50	120

2. METHOD FOR A DRIVING CYCLE DEVELOPMENT

Basically, the process of a driving cycle development involves the following steps:

- recording the driving conditions using one or more vehicles equipped with data acquisition devices;

- analysis of data collected in order to describe the driving conditions;
- development of one or more representative patterns for the existing conditions, based on the recorded speeds and sometimes also on accelerations, starting conditions, gear shifts, temperatures or loads.

The data acquisition consists in recording the travel speed on representative roads, followed by a statistical analysis of all data, to identify a typical pattern.

In time, two main methods for collecting data were identified [7]:

- the *chase car* protocol – a chase car installed with a range-finder laser system collects second-by-second speed/time profiles from hundreds of target vehicles assumed to represent typical driving behavior;
- the *instrumented vehicle* protocol – speed sensors are installed on vehicles and the travel speed of each instrumented vehicle is recorded; the vehicle should follow the traffic flow.

A modern version of the instrumented vehicle protocol is represented by the use of GPS devices, encouraged by the down scaling of the electronic devices, price decrease and performance augmentation of GPS receivers [8]. Using GPS devices for road traffic study presents also other important advantages:

- the existence of a very precise and universal time information;
- the existence of three-dimensional position data, that can be derived to obtain other useful information as height, slope or, combining with time data, velocity and acceleration.

The GPS data acquisition method was used for collecting traffic data in Brasov city. First, there were selected representative routes covering almost the entire city area. Different vehicles were driven over all these routes, for many times, during the entire year 2009. Figure 2 shows an example of data (speed and acceleration) collected on the same track. The upper graph shows the evolution of speed and acceleration on time; the lower graph shows the evolution of speed and acceleration on space.

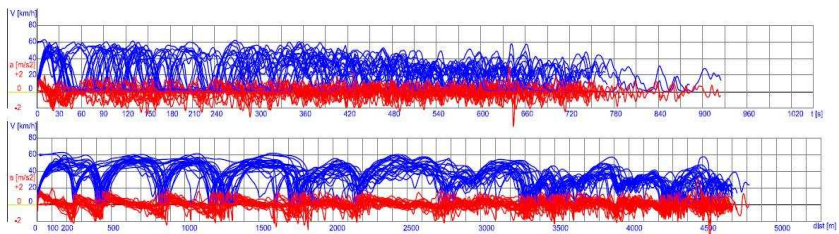


Fig. 2 – Analysis of the vehicle speed (blue) and acceleration (red) for many passings on the same track

It is obvious that is not an easy job to extract a representative driving pattern from the speed/time diagrams. A good method, described also in [5], is to split each diagram in *driving pulses*. For each pulse are calculated the same parameters as for the global cycle (average speed, maximum speed, duration and distance). Then these parameters are statistically analysed. So it is possible to obtain a series of driving pulses, which can lead to a *modal cycle*.

In order to obtain a transitory cycle, we need to calculate the global parameters of the complete driving cycle. Based on data collected for the entire city, the diagrams in figure 3 were plotted. Also, the average and maximum speeds were determined.

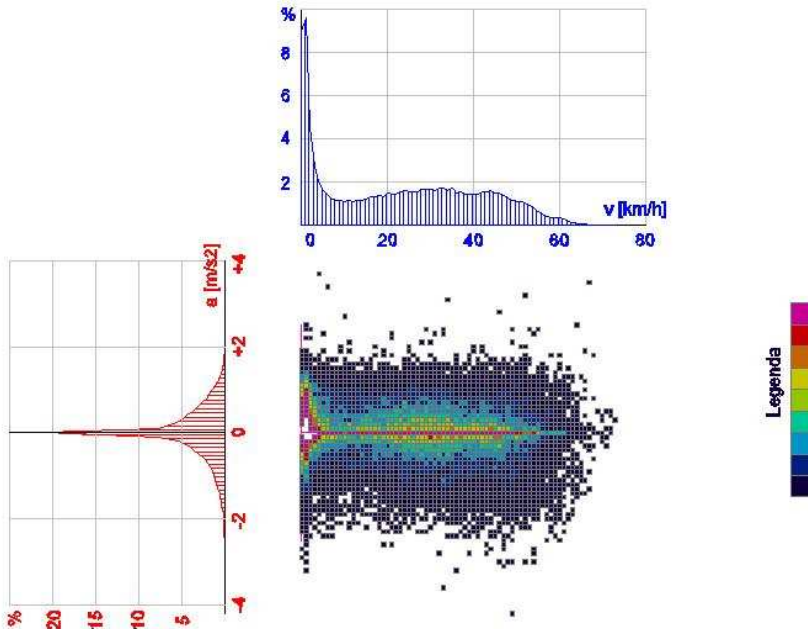


Fig. 3 – Mono- and bi-parametric probability density functions of vehicle speed and acceleration – all urban tracks analysed

All diagrams were created using a custom CAD application, developed in AutoLISP, with the use of extended data associated to the geometric entities (points and lines). The application is in fact a library of functions and global variables. Each function can be called separately, but it depends also by the status of the variables - this mean that a certain order of calling the functions is mandatory.

The first step is to import data from GPS receivers. GPS data are stored in simple text files or gpx files. The content of the selected file is

added in a list - the list is a global variable of the program. Then the track is drawn based on information stored in that list. The geometric elements of a track are points and lines. Each of them has some metadata associated: geographic coordinates, time, speed, acceleration and others.

The next step is to draw the speed versus time diagram for each track. From the diagram it can be extracted the driving parameters. Finally, data from all the speed/time diagrams can be used to calculate the global parameters and to identify the representative driving pattern.

3. BRASOV DRIVING CYCLE

After analysis of all collected data (see figure 2 and figure 3), the parameters determined by experiments, in Brasov, are:

- duration: 710 seconds;
- length: 4.44 km;
- average speed: 22.5 km/h;
- maximum speed: 73 km/h.

The parameters calculated for each of the recorded tracks were compared with the parameters of the global cycle, and also the number and shape of the driving pulses. The speed/time diagrams of the most representative tracks (passings) were used to establish the final proposal of a driving cycle for Brasov city (figure 4).

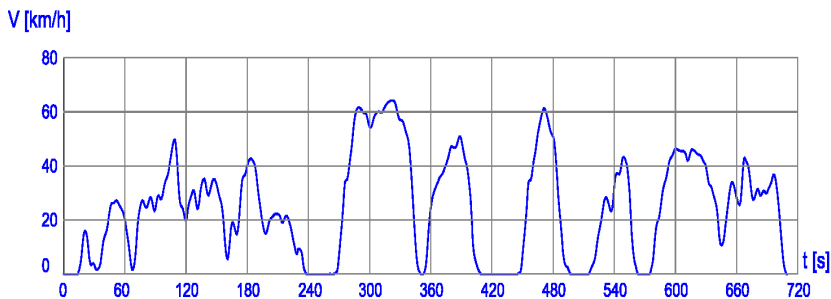


Fig. 4 - Proposed driving cycle for Brasov

The general parameters of the driving cycle were calculated again. The new values are slightly different from those listed above, as effect of the transitory character. The final parameters are:

- duration: 710 seconds;
- length: 4.87 km;
- average speed: 24.7 km/h;
- maximum speed: 64 km/h.

Apparently, there is a big difference between the maximum speed determined previously and the final maximum speed, but we should take into consideration that the maximum of 73 km/h was just a peak value, for all tracks recorded.

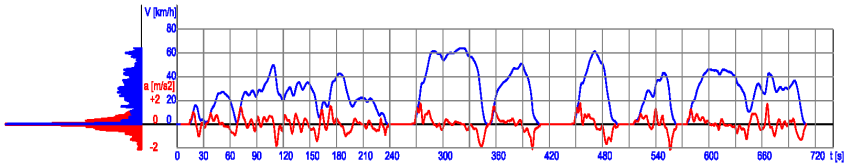


Fig. 5 – Speed and acceleration for the representative driving sequence

For the resulted driving cycle it was calculated the probability density function for speed and acceleration – see the lateral diagram in figure 5. Also the bi-parametric probability density of speed and acceleration may be determined from the original diagrams – figure 7.

Figure 6 shows the similar diagrams for the standard European urban driving cycle (UDC). Comparing the 3D diagram in figure 6 with the 3D diagram in figure 7, it is obvious that the transitory cycle is more realistic than the modal cycle.

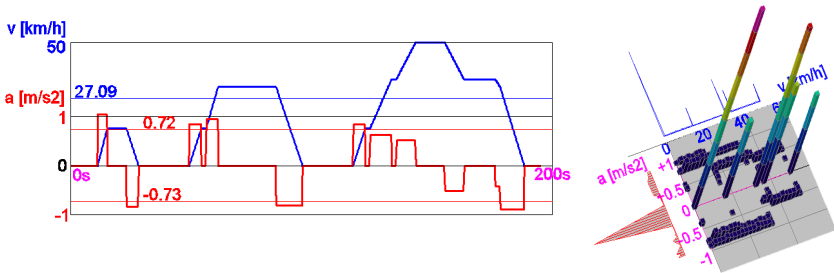


Fig. 6 – Mono- and bi-parametric probability density functions of vehicle speed and acceleration – EDC (European Driving Cycle)

The diagrams on left side of figure 7 represent the probability density of vehicle speed and acceleration for the resulted driving cycle (upper) and for all records cumulated. The diagrams for the single track (the driving cycle) are not so smooth because the number of points is smaller than for the cumulated records. However, the profiles of the diagrams are similar.

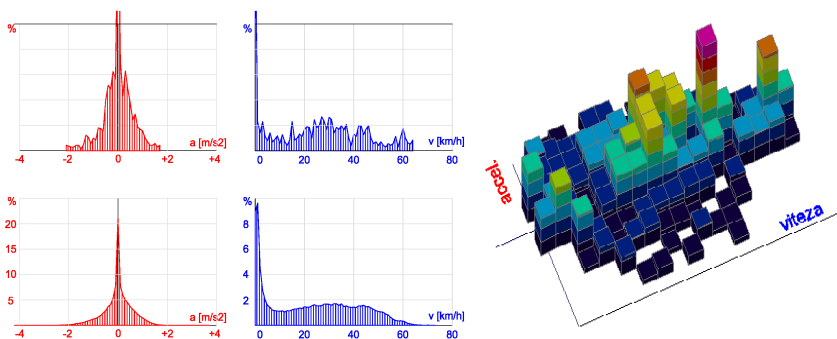


Fig. 7 – Mono- and bi-parametric probability density functions of vehicle speed and acceleration – Brasov Driving Cycle

Finally, a comparison of the parameters of some driving cycles is presented in table 2. The cycles are: the European Urban Driving Cycle ECE 15 (4 times, like in NEDC), the North-American cycle FTP-72, the driving cycle of New York City (NYDC) and the proposed driving cycle for Brasov. Except for the ECE 15 cycle, all other cycles considered are of transitory type.

Tab. 2

Characteristics	unit	ECE 15	FTP-72	NYDC	Brasov
Distance	km	4x1.013	12.07	1.89	4.87
Duration	s	4x195	1369	598	710
Average speed	km/h	18.7	44.6	11.4	24.7
Maximum speed	km/h	50	91.2	44.6	64

4. CONCLUSIONS

A typical driving profile in an urban area consists in a complicated series of accelerations, decelerations and stops. The main goal of the driving cycles is to estimate the emissions level and the fuel consumption for various vehicle models. Since the road traffic is different for different cities, a single driving cycle can not be representative for all cities.

There are significant differences between the parameters listed in table 2. This demonstrates the importance of having a real driving cycle for each area where a certain vehicle model is used.

The driving cycle determined for Brasov city is just a proposal and it is valid for the years 2009-2010. More data will lead us to a more accurate driving cycle. However, significant differences are not expected too soon.

It was demonstrated again that the GPS devices are suitable for collecting traffic data, even in urban areas, where the signal is affected by the buildings. The rate of one record per second is just enough for this purpose, and affordable handheld devices are available on the market.

The data collected for this study can be used also in future traffic studies, in speed analysis or to establish the speed profile of some roads in the city area.

REFERENCES

1. Andre, M., Real-world Driving Cycles for Measuring Cars Pollutant Emissions – Part A: The ARTEMIS European Driving Cycles. INRETS, 2004.
2. Brundell-Freij, K., Ericsson, E., Influence of Street Characteristics, Driver Category and Car Performance on Urban Driving Patterns. ScienceDirect, Elsevier, 2005.
3. Covaciu, D., Florea, D., Preda, I., Timar, J., Using GPS Devices For Collecting Traffic Data. SMAT2008 International Conference, Craiova, 2008.
4. Haan, P.de, Keller, M., Real-world Driving Cycles for Emission Measurements: ARTEMIS and Swiss Driving Cycles, final report. Swiss Agency for Environment, Forests and Landscape (SAEFL), 2001.
5. Liaw, B. Y., Fuzzy Logic Based Driving Pattern Recognition for Driving Cycle Analysis. Journal of Asian Electric Vehicles, Vol.2, No.1, June 2004.
6. Montazeri-Gh,M, Naghizadeh.M, Development of Car Drive Cycle for Simulation of Emissions and Fuel Economy. 15th European Simulation Symposium and Exhibition, ESS 2003 - Simulation in Industry, Delft 2003.
7. Niemeier, D. A., Data Collection for Driving Cycle Development: Evaluation of Data Collection Protocols (part of the CAMP Initiative). Institute of Transportation Studies, University of California, Davis, 1999.
8. Preda, I., Covaciu, D., Florea, D., Ciolan, Gh., Study of In-Traffic Vehicle Behaviour, Based on GPS and Radar Devices. ESFA2009 Conference, București, 2009.
9. Preda, I., Covaciu, D., Ciolan, Gh., Vehicle Dynamics Study Based on GPS Devices. NavMarEdu Conference, Constanța, 2009.

A SHEAR STRESS ANALYSIS OF I-TYPE WELDED SECTIONS (II)

Dan ILINCIOIU¹, Cosmin MIRIȚOIU²

^{1,2}*University of Craiova, Faculty of Mechanics*

Abstract: Based on the analytical model presented in [1], in this paper there are drawn the shear stresses graphics depending on the length x ($x=0..l$, where l is the beam length) for an I-type beam. Those graphics are drawn for all the loading schemes variants presented in fig.3. and fig.4. in chapter 2 and 3 from [1]. In the end there are presented the final conclusions from the shear stress curves.

Keywords: mechanical strength, I-type profile, welding, shear stresses, graphics.

1. INTRODUCTION

For rational design of welded flatbars metallic structures of various types of sections, in addition to the analytical definition of the geometrical characteristics of their section, the strength calculus is essential to highlight if the metallic structure withstands the stresses to which is subjected. Also, in the strength calculus, the shear stresses that occur in the welded joints must be studied to.

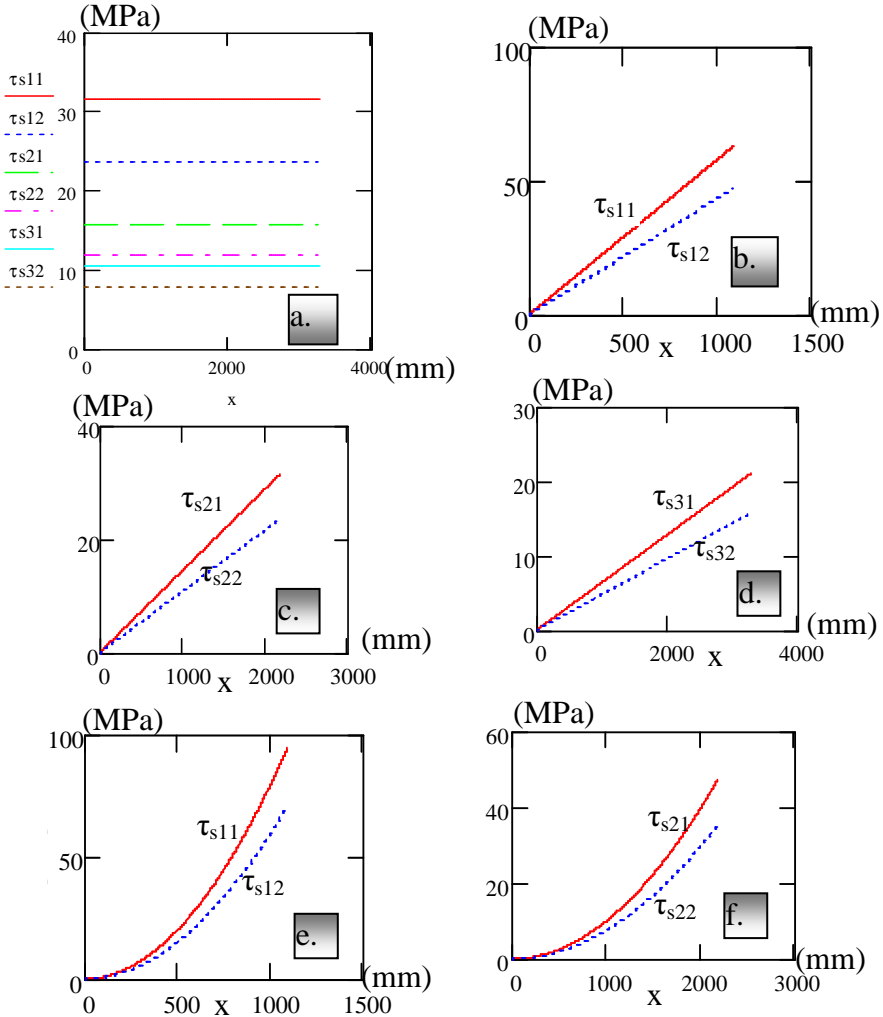
Usually, when welded flatbars metallic constructions are made, the following sections are used: I, U, T, L and their combinations. In most cases, welded flatbars I-type profiles are found to be most used. Therefore, in this paper, we will deal with the study of these types of sections.

Based on the analytical model presented in [1], in this paper there are drawn the shear stresses graphics depending on the length x ($x=0..l$, where l is the beam length) for an I-type beam. Those graphics are drawn for all the loading schemes variants presented in fig.3. and fig.4. in chapter 2 and 3 from [1]. Three values of beam length will be taken into account, depending on it's height (5, 10 , 15 times more of the height). Profile's core thickness will be the one corresponding to STAS I₂₂ profile.

There will also be considered two welding thicknesses of 0,6 and 0,8 of the profile's core thickness.

2. THE SHEAR STRESSES DISTRIBUTION ALONG THE BEAM'S LENGTH

Using the relations (1), (11) and (12) and the shear force calculus formulas from table 1 and shear stress calculus formulas from table 2, from [1], there will be drawn graphics (in fig.1.) which represent the shear stresses distribution along the beam's length.



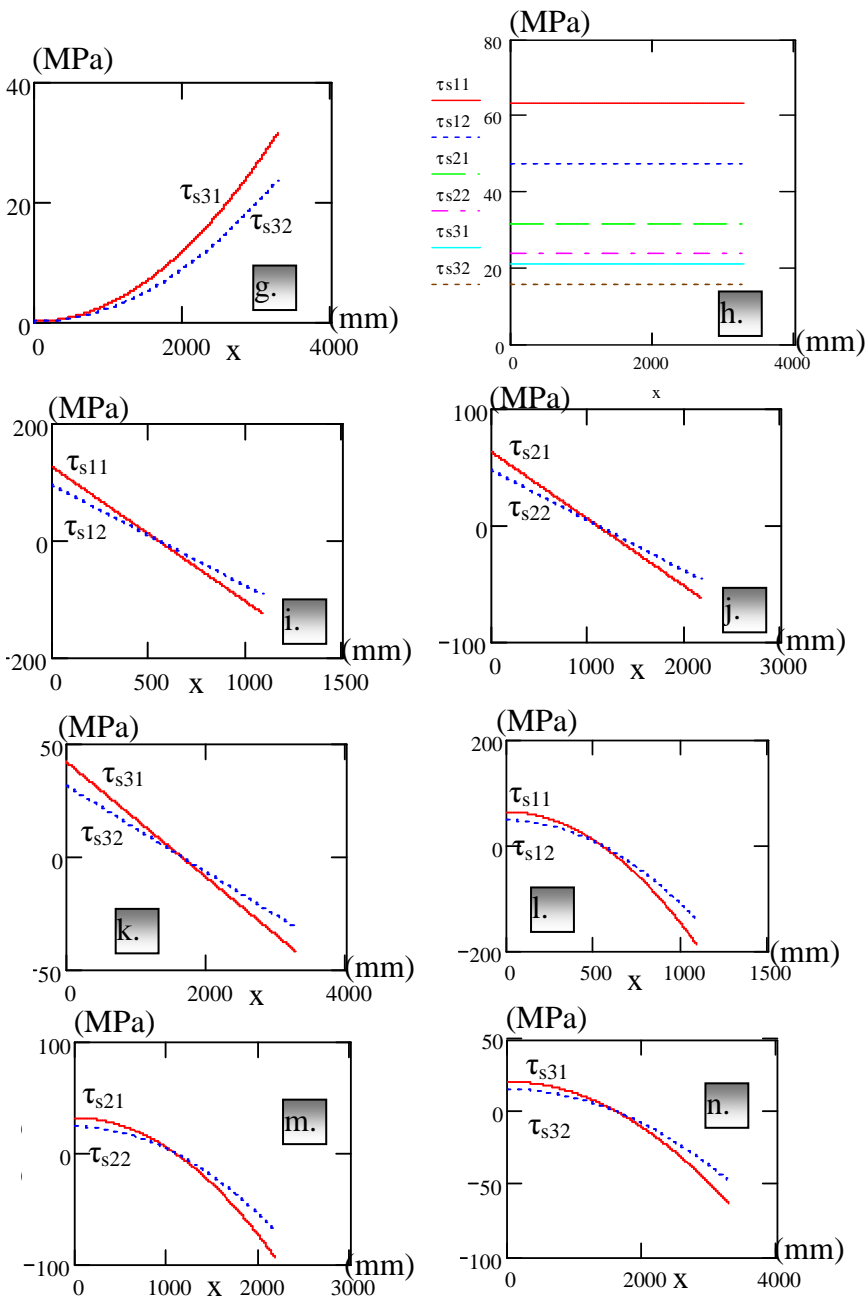


Fig. 1. shear stress distribution along the beam's length

In fig.1.a,...,n, for the shear stresses are used the next symbols: the first index represents the length type (5,10,15 times more of section height), the second index is the used welding type index (0,6 and 0,8 of core's thickness).

3. CONCLUSIONS

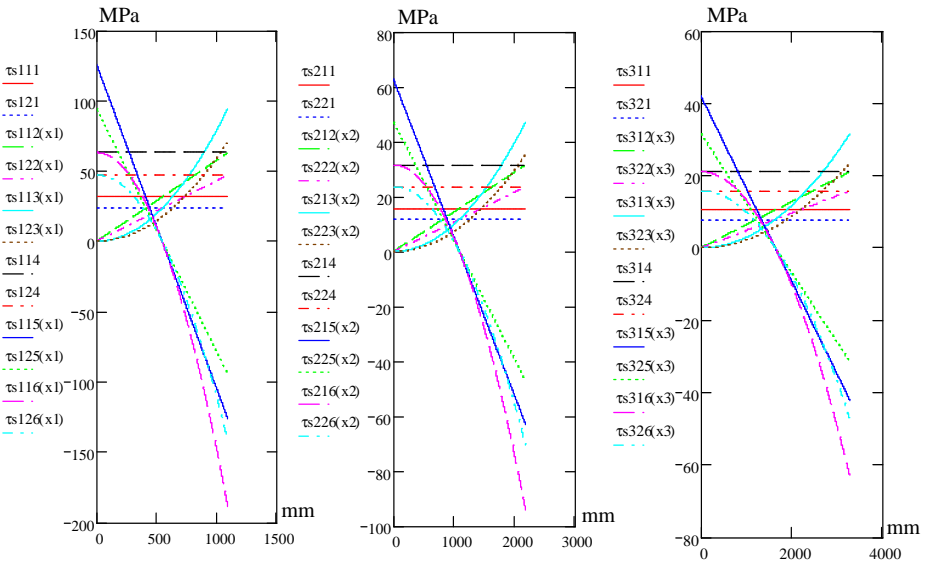


Fig.2. the welding shear stresses curves for each loading variant and length for I_{22} profile

Based on the analytical model presented in [1], in this paper there are drawn the shear stresses graphics depending on the length x ($x=0..l$, where l is the beam length) for an I-type beam. There has been chosen for study the I_{22} section type because it presresents, from the standards, the middle section from the standardised ones.

In fig.2. there are drawn the shear stresses curves for each loading case using the next symbols:

- the first symbol is for the length type (5,10,15 times more of height)
- the second index is for the used welding type index (0,6 and 0,8 of core thickness)
- the third index represents the loading type
- the index for the x length corresponds to the length type (1 is for 5 times more of height, 2 is for 10 times more of height and 3 is for 15 more times of height)

From the two figures, we can extract the following conclusions:

- for the 1 and 4 loading types the welding shear stresses are constant
- for the 2 and 5 loading types, the stresses variation is linear
- the most detrimental case is the sixth loading variant, for lengths 5 time higher than the profile height, the shear stress is almost 200 MPa for the two considered welding thicknesses
- the shear stresses increase with the length scale, except 5 and 6 loading variants

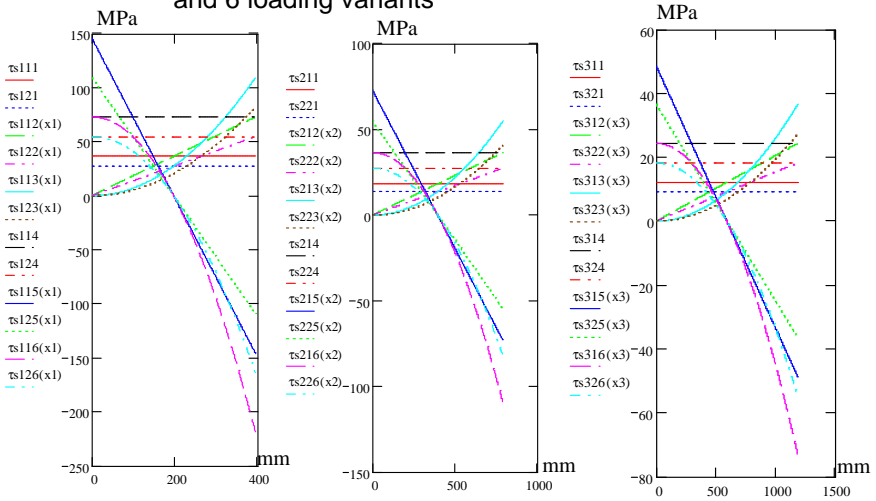


Fig.3 the welding shear stresses curves for each loading variant and length for I_8 profile

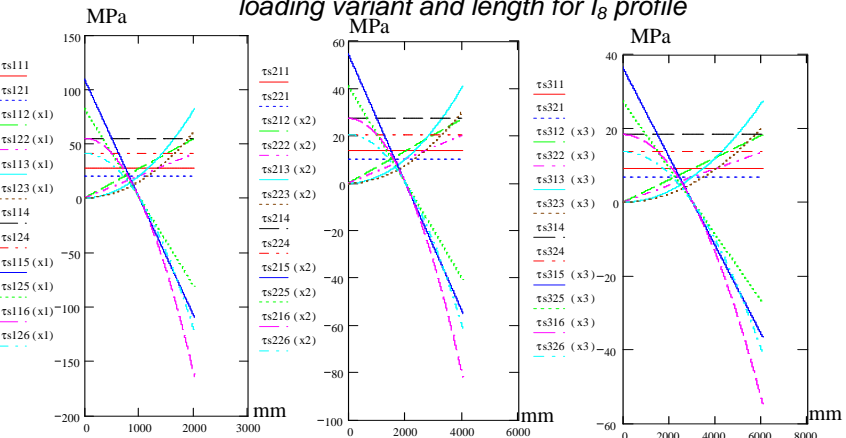


Fig.4. the welding shear stresses curves for each loading variant and length for I_8 profile

In fig.3 and fig.4. there have been drawn the welding shear stresses for I_8 and I_{40} profiles and we can see that the shear stresses curves are the same with the I_{22} shear stresses curves. So the conclusions we have extracted for I_{22} profile can be extended for the I_8 and I_{40} profile (the extreme I-type sections) and for any standardised I-type section.

As a general conclusion, we can see that the shear stresses from the bead decrease with the increase of the section's height.

ACKNOWLEDGMENT

This work was partially supported by the strategic grant POSDRU/88/1.5/S/50783 (2009) co-financed by the European Social Fund- Investing in People, within the Sectoral Operational Programme Human Resources Development 2007-2013.

REFERENCES

1. Ilincioiu, D., Mirițoiu, C., A Shear Stress Analysis of I-type Welded Sections (I), Annals of the University of Craiova, Mechanical Series, Craiova, 2010
2. Ilincioiu, D., Mirițoiu, C., A Geometrical Analysis of INP Rolled Profiles Used at Welded Constructions, The 8th International Conference, Structural Integrity of Welded Structures, pp.58-65, Timișoara 2010
3. Ilincioiu, D., Mirițoiu, C., A Strength Analysis of Welded INP Metallic Profiles, The 8th International Conference, Structural Integrity of Welded Structures, pp.52-58, Timișoara 2010
4. Ilincioiu, D., Mirițoiu, C., Pădeanu, A., Strength of Materials, Universitaria Publishing House, Craiova, 2010
5. Johrend, H., Ilincioiu, D., The Strength of Centrifugal Impellers, Sitech Publishing House, Craiova, 2010

INVESTIGATIONS OF TENSION-TENSION PRE-STRESS EFFECTS ON GLASS REINFORCED COMPOSITE PLATES UNDER THE LOW-VELOCITY IMPACT

KURSUN Ali *, ŞENEL Mahomet **

* Pamukkale University - Turkey

** Dumlupınar University – Turkey

Abstract: In this study, determined of tension-tension pre-stress effects on damage of glass reinforced composite plates under the low-velocity impact. The sample was prepared as a Epoxy-Glass fiber reinforced composite [0 / 90] 2s orientated, 8 layered symmetric composite plate and it's average thickness is 2mm. The sizes of the samples are taken as 140x140mm. The impact tests were conducted with a specially developed vertical drop weight testing machine. After applying 2kN, 4kN and 6kN of unloaded and pre-stressed tension-tension forces, impact tests were made under 23.6 Joule energy. Force-time data obtained from experiments and calculated values were given in forms of graphs.

Keywords: Low velocity impact, composite materials, pre-stress

1. INTRODUCTION

In the literature, impacts are classified as low velocity impacts and high velocity impacts, but there isn't a clear transition between these two categories. Research has shown that there hasn't been a precise result in determining such a transition yet.

Some of the research in the field is on low velocity impacts. They might be thought to be static because they are considered to range from 1 to 10 m/s depending on rigidity of the target, its material features and mass and rigidity of crashing object [1,2].

Most of the studies can be summarized as analysis of effects of impact loads of composites. Almost all of the studies on low velocity impacts in composite structures have been empirical and are generally unstressed or one-way stressed studies. In fact, since the materials were under the effect of multi directional complex loads, such studies are not adequate.

The simplest forms can be seen in airport runways built on composite cages. Even the stationary planes on the runway cause pre-stress on the composite cage.

This pre-stress will in time lead to a fall in strength of composite structure due to following loads and finally end up with collapses on the runway. In this respect, it can be seen how inadequate the studies on unstressed and one-way pre-stress materials are [3–5].

In order to obtain real research conditions, such experimental studies should be carried out on the sample that apply two-way pre-stress on the sample, but this requires a specially designed test machine. Such a study was conducted by B. Whittingham et al [6] specially designed test machine.

They studied the effect of Pre-stress on carbon-fibred/epoxy laminated plates and their response against low velocity impact. Mitrevski et al [7], by using impact tips with various geometric shapes on carbon-fibred / epoxy layered samples under pre-stress, determined empirically the force-time change and the energy amounts which samples consumed.

Thus, they analyzed the effects of impact tips with semi-spherical, conic and jagged geometry. They, then, compared their experimental results with the analytic impact results that Sun and Chattopadhyay [8] had obtained from the pre-loaded samples. Robb et al [9] analyzed empirically the impact behaviors of carbon / epoxy and glass/polyester composites.

In their studies, they saw that while the pre-stress tension applied on the samples increased, contact time of impactor to the sample decreased.

On the other hand, they couldn't see an effect of maximum force on the damage area. Chui et al [10] researched the effect of low-velocity impact on pre-stress quasi-isotropic grafit/epoxy laminated composites plates.

The tests were applied under various energies. They obtained maximum force at tension Pre-stress. As a result, maximum damage occurred under this Pre-stress.

In this study, after applying 2kN, 4kN and 6kN of unloaded and pre-stressed tension-tension forces on the samples, impact tests were made under 23.6 Joule energy. Also, studies were conducted with the

same impact energy without applying any pre-stressed tension and the results were compared.

2. EXPERIMENTAL STUDY

2.1. SAMPLE

In the study, the sample was a composite material composed of unidirectional E-glass continuous fibers and epoxy resin. The samples were prepared by hand lay-up technique at $[0/90]_{2s}$ orientation angle with symmetric 8 layers. Their average thickness was 2mm. For making composite panels, an epoxy matrix based on CY225 resin and HY225 hardener was selected.

The composite layer was produced at 120°C in 3 hours under 0.25MPa pressure, and then it was cooled down at room temperature under the same pressure. The samples were prepared by cutting them $140\times 140\text{mm}$. In order not to damage the composite plates by grips and in order for better clamping; $10\times 100\text{ mm}$ metal sheets were used in the grips of the samples.

2.2. TEST MACHINE

For impact tests, many test techniques are used. Especially to characterize the impact behaviors of composite materials, there isn't a standard test technique. In the literature, there isn't a widespread technique that has been accepted by different countries, researchers or organizations, which causes handicaps while comparing the results obtained from different resources. As such, coming up with a suitable model for impact responses of composite materials becomes impossible.

Despite these obstacles, in order to determine impact resistance of composite materials, several authentic test machines are currently used throughout the world.

For impact test studies, a special test machine was designed in the university laboratory based on weight drop from 5m height. 5m height was sufficient for velocities of 10m/sec and less; and this velocity range corresponded to the velocity projected for low-velocity impacts [1]. Impacts at higher velocities than these are written as high-velocity impacts in the literature [2].

The experiment apparatus is composed of six main parts; namely, L-shaped bottom plate, weight drop tower, elevator engine, control unit, brake system and data collection unit.

Figure 1 shows the general appearance of low-velocity impact test apparatus. The L-shaped bottom plate was made of 50mm thick steel with hydraulic (for pre-stress) and pneumatic (for brake) pistons, sample holders and tower connections.

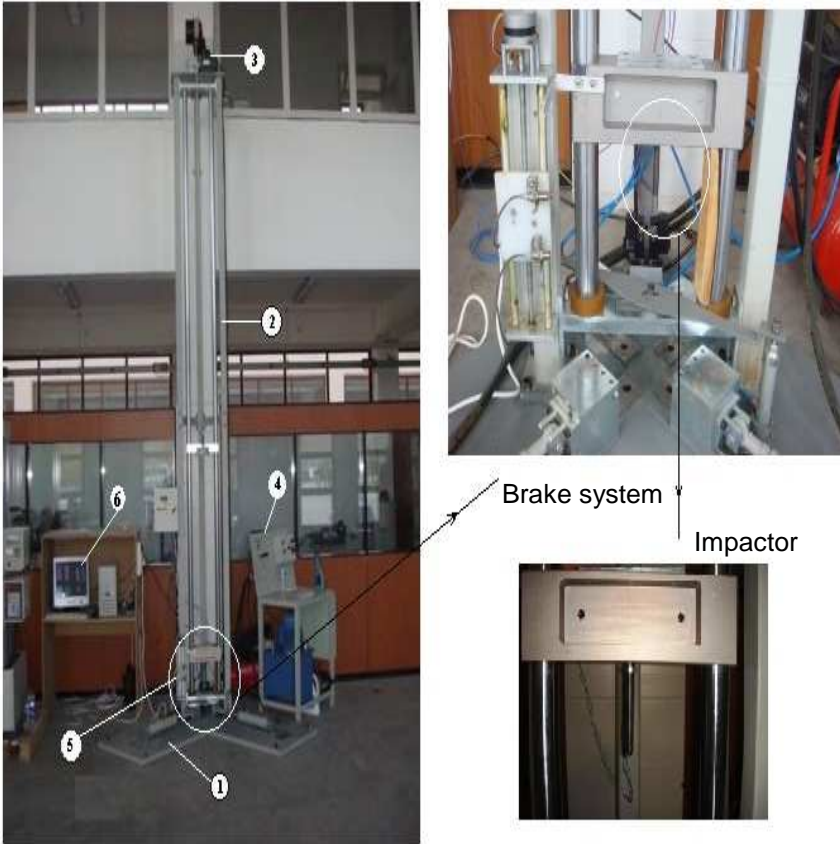


Fig. 1- Drop-weight test machine 1) L-shaped bottom plate, 2) Weight drop tower, 3) Elevator engine, 4) Control unit, 5) Brake system 6) Data collection unit.

Impactor and the weight was bearing to the tower columns of weight drop tower. A piezoelectric force sensor (PCB Quartz ICP Force Sensor (Model 201B04)) placed between the weight and impactor gave the relation between force and time during impact as a diagram with the help of Labview program. The data were transferred to computer from the sensor and thus graphs were obtained to be analyzed.

There was also a sliding electro magnet on the tower to take the weight to desired distance. A control unit near the test machine controlled the magnet and the hydraulic pistons. The brake system was used to prevent a second impact on the sample after the impactor hit the sample and bounced.

This system prevents multiple impacts on sample. If the impactor rebounds after the impact, the brake system turns on and catches impactor immediately. Two optic sensors, a flag, weight holder, two pneumatic pistons, a solenoid valve and a compressor are used in the system (Figure 2).

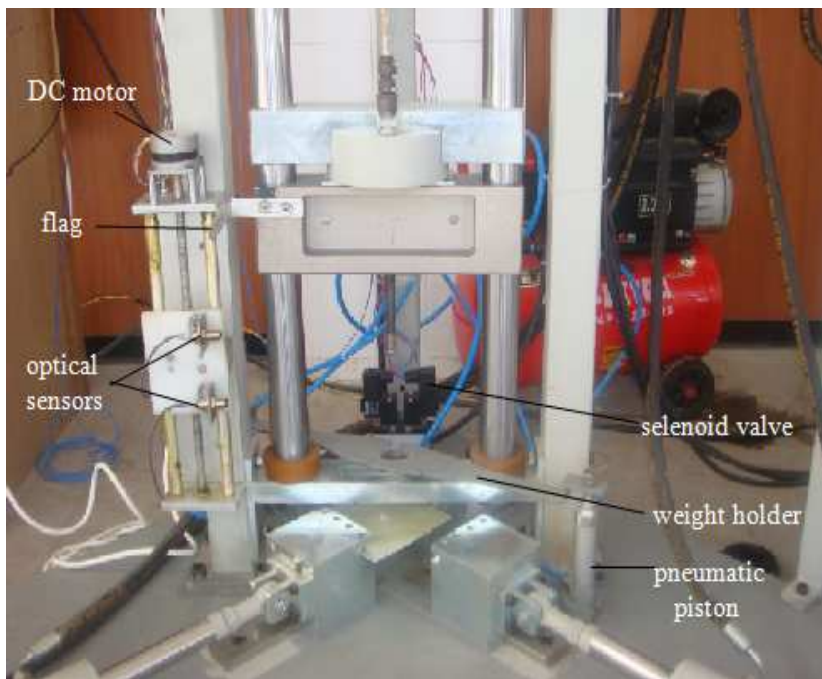
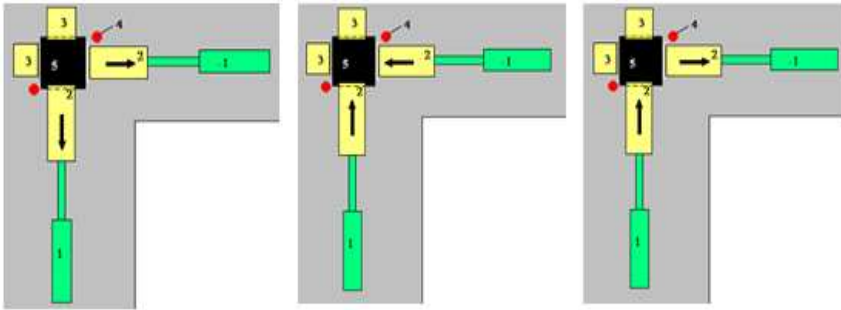


Fig.2 - Brake system

Dynamic impact tests were conducted on a specially designed test machine in such a way to enable pre-stress on two axes. Pre-stress could be achieved on two axes as tension-tension, compression-compression and tension - compression (Shear). By altering the position of the hydraulic rams the desired loading condition is achieved. Figure 3 shows top view of drop weight test rig and its component.



Tension/Tension Compression- Compression Tension/ Compression

Fig. 3 - Top view of drop weight test rig with various preload combinations. 1) Hydraulic pistons 2) Moveable grips, 3) Fixed grips, 4) Cylindrical bars, 5) Sample

The impactor, which was perfectly rigid, had a 12mm diameter hemispherical tup nose. It was located to bottom of the drop weight. Force sensor was mounted between impactor and drop weight (Figure 4). It was calibrated prior to testing. Total mass of impactor used was 3.1 kg.

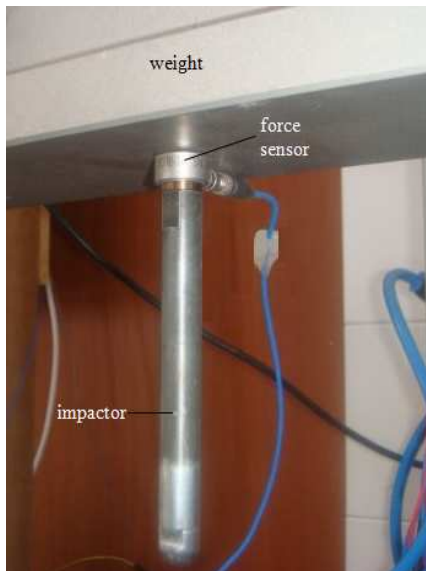


Fig.4 - Force Sensor

2.3 TEST PROCEDURES

A test procedure was developed to determine maximum force, collapse and change in absorbed energy due to the effect of pre-stress on composite plates under the effect of low-velocity impact empirically. Before testing, every sample was checked for structural deformation or dimensional change.

In terms of damage, it is crucial during experiments to locate the impactor right on the centre of the sample. Therefore, the centre was marked on every sample and thus locating the impact right on the centre of the sample was achieved. Later, pre-load was done by hydraulic pistons from control system. Calibration of brake system was adjusted by using optic sensors to contact the semi-spherical impactor to the sample. After completing calibration, the mass was raised to desired height (80cm) by using electro magnet and at the same time calibration adjustments were saved onto the control system. Switching the electro-magnet unit off, the mass was dropped on to the sample. The data obtained from force sensor were saved on the computer to reveal the graphs. PCB Quartz ICP Force Sensor (Model 201B04) was used as force sensor and its calibration had been done before the tests.

3. RESULTS AND DISCUSSION

Impact tests were carried out at 23,6J impact energy after applying 2kN, 4kN and 6kN loaded and unloaded pre-stressed tension-tension forces. In the test results, zero pre-load and pre-stress values were compared to reveal the differences.

Figure 5 shows force-time graphs obtained from the experiments and their comparison. Maximum force was obtained while 6kN. As pre-stress increased, so did maximum force. According to the graphs, while unloaded it reached maximum force, but there was no puncture in the sample; however, the sample was punctured at lower forces due to the effect of pre-stress.

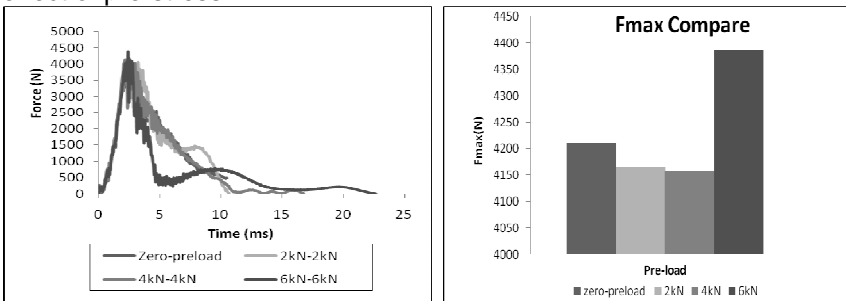


Fig.5 - Force-time graphs and their comparison

Figure 6 shows force-collapse graphs obtained from the experiments as zero-pre-load and pre-stress. The contact of impactor to the sample happened in a very short time. According to the results obtained from the graphs, as pre stress increased, so did deformation. During calculations, it was accepted that there was no friction between impactor and sample, that g-force was ignored during impact, and that the impactor was rigid.

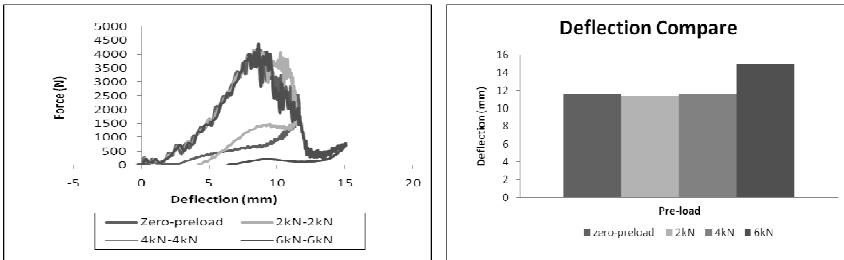


Fig.6 - Force-deflection graphs and their comparison

Figure 7 shows energy-time graphs obtained from experiments and their comparison. Impact energy for every experiment was taken as constant 23.6 J. The graphs show impact energy-time curves and the comparison shows absorbed energy values. In the impact test for unloaded sample, it is seen that the sample wasn't punctured (Fig. 8).

Here, the increase in the absorbed energy means that the impactor went deeper into the sample. It is seen in energy comparison that as pre-load increased, so did absorbed energy values. Although the sample was punctured completely during 4kN and 6kN pre-load, it wasn't punctured completely during 2kN, but damage occurred at the back surface of the sample (Figure 8).

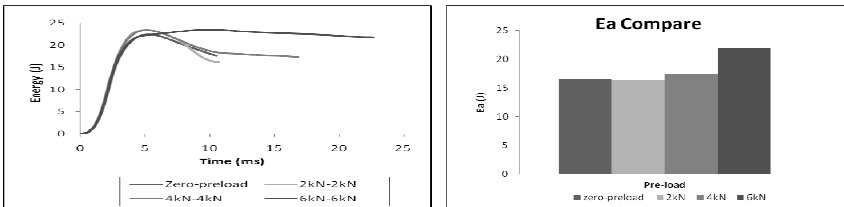


Fig.7- Energy-time graphs and their comparison.

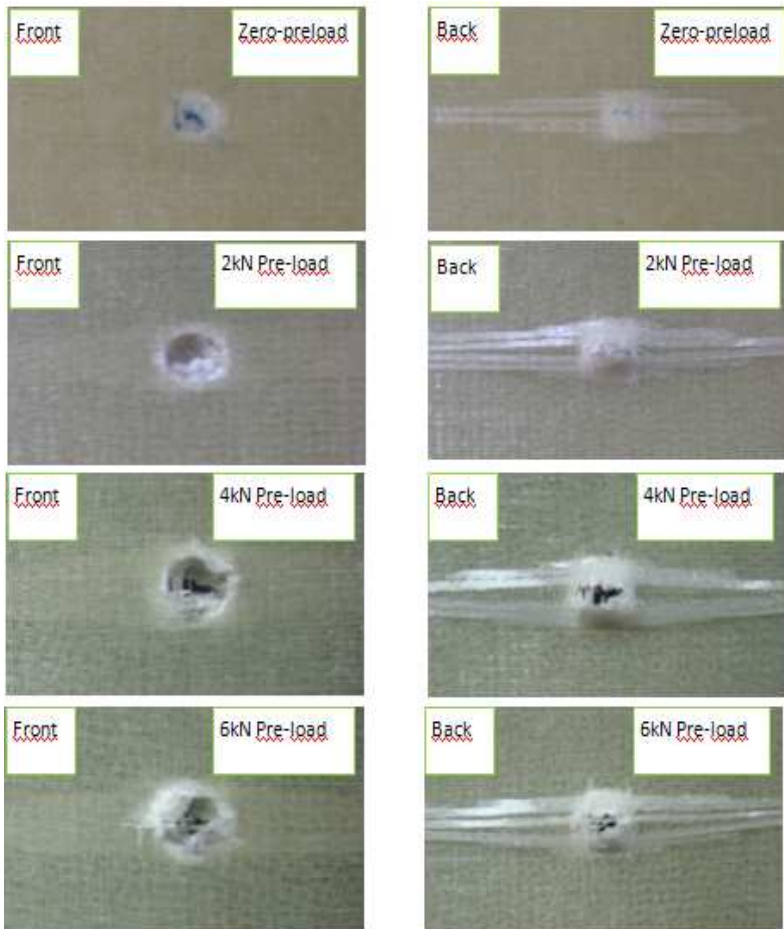


Fig.8 - Images of damaged specimens

4. DISCUSSION AND CONCLUSIONS

According to the data obtained from the experimental studies, rigidity of the material increases due to the effect of pre-stress. Therefore, due to the fall in the flexibility of the material, energy leads to more damage.

As a result, it is seen that tension-tension pre-stress affects strength of composite material enormously. Designers should take pre-stress into account in their composite designs.

5. ACKNOWLEDGMENTS

The authors would like to thank The Science and Technological Research Council of Turkey (TUBITAK) for the financial support of this work.

REFERENCES

1. Sjoblem, P.O., Hartness, J.T. and Cordell, T.M., On low velocity impact testing of composite materials *J Compos. Matei* , 22, 30-52, (1988).
2. Shivakumar, K.N., Elber, W. and IUG, W., Prediction of low velocity impact damage in thin circular laminates, *AIAA J*, 23(3), 442-449, (1988).
3. Abrate, S., Impact on laminated composites. *Appl. Mech. Rev.* Vol:44(4), p:155–90, (1991).
4. Abrate, S., Impact on laminated composites: recent advances. *Amer Soc Mech Eng Vol:47(11)*, p:517–44, (1994).
5. Abrate, S., Impact on composite structures. Cambridge University Press, (1998).
6. Whittingham, B., Marshall I.H., Mitrevski T., Jones R., The response of composite structures with pre-stress subject to low velocity impact damage. *Composite Structures* 66 p.685–698, (2004).
7. Mitrevski T., Marshall I.H., Thomson R.S., Jones R., Low-velocity impacts on preloaded GFRP specimens with various impactor shapes. *Composite Structure Vol.76*, 2009-217 (2006).
8. Sun C.T., Chattopadyay S., Dynamic Response of Anisotropic Laminated Plates Under Initial Stress to Impact of a Mass. *J. Appl. Mech.* Vol. 42, pp 693-698, (1975).
9. Robb M.D., Arnold W.S., Marshall I.H., The Damage Tolerance of GRP laminates under biaxial prestress. *Composite Structures* 32:141-9, (1995).
10. Chiu, ST., Liou, YY., Chang, YC., Ong. CL., Low velocity impact behavior of pre-stressed composite laminates. *Mater Chem Phys Vol:47*, p:268–72, (1997).

RESEARCH REGARDING THE ROUGHNESS OF THE SURFACES TITANIUM UNALOYD MILLING

Marius ZAMFIRACHE

University of Craiova, Faculty of Mechanics

Abstract: This paper presents the results of some experimental research regarding the roughness of the surfaces for titanium unalloyd: Ti35, T40, Ti60 in the case of the milling process.

Keywords: Titanium unalloyd, milling, roughness surfaces, linear functions, analysis regression.

1. INTRODUCTION

At present in technically literature a great number of scientific works appeared. On this way, diverse law and theories was completed or others were discovered.

We refer here to these discoveries related to the part processing using different classical and modern technologies; all of this can conduct to the productivity augmentation, reducing the production cost, a high quality of the products and to the improvement of the work conditions.

The common effort of the researcher and the specialists tend to the obtaining of the competitive products that can easily come in the international changes.

Today, on the world market win that one witch can realize in a shortest possible time, with minimum expenses, high quality products and with reduced retail costs.

In order to apply in production, to complete and improve, to contribute at the rise of the technical and scientific level of our enterprises, and to improve and modernise the applied technologies, all of this challenges must be known by the students and the actual and futures engineers.

The important development of the aero spatial constructions program, and the implants in medical technique has determinate and finally conducted to the whole series of the new materials with a high resistance, with a very good behaviour in use and with a great compatibility with a human body, with a high resistance to the salesman, and in the same time very easy.

Due to the low thermal conductivity during the machining, after 10...20 seconds, the cutting temperatures rise very much, more than 1000 °C.

In this case the technological process can take place in a dangerous environment, equally for the human operator, cutting tool, and the machine tool.

The absence of the cutting fluid can conduct at the ignite of the titanium fine chips (at the high speed), a fact which determinate special security conditions.

The paper presents the study of the cutting system influence upon the roughness of the processed surfaces.

2. EXPERIMENTAL DATA

The chemical characteristics titanium unalloyed and presented in table 1.

Table 1

Titanium unaloyd	Ti %	Fe %	C %	H2 %	N2 %	Si %
T35	99.5	0.12	0.08	0.05	0.015	0.04
T40	99.4	0.12	0.08	0.05	0.015	0.04
T60	99.2	0.30	0.08	0.08	0.015	0.04

In table 2 there are presented mechanical propertis of the researched materials.

Table 2

Titanium unaloyd	Tensile streangh (MPa)	Brinel Hardness (HB)
T35	350-450	min120
T40	400-550	min150
T60	550-750	min170

It was used the forward milling cutter type R245-0.63 P22-12H Coromant with d=60mm, z=6 teeth the plates being mechanically fixed.

The metallic carbide plates are type SPUN 12 03 08 K10.

The geometric parameters of the considered tools are characterized by: $\alpha = 10^\circ$, $\gamma = 5^\circ$, $\lambda_T = 4^\circ$, $\chi_r = 75^\circ$, $\chi_r^i = 15^\circ$.

The levels of the natural variants v, f, a_p , r_n and τ are in geometric progression.

Eighteen experiments were realized by using the special methodology of the planning of experiments.

The levels of the variables are presented in table 3.

Table 3

Symbol	Code	-1	0	+1
v(m/min)	X ₁	40	60	90
f(mm/d)	X ₂	0.05	0.08	0.1
a _p (mm)	X ₃	0.5	0.7	1
r(mm)	X ₄	0.8	1.2	2

It is chosen as a model (to determine the roughness) a polithropical function dependent on the chipping parameters:

$$Ra = a_0 \cdot v^{a_1} \cdot f^{a_2} \cdot a^{a_3} \cdot r^{a_4} \quad (1)$$

During the cutting process, there was used a cutting emulsion liquid of the PE5EP type

3.ANALYZING THE EXPERIMENTAL DATA

In order to measure the roughness of the considered Surf Test 201.

The measurements are shown in table 4: Ra(μm) the roughness surfaces of titanium T35, T60 milling.

Table 4

No.exp	Cod levels values				Ra(μm)	
	X1	X2	X3	X3	T35	T60
X _j						
1	-1	-1	-1	-1	1.8	1.7
2	+1	-1	-1	+1	2.0	2.0
3	-1	+1	-1	+1	2.4	2.2
4	+1	+1	-1	-1	2.3	2.1
5	-1	-1	+1	+1	2.1	2.0
6	+1	-1	+1	-1	2.0	2.0
7	-1	+1	+1	-1	2.5	2.3
8	+1	+1	+1	+1	2.2	2.1
9	0	0	0	0	2.5	2.2
10	0	0	0	0	2.4	2.2
11	0	0	0	0	2.6	2.3
12	0	0	0	0	2.5	2.2

For example, the elements characterized the Ra functions are presented regression indicators are shown in table 5 and in table 6.

Table 5

3.1. PROGRAM FOR DETERMINING THE REGRESION FUNCTIONS

Initial data:

Studied process: miling

Non -dependent variables: $x_1=v$;

Non-dependent variables $x_2=f$;

Non-dependent variables: $x_3=a$

Non-dependent variables $x_4=r$

RESULTS OF THE REGRESSION ANALYSIS

$R^*=0.659 < 1$ == Adequate model.

Significant coefficients

$R_0=20.69 > 1$ == significant variable

$R_1=0.24 < 1$ == non-significant variable

$R_2=6.07 > 1$ == significant non.variable

$R_3=0.04 < 1$ == non significant variable

$R_4 < 0.01 < 1$ == non significant variable

No. exp	Values(Ra)		Errors	
	Meas.	Calc.	Abs.	Rel.
1	2.2	2.181	0.02	1.53
2	2.0	2.038	-0.04	-3.79
3	2.4	2.233	0.17	6.96
4	2.3	2.928	0.37	16.18
5	2.1	2.406	0.29	16.18
6	2.0	2.303	0.10	6.96
7	2.5	2.802	-0.10	-3.79
8	2.2	2.462	0.04	1.53
9	2.5	2.709	-0.21	-13.70
10	2.6	2.709	-0.31	-21.82
11	2.6	2.709	-0.11	-6.60
12	2.7	2.709	-0.11	-6.60

Using computing REGS programs the following functions were determined:

$$Ra = 2.647 \cdot v^{-0.161} \cdot f^{0.806} \cdot a^{0.440} \cdot r^{0.019} \quad (2)$$

(roughness surfaces titan T35 miling)

In order to determine the rougness of the considered Surf Test SJ 201(fig.1, exp.2)

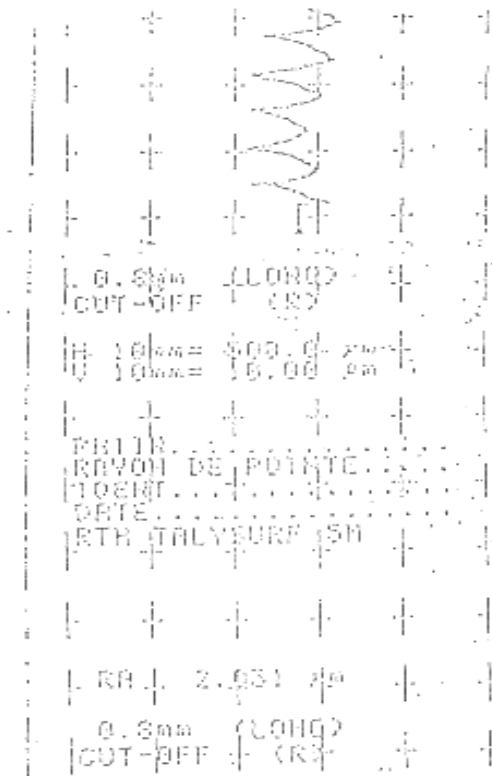


Fig.1

4.CONCLUSIONS

Roughness, as a characteristic factor of surface is determined by the parameters of the cutting system, the geometry of the tool, the material structure, the rigidity of the technological system

In most cases, every SA-MP couple and for every Ra value the f,v, r parameters are significant variables, the cutting depth ap is determined and the cutting velocity has a minimum influence (R2>R1>R3>R4).

The influence factors over the Ra values are: the advance, the cutting velocity, the radius, the cutting depth.

REFERENCES

1. Gheorghe, M., Stancescu, C., Draganescu, F., *Algorithm and computer program to determine multiple variables regression functions*, B.I.P., Bucharest., p.176-189, 1985.
2. Minciu, C., Strajescu, E., Zamfirache, M. , The cutting capacity of the turning tools at the titan alloys machining , University of Maribor-Slovenia, Faculty of Technical Sciences, 26 oct., 1994.
3. Zamfirache, M., *Machinability of titanium alloys by turning*, University Publishing Craiova, 1996.

A STRENGTH ANALYSIS FOR A METALLIC BRIDGE TRUSS STRUCTURE

Cosmin MIRIȚOIU¹, Alina IOVAN²

¹ University of Craiova, Faculty of Mechanics

² University of Craiova, Faculty of Mathematics and Informatics

Abstract: In this paper are shown two methods of stress and strain calculus, different from the 'classic' methods from the 'Strength of Materials', for a metallic bridge truss structure. The first method is analytical, known in recent literature as the 'direct stiffness method', and there are presented step by step the stages and the obtained results by its usage. The second method uses the ANSYS finite element analysis program. There are presented the steps and the results obtained. In the last chapter, are shown the conclusions obtained by using these two methods.

Keywords: trusses, stress, strain, finite element analysis, stiffness matrix

1. INTRODUCTION

The trusses are highly used in metallic constructions, in many variety of forms, representing rigid and economical structures from the material usage point of view.

The trusses are made of bars, considered jointed in nodes, the bar axes being in the same plane. These structures are subjected to bending, the loading is made only in nodes and in the bars there are only axial stresses.

To design rational and economical truss structures, we must follow some considerations:

- the truss structure must have less nodes, because many nodes lead to material and labor expenditure
- the bars subjected to compression must be short
- we must avoid small angles between lattice and base, they must be near 45° (between 30 and 60°)

From the strength calculus point of view, obtaining the nodes displacement, the bars strain and stress under external loading show interest.

In this paper, there are presented two variants of strength calculus for a metallic bridge truss structure that has loadings only in nodes. In fig.1, it is shown a general truss structure.

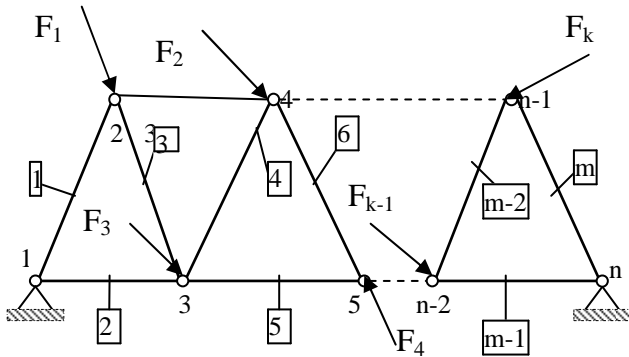


Fig.1. Truss structure with m bars and n nodes

2. STRESS AND STRAIN CALCULUS

For the strain and stress calculus, there are presented two methods:

- method 1: direct stiffness method
- method 2: finite element analysis

The analysed metallic truss structure is presented in fig.2. We observe that it is compound of 11 bars (elements) and 7 nodes. The loadings are nodal, the two vertical forces from nodes 3 and 5 named F_{3y} , F_{5y} . The bars are characterised by length ' l ' and the transversal section area ' A '. The structure is made from steal S275JR.

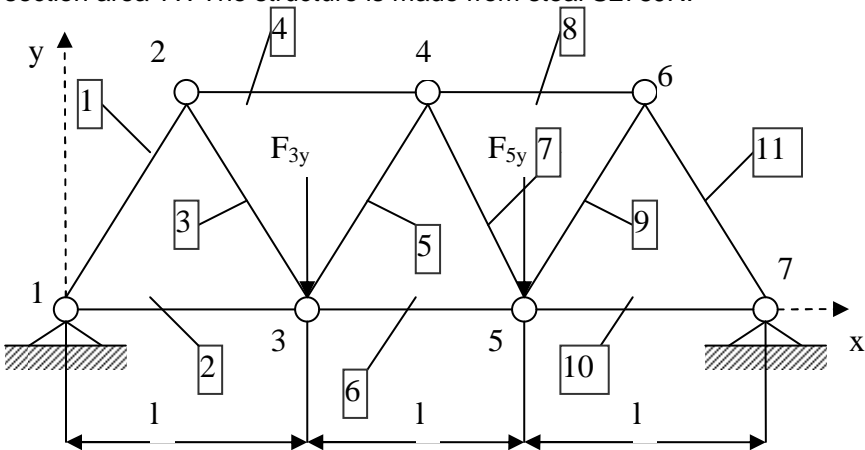


Fig.2. The analysed bridge truss structure

2.1. METHOD 1

To apply this method, we must follow the steps presented below. In some equations, we refer to element 'e' which is one of the 11 bars of the truss structure.

2.1.1. REFERENCE SYSTEMS. NOTATIONS

There is considered two reference systems: an overall system marked with XY and a local reference system marked with xy, for each element. These are presented in fig.3.

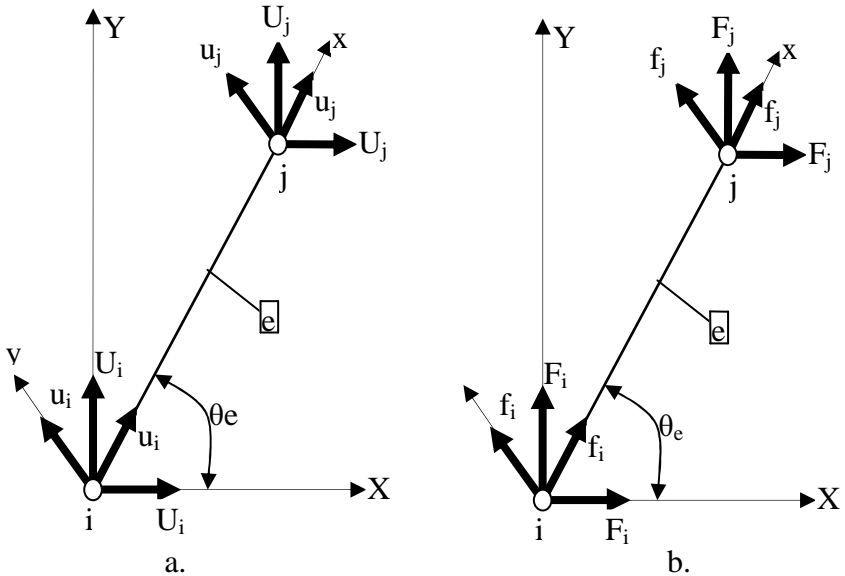


Fig.3.a,b: highlighting the two reference systems for an element 'e', the displacements and forces from nodes 'i', 'j' in both local and global coordinate systems

Further notations are introduced:

- $\{u_{ix}, u_{iy}\}^T, \{u_{jx}, u_{jy}\}^T$: the displacement vector from node 'i' and 'j' in local coordinate system xy
- $\{U_{ix}, U_{iy}\}^T, \{U_{jx}, U_{jy}\}^T$: the displacement vector from node 'i' and 'j' in global coordinate system XY
- $\{f_{ix}, f_{iy}\}^T, \{f_{jx}, f_{jy}\}^T$: the forces vector from node 'i' and 'j' in local coordinate system xy
- $\{F_{ix}, F_{iy}\}^T, \{F_{jx}, F_{jy}\}^T$: the forces vector from node 'i' and 'j' in global coordinate system XY

2.1.2. MATHEMATICAL MODEL OF DISPLACEMENTS. STRESS AND STRAIN CALCULUS

a. Local coordinate system

We write the equation: $[k] \cdot \{u\} = \{f\}$ (1), where:

- $\{u\} = \{u_{ix} \ u_{iy} \ u_{jx} \ u_{jy}\}^T$ is the displacement vector in local coordinate system
- $\{f\} = \{f_{ix} \ f_{iy} \ f_{jx} \ f_{jy}\}^T$ is the force vector in local coordinate system
- $[k] = \frac{EA}{l} \cdot \begin{bmatrix} 1 & -1 \\ -1 & 1 \end{bmatrix}$ is the stiffness matrix in local coordinate system
- E is the Young modulus

b. Global coordinate system

We insert the matrix of coordinate conversion from local to global system marked with $[\lambda]$, having the form presented in relation (2) for a node, and in relation (3) for two nodes.

$$[\lambda] = \begin{bmatrix} \cos(\theta_e) & -\sin(\theta_e) \\ \sin(\theta_e) & \cos(\theta_e) \end{bmatrix} \quad (2)$$

$$[\lambda] = \begin{bmatrix} \cos(\theta_e) & -\sin(\theta_e) & 0 & 0 \\ \sin(\theta_e) & \cos(\theta_e) & 0 & 0 \\ 0 & 0 & \cos(\theta_e) & -\sin(\theta_e) \\ 0 & 0 & \sin(\theta_e) & \cos(\theta_e) \end{bmatrix} \quad (3)$$

In fig.3, it is presented the angle θ_e between the axis X and the element 'e'. The stiffness matrix will be:

$$[k] = \frac{AE}{l} \cdot \begin{bmatrix} 1 & 0 & -1 & 0 \\ 0 & 0 & 0 & 0 \\ -1 & 0 & 1 & 0 \\ 0 & 0 & 0 & 0 \end{bmatrix} \quad (4)$$

Taking into account the matrix $[\lambda]$, we can write the following equations: $\{U\} = [\lambda] \cdot \{u\}$ (5), $\{F\} = [\lambda] \cdot \{f\}$ (6)

where $\{U\}$ and $\{F\}$ are the vectors of nodal displacement and forces in global coordinate system.

From (5) and (6), we acquire: $\{u\} = [\lambda]^{-1} \cdot \{U\}$ (7), $\{f\} = [\lambda]^{-1} \cdot \{F\}$ (8)

We put (7) in (8) and we obtain: $[k] \cdot [\lambda]^{-1} \cdot \{U\} = [\lambda]^{-1} \cdot \{F\}$ (9)

Multiplying at left with $[\lambda]$, we achieve: $[\lambda] \cdot [k] \cdot [\lambda]^{-1} \cdot \{U\} = \{F\}$ (10)

Equilibrium equation in global coordinate system has the form:

$$[K^{(e)}] \cdot [U] = \{F\} \quad (11)$$

Comparing (10) with (11), we obtain the stiffness matrix in global coordinate system for the element 'e': $[K^{(e)}] = [\lambda] \cdot [k] \cdot [\lambda]^{-1}$ (12)

Detailed, the stiffness matrix is:

$$[K^{(e)}] = \begin{bmatrix} \frac{\cos^2(\theta_e) \cdot EA}{l} & \frac{EA \cdot \cos(\theta_e) \sin(\theta_e)}{l} & -\frac{\cos^2(\theta_e) \cdot EA}{l} & -\frac{\cos(\theta_e) \sin(\theta_e) \cdot EA}{l} \\ \frac{\cos(\theta_e) \sin(\theta_e) \cdot EA}{l} & \frac{\sin^2(\theta_e) \cdot EA}{l} & -\frac{\cos(\theta_e) \sin(\theta_e) \cdot EA}{l} & -\frac{\sin^2(\theta_e) \cdot EA}{l} \\ -\frac{\cos^2(\theta_e) \cdot EA}{l} & -\frac{\cos(\theta_e) \sin(\theta_e) \cdot EA}{l} & \frac{\cos^2(\theta_e) \cdot EA}{l} & \frac{EA \cdot \cos(\theta_e) \sin(\theta_e)}{l} \\ -\frac{\cos(\theta_e) \sin(\theta_e) \cdot EA}{l} & -\frac{\sin^2(\theta_e) \cdot EA}{l} & \frac{\cos(\theta_e) \sin(\theta_e) \cdot EA}{l} & \frac{\sin^2(\theta_e) \cdot EA}{l} \end{bmatrix}$$

After determining the stiffness matrix for each element of the truss structure, we calculate the assembled stiffness matrix for the whole system. This matrix has the number of columns and rows dependent on the nodes degrees of freedom. For example, for a system with n nodes, with two degrees of freedom, the assembled stiffness matrix will have the form presented in relation (13).

$$[K] = \begin{bmatrix} K_{1,1} & K_{1,2} & \dots & K_{1,n} & \dots & K_{1,2n-1} & K_{1,2n} \\ K_{2,1} & K_{2,2} & \dots & K_{2,n} & \dots & K_{2,2n-1} & K_{2,2n} \\ \dots & \dots & \dots & \dots & \dots & \dots & \dots \\ K_{2n-1,1} & K_{2n-1,2} & \dots & K_{2n-1,n} & \dots & K_{2n-1,2n-1} & K_{2n-1,2n} \\ K_{2n,1} & K_{2n,2} & \dots & K_{2n,n} & \dots & K_{2n,2n-1} & K_{2n,2n} \end{bmatrix} \quad (13)$$

The elements from the assembled stiffness matrix are corresponding to nodal displacement on the axes of global coordinate system. For example, considering node 1, it has two nodal displacements U_{1X} and U_{1Y} . From (13) corresponding to displacement U_{1X} , we have:

- on column: $K_{1,1}; K_{2,1}; \dots; K_{2n-1,1}; K_{2n,1}$
- on row: $K_{1,1}; K_{1,2}; \dots; K_{1,n}; K_{2,2n-1}; K_{2,2n}$

In the same way, for U_{1Y} , we have:

- on column: $K_{1,2}; K_{2,2}; \dots; K_{2n-1,2}; K_{2n,2}$
- on row: $K_{2,1}; K_{2,2}; \dots; K_{2,n}; K_{2,2n-1}; K_{2,2n}$

Then, the boundary conditions are inserted. The fixed nodes have zero displacements. The column and row corresponding to those displacements 'are cut' from the global assembled matrix. The left matrix is multiplied with the left nodal displacement vector (corresponding to remaining unfixed nodes) and is equaled with the nodal forces vector in the global coordinate system. In this way, it is obtained the displacement for each node. After this operation, we multiply the assembled stiffness matrix from (13) with a nodal displacement vector for the whole system, determining the reaction

forces of the truss structure. The relation used is similar with (11), where the unknown elements are found in matrix {F}.

The next step is to compute the stresses and strains of the bars. First, we determine the displacement of an element 'e' ('d^(e)') using relation (14).

$$d^{(e)} = U_{ix} \cdot \cos(\theta_e) + U_{iy} \cdot \sin(\theta_e) - U_{ix} \cdot \cos(\theta_e) - U_{iy} \cdot \sin(\theta_e) \quad (14)$$

After that, the displacement is divided with the initial length of the element 'e' to obtain its strain. Considering that the loading is in the elastic domain, we can apply the Hooke's law to determine the axial stress: $\sigma^{(e)} = E \cdot \varepsilon^{(e)}$ (15)

To demonstrate the upper theoretical relations previously defined, this method will be used for a particular case defined in this way:

$$l = 2300 \text{ mm}; A = 2250 \text{ mm}^2; F_{3Y} = 500 \text{ kN}; F_{5Y} = 650 \text{ kN}; E = 210000 \text{ MPa}; \nu = 0.3.$$

For the calculus, we follow the schematization from fig.2. We determine the stiffness matrix in the own reference system for each element with (4).

$$[k^{(1)}] = \frac{2250 \cdot 2,1 \cdot 10^5}{2300} \cdot \begin{bmatrix} 1 & 0 & -1 & 0 \\ 0 & 0 & 0 & 0 \\ -1 & 0 & 1 & 0 \\ 0 & 0 & 0 & 0 \end{bmatrix} = \begin{bmatrix} 2,054 \cdot 10^5 & 0 & -2,054 \cdot 10^5 & 0 \\ 0 & 0 & 0 & 0 \\ -2,054 \cdot 10^5 & 0 & 2,054 \cdot 10^5 & 0 \\ 0 & 0 & 0 & 0 \end{bmatrix}$$

$$[k^{(1)}] = [k^{(2)}] = [k^{(3)}] = \dots = [k^{(11)}] \quad (16)$$

We write the angles between axes x and X:

$$\theta_1=60^\circ, \theta_2=0^\circ, \theta_3=120^\circ, \theta_4=0^\circ, \theta_5=60^\circ, \theta_6=0^\circ, \theta_7=120^\circ, \theta_8=0^\circ, \theta_9=60^\circ, \theta_{10}=0^\circ, \theta_{11}=120^\circ \quad (17)$$

We calculate the matrix of coordinate conversion from local to global system and the stiffness matrix for each element 'e' with (18).

$$[K^{(1)}] = [K^{(5)}] = [K^{(9)}] = \begin{pmatrix} 5,136 \cdot 10^4 & 8,896 \cdot 10^4 & -5,136 \cdot 10^4 & -8,896 \cdot 10^4 \\ 8,896 \cdot 10^4 & 1,541 \cdot 10^5 & -8,896 \cdot 10^4 & -1,541 \cdot 10^5 \\ -5,136 \cdot 10^4 & -8,896 \cdot 10^4 & 5,136 \cdot 10^4 & 8,896 \cdot 10^4 \\ -8,896 \cdot 10^4 & -1,541 \cdot 10^5 & 8,896 \cdot 10^4 & 1,541 \cdot 10^5 \end{pmatrix}$$

$$[K^{(2)}] = [K^{(4)}] = [K^{(6)}] = [K^{(8)}] = [K^{(10)}] = \begin{pmatrix} 2,054 \cdot 10^5 & 0 & -2,054 \cdot 10^5 & 0 \\ 0 & 0 & 0 & 0 \\ -2,054 \cdot 10^5 & 0 & 2,054 \cdot 10^5 & 0 \\ 0 & 0 & 0 & 0 \end{pmatrix} \quad (18)$$

$$[K^{(3)}] = [K^{(7)}] = [K^{(11)}] = \begin{pmatrix} 5,136 \cdot 10^4 & -8,896 \cdot 10^4 & -5,136 \cdot 10^4 & 8,896 \cdot 10^4 \\ -8,896 \cdot 10^4 & 1,541 \cdot 10^5 & 8,896 \cdot 10^4 & -1,541 \cdot 10^5 \\ -5,136 \cdot 10^4 & 8,896 \cdot 10^4 & 5,136 \cdot 10^4 & -8,896 \cdot 10^4 \\ 8,896 \cdot 10^4 & -1,541 \cdot 10^5 & -8,896 \cdot 10^4 & 1,541 \cdot 10^5 \end{pmatrix}$$

Considering that the displacements from nodes 1 and 7 are zero, we write the assembled global matrix 'cutting' the rows and columns corresponding to those displacements.

$$[K] = \begin{pmatrix} K_{11} & K_{12} & K_{13} & K_{14} & K_{15} & K_{16} & K_{17} & K_{18} & K_{19} & K_{110} \\ K_{21} & K_{22} & K_{23} & K_{24} & K_{25} & K_{26} & K_{27} & K_{28} & K_{29} & K_{210} \\ K_{31} & K_{32} & K_{33} & K_{34} & K_{35} & K_{36} & K_{37} & K_{38} & K_{39} & K_{310} \\ K_{41} & K_{42} & K_{43} & K_{44} & K_{45} & K_{46} & K_{47} & K_{48} & K_{49} & K_{410} \\ K_{51} & K_{52} & K_{53} & K_{54} & K_{55} & K_{56} & K_{57} & K_{58} & K_{59} & K_{510} \\ K_{61} & K_{62} & K_{63} & K_{64} & K_{65} & K_{66} & K_{67} & K_{68} & K_{69} & K_{610} \\ K_{71} & K_{72} & K_{73} & K_{74} & K_{75} & K_{76} & K_{77} & K_{78} & K_{79} & K_{710} \\ K_{81} & K_{82} & K_{83} & K_{84} & K_{85} & K_{86} & K_{87} & K_{88} & K_{89} & K_{810} \\ K_{91} & K_{92} & K_{93} & K_{94} & K_{95} & K_{96} & K_{97} & K_{98} & K_{99} & K_{910} \\ K_{101} & K_{102} & K_{103} & K_{104} & K_{105} & K_{106} & K_{107} & K_{108} & K_{109} & K_{1010} \end{pmatrix} \quad (19)$$

$$\left\{ \begin{array}{l} K_{11} = k_{331} + k_{333} + k_{114} = 3,08 \cdot 10^5 \\ K_{21} = k_{431} + k_{433} + k_{214} = 2,91 \cdot 10^{-11} \\ K_{31} = k_{133} = -5,14 \cdot 10^4; K_{41} = k_{233} = 8,9 \cdot 10^4; \\ K_{51} = k_{314} = -2,05 \cdot 10^5; \\ K_{12} = k_{341} + k_{343} + k_{124} = 4,37 \cdot 10^{-11} \\ K_{22} = k_{441} + k_{443} + k_{224} = 3,08 \cdot 10^5 \\ K_{32} = k_{143} = 8,9 \cdot 10^4; K_{42} = k_{243} = -1,54 \cdot 10^5; \\ K_{13} = k_{313} = -5,14 \cdot 10^4; K_{23} = k_{413} = 8,9 \cdot 10^4; \\ K_{33} = k_{332} + k_{113} + k_{115} + k_{116} = 5,14 \cdot 10^5 \\ K_{43} = k_{432} + k_{213} + k_{215} + k_{216} = 2,91 \cdot 10^{-11} \\ K_{95} = k_{318} = -2,05 \cdot 10^5 \end{array} \right. \quad (20.a)$$

In (19), the parameters K_{ij} ($i, j = 1..10$) represent the elements of the assembled stiffness matrix $[K]$, and their values are given in (20) and (22). The factors symbolization is: k is the component of stiffness matrix for an element 'e'; a, b are the index the represent the row and column position of k components ($a, b = 1..4$); c represents the number of the studied element 'e' ($c = 1..11$). The parameters that have the value zero, haven't been written in relations (20, 22).

The matrix of force projection that act in each node, in the global reference system, is marked with $\{F\}$ (relation (21)). We exclude nodes 1 and 7 because they have zero displacement.

$$\{F\} = \{F_{2X} \ F_{2Y} \ F_{3X} \ F_{3Y} \ F_{4X} \ F_{4Y} \ F_{5X} \ F_{5Y} \ F_{6X} \ F_{6Y}\}^T = \{0 \ 0 \ 0 \ -5 \cdot 10^5 \ 0 \ 0 \ 0 \ -65 \cdot 10^4 \ 0 \ 0\}^T \quad (21)$$

Using (11), we determine the X,Y displacement of nodes 2..6 (relation (23)).

$$\left\{ \begin{array}{l}
K_{53} = k_{315} = -5,14 \cdot 10^4; K_{63} = k_{415} = -8,9 \cdot 10^4; \\
K_{73} = k_{316} = -2,05 \cdot 10^5; \\
K_{14} = k_{323} = 8,9 \cdot 10^4; K_{24} = k_{243} = -1,54 \cdot 10^5; \\
K_{34} = k_{342} + k_{123} + k_{125} + k_{126} = 4,37 \cdot 10^{-11} \\
K_{44} = k_{442} + k_{223} + k_{225} + k_{226} = 3,08 \cdot 10^5 \\
K_{54} = k_{325} = -8,9 \cdot 10^4; K_{64} = k_{425} = -1,54 \cdot 10^5; \\
K_{15} = k_{134} = -2,05 \cdot 10^5; \\
K_{35} = k_{135} = -5,14 \cdot 10^4; K_{45} = k_{235} = -8,9 \cdot 10^4; \\
K_{55} = k_{334} + k_{335} + k_{337} + k_{118} = 5,14 \cdot 10^5 \\
K_{65} = k_{434} + k_{435} + k_{437} + k_{218} = 2,91 \cdot 10^{-11} \\
K_{75} = k_{137} = -5,14 \cdot 10^4; K_{85} = k_{237} = 8,9 \cdot 10^4; \\
K_{36} = k_{145} = -8,9 \cdot 10^4; K_{46} = k_{245} = -1,54 \cdot 10^5; \\
K_{56} = k_{344} + k_{345} + k_{347} + k_{128} = 4,37 \cdot 10^{-11} \\
K_{66} = k_{444} + k_{445} + k_{447} + k_{228} = 3,08 \cdot 10^5 \\
K_{76} = k_{147} = 8,9 \cdot 10^4; K_{86} = k_{247} = -1,54 \cdot 10^5; \quad (22) \\
K_{37} = k_{136} = -2,05 \cdot 10^5; \\
K_{57} = k_{317} = -5,14 \cdot 10^4; K_{67} = k_{417} = 8,9 \cdot 10^4; \\
K_{77} = k_{336} + k_{117} + k_{119} + k_{1110} = 5,14 \cdot 10^5 \\
K_{87} = k_{436} + k_{217} + k_{219} + k_{2110} = 2,91 \cdot 10^{-11} \\
K_{97} = k_{319} = -5,14 \cdot 10^4; K_{107} = k_{419} = -8,9 \cdot 10^4 \\
K_{1010} = k_{448} + k_{449} + k_{4411} = 3,08 \cdot 10^5 \\
K_{58} = k_{327} = 8,9 \cdot 10^4; K_{68} = k_{427} = -1,54 \cdot 10^5; \\
K_{78} = k_{346} + k_{127} + k_{129} + k_{1210} = 4,37 \cdot 10^{-11} \\
K_{88} = k_{446} + k_{227} + k_{229} + k_{2210} = 3,08 \cdot 10^5 \\
K_{98} = k_{329} = -8,9 \cdot 10^4; K_{108} = k_{429} = -1,54 \cdot 10^5; \\
K_{59} = k_{138} = -2,05 \cdot 10^5; \\
K_{79} = k_{139} = -5,14 \cdot 10^4; K_{89} = k_{239} = -8,9 \cdot 10^4; \\
K_{99} = k_{338} + k_{339} + k_{3311} = 3,08 \cdot 10^5 \\
K_{109} = k_{438} + k_{439} + k_{4311} = 2,91 \cdot 10^{-11} \\
K_{710} = k_{149} = -8,9 \cdot 10^4; K_{810} = k_{249} = -1,54 \cdot 10^5; \\
K_{910} = k_{348} + k_{349} + k_{3411} = 4,37 \cdot 10^{-11}
\end{array} \right.$$

$$U_{2X}=3,138; U_{2Y}=-5,382; U_{3X}=-0,609; U_{3Y}=-11,115; U_{4X}=0,047; U_{4Y}=-11,818; U_{5X}=0,468; U_{5Y}=-11,899; U_{6X}=-3,326; U_{6Y}=-5,814. (23)$$

We insert into the main matrix [U] the displacements of nodes 1 and 7 (relation (24)). The force matrix {F} has the form from relation (25), where there are marked with R_{1X} , R_{1Y} , R_{7X} , R_{7Y} the reaction forces from nodes 1 and 7.

$$[U]= [U_{1X} U_{1Y} U_{2X} U_{2Y} U_{3X} U_{3Y} U_{4X} U_{4Y} U_{5X} U_{5Y} U_{6X} U_{6Y} U_{7X} U_{7Y}]^T (24)$$

$$\{F\}= \{R_{1X} R_{1Y} F_{2X} F_{2Y} F_{3X} F_{3Y} F_{4X} F_{4Y} F_{5X} F_{5Y} F_{6X} F_{6Y} R_{7X} R_{7Y}\}^T (25)$$

In the global stiffness matrix will be inserted the rows and columns corresponding to U_{1X} , U_{1Y} , U_{7X} , U_{7Y} and a new assembled stiffness matrix, [KG], will be 14x14. The relation (26) will be used to determine the reaction forces from nodes 1 and 7.

$$[KG] \cdot [U] = \{F\} \Rightarrow R_{1X} = k_{131} \cdot U_{2X} + k_{141} \cdot U_{2Y} + k_{132} \cdot U_{3X} + k_{142} \cdot U_{3Y};$$

$$R_{1Y} = k_{231} \cdot U_{2X} + k_{241} \cdot U_{2Y} + k_{232} \cdot U_{3X} + k_{242} \cdot U_{3Y};$$

$$R_{7X} = k_{3110} \cdot U_{5X} + k_{3210} \cdot U_{5Y} + k_{1311} \cdot U_{6X} + k_{1411} \cdot U_{6Y}; (26)$$

$$R_{7Y} = k_{4110} \cdot U_{5X} + k_{4210} \cdot U_{5Y} + k_{2311} \cdot U_{6X} + k_{2411} \cdot U_{6Y}.$$

$$\text{Numerically, we obtain: } R_{1X} = 4,427 \cdot 10^5; R_{1Y} = 5,501 \cdot 10^5;$$

$$R_{7X} = -4,425 \cdot 10^5; R_{7Y} = 5,999 \cdot 10^5. (27)$$

Using (14), (15) and the indications from subitem 2.1.2, for each element 'e', we determine the axial stress and strain (relations (28), (29)).

$$\varepsilon_1 = -1,344 \cdot 10^{-3}; \varepsilon_2 = -2,648 \cdot 10^{-4}; \varepsilon_3 = 1,344 \cdot 10^{-3}; \varepsilon_4 = -1,344 \cdot 10^{-3}; \varepsilon_5 = -1,221 \cdot 10^{-4}; \varepsilon_6 = -4,683 \cdot 10^{-4}; \varepsilon_7 = -1,22 \cdot 10^{-4}; \varepsilon_8 = -1,467 \cdot 10^{-3}; \varepsilon_9 = 1,466 \cdot 10^{-3}; \varepsilon_{10} = -2,035 \cdot 10^{-4}; \varepsilon_{11} = -1,466 \cdot 10^{-3}; (28)$$

$$\sigma_1 = -282,308; \sigma_2 = -55,604; \sigma_3 = 282,26; \sigma_4 = -282,222; \sigma_5 = -25,64; \sigma_6 = 98,335; \sigma_7 = -25,624; \sigma_8 = -307,97; \sigma_9 = -307,948; \sigma_{10} = -42,73; \sigma_{11} = -307,885; (29)$$

2.2. METHOD 2

In this method, the strain and stress for each element 'e' is computed using ANSYS. In general, at any finite element analysis program, the next steps must be followed:

- defining the geometry (keypoints and bars)
- defining the element type
- defining material properties (Young modulus, Poisson factor and so on)
- defining the boundary conditions (loadings, displacements and so on)
- meshing the bars
- solving the problem, obtaining and analysing the solution

For this case, following the above steps, we obtain the displacement values in fig.4.a,b (graphical) and fig.5.a,b (numerical).

The stresses are listed in fig.6. The strains can be computed by dividing the stress for each element to Young modulus.

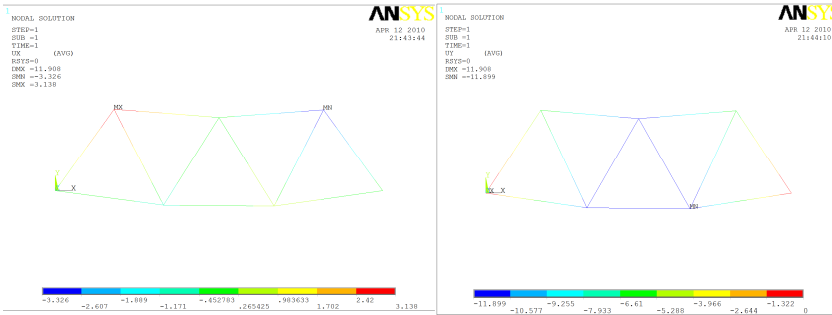


Fig. 4.a.b. graphics of nodal displacements on X,Y axes

PRINT U NODAL SOLUTION PER NODE

***** POST1 NODAL DEGREE OF FREEDOM LISTING *****

LOAD STEP= 1 SUBSTEP= 1
TIME= 1.0000 LOAD CASE= 0

THE FOLLOWING DEGREE OF FREEDOM RESULTS ARE IN THE GLOBAL COORDINATE SYSTE

NODE	UX
1	0.0000
2	3.1383
3	-0.60892
4	0.46640E-01
5	0.46640
6	-3.3256
7	0.0000

MAXIMUM ABSOLUTE VALUES
NODE 6
VALUE -3.3256

PRINT U NODAL SOLUTION PER NODE

***** POST1 NODAL DEGREE OF FREEDOM LISTING *****

LOAD STEP= 1 SUBSTEP= 1
TIME= 1.0000 LOAD CASE= 0

THE FOLLOWING DEGREE OF FREEDOM RESULTS ARE IN THE GLOBAL COORDINATE SYSTEM

NODE	UY
1	0.0000
2	-5.3015
3	-11.115
4	-11.818
5	-11.899
6	-5.8142
7	0.0000

MAXIMUM ABSOLUTE VALUES
NODE 5
VALUE -11.899

Fig.5.a.b. numerical values of nodal displacements

PRINT ELEMENT TABLE ITEMS PER ELEMENT

***** POST1 ELEMENT TABLE LISTING *****

STAT	CURRENT
ELEM	SAXL
1	-282.26
2	-55.597
3	282.26
4	-282.26
5	-25.660
6	98.363
7	25.660
8	-307.92
9	307.92
10	-42.767
11	-307.92

MINIMUM VALUES
ELEM 11
VALUE -307.92

MAXIMUM VALUES
ELEM 9
VALUE 307.92

Fig.6. values of axial stress

3. CONCLUSIONS

From the two methods previously used, we can extract the following conclusions:

- the two calculus variants lead to similar results; the values of displacements and stresses are almost the same, the difference appears only at tenth or hundredth of the value because of the approximation used
- the analytical method used is easy to be applied with a mathematical modelling program (like Matlab, Maple, MathCAD and so on)
- the analytical method can be applied to any form of bridge truss structure, the only parameter that will change is the global assembled stiffness matrix
- the maximum axial stresses are obtained in bars 8 and 11 (almost 308 MPa); if we desire a less stress, we must improve the transversal section area of the bars. For example, for a section area of 3000 mm², the bar 8 will have a stress of 231 MPa, and the bar 11 will have a stress of 230,887 MPa.

4. ACKNOWLEDGMENT

This work was partially supported by the strategic grant POSDRU/88/1.5/S/50783 (2009), co-financed by the European Social Fund – Investing in People, within the Sectoral Operational Programme Human Resources Development 2007-2013.

REFERENCES

1. Dalaban, C., Juncan, N., s.a., Construcții Metalice, Editura Didactică și Pedagogică, București, 1983
2. Dumitru, N., Margine, A., Bazele Modelării în Ingineria Mecanică, Editura Universitaria, Craiova, 2002
3. Ilincioiu, D., Rezistența Materialelor, Ediția a-II-a, Editura ROM TPT, Craiova, 2007
4. Moaveni, S., Finite Element Analysis. Theory and Application with Ansys, Prentice Hall, New Jersey, 1999
5. Negru, M., Bazele Proiectării Asistate de Calculator, Editura Universitaria, Craiova, 2004
6. Zienkiewicz, O., C., Taylor, R., L., The Finite Element Method, fifth edition, Volume 1: The Basis, Butterworth-Heinemann, London, 2000
7. Zienkiewicz, O., C., Taylor, R., L., The Finite Element Method, fifth edition, Volume 2: Solid Mechanics, Butterworth-Heinemann, London, 2000

STUDY OF TECHNOLOGIES FOR RECOVERING SILICONE RUBBER FROM COMPOSITE INSULATORS

Daniel POPESCU

University of Craiova, Faculty of Mechanics

Abstract: The paper presents a technique for recovering silicone rubber used in composite insulators. It is presented the way in which the material is obtained by mechanical stripping, grinding and compacting of the resulting powder. There are also presented the technological characteristics of the obtained silicone rubber.

Keywords: silicone rubber, recovery technique, composite insulator

1. INTRODUCTION

Silicone rubber is a polymer from the elastomers group presenting a set of special physical properties such as:

- resistance to long time exposure to dry temperatures up to 200° C;
- flexible at temperatures between -60 ... -90° C;
- lasting elasticity at both high and low temperatures;
- wear resistant;
- neutral from olfactory and gustatory point of view;
- resistant to external chemical agents;
- good recycling capacity;
- good thermal insulation;

2. STUDY OF THE PROPOSED TECHNOLOGY FOR SILICONE RUBBER RECOVERY

Silicone rubber is a composite material whose physical and chemical characteristics which allow recovery only through mechanical operations, in order to maintain its original characteristics.

For this reason, two variants of mechanical insulation stripping were analyzed. These two variants are presented in the following tables:

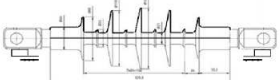
TEHNOLOGIE RECUPERARE CAUCIUC SILICONIC PRIN DECOPERTARE MECANICĂ VARIANTA I								
Nr. op. și fază	Denumirea operației și fazei	Schită operație	Scula	n	t (mm)	s	T _{op} (min)	
							t _b (min)	t _a (min)
1.0	Prins (și desprins) piesa pe mașina de frezat		Freza disc D=160 mm	100 rot/min	4	50 mm/min	14,04	1,2
1.1	Frezat longitudinal cauciuc l=323 mm (de 2 ori)							
2.0	Prins (și desprins) piesa pe strung		Cuțit de retezat	200 rot/min	3	0,2 mm/rot	3,87	2,7
2.1	Strunjire de rețezare cauciuc (2 strunjiri $\Phi 44 \rightarrow \Phi 35$; 16 strunjiri $\Phi 29,5 \rightarrow \Phi 16,3$)							
2.2	Desprins cauciuc prin tragere mecanică		Timpul operativ total pentru varianta I: T _{op1} = 43,66 min					

Table 1 – Silicone rubber recovery – variant 1

TEHNOLOGIE RECUPERARE CAUCIUC SILICONIC PRIN DECOPERTARE MECANICĂ VARIANTA II									
Nr. op. și fază	Denumirea operației și fazei	Schită operație	Scula	n	t	s	T _{op}		
							t _b (min)	t _a (min)	
1.0	Prins (și desprins) piesa pe strung		Cuțit de canelat radial	400 rot/min	3 mm	0,28 mm/rot	1,38	2,7	
1.1	Strunjire exterioară radială cauciuc (2 strunjiri $\Phi 44 \rightarrow \Phi 35$; 16 strunjiri $\Phi 29,5 \rightarrow \Phi 16,3$)								
1.2	Strunjire longitudinală interioară (2 strunjiri $\Phi 44 \rightarrow \Phi 35$; 16 strunjiri $\Phi 29,5 \rightarrow \Phi 16,3$)								
1.3	Rețezare bară fibră sticlă		Cuțit de retezat	200 rot/min	3 mm	0,20 mm/rot	0,23	0,35	
2.1	Separare cauciuc (inelele rezultate) de bara de fibră de sticlă	Timpul operativ total pentru varianta II: T _{op1} = 18,45 min						0,10	0,25

Table 2 – Silicone rubber recovery – variant 2

The products obtained as the result of mechanical stripping are presented in fig. 1 and 2:



Fig 1 – Silicone rubber recovered by milling and ripping



Fig. 2 – Silicone rubber recovered by multiple turning ripping

The technological system used for mechanical stripping of the composite insulator is presented in fig. 3:



Fig. 3 – Technological system used at mechanical stripping

By comparing the operational time for obtaining the technological products in both variants, it can be observed that in the second variant the time is shortened approximately 2.4 times ($t_b = 2.4 t_{b1}$). Also the second variant is more efficient taking into account the amount of boring dust produced.

In order to re-insert the resulting silicone rubber powder back into the production cycle, the following conditions must be met:

- relatively uniform distribution of particles;
- no contamination (with dust or metallic impurities);

The schematic diagram presented in fig. 4 shows the way in which the new technological product (fig. 5) was obtained:

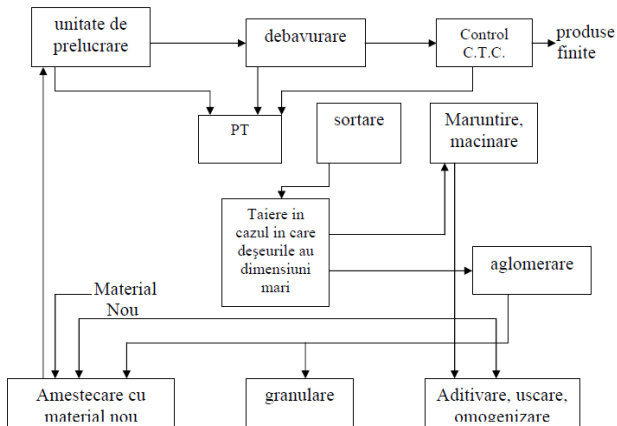


Fig. 4 – Block schematics of silicone rubber recovery technology



Fig. 5 – Silicone rubber powder

For the final technological product (PT) obtained from material stripping from the fiberglass rod of the composite insulator, the following quantities of silicone rubber were taken into account:

Nr. Izolatoare compozite folosite pentru decopertare	Masă izolator (kg/buc)	Masă tijă decopertată (kg/buc)	Masă șpan cauciuc silionic (g/buc)	Masă tile cauciuc silionic (kg/buc)	Obs.
2	2,1	1,125	150	0,500	

Table 3 – Silicone rubber quantities employed for the technological product PT

3. CONCLUSIONS

1. By comparing the two variants, in the second case the material loss is smaller than in the case of the first variant.
2. The grain size obtained through grinding was 1 – 3 mm measured with a KREKER device.
3. The profile of the powder obtained is the one shown in fig. 5.
4. Compacting was performed through specific procedures, taking into account the quantity and quality of recovered silicone rubber, the grinding technology used and the type of adhesive used (polyol polyether, methylene diisocyanate - MDI, dibutylamine - DBA). The end product is shown in fig. 6:



Fig. 6 – Obtained technological product

5. The characteristics of the obtained silicone rubber are presented below:

	Density	Young's Modulus	Yield Strength	Ultimate Tensile	Compressive Strength	Shear Modulus	Ductility	Maximum Temperature	Thermal Expansion	Electrical Resistivity	Electrical Conductivity	Dielectric Strength	Strength-to-Weight	Stiffness-to-Weight Ratio	Resilience	Rupture Work
Natural rubber	920 kg/m ³	0.002 GPa	21 MPa	24 MPa	30 MPa	0.0007 GPa	650 % elongation at break	300 °C	10 ⁻¹⁰ m ³ /°C	5.0E+16 nΩ-m	3.45E-14 % IACS	19.5 MV/m	22.8 kN-m/kg	0.00217 MN-m/kg	5250 kJ/m ³	150 MJ/m ³
Silicone rubber	1290 kg/m ³	0.0065 GPa	2.5 MPa	2.5 MPa	20 MPa	0.01 GPa	180 % elongation at break	200 °C	270 ⁻¹⁰ m ³ /°C	1.0E+22 nΩ-m	1.72E-19 % IACS	22 MV/m	1.94 kN-m/kg	0.00504 MN-m/kg	192 kJ/m ³	4.5 MJ/m ³

Table 4 – Normal/silicone rubber characteristics comparison

6. The variation of the elasticity modulus is given in fig. 7, 8:

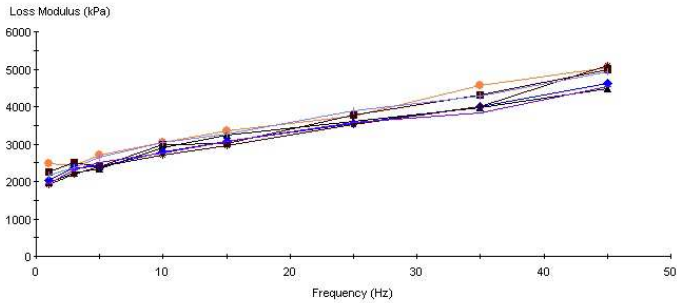


Fig. 7 – Variation of loss elasticity modules

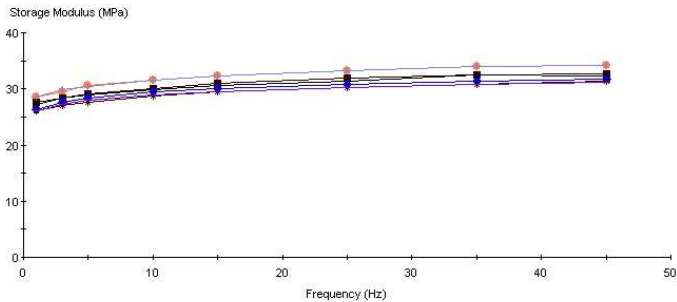


Fig. 8 – Variation of storage elasticity modules

REFERENCES

1. D. POPESCU, Tehnologii de recuperare și utilizare a materialelor din izolatoarele compozite cu izolație externă de cauciuc, Contract de cercetare dezvoltare din planul sectorial de cercetare dezvoltare MEF, 2008
2. D. POPESCU, ST. BUZATU, R. GAVRILA, Annals of DAAAM for 2010 & Proceedings of the 21st International DAAAM Symposium, ISBN 978-3-901509-73-5, ISSN 1726-9679, pp 0003 - Study of Surface Roughness at Finishing of Recovered Silicone Rubber, 2010
3. DEMAG PLASTIC GROUP, Liquid Silicone Rubber Injection Rubber, Processes Machine Technology, Application
4. L. MOLNÁR, A. HUBA, Measurement Of Dynamic Properties Of Silicone Rubbers, Periodica Polytechnica Ser. Mech. Eng. vol. 45, no. 1, pp. 87–94, 2001
5. P. G. SLADE, Electrical Contacts: Principles and Applications, CRC Press. p. 823. ISBN 0824719344, 1999

MODELING WITH FINITE ELEMENT METHOD THE CONVECTIVE HEAT TRANSFER IN CIVIL BUILDING EPS INSULATED WALLS

Mădălina CĂLBUREANU, Raluca MALCIU, Dragoș TUTUNEA,
Alexandru DIMA

Faculty of Mechanics, University of Craiova

Abstract: In this paper we present the analysis of convective heat transfer in the walls of a house insulated with polystyrene. We start the simulation using a real model of a house and then we make the model in Solidworks 2009. We run the model in Solidworks Thermal study after we insert the initial conditions. We notice that the obtained results indicate a problem which occurs inside the brick, the dew-point appearance. Further investigations must be made to solve this problem.

Keywords: convective heat transfer, finite element modeling,

1. INTRODUCTION

Thermal insulation normally has the greatest relative significance for heat loss in new buildings. When the insulation is very thick, thermal bridges have a great relative significance for the total heat loss. In new buildings low temperatures occur mostly around windows and at penetrations for services.

In existing buildings there are a number of problems at present due to a level of humidity that is too high in relation to moisture production, air change rate and the class of thermal bridge. If the surface temperatures were higher, these problems would be more limited in scope.

Thermal insulated walls are crossed from the outside to inside by:

- A heat flow caused by the difference of temperatures;
- A flow of moisture, as water vapor, determined by the difference between the partial pressures of water vapor in moist air from both sides of the walls.

The insulating properties of the materials will get worse, if moisture vapor condenses while crossing the layer of thermal insulation. This effect will be further amplified if freezing occurs in the condensed mois-

ture, which is very probably when the temperatures are negative on the cold insulation front. It becomes obvious in these circumstances that it is important to check the condensing inside the insulation and to action in order to eliminate the condensation danger.

Condensing checking inside insulation layer is realized in several phases as follows:

- Plot the variation of p'' , the water vapor saturation pressure inside insulation, dependent on local temperature variation. It is considered that the temperature varies linearly in the layer of insulating material.
- Plot the variation of p' , the water vapor partial pressure inside the insulation, considering that it varies linearly in the layer of insulating material.
- Comparing the two curves, two situations are possible:
 - a) If the two curves do not intersect and $p'' > p'$ in any section, then there is no danger of condensation within the insulation layer;
 - b) If the two curves intersect, i.e. there are sections where $p'' < p'$, then in that area, called *the condensation zone*, the moisture condensation and all its negative effects will appear.

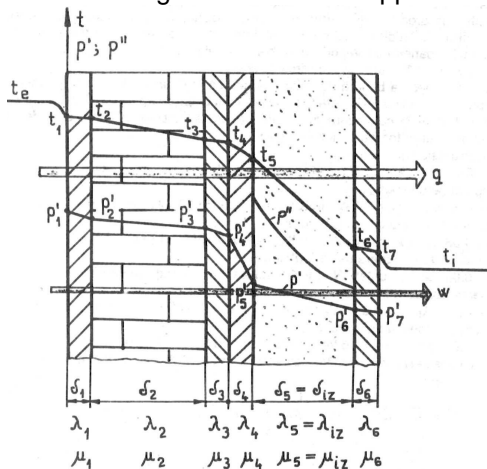


Fig. 1 The variations of temperature, of the moisture vapor saturation pressure p'' and of their partial pressure p' inside a wall provided with thermal insulation.

The dew point temperature is defined as the temperature at which the air becomes saturated with water vapor, when the air is cooled by removing sensible heat. It is very important because it is directly related to the amount of water vapor in the air and it can be used to determine other variables (e.g., vapor pressure, relative humidity, wet bulb temperature and vapor pressure deficit). In addition, the dew point measured during night time is often a good approximation for the minimum temperature of next morning.

The dew-point in brick cladding is typically in the interior of the cladding, increasing the chance of the condensing the moisture within the wall, possibly freezing and causing damage. The thermal bridges occur around the windows due the bad insulation with EPS in those areas.

The EPS is a recyclable product, with a long life– having a stable thermal resistance value, typically above 3 K·m²/W. Its exposure to sun will deteriorate the product, solvents or solvent based materials attack it irreversible and temperatures above 74°C or 165°F will melt it. Its incompatibility with certain thermoplastics and inflammability transform its existence and utilization into a permanent debate.

2. MODELLING HOUSE WALLS WITH FINITE ELEMENT METHOD

As physical model for finite element analysis we use the window of a residential house from Craiova, Romania. The real conditions of building wall execution were used as input data for heat transfer analysis. So, it was considered as follows: the internal temperature 20[°C], the external temperature -15[°C], the interior convection coefficient $\alpha_i = 7$ [W/m²K], the exterior convection coefficient $\alpha_e = 17$ [W/m²K].

Table 1 presents the main dimensions and the material properties for the layers – external plaster including decorative paint, expanded polystyrene, Porotherm brick and interior plaster including paint.

Table 1 Dimensions and material properties for layers

No.	Materials	Width [mm]	Height [mm]	Thermal conductivity [W/mK]	Thick-ness [m]	Mass Density [kg/m ³]	Specific heat [J/kgK]
1	Plaster exterior	3000	2500	0,93	0,02	1800	840
2	Expanded Polystyrene EPS 20	3000	2500	0,029	0,05	30	1460
3	Portherm Brick	3000	2500	0,8	0,2	1300	870
4	Plaster interior	3000	2500	0,93	0,02	1800	840
5	Glass	1360	860	0,74976	0,004	2457,6	834,61
6	Air	1360	860	0,027	0,004	1,1	1000
7	PVC	1500	1000	0,147	0,07	1300	1355

The red frame from the picture of the house (Fig. 2) includes the part of the wall analyzed with the finite element method, using SOLIDWORKS.

The Fig. 3 shows the meshed building wall and all the layers including the window and the model of the building wall in Solidworks programming environment is presented in Fig. 4.

The temperature map in all the layers of the wall was obtained as revealed by Fig. 5.



Fig. 2 The residential house used as real model

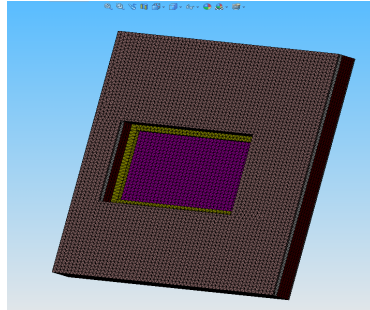


Fig. 3 Building wall meshed

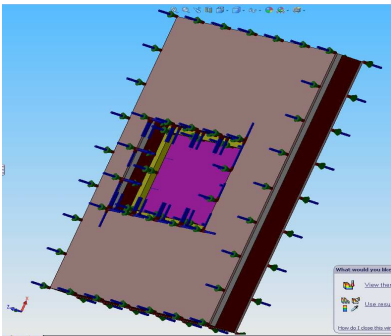


Fig. 4 The building wall modelled in SOLIDWORKS 2009 environment

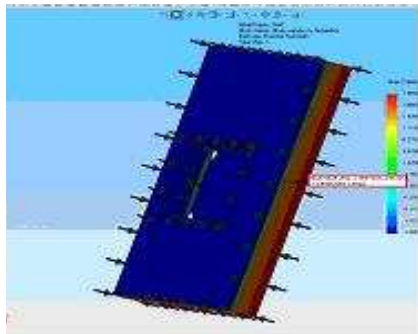


Fig. 5 The temperature map in all the layers of the wall

3. EXPERIMENTAL DATA

Using SOLIDWORKS 2009 programming environment for the finite element analysis, the thermal results are presented in the next pictures. The used mathematical models give us the results from the next SOLIDWORKS panels.

The apparition of the dew-point in the interior of the brick is presented in Figure 6. This is a very bad situation for the chemical and mechanical stability of the material, when the problem is for long time (four-five month per year). The dew-point appears in interior of the brick in node 6424 ($x = 642.29$, $y = -1083$, $z = -337.82$).

It was noticed that the 14°C temperature is obtained for the 1884-1891 nodes ($z = -333.82$) inside the brick.

Figure 7 presents the thermal bridges around the windows with big differences of temperature because of the bad building technology. The resultant gradient of temperature map in the wall is presented in Fig. 8 and the resultant heat flux on Z axis in the wall in Fig. 9.

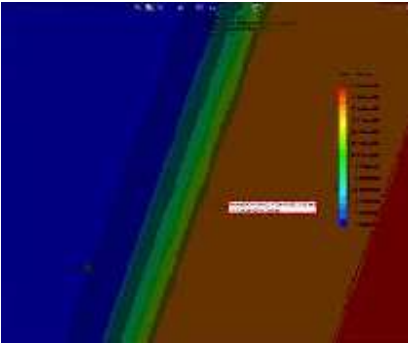


Fig. 6 The dew-point appears in interior of the brick in node 6424 ($x=642.29$, $y=-1083$, $z=-337.82$)

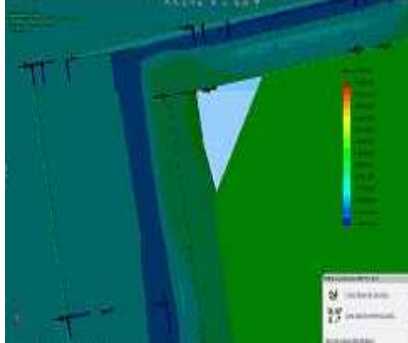


Fig. 7 The thermal bridge around the windows

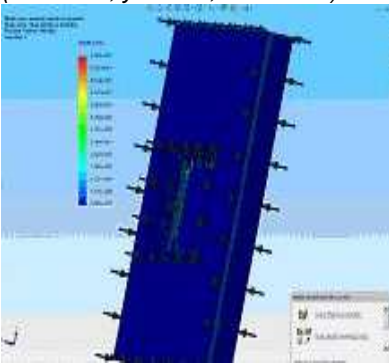


Fig. 8 The resultant gradient of temperature map

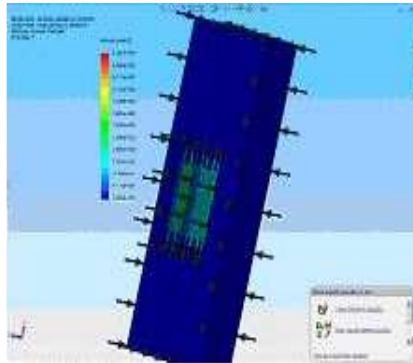


Fig. 9 The resulting heat flux on z axis

The separation between the layers of the wall (brick, EPS insulation, exterior and interior plaster) and the temperature distribution are presented in Fig. 10. Table 2 presents the resultant heating flux distribution per node on X, Y and Z direction and the distribution of the heat flux with the corresponding node coordinates are shown in Table 3. Table 4 presents the node coordinates and the corresponding temperature gradient. The transversal plane where the dew-point occurs (interior of the brick) is represented in Fig. 11. Around the window, the thermal bridge leads to the map presented in Fig. 12, for example in the plane determined by $(-150, 14^\circ, 57)$. The section through the wall including the window shows the thermal heat flux distribution as Fig.13 presents.

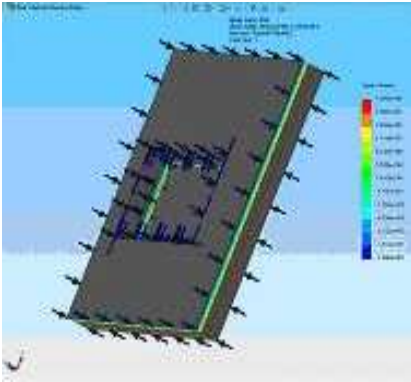


Fig. 10 The separation line between the wall layers and the temperature distribution

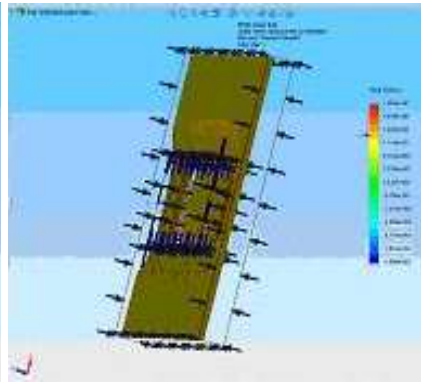


Fig. 11 The transversal plane where the dew-point occurs (interior of the brick)

Table 2 The resultant heating flux distribution per node

Node	HFLUXX	HFLUXY	HFLUXZ	HFLUXN
1	1.08331e+000	5.04996e+000	1.49503e+002	1.49592e+002
2	-4.15171e-005	4.64487e+000	1.49569e+002	1.49641e+002
3	3.59438e-005	4.09991e+000	1.49580e+002	1.49636e+002
4	1.21351e-004	4.09944e+000	1.49564e+002	1.49620e+002
5	-1.43984e+000	4.09718e+000	1.49524e+002	1.49587e+002
6	-5.39643e+000	2.04747e+000	1.49484e+002	1.49595e+002
7	-6.47271e+000	-2.00077e-003	1.49462e+002	1.49602e+002

Table 3 Node coordinates and corresponding heat flux

Node	X (mm)	Y (mm)	Z (mm)	HFLUXN (W/m ²)
6997	294.539	1160.68	-507.705	5.00674e+002
7001	440.495	1157.2	-500.446	4.94665e+002
6947	1028.71	-113.144	-503.961	4.90309e+002
6918	1031.22	936.392	-502.262	4.83897e+002
7008	736.304	1164.33	-503.942	4.83185e+002
7086	-60.7218	-55.1474	-512.288	4.79583e+002
6939	1032.34	174.952	-502.748	4.79200e+002
1544	57.4487	-380.748	-537.817	4.78588e+002
1491	914.591	-380.748	-537.817	4.78346e+002
6931	1032.34	476.078	-502.75	4.77876e+002
6954	935.996	-425.232	-505.456	4.77778e+002
6943	1031.58	18.9316	-501.437	4.76650e+002
6935	1032.42	331.436	-501.888	4.76283e+002

Table 4 Node coordinates and corresponding temperature gradient

Node	X (mm)	Y (mm)	Z (mm)	GRADN (K/m)
1076	596.411	827.156	-532.438	5.54242e+003
1226	541.216	938.204	-533.127	5.54240e+003
1227	612.882	938.204	-533.127	5.54239e+003
1078	612.882	824.871	-533.127	5.54233e+003
1090	291.809	-64.8552	-532.701	5.54232e+003
1113	701.02	747.029	-530.817	5.54232e+003
1098	612.882	824.871	-530.128	5.54232e+003
1079	541.216	824.871	-533.127	5.54232e+003

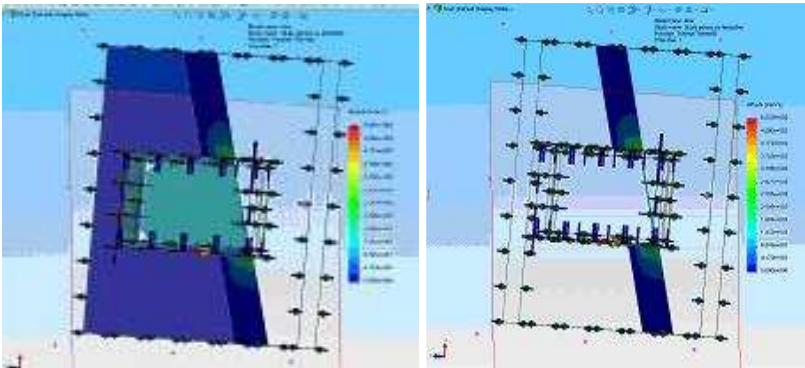


Fig. 12 The resultant heat flux in Fig. 13 Section with the resulting the plane (-150.00, 14°, 57°) heat flux

The most important results show that:

- Thermal bridges around the windows (except the panes) give the largest individual contribution (31.48%).
- The heat loss from the external walls junctions is in the low end (1.3%).
- The heat loss through the windows gives the biggest contribution to the total heat loss.
- In older Romanian buildings (high value) with average thermal bridges the proportion of heat loss from thermal bridges for both building types is 19.20%.
- With a modern Romanian insulation standard (medium value), but unchanged (medium value) thermal bridges, their contribution will rise to 30.32%. This contribution will be 58% with heavy thermal bridges (high value) and reduced to 13% with minimum thermal bridges.
- In low energy buildings (low value) with average thermal bridges the proportion of heat loss from thermal bridges for both building types

is 48.51%. With a modern insulation standard (medium value) but unchanged thermal bridges, their contribution will amount to 30.32%.

It is evident that it is important to assess linear thermal bridges where there are a lot of these around windows and along horizontal lines, while the contribution due to external vertical edges on walls is normally moderate.

4. CONCLUSIONS

The important conclusion is that the EPS insulation has to be thicker than 5 cm at least 8 cm in order to influence the dew-point migration from exterior of the brick to inside EPS cladding for better execution and exploitation.

For a winter in Southern East Europe such in Craiova, Romania, where the medium temperature is -10° , the negative influence of the dew-point occurring in the brick wall is maintained for 4 months annually. Even the high quality of the Porotherm brick as humidity resistance, the negative effects will appear in time. It is necessary to ensure that relative humidity in the room is sufficiently low, in order to avoid condensation in buildings with severe thermal bridges. This is achieved by making sure that moisture production is low and there is a sufficiently large rate of air change. In the case of supplementary insulation on the interior wall side, there may also be a risk that the air change rate has to be increased; this may lead to increased energy consumption.

REFERENCES

1. J. Mohelníková, O. Mišák "Energy Rating Concept and Retrofit of Building Envelopes" in Proceedings of the 5th WSEAS International Conference on Environment, Ecosystems and Development, Venice, Italy, November 20-22, 2006 pp148-152.
2. V. Bukarica, Z. Tomsic, Energy efficiency in Croatian residence and service sector – analysis of potentials, barriers and policy instruments, 3rd IASME/WSEAS Int. Conf. on Energy & Environment, University of Cambridge, UK, February 23-25, 2008, pp 61-66.
3. J. Duffie, W.A. Beckmann, Solar Engineering of Thermal Processes, John Wiley & Sons, New York, 1991.
4. F.P. Incropera, D.P. Witt, Fundamentals of Heat and Mass Transfer. John Willey Sons, New York 1996.
5. OPET CR - Thermal bridges in residential buildings in Denmark, Brno, 2002

INDEX

A

ALEXANDROV Alexander	48
ANOAIICA Paul Gabriel	99
ARA Emre	107
AYKUL Halil	27, 42, 107

B

BOZZINI Fausto	99
----------------	----

C

CĂLBUREANU Mădălina	208
CÂMPIAN Vasile	161
CATANEANU Mihnea	155
CIOLAN Gheorghe	144
COVACIU Dinu	161
CRACIUNOIU Nicolae	3, 15, 62, 124

D

DAHAN Marc	88
DALKIZ Mehmet	42
DIACONESCU Cristian	62
DIMA Alexandru	208
DUMITRU Ilie	155
DUMITRU Nicolae	62, 124

F

FLOREA Daniela	161
----------------	-----

H

HADJOV Kliment	48
HALLIL Giunai	48
HANDA James	130

I

ILINCIOIU Dan	80, 169
IORDACHITA Iulian	130
IOVAN Alina	191
ISPAS Nicolae	144

J

JACKSON L. Robert	3
-------------------	---

K

KARA Emre	27, 42
KURSUN Ali	175

M

MALCIU Raluca	208
MANEA Ion	124
Marcin BALICKI	130
MARGHITU B. Dan	3, 15, 62
MARIN Mihnea	48

MILENOVA Milena	48
MIRIȚOIU Cosmin	80, 169, 191
O	
ÖZYILMAZ Emre	27, 42, 107
P	
POPESCU Daniel	202
POPESCU Simion	155
POPESCU Traian	155
PREDA Ion	144, 161
R	
RACILA Laurentiu	88
Russell TAYLOR	130
S	
SAYMAN Onur	27, 107
SEMENESCU Danel	124

ŞENEL Mahomet	175
SEUNGHUN Lee	15
T	
TUTUNEA Dragoş	208
U	
UNERI Ali	130
V	
VINATORU Matei	155
W	
WILSON W. Everett	3
Z	
ZAMFIRACHE Marius	185